

Memory Effects in Premixed Flames: Unraveling Transient Flame Dynamics with the Flame Particle Tracking Method

Zur Erlangung des akademischen Grades eines

DOKTORS DER INGENIEURWISSENSCHAFTEN

von der KIT-Fakultät für Chemieingenieurwesen und Verfahrenstechnik des

Karlsruher Instituts für Technologie (KIT)

genehmigte

DISSERTATION

von

M.Sc. Thorsten Thomas Zirwes

Tag der mündlichen Prüfung:

28.10.2021

Erstgutachter:

Prof. Dr.-Ing. Henning Bockhorn

Zweitgutachter:

Prof. Dr. rer. nat. habil. Ulrich Maas



This document is licensed under a Creative Commons Attribution-ShareAlike 4.0 International License (CC BY-SA 4.0): <https://creativecommons.org/licenses/by-sa/4.0/deed.en>

Acknowledgments



IRST and foremost, I want to thank Prof. Dr.-Ing. Henning Bockhorn for his enormous support and guidance throughout my time at the Engler-Bunte-Institute. I also want to sincerely thank Dr.-Ing. Feichi Zhang, with whom I had countless scientific discussions and who taught me a lot about combustion simulations. I am grateful for the many helpful discussions with Dr.-Ing. Peter Habisreuther as well as Prof. Dr.-Ing. Dimosthenis Trimis, Prof. Dr.-Ing. Nikolaos Zarzalis and my colleagues at the chair of combustion technology.

Furthermore, I want to thank Prof. Dr. Martin Frank, Dr.-Ing. Jordan A. Denev and Dr. Ivan Kondov from the Steinbuch Centre for Computing for their support. Thanks also to my colleagues Dr. Mehmet Soysal for all the barbecue evenings and Dr. Marco Berghoff for his help with this L^AT_EX template.

During my research, I had the opportunity to partake in many fruitful collaborations. I enjoyed the video calls with Univ.-Prof. Dr. rer. nat. Michael Pfitzner and Dr.-Ing. Maximilian Hansinger discussing partially premixed flames; the work on flame-wall interaction with Prof. Dr.-Ing. Christian Hasse, Matthias Steinhausen, Dr. rer. nat. Thomas Häber and apl. Prof. Dr. Rainer Suntz; the discussions with Dr.-Ing. Arne Scholtissek about flamelet equations; modeling sulfur combustion with Dr.-Ing. Nadia Sebbar and the development of biomass simulation tools with Dr.-Ing. Salar Tavakkol. I want to especially thank Prof. Ping Wang and Prof. Zheng Chen for inviting me to China and to Prashant Shrotriya and Yiqing Wang for their hospitality.

Acknowledgments

Thanks to Philipp Martin for his regex expertise and my friends Daniel, Jacob, Lukas, Simon and Fredi for keeping me motivated during the work on this thesis. Last but not least, I want to thank my parents for their unconditional support.

For this work, resources from the national supercomputer Cray XC40 Hazel Hen and the national supercomputer HPE Apollo Hawk at the High Performance Computing Center Stuttgart (HLRS) and the computational resources ForHLR II and HoreKa at KIT funded by the Ministry of Science, Research and the Arts Baden-Württemberg and DFG (“Deutsche Forschungsgemeinschaft”) were utilized. I gratefully acknowledge the Gauss Centre for Supercomputing e.V. (www.gauss-centre.eu) for the computing time on the GCS supercomputer JUWELS at the Jülich Supercomputing Centre (JSC). Figures have been created with Matplotlib [1] and ParaView [2, 3].

Contents

Acknowledgments	i
1 Introduction and Motivation	1
1.1 The Role of Combustion	1
1.2 Simulation of Combustion Processes	2
1.3 Motivation and Goals	5
1.4 Thesis Outline	7
2 Theoretical Background	9
2.1 Important Quantities for Combustion	9
2.1.1 Mixture Properties	9
2.1.2 Flame Thickness	10
2.1.3 Flame Speed	10
2.1.4 Flame Time Scales	15
2.2 Flame-turbulence Interaction	16
2.3 Flame Stretch	21
2.3.1 Mathematical Representation	21
2.3.2 Geometric Interpretation	24
2.3.3 Physical Interpretation	26
2.3.4 Mean Flame Stretch	27
2.3.5 Related Flame Stretch Concepts	28
2.4 Markstein Numbers and Transient Effects	29
3 Development of Numerical Tools	33
3.1 Efficient DNS Solver for High Performance Computing	33
3.1.1 Balance Equations	33

3.1.2	Thermodynamic Properties	35
3.1.3	Mass Diffusion	36
3.1.4	Transport Properties	36
3.1.5	Finite Volume Method	39
3.1.6	Structure of the DNS Solver	41
3.2	Flame Particle Tracking	42
3.2.1	Theoretical Background	42
3.2.2	Literature Overview	45
3.2.3	Novel Tracking Method based on Barycentric Coordinates	46
3.2.4	Computational Performance	55
3.2.5	Validation	57
3.2.6	Application to Other Physical Setups	60
3.2.7	Summary	61
4	Results and Discussion	63
4.1	Equivalence Ratio Fluctuations in One-dimensional Flames . . .	64
4.1.1	Harmonically Oscillating Upstream Equivalence Ratio . .	65
4.1.2	Evaluation of the Amplitude Response	72
4.1.3	Sudden Change of Equivalence Ratio	75
4.1.4	Evaluation of Flame Relaxation Times	77
4.1.5	Conclusions	80
4.2	Oscillating Laminar Bunsen Flames	82
4.2.1	Computational Setup	82
4.2.2	Steady-state Bunsen Flames	84
4.2.3	Dynamics of Oscillating Bunsen Flames	84
4.2.4	Global Flame Properties	88
4.2.5	Application of Flame Particles	92
4.2.6	Conclusions	97
4.3	Memory Effects in Turbulent Flames	99
4.3.1	Computational Setup	99
4.3.2	Turbulent Flame Speed	101
4.3.3	Simulation of Flame Particles	103
4.3.4	Moderate Flame Stretch Regime	104
4.3.5	Effect of Time Histories on Local Correlations	108
4.3.6	Connection to Oscillating Laminar Flames	113
4.3.7	High Flame Stretch Regime	114
4.3.8	Characteristic Flame Particle Trajectories	116
4.3.9	Regime Overview	120
4.3.10	Conclusions	121
5	Summary	123

6	Zusammenfassung	129
A	Scaling Laws for the Flame Speed	137
B	Tensor Notation and Conventions	143
B.1	OpenFOAM®'s Notation	143
B.1.1	Dyadic Product	144
B.1.2	Dot Product	145
B.1.3	Double Dot Product	146
B.1.4	Other Tensor Operations	146
B.2	Calculus Operators	148
B.2.1	Gradient	148
B.2.2	Divergence	149
B.2.3	Curl	149
B.2.4	Special Cases	150
B.3	Identities	151
B.4	Applications	153
B.4.1	Dissipation Rate	153
B.4.2	Diffusive Momentum Flux	153
B.4.3	Total Normal Stretch	154
C	Additional Equivalence Ratio Fluctuation Plots	155
D	High-frequency Pulsatile Flows	159
D.1	Analytic Expressions for the Pressure Gradient	159
D.2	Computational Setup	162
D.3	Steady-state Pipe Flow	164
D.4	Oscillating Flows	167
D.5	Compressibility Effects	175
D.6	Summary	178
E	Performance Optimizations for Large-scale Parallel Simulations	179
E.1	Computation of Chemical Reaction Rates	180
E.2	Optimization of Chemical Reaction Rate Computations	183
E.2.1	Operator Splitting with Sundials	183
E.2.2	Automatic Code Generation for Fast Chemistry Kernels	184
E.2.3	Evaluation of Performance Improvement	190
E.3	Load Balancing	191
E.3.1	Measurements	193
E.3.2	Load Balancing Implementation	194
E.3.3	Performance Improvement	197
E.4	Parallel Scaling	198

E.5	Summary	200
F	Validation of the DNS Solver	203
F.1	Convection-diffusion Equation	203
F.2	Taylor–Green Vortex	205
F.2.1	2D Taylor–Green Vortex	206
F.2.2	3D Taylor–Green Vortex	208
F.3	Canonical Flame Setups	210
F.3.1	Auto-ignition	211
F.3.2	Freely Propagating Flame	212
F.4	Comparison with Experimental Measurements	214
	List of Figures	219
	List of Tables	227
	Bibliography	229

Introduction and Motivation

1.1 The Role of Combustion

Transitioning to a sustainable energy supply in the future is one of the largest and most pressing challenges of our time. While technologies utilizing renewable energy concepts are on the rise, combustion will play a key role for providing the world's energy for at least the next two decades. In its Energy Outlook 2020 [4], British Petroleum estimates that in 2030, depending on the prognosis model, between 60 % and 80 % of the global primary energy consumption will be provided by oil, gas, biofuels and hydrogen. Similarly, in its business-as-usual prognosis, the International Energy Agency (IEA) predicts that 80 % of the primary energy in 2050 might still be supplied by coal, natural gas, oil and biofuels [5], which is only slightly lower than the current value.

While combustion based technologies will remain a significant factor proportionally in the world's energy supply, the global total energy demand continues to rise. Depending on the model, the world's energy consumption will increase by up to 25 % until 2050 [4]. This increase is mainly driven by India and other emerging Asian economies. As a consequence, even though the share of renewable energy based technologies increases, the growing energy demand will likely lead to an increase of energy provided by fossil fuels in the near future. This trend is also present in many sectors of the economy. For example, while land-based transport technologies will shift toward battery electric vehicles and fuel cells, aviation and

marine transport will continue to be combustion based with a shift from oil-based fuels to biofuels [5].

The use of hydrogen for decarbonizing future power generation has gained increasing interest both in the scientific community and from policy makers. For example, in 2020, the European Union has devised a hydrogen strategy in order to reach carbon neutrality by 2050 [6]. Also in 2020, Germany has introduced its national hydrogen strategy, which outlines the role of hydrogen to reach greenhouse gas neutrality in 2030 in Germany [7]. The goal of these projects is to use electricity from renewable energy sources to produce hydrogen. As carbon-free fuel, hydrogen has the potential to drastically reduce global CO₂ emissions either from conventional combustion or use in fuel cells. It will also be used in the synthesis of fuels to be used in traditional technologies, e.g. in gas turbines or aviation, and as a replacement of fossil hydrogen in the chemical industry. These fuels are commonly called eFuels, because they are ultimately produced from renewably generated electricity, and can be used as chemical energy storage from surplus electricity (Power-To-X). Additionally, hydrogen is considered as an additive for other fuels to improve combustion stability [8]. Due to the importance of hydrogen for the future energy economy, most of the combustion simulations discussed in this work are based on hydrogen flames.

Because combustion based energy systems will be part of the future energy landscape, current issues regarding CO₂ and other greenhouse gas emissions with respect to global warming, as well as other harmful emissions like nitric oxides (NO_x), noise, aerosols and soot have to be addressed. However, the necessary improvement of current technologies in terms of efficiency and the design of novel energy conversion systems to comply with stricter emission limits requires precise knowledge of the underlying physics governing combustion under technically relevant conditions. However, combustion processes are characterized by a large range of relevant time and length scales and many physical processes mutually interacting with each other [9]. This makes experimental and theoretical investigation of combustion difficult and demands further research. Numerical simulations have proven to be an effective way of studying the complexity in combustion processes.

1.2 Simulation of Combustion Processes

Numerical simulations have been established as a useful tool for investigating phenomena in practical engineering applications, especially when experimental

measurements are not possible due to extreme pressures or temperatures, relevant time scales that are too fast to be resolved by currently available measurement techniques, inaccessibility due to complex geometries or simply prohibiting costs for manufacturing experimental rigs [10]. In the last decades, many different simulation techniques have emerged that generally represent a trade-off between accuracy and demands in computational power.

The most accurate simulation technique commonly used is known as direct numerical simulation (DNS). With this method, the fundamental governing equations describing the underlying physical phenomena are solved directly. In the context of combustion, this means that a large number of processes has to be described accurately¹. In this work, the Navier–Stokes equations are used to simulate the flow of gas in the different laminar and turbulent flame configurations. Most combustion processes utilized in engineering applications occur in turbulent flows [11]. Turbulent flow is characterized by vortices, commonly known as turbulent eddies, that enhance mixing and dissipate from larger to smaller vortices. Although this process follows certain statistics [12, 13], turbulent flows are often described as chaotic, which makes accurate simulations challenging.

Another challenging aspect of combustion DNS are the chemical reactions. Even simple fuels like methane react via hundreds of chemical reactions and intermediate chemical species [14]. The reaction rates of these reactions depend exponentially on the temperature and are coupled with each other, complicating an accurate simulation further. Additionally, there is a strong mutual interaction between the turbulent flow structures and the chemical reactions [15, 16]. Lastly, on a micro-scale, molecular diffusion can affect flames and their response to turbulent flows significantly, as each chemical species has its own diffusion coefficient and thereby different diffusion velocity, leading to complex concentration profiles within flames [17].

For moderate turbulence intensities, the flame can be described as a collection of flamelets. This assumes that any part of the turbulent flame can be represented by a corresponding laminar flame, whose shape has been distorted by the turbulent fluctuations. However, the effect of the flame-flow interactions can strongly affect the local flame properties. For example, by wrinkling the flame, parts of the flame get curved, which focuses or defocuses diffusive mass and heat fluxes. This in turn

¹ Some authors use the term DNS in the context of combustion if at least the flow is resolved, but employ simplifications for diffusion (e.g. unity Lewis number) or chemical reactions (e.g. global one-step reaction). In this work, DNS refers to the detailed modeling of not only the flow, but to using the finite rate chemistry model and detailed molecular diffusion as well.

leads to changes in local mixing ratios of fuel and oxidizer, which directly affects the chemical reaction rates and thus the flame speed. This complex process can be formally described by the concept of flame stretch, which is a measurement of how strongly the flame is locally disturbed by the flow. Because of this, a detailed investigation of the effect of flame stretch on local flame properties is necessary to understand the flame dynamics. Therefore, in this work, the focus lies on performing DNS to provide new insights into the effect of unsteady flame stretch on flame speeds in turbulent flames.

DNS of more complex combustion cases has only been possible since the last few decades with the increased computational power of high performance computing (HPC) clusters, more commonly known as supercomputers. The reason is that the aforementioned complex physical processes take place on a large range of time and length scales. The largest relevant length scales, e.g. given by the dimensions of an engine or gas turbine, may be on the order of meters, while the smallest vortices of the turbulent flow and the thickness of the reaction layer in the flames are in the sub-millimeter scale [10]. Similarly, the time scale of the slowest chemical reactions, e.g. NO_x formation, can be more than ten orders of magnitudes apart from the fastest chemical reactions, e.g. radical reactions in partial equilibrium [18]. Since all relevant processes have to be resolved in DNS both spatially and temporally, this leads to an enormous requirement of computational power only available on today's largest supercomputers. However, the insights gained from DNS are invaluable and can help to understand the physical complexity of turbulent flames and ultimately derive simplified models. Some examples of recent combustion DNS include the investigation of ignition phenomena [19], lifted flames [20], spray flames [21, 22], hydrogen flames [23, 24] and moderate or intense low oxygen dilution (MILD) [25].

Due to the large-scale nature of DNS, a single simulation might generate terabytes of data. Evaluating and analyzing this large amount of data poses a challenge even today. Different approaches have been developed to extract useful information from DNS databases [26] like gathering statistical data [27, 28], applying machine learning techniques to simplify the underlying chemical kinetics or abstracting the turbulence-flame interaction [29–32], identifying dissipation elements in reactive flows [33–37] or principal component analysis [38, 39]. However, most of these evaluations are based on instantaneous snapshots from DNS. In reality, the time history of each point on the flame may significantly affect the instantaneously observed flame properties. Studying these transient effects requires special methods, which employ Lagrangian reference frames to track points on the flame

surface. One of these methods is the recently developed flame particle tracking method (FPT), which is a main focus of this work.

1.3 Motivation and Goals

In this work, direct numerical simulations employing detailed diffusion models and the finite rate chemistry model are performed for laminar and turbulent flames on Germany's largest supercomputers. The goal is to apply the recently developed flame particle tracking method to systematically study the effect of the time history or memory effect on the local flame statistics and to derive a model to describe the Damköhler number dependent flame speed and flame stretch correlation.

With the increase in computational power, it becomes feasible to perform large eddy simulations (LES) of complex combustion cases, where parts of the flame are resolved. In this case, accurate models for the computation of local flame speeds have to be utilized. One classical approach is to formulate the local flame speed as a function of the local flame stretch. Although the concept of flame stretch is later introduced in chapter 2, a brief general introduction to the problem is given here. Figure 1.1 on the left shows the correlation between flame speed and flame

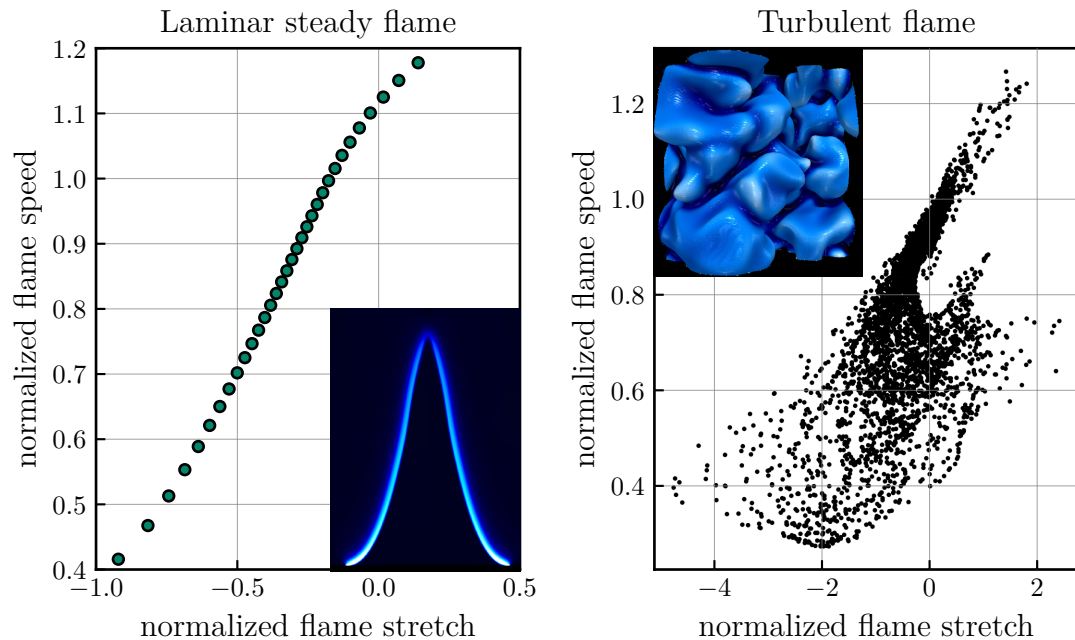


Figure 1.1: Correlation between flame speed and flame stretch of a lean premixed laminar steady hydrogen-air Bunsen flame from section 4.2 (left) and a turbulent premixed lean hydrogen-air flame from section 4.3 (right).

stretch for a laminar, steady-state hydrogen-air Bunsen flame, later presented in section 4.2. The pictogram in the plot on the left shows the heat release rate in the Bunsen flame. Because the flow is laminar, the flame surface is smooth and in steady-state. Plotting the flame speed against the flame stretch on every position along the flame results in a nearly linear correlation. Although the correlation does not necessarily have to be linear, a unique assignment of any stretch value to a flame speed value is possible.

On the right of Fig. 1.1, the flame speed to flame stretch correlation is plotted for a turbulent hydrogen-air flame from section 4.3. The pictogram on the right shows the wrinkled flame front due to the interaction of the flame with the turbulent flow. In the turbulent case, plotting instantaneous values of flame speed against instantaneous values of flame stretch leads to a large scattering [40, 41]. Explaining and adequately modeling this scattering observed in turbulent flames has remained an open question [42–44].

Therefore, the aim of this work is to perform direct numerical simulations to study the local correlation of flame speed and unsteady flame stretch to explain the scattering in turbulent flames. This is done together with the recently developed flame particle tracking (FPT) method [45] to track specific mathematical points, called material points, on the flame over time. These points can be interpreted as massless and sizeless points that co-move with the flame. Instead of evaluating instantaneous snapshots of the flame, which is typically done, the particle tracking allows recording quantities like flame speed and flame stretch over time and thereby the time history of these quantities can be taken into account. Additionally, they can be tracked together with the contributions of the convective, diffusive and chemical reaction rate terms to the species balance equations to understand the thermo-physical trajectories leading to any point on the scattered correlation in Fig. 1.1 on the right.

However, to achieve this goal, several prerequisites have to be met. First, in order to make the large-scale simulation of turbulent flames on supercomputers possible, several performance optimizations of the simulation code have to be implemented in the in-house DNS code, without decreasing the accuracy of the simulation. They are described in appendix E. Secondly, the FPT method suffers in its original implementation as a post-processing step from limitations regarding the total number of flame particles and storage space for the DNS data. Because of this, a new method for FPT based on barycentric coordinates has been developed, which can be used fully parallel during the simulation, allows the use of tens of millions of particles without affecting the total simulation times and also allows

for the first time the fully parallel evaluation of the flame consumption speeds for each flame particle (see section 3.2). The time history analysis in the turbulent flames is supported by studying systematically transient effects in controlled one-dimensional and two-dimensional laminar flames to explain the findings from the turbulent flames. This is also the first time FPT has been applied to laminar flames. With these new insights, the correlation of local flame speeds and local flame stretch can be significantly improved by taking the time history effects on the transiently stretched flame front into account.

1.4 Thesis Outline

Chapter 2 introduces important quantities used throughout this thesis. Additionally, a comprehensive discussion about flame stretch and transient effects is given. Chapter 3 describes the implementation of the DNS solver used for the simulations in this work and gives an overview of the flame particle tracking (FPT) method, including the implementation details of the new in situ tracking approach. Chapter 4 presents the numerical cases for studying transient effects in premixed flames. To systematically investigate the effect of flow transients on the flame dynamics, first one-dimensional flames are studied in section 4.1. Two different one-dimensional flame setups are introduced that allow to quantify the amplitude response of consumption speed to equivalence ratio oscillations and to assess the flame's relaxation time to instantaneous changes in local equivalence ratio. Two-dimensional oscillating laminar Bunsen flames are investigated in section 4.2 to reveal the frequency dependence of the flame speed sensitivity to flame stretch and to propose an improvement to the turbulent flame speed model by Schmid. Also, the flame particle tracking method is for the first time applied to a laminar flame to gain an insight into the flame speed and flame stretch correlation in the oscillating flames. The focus in section 4.3 lies on applying the flame particle tracking method to turbulent flames to systematically investigate the influence of the flame relaxation times on the local flame speed and flame stretch correlation. Two regimes are identified, a moderate and a high flame stretch regime, and the consequence for the modeling of local flame speeds is explored. Chapter 5 and chapter 6 summarize the key findings of this thesis.

Additional information is provided in the appendices: Appendix A provides a derivation of the scaling laws for the laminar flame speed. An overview of the tensor notation used in OpenFOAM® and this work is given in appendix B. Appendix D presents the physical basics of high-frequency pulsatile flows to

supplement the oscillating flame simulations in section 4.2. Appendix E details the performance optimization developed in this work, which in some cases can reduce total simulation times by 70% compared to OpenFOAM®'s standard implementation. Several validation cases for the DNS solver and the optimized code are discussed in appendix F.

Theoretical Background

2.1 Important Quantities for Combustion

Throughout this work, different quantities will be used that are relevant to describe combustion processes, like flame speed, flame thickness and the characteristic flame time scale. These quantities are defined in this section.

2.1.1 Mixture Properties

Since in this work only premixed flames are discussed, where the fuel and oxidizer are fully mixed before the combustion takes place, the mixing ratio of fuel and oxidizer is an important quantity. It is used in this work in terms of the equivalence ratio ϕ and is defined as the ratio of the mass fraction Y of fuel to oxidizer in the current mixture divided by the fuel to oxidizer ratio in the stoichiometric mixture (st):

$$\phi = \frac{\left(\frac{Y_{\text{fuel}}}{Y_{\text{oxidizer}}}\right)}{\left(\frac{Y_{\text{fuel}}}{Y_{\text{oxidizer}}}\right)_{\text{st}}} \quad (2.1)$$

A value of unity indicates a stoichiometric mixture, $\phi < 1$ characterizes lean combustion and $\phi > 1$ means fuel rich conditions. For the definition of the local equivalence ratio ϕ_{loc} , see section 4.1.1.

2.1.2 Flame Thickness

The flame thickness in premixed flames characterizes the thickness of the flame front. Depending on the definition, it may include the preheat zone, reaction zone and parts of the post-oxidation zone. In this work, the flame thickness is evaluated as the thermal thickness δ_{th} :

$$\delta_{\text{th}} \equiv \frac{\max(T) - \min(T)}{\max\left(\frac{\partial T}{\partial x}\right)} \quad (2.2)$$

where T is the temperature through the flame front, from the cold fresh gas temperature to the hot burnt gases. The quantities in Eq. (2.2) are evaluated from a steady-state, planar, freely propagating flame computed with the one-dimensional flame solver by Cantera [46].

In the context of flame-turbulence interaction, described in section 2.2, the flame thickness is often expressed as

$$\delta \equiv \frac{a}{s_{L,0}} \quad (2.3)$$

where a is the thermal diffusivity and $s_{L,0}$ the laminar flame speed. If the flame thickness is computed from the local quantities in turbulent flames, other approaches exist [47, 48].

2.1.3 Flame Speed

The flame speed generally describes how fast a flame moves relative to the gas flow (displacement speed s_d) or how fast it can consume the fuel (consumption speed s_c). For a planar, steady-state laminar flame, s_d and s_c are the same, known as the laminar flame speed $s_{L,0}$. In general, however, displacement and consumption speed differ.

The consumption speed can be derived by integrating the balance equation of the fuel species F by assuming steady-state ($\partial/\partial t = 0$) and a one-dimensional, planar flame:

$$s_c \equiv \frac{\int_{-\infty}^{+\infty} \dot{\omega}_F \, dn}{\rho_0 (Y_{F,b} - Y_{F,0})} \quad (2.4)$$

where ρ is the gas mixture density and $\dot{\omega}_F$ the chemical reaction rate of the fuel species. The subscript 0 indicates the fresh gas conditions and b the burnt gas. In practice for non-planar flames, the integration is performed in the normal direction n of the flame front, although different approaches exist [35, 49].

The displacement speed s_d expresses how fast the flame moves relative to the fluid flow. Because this is an important quantity both for the flame stretch discussed in section 2.3 and the flame particle tracking method from section 3.2, it is discussed here in more detail.

To derive the expression for the displacement speed, consider a general surface moving with the velocity \vec{w} . Its displacement velocity \vec{u}_d is measured relative to the fluid velocity \vec{u} , which is expressed as:

$$\vec{u}_d = \vec{w} - \vec{u} \quad (2.5)$$

Since a flame only propagates in the normal direction, its displacement velocity reduces to the displacement speed s_d :

$$\vec{u}_d = (\vec{u}_d \cdot \vec{n}) \vec{n} = s_d \vec{n} \quad (2.6)$$

The flame front can be described by an iso-surface of a scalar field at an appropriate value. This can for example be iso-surfaces of the temperature or fuel mass fraction at the respective values found at the maximum of the net fuel reaction rate or heat release rate in a laminar, unstretched, one-dimensional flame.

The unit normal vector \vec{n} on this iso-surface can be defined with the gradient of the scalar field at each point on the iso-surface. The definition of the normal vector depends on the direction of the gradient of the scalar field φ at the flame front regarding the fresh and burnt gases.

$$\vec{n} = \pm \frac{\nabla \varphi}{|\nabla \varphi|} \quad (2.7)$$

The sign is positive for gradients pointing in the direction of the fresh gas (like the fuel mass fraction gradient) and negative for gradients pointing toward the burnt gas (like the temperature gradient). By using this sign convention the unit normal vector always points toward the fresh gas.

The movement of a point on the iso-surface can be described by the material derivative of the iso-surface with respect to its total movement velocity \vec{w} :

$$\frac{d\varphi}{dt} = \frac{\partial \varphi}{\partial t} + \vec{w} \cdot \nabla \varphi = 0 \quad (2.8)$$

\vec{w} is the velocity a point has to move to stay on the surface. The absolute movement speed of the flame front s_a is defined as

$$s_a \equiv \vec{w} \cdot \vec{n} \quad (2.9)$$

Dividing Eq. (2.8) by $\pm |\nabla\varphi|$ yields:

$$\frac{1}{\pm |\nabla\varphi|} \frac{\partial\varphi}{\partial t} + \frac{1}{\pm |\nabla\varphi|} \vec{w} \cdot \nabla\varphi = 0 \quad (2.10)$$

Rearranging Eq. (2.10) and moving the norm of the gradient inside the dot product forms:

$$\vec{w} \cdot \underbrace{\frac{\nabla\varphi}{\pm |\nabla\varphi|}}_{=\vec{n}} = - \frac{1}{\pm |\nabla\varphi|} \frac{\partial\varphi}{\partial t} \quad (2.11)$$

Substituting the definition of the unit normal vector of the iso-surface in Eq. (2.7), an expression for the absolute speed of the flame front movement can be obtained:

$$s_a \equiv \vec{w} \cdot \vec{n} = \mp \frac{1}{|\nabla\varphi|} \frac{\partial\varphi}{\partial t} \quad (2.12)$$

Each vector on the flame surface can be split into a normal and tangential part with respect to the surface. The normal part of an arbitrary vector \vec{a} is

$$\vec{a}_n \equiv (\vec{a} \cdot \vec{n}) \vec{n} \quad (2.13)$$

and the tangential part can therefore be computed by subtracting the normal part from the vector:

$$\vec{a}_t = \vec{a} - \vec{a}_n = \vec{a} - (\vec{a} \cdot \vec{n}) \vec{n} \quad (2.14)$$

The absolute velocity of the flame front \vec{w} and the fluid velocity \vec{u} are therefore:

$$\vec{w} = \vec{w}_t + \vec{w}_n = \vec{w}_t + (\vec{w} \cdot \vec{n}) \vec{n} \quad (2.15)$$

$$\vec{u} = \vec{u}_t + \vec{u}_n = \vec{u}_t + (\vec{u} \cdot \vec{n}) \vec{n} \quad (2.16)$$

\vec{w}_t is the surface velocity tangential to itself. Because the flame only propagates normal to itself, the tangential velocity of the flame is usually assumed to arise only from the tangential movement of the fluid:

$$\vec{w}_t = \vec{u}_t \quad (2.17)$$

Using this assumption, the relative motion of the flame front to the fluid flow becomes:

$$\vec{w} - \vec{u} = \underbrace{\vec{w}_t - \vec{u}_t}_{=\vec{u}_t - \vec{u}_t=0} + \vec{w}_n - \vec{u}_n = (\vec{w} \cdot \vec{n}) \vec{n} - (\vec{u} \cdot \vec{n}) \vec{n} \quad (2.18)$$

The displacement speed s_d of the flame is defined as the movement of the flame front, represented by the movement of an iso-surface, relative to its local fluid velocity field \vec{u} :

$$s_d \vec{n} = \vec{w} - \vec{u} = (\vec{w} \cdot \vec{n}) \vec{n} - (\vec{u} \cdot \vec{n}) \vec{n} \quad (2.19)$$

Multiplying Eq. (2.19) by \vec{n} (because the flame propagates normal to itself) to generate a scalar quantity, yields:

$$s_d \equiv (\vec{w} - \vec{u}) \cdot \vec{n} = \vec{w} \cdot \vec{n} - \vec{u} \cdot \vec{n} \quad (2.20)$$

The displacement speed is therefore the difference in the movement of the flame in its normal direction and the normal direction of the fluid velocity.

Substituting $\vec{w} \cdot \vec{n}$ from Eq. (2.12) and \vec{n} from Eq. (2.7) into Eq. (2.20) yields:

$$s_d = \mp \underbrace{\frac{1}{|\nabla\varphi|} \frac{\partial\varphi}{\partial t}}_{=\vec{w} \cdot \vec{n}} - \underbrace{\vec{u} \cdot \frac{\nabla\varphi}{\pm|\nabla\varphi|}}_{=\vec{u} \cdot \vec{n}} \quad (2.21)$$

Factoring out the inverse gradient norm and accounting for the signs, the expression for s_d becomes:

$$s_d = \frac{1}{\mp|\nabla\varphi|} \left(\frac{\partial\varphi}{\partial t} + \vec{u} \cdot \nabla\varphi \right) = \frac{1}{\mp|\nabla\varphi|} \frac{D\varphi}{Dt} \quad (2.22)$$

The expression inside the parentheses is the substantial derivative of the scalar field φ in the volume of the computational domain moving within the fluid velocity field \vec{u} or $D/Dt = \partial/\partial t + \vec{u} \cdot \nabla$. This is not to be confused with the material derivative $d/dt = \partial/\partial t + \vec{w} \cdot \nabla$ of the (iso-)surface from Eq. (2.8), formed by constant values of φ , moving with the surface velocity \vec{w} .

If φ is chosen to be a scalar for which a balance equation is solved in the simulation, the material derivative of the scalar field from Eq. (2.22) is a known quantity in the simulation. Its value on the iso-surface defining the flame front can therefore be used to represent the displacement speed. Choosing the fuel mass fraction for representing the iso-surface, the substantial derivative can be substituted from

the balance equation of species masses (see also the discussion about balance equations in section 3.1.1 and Eq. (3.4)):

$$\rho \frac{DY_F}{Dt} = \dot{\omega}_F - \nabla \cdot \vec{j}_F \quad (2.23)$$

so that

$$\vec{n} = \left(\frac{\nabla Y_F}{|\nabla Y_F|} \right)_{Y_F=Y_{F,iso}} \quad (2.24)$$

$$s_d = - \left(\frac{1}{|\nabla Y_F|} \frac{DY_F}{Dt} \right)_{Y_F=Y_{F,iso}} = - \frac{1}{\rho |\nabla Y_F|} \left(\dot{\omega}_F - \nabla \cdot \vec{j}_F \right) \quad (2.25)$$

In the case of the fuel mass fraction as iso-surface, the displacement speed can be divided into the contributions from diffusion $\nabla \cdot \vec{j}_F$ and chemical reactions $\dot{\omega}_F$. By inserting the definition of the diffusive mass flux from Eq. (3.18) following a Fick-like approach, the displacement speed becomes:

$$s_d = - \frac{\dot{\omega}_F}{\rho |\nabla Y_F|} - \frac{1}{\rho |\nabla Y_F|} \nabla \cdot (\rho D_{m,F} \nabla Y_F) \quad (2.26)$$

The second term on the r.h.s. of Eq. (2.26) can be further split into two components. Multiplying Eq. (2.24) by $|\nabla Y_F|$ yields:

$$\nabla Y_F = \vec{n} |\nabla Y_F| \quad (2.27)$$

Therewith, the second term reads:

$$\frac{1}{\rho |\nabla Y_F|} \nabla \cdot (\rho D_{m,F} \nabla Y_F) = \frac{1}{\rho |\nabla Y_F|} \nabla \cdot (\rho D_{m,F} \vec{n} |\nabla Y_F|) \quad (2.28)$$

Using the product rule, the divergence operator is split into:

$$\nabla \cdot (\rho D_{m,F} \vec{n} |\nabla Y_F|) = \rho D_{m,F} |\nabla Y_F| \nabla \cdot \vec{n} + \vec{n} \cdot \nabla (\rho D_{m,F} |\nabla Y_F|) \quad (2.29)$$

Substituting Eq. (2.29) back into Eq. (2.28) yields:

$$\frac{1}{\rho |\nabla Y_F|} \nabla \cdot (\rho D_{m,F} \nabla Y_F) = D_{m,F} \nabla \cdot \vec{n} + \frac{1}{\rho |\nabla Y_F|} \vec{n} \cdot \nabla (\rho D_{m,F} |\nabla Y_F|) \quad (2.30)$$

The directional derivative of an arbitrary scalar a into a direction \vec{b} is defined as:

$$\nabla a \cdot \frac{\vec{b}}{|\vec{b}|} \equiv \frac{\partial a}{\partial b} \quad (2.31)$$

Taking the dot product of Eq. (2.24) with \vec{n} , multiplying by $|\nabla Y_F|$ and comparing with the directional derivative results in:

$$\nabla Y_F \cdot \vec{n} = |\nabla Y_F| \equiv \frac{\partial Y_F}{\partial n} \quad (2.32)$$

With Eq. (2.30), Eq. (2.31) and Eq. (2.32), the local displacement speed becomes:

$$s_d = \underbrace{-\frac{\dot{\omega}_F}{\rho |\nabla Y_F|}}_{s_{d,\text{chem}}} - \underbrace{D_{m,F} \nabla \cdot \vec{n}}_{s_{d,\text{diff,tang}}} - \underbrace{\frac{1}{\rho |\nabla Y_F|} \frac{\partial}{\partial n} \left(\rho D_{m,F} \frac{\partial Y_F}{\partial n} \right)}_{s_{d,\text{diff,norm}}} \quad (2.33)$$

The first term on the r.h.s. is the movement of the flame front driven by chemical reactions. The second term is the tangential component of the influence of diffusion and is a function of the curvature $\nabla \cdot \vec{n}$. The third term describes the effect of diffusion in the normal direction.

In contrast to the consumption speed, which is independent of the choice of iso-surface, the displacement speed strongly depends on the choice of iso-surface. To minimize this dependency, the density weighted displacement speed s_d^* is defined as:

$$s_d^* = \frac{\rho}{\rho_0} s_d = \frac{\rho}{\rho_0} (\vec{w} - \vec{u}) \cdot \vec{n} = \frac{\rho}{\rho_0} \frac{1}{|\nabla \varphi|} \frac{D\varphi}{Dt} \quad (2.34)$$

where ρ_0 is the density in the unburnt mixture. Recently, more work has been focused on the relationship between consumption and displacement speed [50], based on analyses from flame stretch theory.

2.1.4 Flame Time Scales

Combustion is governed by many different time scales. There is not only a distinction between the time scale of the flame and the flow, but also between different processes like reaction and diffusion. In addition, chemical time scales can be defined for every species or chemical reaction. In this work, the characteristic time scale for the flame is defined as the flame transit time

$$\tau_c \equiv \frac{\delta_{\text{th}}}{s_{L,0}} \quad (2.35)$$

where the thermal thickness δ_{th} and laminar flame speed $s_{L,0}$ are evaluated in a freely propagating flame. It is the characteristic time required to cross the flame front. This time scale is also sometimes referred to as chemical time scale.

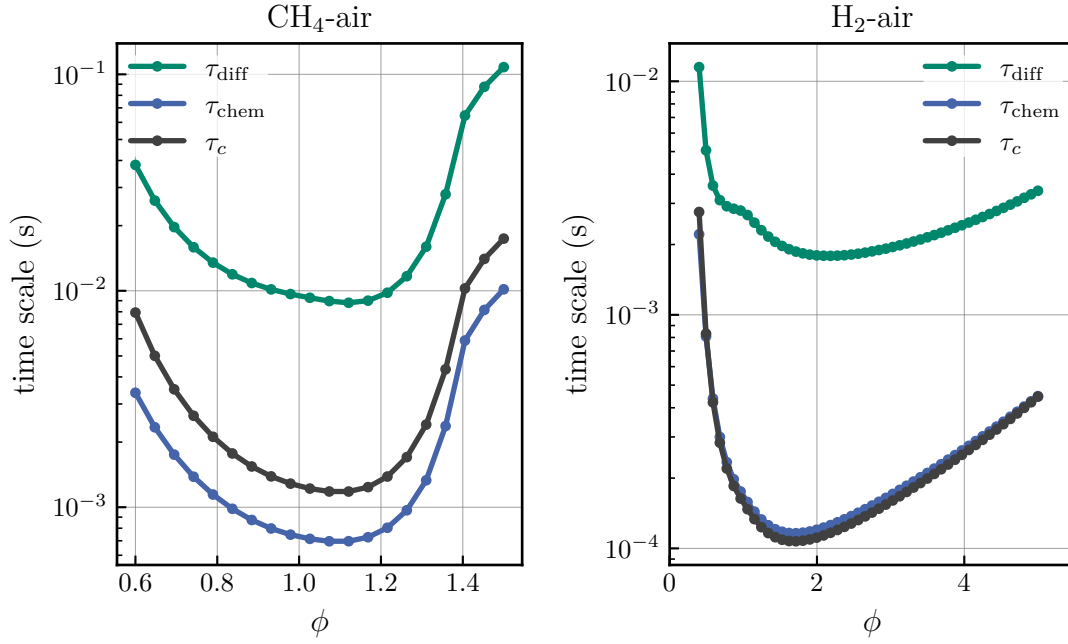


Figure 2.1: Different time scales evaluated from freely propagating flames at atmospheric conditions according to Eqs. (2.35) to (2.37). Hydrogen flames are computed with a reaction mechanism by Li et al. [51] and methane flames by a reaction mechanism by Kee [52].

Figure 2.1 shows the flame transit time τ_c together with two possible definitions of chemical and diffusive time scales for methane and hydrogen-air flames at atmospheric conditions:

$$\tau_{\text{chem}} = \rho_0 (\max(T) - \min(T)) \left(\frac{c_p}{\dot{q}} \right)_{\text{at position of } \max(\dot{q})} \quad (2.36)$$

$$\tau_{\text{diff}} = \frac{\delta_{\text{th}}^2}{a_0} \quad (2.37)$$

Here, c_p is the isobaric heat capacity of the gas mixture and \dot{q} the heat release rate (see section 3.1.1 for more details). Again, all quantities are evaluated from freely propagating flames, with the thermal diffusivity a_0 evaluated in the unburnt gas. Especially for the hydrogen flames, τ_{chem} and τ_c show a good agreement.

2.2 Flame-turbulence Interaction

The properties discussed so far have been related to laminar flames. However, based on the laminar flame properties, i.e. flame speed and thickness, a characterization of flame-turbulence interaction can be approximated. As described in the introduction in chapter 1, vortices of different lengths and velocities cause

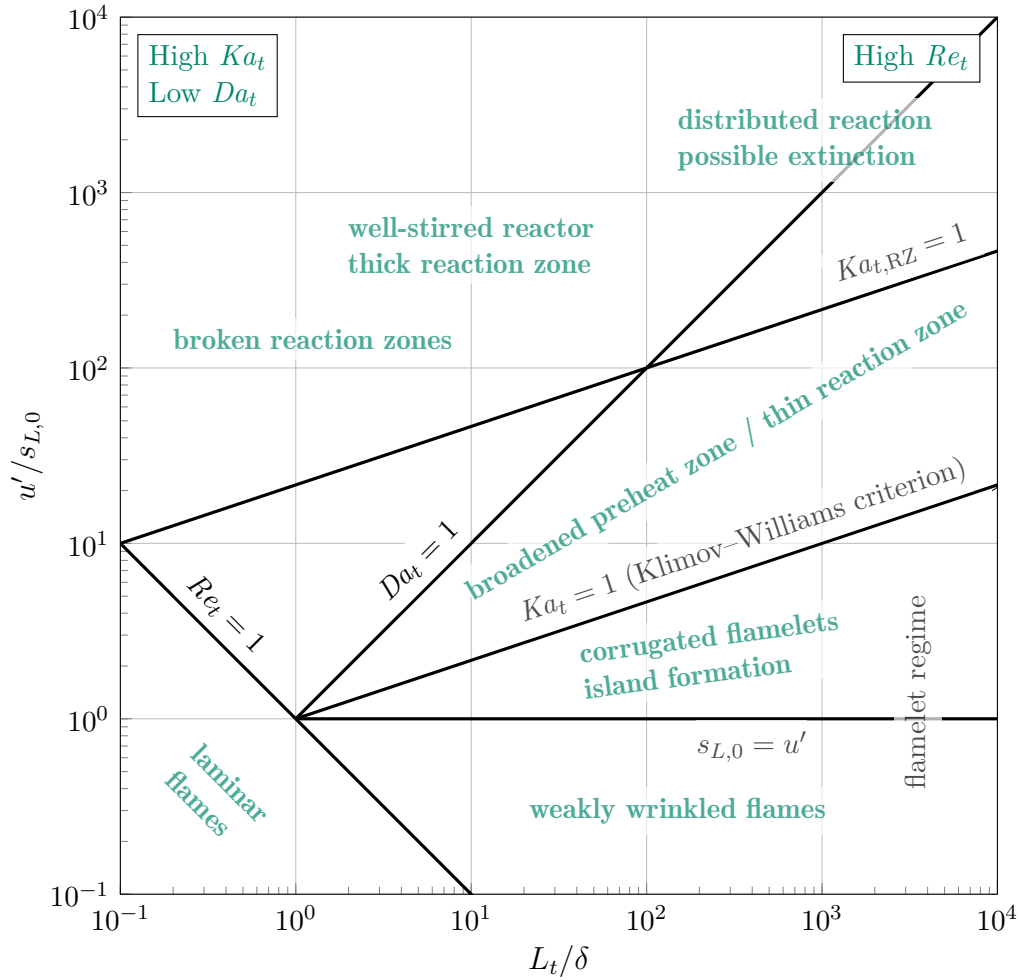


Figure 2.2: Composed Borghi-Peters regime diagram for premixed flame-turbulence interaction assuming $Pr = 1$ and $Ka_{t,RZ} = 1 \hat{=} Ka_t = 100$.

fluctuations in turbulent flows. These vortices interact with the flame. Depending on the global turbulence characteristics of the flow, more specifically the integral length scale L_t and the turbulent velocity fluctuations u' , compared to the characteristic length and velocity of a laminar flame, different interaction regimes can be identified.

The influence of turbulence on premixed flames is often described by the regime diagram by Borghi [15] and Peters [16, 53], with additions by Abdel et al. [54] and Poinot et al. [55], shown in Fig. 2.2. It should be noted that this is only an

idealized view on flame-turbulence interaction [56]. For the construction of the regime diagram, three dimensionless numbers are defined:

$$Re_t = \frac{u' L_t}{\nu} \quad (2.38)$$

$$Da_t = \frac{\tau_{\text{flow}}}{\tau_{\text{chem}}} \quad (2.39)$$

$$Ka_t = \frac{\tau_{\text{chem}}}{\tau_{\text{Kol}}} \quad (2.40)$$

The first characteristic number is the turbulent Reynolds number Re_t . It can be regarded as the ratio of turbulent momentum transport to laminar momentum transport. ν is the kinematic viscosity of the gas. For $Re_t \ll 1$, flames are considered laminar. L_t is the integral length scale of the turbulent flow and u' is the root mean squared velocity fluctuation of the turbulent flow. Re_t can be expressed in terms of the characteristic flame properties by using the Prandtl number $Pr = \nu/a$, where a is the thermal diffusivity. With Eq. (2.3), the turbulent Reynolds number can be expressed as

$$Re_t = \frac{u' L_t}{a Pr} \stackrel{\text{Eq. (2.3)}}{=} \frac{u' L_t}{\delta_{sL,0} Pr} \quad (2.41)$$

The turbulent Damköhler number compares the time scale of the flow with the time scale of the chemical reactions or the flame. For low Damköhler numbers $Da_t \ll 1$, the time scale of the flow or mixing is much smaller than that of the chemical reactions, leading to a well-stirred reactor condition. With Eq. (2.3) and using the length scales and characteristic velocities of the flow and flame, the turbulent Damköhler number can be written as:

$$Da_t = \frac{\left(\frac{L_t}{u'}\right)}{\left(\frac{\delta}{s_{L,0}}\right)} \quad (2.42)$$

The turbulent Karlovitz number compares the time scales of the flame with the smallest time scales of the flow, the Kolmogorov time scale τ_{Kol} . Again, defining the time scales by the characteristic length scales and velocities, and using that the Reynolds number at the Kolmogorov scale is unity

$$Re_{\text{Kol}} = \frac{u_{\text{Kol}} \eta}{\nu} = 1 \quad (2.43)$$

where u_{Kol} is the characteristic velocity at the Kolmogorov scale, the turbulent Karlovitz number becomes

$$Ka_t = \frac{\frac{\delta}{s_{L,0}}}{\frac{\eta}{u_{\text{Kol}}}} \stackrel{\text{Eq. (2.43)}}{=} \frac{\frac{\delta}{s_{L,0}}}{\frac{\eta^2}{\nu}} \stackrel{\text{Eq. (2.3)}}{=} \frac{\frac{\delta}{s_{L,0}}}{\frac{\eta^2}{Pr \frac{\delta}{s_{L,0}}}} = \frac{\delta^2}{\eta^2} Pr \quad (2.44)$$

where η is the Kolmogorov length. In this way, the turbulent Karlovitz number can be regarded as the ratio of the squared flame thickness to the squared Kolmogorov length. An alternative definition of the turbulent Karlovitz number compares the length scale of the reaction layer within the flame front to the Kolmogorov length. For most flames, the reaction layer is approximately one tenth of the length scale of the flame front, so that the turbulent Karlovitz number with respect to the reaction zone (RZ) thickness becomes:

$$Ka_{t,\text{RZ}} = \frac{(0.1\delta)^2}{\eta^2} Pr \quad \text{or} \quad Ka_{t,\text{RZ}} = 1 \hat{=} Ka_t = 100 \quad (2.45)$$

The different regimes in Fig. 2.2 can now be explored using these characteristic numbers. On the bottom left, $Re_t \ll 1$ marks the laminar flame regime. On the bottom right, the velocity fluctuations are smaller than the flame speed $u' \ll s_{L,0}$, so that the flame front is only weakly deformed. Above that domain, $u' > s_{L,0}$ but the smallest length scales of the flow η are larger than the flame thickness δ or $Ka_t < 1$. Because of this, the flame is corrugated but the turbulence cannot penetrate the flame front, leaving its inner structure intact. In this regime, the turbulent flame speed s_T , which measures the global fuel consumption rate, increases as a consequence of the increase in flame surface area. This is known as Damköhler's first hypothesis or the regime of large scale turbulence [57]. Because of this, the turbulent flame speed can be approximately expressed as

$$\frac{s_T}{s_{L,0}} = \frac{A_t}{A_0} \quad (2.46)$$

where A_t is the surface area of the turbulent flame and A_0 the flame surface area of a flame in laminar flow in the same setup. In this regime, the flame can be considered as a collection of laminar flame segments placed into the turbulent flow, called flamelets. Therefore, this regime is also known as the flamelet regime.

Moving higher in the regime diagram, the Kolmogorov length becomes smaller than the flame front $Ka_t > 1$ but is still larger than the reaction zone thickness $Ka_{t,\text{RZ}} < 1$. Therefore, the reaction zone is mostly unaffected by the turbulent fluctuations, but the preheat zone becomes broadened due to vortices penetrating into the

flame front and enhancing the mixing [58]. Moving further above this regime, eventually the Kolmogorov length can penetrate the reaction zone ($Ka_{t,RZ} > 1$) and the mixing time scales become smaller than the chemical time scales ($Da_t < 1$), leading to broadened reaction zones. In this limit, the influence of the turbulence on the turbulent flame speed can be described by an increase in the effective diffusion coefficients. This is known as Damköhler's second hypothesis or small scale turbulence. With the increase in computational power, direct numerical studies of these effects are becoming possible [23, 56, 59]. From thermal theory, it is known that the flame speed of a laminar flame can be estimated as (see appendix A for the details):

$$s_{L,0} \propto \sqrt{\frac{a}{\tau_{\text{chem}}}} \quad (2.47)$$

In analogy to this, the turbulent flame speed can be expressed as

$$s_T \propto \sqrt{a + a_t} \quad (2.48)$$

where a_t is the turbulent thermal diffusivity. Dividing this by Eq. (2.47), considering only the diffusivity dependence and using $a_t \sim u' L_t$ and $a = \nu$ for $Pr = 1$ yields

$$\frac{s_T}{s_{L,0}} \propto \sqrt{1 + \frac{a_t}{a}} = \sqrt{1 + \frac{u' L_t}{\nu}} = \sqrt{1 + Re_t} \stackrel{Re_t \gg 1}{\approx} \sqrt{Re_t} \quad (2.49)$$

For a more in-depth discussion of the regime diagram and flame-turbulence interaction, see [9–11, 14, 17, 60–65].

Schmid [66, 67] developed a model for the turbulent flame speed that describes its dependence based on u' and Da_t :

$$\frac{s_T}{s_{L,0}} \approx 1 + \frac{u'}{s_{L,0}} (1 + Da_t^{-2})^{-\frac{1}{4}} \quad (2.50)$$

In the limit of $Da_t \gg 1$, this relation reduces to $s_T = s_L + u'$, which corresponds to Eq. (2.46). For $Da_t \ll 1$, Eq. (2.49) is recovered [66]. This model has been used in previous simulations [68, 69] and is later discussed in section 4.2.

So far, flame-turbulence interaction has been considered for global properties like the turbulent flame speed based on global characteristic numbers like the turbulent Karlovitz number and the turbulent Damköhler number. However, to understand the cause for the effect of turbulent fluctuations on the flame, the local interaction of flames with the non-uniform turbulent flow have to be considered. A fundamental quantity, that describes how strongly flow non-uniformities affect the flame, is the flame stretch. It measures how strongly the flame is deformed,

thus leading to a change in diffusive fluxes and in turn chemical reaction rates, and thus changing the local flame speeds. Because the flame stretch and flame speed interaction plays a key role for flame dynamics, flame stretch is discussed in the next section in detail.

2.3 Flame Stretch

As shown in the introduction in Fig. 1.1, flame stretch is a key quantity directly affecting the local flame speed. Because of this, its significance for the memory effect in turbulent flames discussed in section 4.3 and a comprehensive discussion on flame stretch, its definition as well as physical interpretation is given in this section.

2.3.1 Mathematical Representation

The concept of flame stretch was introduced by Karlovitz [70] and later more formally defined [71, 72]. Flame stretch K is the Lagrangian time derivative of the logarithmic area of a surface element δA on the flame front [73]:

$$K(p, q, t) \equiv \frac{1}{\delta A(p, q, t)} \frac{d(\delta A(p, q, t))}{dt} \quad (2.51)$$

p and q are the coordinates on the curvilinear surface local coordinate system. Therefore, flame stretch is a local quantity defined at every point on the flame surface. A more commonly used notation is [74–78]:

$$K \equiv \frac{1}{A} \frac{dA}{dt} \quad (2.52)$$

Again, A is the area of an infinitesimal surface element.

Equation (2.52) can be expressed in terms of the local velocity of the iso-surface \vec{w} :

$$K \equiv \frac{1}{A} \frac{dA}{dt} = \nabla_t \cdot \vec{w} \quad (2.53)$$

More specifically, \vec{w} is the movement velocity of points on the surface and ∇_t the tangential gradient operator.

The term $\nabla_t \cdot \vec{w}$ shows that the change in area is created when two adjacent points on the surface move with different velocities \vec{w} . Therefore, their relative distance and therewith the area of surface elements will change over time (see Fig. 2.3).

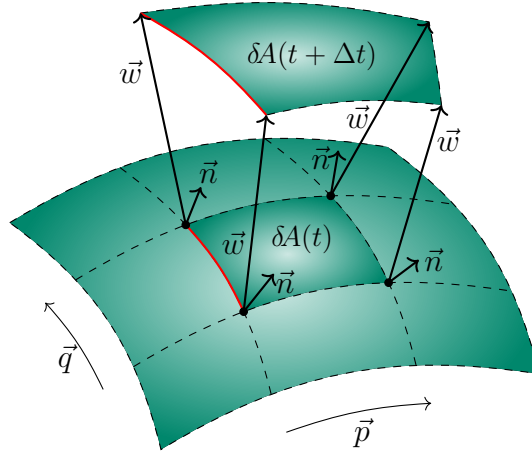


Figure 2.3: Stretch resulting from gradients of the absolute velocity \vec{w} along the surface ($\nabla_t \cdot \vec{w} \neq 0$). This means that the points on the surface move in different directions and/or with different speeds. Therefore, the distance between the points (red line) changes and therewith the area of the surface elements δA .

This difference in movement is only relevant along the surface since all points are by definition located on the surface. So instead of using the divergence operator

$$\nabla \cdot \vec{a} \equiv \vec{e}_x \cdot \frac{\partial \vec{a}}{\partial x} + \vec{e}_y \cdot \frac{\partial \vec{a}}{\partial y} + \vec{e}_z \cdot \frac{\partial \vec{a}}{\partial z} \quad (2.54)$$

the tangential divergence operator has to be applied

$$\nabla_t \cdot \vec{a} \equiv \vec{e}_p \cdot \frac{\partial \vec{a}}{\partial p} + \vec{e}_q \cdot \frac{\partial \vec{a}}{\partial q} \quad (2.55)$$

where \vec{a} is an arbitrary vector field, \vec{e}_x , \vec{e}_y and \vec{e}_z are the unit base vectors of a Cartesian coordinate system and \vec{e}_p and \vec{e}_q (see Fig. 2.3) are the unit base vectors of the tangent plane coordinate system of the surface. Another way of expressing the tangential divergence operator is by taking the divergence operator and removing the normal component. The projection of a gradient in the normal direction can be expressed with directional derivatives. Since the stretch expression involves gradients of vectors, which yield rank 2 tensors, this projection in the normal direction has to be done twice in order to obtain a scalar:

$$\nabla_n \cdot \vec{a} \equiv \vec{n} \cdot (\vec{n} \cdot \nabla \vec{a}) \quad (2.56)$$

With this result, the flame stretch can be expressed as:

$$K = \nabla_t \cdot \vec{w} = \nabla \cdot \vec{w} - \nabla_n \cdot \vec{w} = \nabla \cdot \vec{w} - \vec{n} \cdot \vec{n} \cdot \nabla \vec{w} \quad (2.57)$$

A useful expression is obtained by splitting the velocity vector \vec{w} into its tangential and normal components and substituting it back in Eq. (2.53) (see also appendix B.4.3 for details):

$$K = \nabla_t \cdot \vec{w} = \nabla_t \cdot (\vec{w}_t + \vec{w}_n) = \nabla_t \cdot \vec{w}_t + \nabla_t \cdot \vec{w}_n = \underbrace{\nabla_t \cdot \vec{w}_t}_{\text{total tangential strain}} + \underbrace{(\vec{w} \cdot \vec{n}) \nabla \cdot \vec{n}}_{\text{total normal strain}} \quad (2.58)$$

Equation (2.58) identifies the two components of flame stretch leading to a change in surface area. In practice, however, flame stretch is often split into two different expressions.

Instead of splitting the flame stretch based on the normal and tangential velocity components as in Eq. (2.58), it can be split by replacing the total velocity \vec{w} by the fluid velocity \vec{u} and displacement speed s_d from Eq. (2.19):

$$K = \nabla_t \cdot \vec{w} = \nabla_t \cdot \vec{u} + \nabla_t \cdot (s_d \vec{n}) \quad (2.59)$$

The first term on the r.h.s. is the aerodynamic strain:

$$\nabla_t \cdot \vec{u} = \underbrace{\nabla_t \cdot \vec{u}_t}_{\text{aerodynamic tangential strain}} + \underbrace{(\vec{u} \cdot \vec{n}) \nabla \cdot \vec{n}}_{\text{aerodynamic normal strain}} = \underbrace{(\underline{\underline{\mathbf{I}}} - \vec{n}\vec{n})}_{\text{projection in the tangential direction}} : \underline{\underline{\mathbf{S}}} \quad (2.60)$$

The flame stretch can be rewritten as:

$$K = \nabla_t \cdot \vec{u} + s_d \nabla \cdot \vec{n} = K_s + K_c \quad (2.61)$$

$K_s = \nabla_t \cdot \vec{u}$ is the aerodynamic strain and $K_c = s_d \nabla \cdot \vec{n}$ the flame stretch due to the movement of a curved flame front with the displacement speed.

Aerodynamic strain is the contribution of the fluid flow $\nabla_t \cdot \vec{u}$ to the total stretch $\nabla_t \cdot \vec{w}$. It is also linked to the aerodynamic strain rate tensor $\underline{\underline{\mathbf{S}}}$:

$$\underline{\underline{\mathbf{S}}} \equiv \text{symm}(\nabla \vec{u}) = \frac{1}{2} \left(\nabla \vec{u} + (\nabla \vec{u})^\top \right) \quad (2.62)$$

The (total) aerodynamic strain is often referred to as *tangential strain* a_T . This is justified because it is the *tangential* gradient of the fluid velocity or the tangential projection of the strain rate tensor. However, as shown in Eq. (2.60), the total aerodynamic strain consists of a normal strain including curvature and a tangential strain and summarizes the contribution of the fluid flow field to flame stretch. The different ways of splitting the flame stretch are summarized in Fig. 2.4.

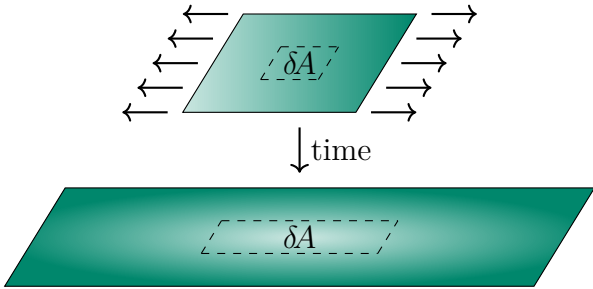


Figure 2.5: Simplified visualization of tangential strain. As a surface is pulled apart in a tangential direction, the area of its surface elements δA changes.

The expression for the normal strain in Eq. (2.58) contains two factors: The velocity of the surface in the normal direction $\vec{w} \cdot \vec{n}$ and the curvature $\kappa = \nabla \cdot \vec{n}$. Normal strain is therefore created whenever a curved surface moves normal to itself. This is analogous to an inflating balloon: the balloon’s surface only moves normal to itself. As the balloon is inflated, its surface area grows. If two points move along their normal direction while the normal direction is not the same for the two points ($\nabla \cdot \vec{n} \neq 0$), the relative distance between the points will change over time and therewith the surface area of the surface elements. This is illustrated in Fig. 2.6. No velocity gradients along the surface are needed to create normal strain. Even if all points have the same normal velocity component (like a symmetrically expanding sphere), as long as the surface moves normal to itself and has a non-zero curvature, its area will change. For pure tangential straining on the other hand, the existence of a tangential velocity component is not sufficient to create stretch. Without gradients of the tangential velocity component along the surface, the surface only translates tangential to itself without changing its area.

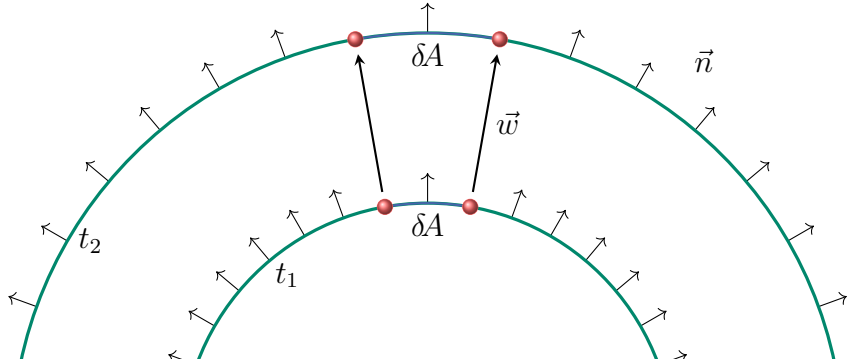


Figure 2.6: A curved surface moving normal to itself will always increase or decrease its surface area, depending on whether the curvature is convex or concave in relation to the direction of movement. Here, the surface expands outwardly over time, so the area δA increases and the curvature $\kappa = \nabla \cdot \vec{n}$ decreases. The distance between points moving along the normal direction increases.

2.3.3 Physical Interpretation

Flame stretch K can affect the properties of flames. It influences the thermo-diffusive fluxes, changes the thickness of the flame and can even be a cause of extinction [10].

As shown in the previous sections, curvature κ contributes to flame stretch. One way of visualizing the effect of flame stretch is by considering a curved flame front. Figure 2.7 shows diffusive fluxes of energy and reactant species (react) at a curved flame front. The effect of curvature on the flame depends on two factors: first, if the flame is limited by heat or mass diffusion, and second, the difference in diffusion velocity of fuel and oxidizer. The first case is usually quantified by the Lewis number Le :

$$Le = \frac{a}{D} \quad (2.63)$$

a is the thermal diffusivity and D the species diffusivity. Different methods exist for computing D in multi-component mixtures in the context of the Lewis number [79].

In Fig. 2.7, the flame is curved negatively, like the tip of a Bunsen flame. Heat diffuses from the hot burnt gases to the cold fresh gases. In this case, the heat flux is focused due to the negative curvature. For flames with $Le > 1$, the focusing of the heat flux is what dominates the flame behavior and leads to stronger heating of the fresh gases compared to a planar flame. Because of this, flames with $Le > 1$ have an increased flame speed and heat release rate at negatively curved parts of the flame.

For flames with $Le < 1$, the species mass fluxes are relevant. The mass fluxes of the reactant species are defocused. For hydrogen flames, where the fuel species H_2

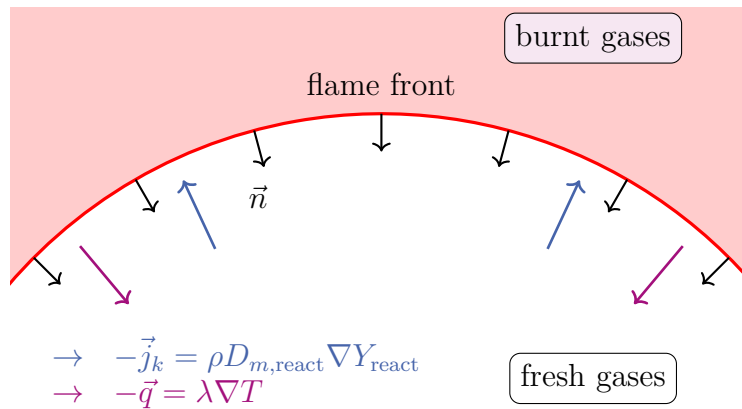


Figure 2.7: Diffusive fluxes of energy \vec{q} and species \vec{j}_k at a curved flame front.

is much lighter than oxygen O_2 and therefore diffuses faster, the fuel concentration is locally lowered. If the flame is globally lean, this leads to a local reduction of the equivalence ratio ϕ , lowering local flame speeds. In extreme cases, this leads to tip opening of Bunsen flames, as shown later in section 4.2. A similar illustration of the effect of flame stretch can be made by considering the curvature of streamlines in stagnation point flames [17].

2.3.4 Mean Flame Stretch

Because flame stretch K is a local quantity, each point on the flame surface may experience different stretching. A useful quantity is therefore the area mean stretch \bar{K} :

$$\bar{K}(t) \equiv \frac{1}{A(t)} \int_{A(t)} K \, dA \quad (2.64)$$

Expressing the tangential component of \vec{w} as $\vec{w}_t = \nabla \times (\vec{w} \times \vec{n})$, an equivalent expression of flame stretch can be formulated:

$$K = (\vec{w} \cdot \vec{n}) \nabla \cdot \vec{n} + \nabla_t \cdot \vec{w}_t = (\vec{w} \cdot \vec{n}) \nabla \cdot \vec{n} - \vec{n} \cdot \nabla \times (\vec{w} \times \vec{n}) \quad (2.65)$$

The integral in Eq. (2.64) becomes:

$$\bar{K}(t) = \frac{1}{A(t)} \int_{A(t)} (\vec{w} \cdot \vec{n}) \nabla \cdot \vec{n} \, dA - \frac{1}{A(t)} \int_{A(t)} \nabla \times (\vec{w} \times \vec{n}) \cdot \vec{n} \, dA \quad (2.66)$$

The first term on the r.h.s. of Eq. (2.66) is the influence of the total normal stretch and the second term the influence of the total tangential stretch. The effect of both terms can be illustrated by considering when the mean stretch becomes zero. The first term becomes zero if the flame is stationary ($\vec{w} \cdot \vec{n} = 0$) or if the flame is not curved ($\nabla \cdot \vec{n} = 0$). This means, that the flame will not change its shape over time since it either does not move normal to itself or remains planar. The second term is zero if no tangential velocity component exists ($\vec{w} \times \vec{n} = 0$). By applying Stoke's theorem, the second term can be rewritten to:

$$\int_{A(t)} \nabla \times (\vec{w} \times \vec{n}) \cdot \vec{n} \, dA = \int_{\partial A(t)} (\vec{w} \times \vec{n}) \cdot d\vec{l} \quad (2.67)$$

where $\partial A(t)$ is the edge of $A(t)$ and $d\vec{l}$ the line vector of the edge. This term vanishes if $A(t)$ is a closed surface. Because tangential strain does not change the shape of the flame, the overall area cannot increase or decrease if the surface is closed. A flame that does not have a closed surface can compensate non-zero mean

tangential stretch by expanding beyond its current edges and therefore change its total area.

2.3.5 Related Flame Stretch Concepts

Some authors have proposed different methods to express the flame stretch dependence of the flame speed. Dopazo et al. [28, 80–82] have highlighted the importance of the effective normal strain for the displacement speed. While the flame stretch is the relative change of the infinitesimal flame surface area, the effective normal strain $a_{e,N}$ is defined as the relative change of the infinitesimal distance between two iso-surfaces. This can be expressed with the definitions of the divergence and its normal and tangential variants:

$$\lim_{V \rightarrow 0} \left(\frac{1}{V} \frac{dV}{dt} \right) \equiv \nabla \cdot \vec{w} \quad (2.68)$$

$$\lim_{A \rightarrow 0} \left(\frac{1}{A} \frac{dA}{dt} \right) \equiv \nabla_t \cdot \vec{w} \quad (2.69)$$

$$\lim_{x \rightarrow 0} \left(\frac{1}{x} \frac{dx}{dt} \right) \equiv \nabla_n \cdot \vec{w} \quad (2.70)$$

Equation (2.68) is the definition of the divergence operator, where V is the volume of a volume element and \vec{w} the velocity of its surfaces. The tangential divergence of the surface velocity \vec{w} , as discussed above, is defined as the flame stretch (see Eq. (2.53)). Lastly, the infinitesimal change of the relative distance between two iso-surfaces x is the normal projection of the divergence operator ∇_n . If the volume of a volume element V is approximated as the surface area at one of its surfaces A times the side length of the volume element x , $V \approx Ax$, the three expressions can be related by

$$\frac{1}{V} \frac{dV}{dt} = \frac{1}{Ax} \frac{dAx}{dt} = \frac{x}{Ax} \frac{dA}{dt} + \frac{A}{Ax} \frac{dx}{dt} = \frac{1}{A} \frac{dA}{dt} + \frac{1}{x} \frac{dx}{dt} \quad (2.71)$$

or equivalently

$$\nabla \cdot \vec{w} = \nabla_t \cdot \vec{w} + \nabla_n \cdot \vec{w} \quad (2.72)$$

In the context of combustion, the effective normal strain can be formulated as:

$$a_{e,N} = \frac{1}{x} \frac{dx}{dt} = \nabla_n \cdot \vec{w} = \nabla_n \cdot \vec{u} + \frac{\partial s_d}{\partial n} \quad (2.73)$$

It is therefore related to a change of the flame thickness.

Another flame stretch concept, known as strong stretch, has been developed by de Goey et al. [83–85]. It considers the relative change of mass M in a volume element and is defined as

$$K_{\text{strong}} = \frac{1}{M} \frac{dM}{dt} = \frac{1}{\rho} \left(\frac{\partial \rho}{\partial t} + \nabla \cdot (\rho \vec{w}) \right) \quad (2.74)$$

2.4 Markstein Numbers and Transient Effects

The local flame speed along the flame surface is not constant in general. One reason has been given in section 2.3.3, where flame stretch leads to locally modified equivalence ratios. Because of this, local flame speed can be expressed as a function of flame stretch, as shown in the case of laminar flames in Fig. 1.1. In the simplest case, the flame speed s is assumed to be only a function of flame stretch K . A first order Taylor expansion for the unstretched flame yields

$$s \approx s_{L,0} + \frac{\partial s}{\partial K} \Delta K \quad (2.75)$$

where the Taylor expansion is done around $\Delta K = K - 0$. This is known as the linear Markstein model [86]. Due to being a first order expansion, the linear model is only valid for small values of ΔK . Usually, this relation is written in non-dimensional form. The Markstein length \mathcal{L} is the flame speed's sensitivity to flame stretch

$$\mathcal{L} \equiv - \left. \frac{\partial s}{\partial K} \right|_{K=0} \quad (2.76)$$

Dividing Eq. (2.75) by $s_{L,0}$, substituting Eq. (2.76) back in Eq. (2.75), and normalizing the Markstein length with the flame thickness and the flame stretch with the flame time scale, yields:

$$\frac{s}{s_{L,0}} = 1 - \underbrace{\frac{\mathcal{L}}{\delta_{\text{th}}}}_{\equiv Ma} \underbrace{\tau_c K}_{\equiv Ka} = 1 - MaKa \quad (2.77)$$

In the dimensionless form, two characteristic numbers appear: the Markstein number Ma , which is the dimensionless, negative sensitivity of the flame speed to flame stretch, and the Karlovitz number Ka , which is the dimensionless flame stretch. Likewise, $Ka_c = s_d \nabla \cdot \vec{n} \tau_c$ is the normalized flame stretch due to the curvature contribution and $Ka_s = \nabla_t \cdot \vec{u} \tau_c$ the normalized aerodynamic straining.

For larger stretch ranges, the flame stretch and flame speed correlation is, in general, not linear. Therefore, different approaches have been developed to

take this into account. For spherically expanding flames, different non-linear extrapolation methods have been derived and tested [87–92]. However, spherically propagating flames are not subjected to tangential straining, thus experiencing not all components of flame stretch from Eq. (2.61).

A different approach is based on using two different Markstein lengths or Markstein numbers. The details differ depending on the author [93–95], but usually different Markstein lengths are defined for curvature and either aerodynamic strain or total flame stretch, for example [96]:

$$s = s_{L,0} - \mathcal{L}_c \kappa s_{L,0} - \mathcal{L}_K K \quad (2.78)$$

In this way, the effect of curvature κ is handled separately from the effect of flame stretch. Matalon et al. [97] have derived expressions for the different Markstein lengths with varying degrees of simplifications. It should, however, be noted, that the Markstein lengths differ depending if the stretch dependence of the consumption speed s_c or displacement speed s_d is considered. For the displacement speed, they also differ depending on the iso-surface where the displacement speed is evaluated on [96, 98–100].

In practice, finding an accurate expression for the Markstein length a priori is difficult, especially in simulations with detailed reaction mechanisms, as every species has a different sensitivity to flame stretch [101, 102] and there is also a complex pressure dependence [103]. Therefore, in this work, the Markstein numbers are evaluated directly from the flame speed sensitivity to flame stretch from Eq. (2.76). Additionally, the aforementioned relations assume steady-state flames. In transient flames, however, the flame cannot instantly adapt to changing flow and stretch conditions as different processes (diffusion, chemical reactions) and also each species is governed by different time scales. This leads to a time dependence in the flame speed and flame stretch correlation, which is referred to as time history effect, non-locality effect or memory effect.¹

Transient effects on the local flame dynamics have been investigated experimentally and numerically with oscillating flames [107–117], flame-vortex interaction [118] and transient flammability and extinction limits [119–122]. With increasing frequency, the flame’s response to the fluctuations is generally attenuated and for very high frequencies, the flame cannot react to the oscillations at all. This transient response of the flame is also observed for extinction events, where a

¹ This is not to be confused with the term memory effect specifically used in the context of stratified flames [104–106].

flame can be subjected temporarily to flame stretch above its extinction stretch without extinguishing depending on the frequency [17, 123]. The reason is that the flame requires a certain relaxation time to adapt to the current flow conditions, and with very high frequencies, the flame cannot reach a quasi-steady state.

Another modeling concept based on the local flame stretch are the flamelet equations derived by Scholtissek et al. [124–126]. These flamelet equations contain the flame stretch and the curvature as parameters, so that in theory, solutions of the new flamelet equations at different stretch and curvature values can be tabulated. In practice, however, it has been found that a direct tabulation of stretch and curvature for transient flame cases is difficult due to the memory effect. Therefore, having a description of the effect of flame stretch based on the flame relaxation time would be beneficial.

In analogy to the Markstein concept for laminar flames, a turbulent Markstein number has been proposed [127]. Again, the details differ depending on the author, but a turbulent Markstein number may be defined as [128]

$$\frac{s_T}{s_{L,0}} = 1 - Ma_t \frac{u'/L_t}{\bar{s}_{L,0}^2/a} \quad (2.79)$$

A similar approach has been developed by Weiß et al. [129, 130], who defined a turbulent Markstein number based on a frequency dependent efficiency factor I_0

$$\bar{s}_L = s_{L,0} \left(1 - \underbrace{Ka_t I_0 Ma}_{Ma_t} \right) \quad (2.80)$$

The efficiency factor is usually used to compute the surface-averaged local flame speed $\bar{s}_L = I_0 s_{L,0}$ [131], e.g. to have an exact expression for Damköhler's first hypothesis:

$$\frac{s_T}{s_{L,0}} = I_0 \frac{A_t}{A_0} \quad (2.81)$$

Hemchandra et al. [132] note, that there is “no systematic analysis or discussion of the fundamental nature of non-local flame surface response or its influence on the local consumption speed”. Im et al. [133] find that “the detailed functional characteristics of Ma_t are unknown at the moment. Considering the highly transient nature of turbulent flames, additional effects such as unsteady attenuation [134] may also need to be accounted for”.

This work aims to address the aforementioned open questions regarding the effect of transient effects on the flame speed and flame stretch correlation. The flame relaxation time is quantified in section 4.1 for one-dimensional model flames.

However, tracking local quantities like flame speed and flame stretch over time on two or three-dimensional flames is not trivial, as it is not immediately clear which point on an iso-surface at time t_1 corresponds to which point on the same iso-surface at a later time t_2 . Because of this, the recently developed flame particle tracking (FPT) method is employed in this work, which allows to record the thermo-physical trajectories of material points on the flame surface. The method together with significant improvements in the formulation of the numerical tracking algorithm are presented in the next chapter.

Development of Numerical Tools

3.1 Efficient DNS Solver for High Performance Computing

The focus of this work lies on the detailed analysis of local flame dynamics. As explained in section 1.2, the direct numerical simulation (DNS) of flames relies on an accurate computation of detailed molecular diffusive fluxes and chemical reaction rates and also requires large computational resources, possible only with modern supercomputers. Therefore, several improvements have been developed for an in-house DNS solver in this work, that is able to compute detailed flame properties and is also suited for high performance computing. In this section, the details for modeling flames in the DNS solver are presented as well as a brief overview of the structure of the code. Further information are included in appendix E and appendix F.

3.1.1 Balance Equations

For the simulation of reacting flows in this work, it is assumed that the gas flow can be described as a continuum. Since all flame setups take place at atmospheric conditions, this assumption is valid. The balance equations that describe the reacting flow are therefore based on the fully compressible Navier–Stokes equations, including conservation of energy and conservation of species masses and assuming ideal gases and perfect mixtures.

First, the conservation of total mass for a compressible fluid reads [10]:

$$\frac{\partial \rho}{\partial t} + \nabla \cdot (\rho \vec{u}) = 0 \quad (3.1)$$

where ρ is the gas mixture density, t is time and \vec{u} is the bulk fluid velocity. The momentum balance equation is

$$\frac{\partial (\rho \vec{u})}{\partial t} + \nabla \cdot (\rho \vec{u} \vec{u}) = -\nabla p + \nabla \cdot \underline{\underline{\tau}} + \rho \sum_k Y_k \vec{f}_k \quad (3.2)$$

where p is the pressure, Y_k is the mass fraction of species k , \vec{f}_k are body forces and $\underline{\underline{\tau}}$ is the stress tensor. It is computed using the Stokes assumption for a Newtonian fluid:

$$\underline{\underline{\tau}} = \mu \left(\nabla \vec{u} + (\nabla \vec{u})^T - \frac{2}{3} \underline{\underline{I}} \nabla \cdot \vec{u} \right) \quad (3.3)$$

$\underline{\underline{I}}$ is the identity tensor and μ the dynamic viscosity of the gas mixture. The balance equation for the species masses is implemented in terms of the species mass fractions Y_k :

$$\frac{\partial (\rho Y_k)}{\partial t} + \nabla \cdot (\rho (\vec{u} + \vec{u}_c) Y_k) = \dot{\omega}_k - \nabla \cdot \vec{j}_k, \quad k = 1 \dots N - 1 \quad (3.4)$$

$\dot{\omega}_k$ is the reaction rate of species k and N the total number of species. The correction velocity \vec{u}_c assures that the sum of all diffusive fluxes \vec{j}_k is zero:

$$\vec{u}_c = -\frac{1}{\rho} \sum_k \vec{j}_k \quad (3.5)$$

The diffusive mass flux \vec{j}_k of species k is further detailed in section 3.1.3.

The energy balance is expressed for the total sensible enthalpy $h_s + \frac{1}{2} \vec{u} \cdot \vec{u}$:

$$\frac{\partial (\rho (h_s + \frac{1}{2} \vec{u} \cdot \vec{u}))}{\partial t} + \nabla \cdot \left(\rho \vec{u} (h_s + \frac{1}{2} \vec{u} \cdot \vec{u}) \right) = -\nabla \cdot \vec{q} + \frac{\partial p}{\partial t} - \sum_k h_k^\circ \dot{\omega}_k \quad (3.6)$$

with

$$-\nabla \cdot \vec{q} = \underbrace{\nabla \cdot \left(\frac{\lambda}{c_p} \nabla h_s \right) - \sum_k \nabla \cdot \left(\frac{\lambda}{c_p} h_{s,k} \nabla Y_k \right)}_{=\nabla \cdot (\lambda \nabla T)} - \sum_k \nabla \cdot \left(h_{s,k} \hat{\vec{j}}_k \right) \quad (3.7)$$

c_p is the isobaric heat capacity of the gas mixture, λ the mixture's heat conductivity and T the temperature. The sensible enthalpy $h_{s,k}$ of species k and the sensible enthalpy of the mixture h_s for ideal gases are computed from

$$h_{s,k} = h_k - h_k^\circ, \quad h_s = \sum_k Y_k h_{s,k} \quad (3.8)$$

where $h_k^\circ \equiv h_k(298 \text{ K})$ is the enthalpy of formation of species k and the corrected diffusive mass flux \hat{j}_k is

$$\hat{j}_k = \vec{j}_k - Y_k \sum_k \vec{j}_k \quad (3.9)$$

Fourier's second law for heat conduction $\nabla \cdot (\lambda \nabla T)$ is rewritten in Eq. (3.7) so that the first term on the r.h.s. of Eq. (3.7) can be discretized implicitly.

The connection between density, pressure and temperature is given by the ideal gas law:

$$\rho = \frac{p\bar{M}}{\mathcal{R}T} \quad (3.10)$$

\bar{M} is the mean molar mass of the mixture and \mathcal{R} is the universal gas constant.

3.1.2 Thermodynamic Properties

The balance equations presented in section 3.1.1 contain thermodynamic properties. These properties are computed from the pure species properties, i.e. specific molar enthalpy \tilde{h}_k , specific molar entropy \tilde{s}_k and specific molar isobaric heat capacity $\tilde{c}_{p,k}$ of each species k , based on JANAF polynomials [135]:

$$\frac{\tilde{c}_{p,k}}{\mathcal{R}} = a_{k,0} + a_{k,1}T + a_{k,2}T^2 + a_{k,3}T^3 + a_{k,4}T^4 \quad (3.11)$$

$$\frac{\tilde{h}_k}{\mathcal{R}T} = a_{k,0} + \frac{a_{k,1}}{2}T + \frac{a_{k,2}}{3}T^2 + \frac{a_{k,3}}{4}T^3 + \frac{a_{k,4}}{5}T^4 + \frac{a_{k,5}}{T} \quad (3.12)$$

$$\frac{\tilde{s}_k}{\mathcal{R}} = a_{k,0} \ln T + a_{k,1}T + \frac{a_{k,2}}{2}T^2 + \frac{a_{k,3}}{3}T^3 + \frac{a_{k,4}}{4}T^4 + a_{k,6} \quad (3.13)$$

The corresponding mass specific quantities are:

$$c_{p,k} = \frac{\tilde{c}_{p,k}}{M_k}, \quad h_k = \frac{\tilde{h}_k}{M_k}, \quad s_k = \frac{\tilde{s}_k}{M_k} \quad (3.14)$$

M_k is the molar mass of species k . The mixture properties are computed from the mixing rules for ideal mixtures:

$$\bar{M} = \sum_k X_k M_k = \left(\sum_k \frac{Y_k}{M_k} \right)^{-1} \quad (3.15)$$

$$h = \sum_k Y_k h_k = \frac{1}{\bar{M}} \sum_k X_k \tilde{h}_k \quad (3.16)$$

$$c_p = \sum_k Y_k c_{p,k} = \frac{1}{\bar{M}} \sum_k X_k \tilde{c}_{p,k} \quad (3.17)$$

$X_k = Y_k \frac{\bar{M}}{M_k}$ is the mole fraction of species k .

3.1.3 Mass Diffusion

All simulations presented in this work apply the mixture-averaged diffusion model, also known as Hirschfelder–Curtiss approximation. This approximation allows to simplify the Maxwell–Stefan equations to yield a closed expression for the species diffusion fluxes (neglecting the correction velocity for the sake of discussion) [136]:

$$\begin{aligned} \vec{j}_k = & -\rho D_{m,k} \nabla Y_k \\ & - Y_k \rho D_{m,k}^{\text{mole}} \left(1 - \frac{M_k}{\bar{M}} \right) \frac{1}{p} \nabla p - D_k^T \frac{1}{T} \nabla T + \rho D_{m,k}^{\text{mole}} \frac{M_k}{\bar{M}} \frac{\rho}{p} Y_k \left(\sum_i Y_i \vec{f}_i - \vec{f}_k \right) \end{aligned} \quad (3.18)$$

$D_{m,k}$ is the diffusion coefficient of species k for the current mixture relative to the mass fraction gradient and $D_{m,k}^{\text{mole}}$ is the diffusion coefficient relative to the mole fraction gradient. The terms in the second line of Eq. (3.18) are the pressure diffusion, thermal diffusion and species movement due to external forces, which are neglected in this work. Pressure diffusion is typically relevant only for high Mach number flames where considerable pressure gradients occur, external forces can be omitted because no charged particles are included in the simulation and thermal diffusion plays a subordinate role for the methane and very lean hydrogen flames that are the focus of this work.

3.1.4 Transport Properties

To compute the transport properties for each species, the following gas kinetic quantities have to be provided for each species:

- the molecule geometry (mono-atomic, linear, non-linear);
- the Lennard–Jones collision diameter as $10^{10}\sigma_k$;
- the Lennard–Jones well-depth as ϵ_k/k_B ;
- the rotational relaxation collision number $Z_{\text{rot},k}$ at $T = 298$ K;
- the dipole moment as $10^{25}\bar{\mu}_k/\sqrt{10}$;
- the polarizability as $10^{30}\alpha_k$.

The transport properties, i.e. the dynamic viscosity μ_k , heat conductivity λ_k and binary diffusion coefficients $\mathcal{D}_{k,i}$ for each species, are computed from the Chapman–Enskog solution of the Boltzmann equation [52, 137]:

$$\mu_k = \frac{5}{16} \frac{\sqrt{\pi M_k k_B T}}{\pi \sigma_k^2 \Omega_{kk}^{(2,2)*} \sqrt{N_A}} \quad (3.19)$$

$$\mathcal{D}_{k,i} = \frac{1}{p} \frac{3}{16 \pi \sigma_{i,k}^2 \Omega_{i,k}^{(1,1)*}} \sqrt{\frac{2 \pi k_B^3 T^3}{m_{i,k}}} \quad (3.20)$$

$$\lambda_k = \frac{\mu_k}{M_k} (f_{\text{trans},k} \tilde{c}_{v,\text{trans}} + f_{\text{rot},k} \tilde{c}_{v,\text{rot},k} + f_{\text{vib},k} \tilde{c}_{v,\text{vib},k}) \quad (3.21)$$

k_B is the Boltzmann constant, N_A Avogadro’s constant and σ_k the Lennard–Jones collision diameter of species k . The reduced mass $m_{i,k}$, reduced Lennard–Jones collision diameter $\sigma_{i,k}$ and reduced Lennard–Jones well-depth $\epsilon_{i,k}$ of species i and k are calculated from:

$$m_{i,k} = \frac{M_i M_k}{N_A (M_k + M_i)}, \quad \epsilon_{i,k} = \sqrt{\epsilon_i \epsilon_k} \xi^2, \quad \sigma_{i,j} = \frac{1}{2} (\sigma_i + \sigma_k) \xi^{-\frac{1}{6}} \quad (3.22)$$

where ϵ_k is the Lennard–Jones well-depth of species k . ξ is a correction for the interaction of non-polar and polar species. If both species i and k are polar (polarizability $\alpha_i > 0$ and $\alpha_k > 0$), or both species are non-polar ($\alpha_i = 0$ and $\alpha_k = 0$), ξ is unity. If one species is polar (species p) and the other is non-polar (species n), ξ is obtained from [138, 139]:

$$\xi = 1 + \frac{1}{4} \alpha_n^* \bar{\mu}_p^{*2} \sqrt{\frac{\epsilon_p}{\epsilon_n}}, \quad \alpha_n^* = \frac{\alpha_n}{\sigma_n^3}, \quad \bar{\mu}_p^* = \frac{\bar{\mu}_p}{\sqrt{\sigma_p^3 \epsilon_p}} \quad (3.23)$$

$\bar{\mu}_p$ is the dipole moment of species p and α_n the polarizability of species n . The collision integrals $\Omega_{i,k}^{(1,1)*}$ are computed from collision integrals $\Omega_{i,k}^{(2,2)*}$ [140, 141]:

$$\Omega_{i,k}^{(1,1)*} = \frac{\Omega_{i,k}^{(2,2)*}}{A_{i,k}^*} \quad (3.24)$$

$A_{i,k}^*$ and $\Omega_{i,k}^{(2,2)*}$ are tabulated [17, 142] as functions of the reduced temperature $T_{i,j}^*$ and the reduced dipole moment $\delta_{i,k}^*$:

$$\delta_{i,k}^* = \frac{1}{2} \frac{\bar{\mu}_{i,k}^2}{\epsilon_{i,k} \sigma_{i,k}^3}, \quad \bar{\mu}_{i,k} = \sqrt{\bar{\mu}_i \bar{\mu}_k}, \quad T_{i,j}^* = \frac{k_B T}{\epsilon_{i,k}} \quad (3.25)$$

λ_i is calculated based on the following parameters:

$$f_{\text{vib},k} = \frac{p \mathcal{D}_{k,k} M_k}{\mu_k \mathcal{R} T} \quad (3.26)$$

$$f_{\text{trans},k} = \frac{5}{2} \left(1 - \frac{2 \tilde{c}_{v,\text{rot},k} A_k}{\pi \tilde{c}_{v,\text{trans}} B_k} \right) \quad (3.27)$$

$$f_{\text{rot},k} = f_{\text{vib},k} \left(1 + \frac{2 A_k}{\pi B_k} \right) \quad (3.28)$$

$$A_k = \frac{5}{2} - f_{\text{vib},k} \quad (3.29)$$

$$B_k = Z_{\text{rot},k} \frac{F_k(298 \text{ K})}{F_k(T)} + \frac{2}{\pi} \left(\frac{5 \tilde{c}_{v,\text{rot},k}}{3 \mathcal{R}} + f_{\text{vib},k} \right) \quad (3.30)$$

$$\tilde{c}_{v,\text{trans}} = \frac{3}{2} \mathcal{R} \quad (3.31)$$

$$F_k(T) = 1 + \frac{\pi^{\frac{3}{2}}}{\sqrt{T_k^*}} \left(\frac{1}{2} + \frac{1}{T_k^*} \right) + \left(\frac{\pi^2}{4} + 2 \right) \frac{1}{T_k^*} \quad (3.32)$$

$$T_k^* = \frac{k_b T}{\epsilon_k} \quad (3.33)$$

$$\tilde{c}_{v,\text{rot},k} = \begin{cases} 0, & \text{if mono-atomic} \\ \mathcal{R}, & \text{if linear} \\ \frac{3}{2} \mathcal{R}, & \text{otherwise} \end{cases} \quad (3.34)$$

$$\tilde{c}_{v,\text{vib},k} = -\tilde{c}_{v,\text{rot},k} + \tilde{c}_{p,k} - \frac{5}{2} \mathcal{R} \quad (3.35)$$

To save computing time, λ_k , $\mathcal{D}_{k,i}$ and $\sqrt{\mu_k}$ are calculated once at the start of the simulation at 50 equidistant temperatures and only the fits in the following expressions are evaluated during the simulation:

$$\lambda_k = \sqrt{T} (d_{k,0} + d_{k,1} \ln T + d_{k,2} \ln^2 T + d_{k,3} \ln^3 T + d_{k,4} \ln^4 T) \quad (3.36)$$

$$\mathcal{D}_{k,i} = \frac{1}{p} T^{\frac{3}{2}} (c_{ki,0} + c_{ki,1} \ln T + c_{ki,2} \ln^2 T + c_{ki,3} \ln^3 T + c_{ki,4} \ln^4 T) \quad (3.37)$$

$$\sqrt{\mu_k} = T^{\frac{1}{4}} (b_{k,0} + b_{k,1} \ln T + b_{k,2} \ln^2 T + b_{k,3} \ln^3 T + b_{k,4} \ln^4 T) \quad (3.38)$$

The mixing rules for the transport properties of the gas mixture are [137]:

$$\lambda = \frac{1}{2} \left(\sum_i X_i \lambda_i + \frac{1}{\sum_i \frac{X_i}{\lambda_i}} \right) \quad (3.39)$$

$$\mu = \sum_i \frac{\mu_i X_i}{\sum_k \Phi_{i,k} X_k} \quad (3.40)$$

$$\Phi_{i,k} = \frac{\left(1 + \sqrt{\frac{\mu_i}{\mu_k} \sqrt{\frac{M_k}{M_i}}} \right)^2}{\sqrt{8 \left(1 + \frac{M_i}{M_k} \right)}} \quad (3.41)$$

where $\Phi_{i,k}$ is a coefficient for the Wilke mixing rule to obtain accurate viscosity values for the reacting gas mixture. The mixture averaged diffusion coefficients are computed from [52]:

$$D_{m,k}^{\text{mole}} = \frac{1 - Y_k}{\sum_{j \neq k} \frac{X_j}{\mathcal{D}_{j,k}}} \quad (3.42)$$

$$D_{m,k} = \left(\sum_{i \neq k} \frac{X_i}{\mathcal{D}_{k,i}} + \frac{X_k}{1 - Y_k} \sum_{i \neq k} \frac{Y_i}{\mathcal{D}_{k,i}} \right)^{-1} \quad (3.43)$$

3.1.5 Finite Volume Method

To solve the balance equations from section 3.1.1 numerically, the finite volume method (FVM) is employed. In this method, the simulation domain is subdivided into control volumes, also called cells. The balance equations are then expressed in their integral form and convective and diffusive terms are evaluated by summing the fluxes over the cell faces. For an overview of the finite volume method,

see [143–145]. Here, only important aspects for the simulations conducted in this work are detailed.

The temporal discretization scheme for all simulations discussed in this work is the second order backward scheme:

$$\frac{\partial(\rho\varphi)}{\partial t} \approx \frac{(c_n\rho_n\varphi_n) - (c_{n-1}\rho_{n-1}\varphi_{n-1}) + (c_{n-2}\rho_{n-2}\varphi_{n-2})}{\Delta t_n} \quad (3.44)$$

where φ is an arbitrary quantity and n is the index of the next time step. The weighting coefficients c for non-uniform time steps are

$$c_n = 1 + \frac{\Delta t_n}{\Delta t_n + \Delta t_{n-1}} \quad (3.45)$$

$$c_{n-2} = \frac{\Delta t_n^2}{\Delta t_{n-1}(\Delta t_n + \Delta t_{n-1})} \quad (3.46)$$

$$c_{n-1} = c_n + c_{n-2} \quad (3.47)$$

where $\Delta t_n = t_n - t_{n-1}$ and $\Delta t_{n-1} = t_{n-1} - t_{n-2}$. In this way, all balance equations are solved implicitly, employing conjugate gradient solvers for the linearized set of equations [146, 147].

For numerical stability, the time step is adjusted to ensure a maximum Courant–Friedrichs–Lewy (*CFL*) number for all simulations presented in this work between 0.1 and 0.2:

$$CFL_c = \frac{1}{2}\Delta t \frac{\sum_f |\vec{u}_f \cdot \vec{n}_f| A_f}{V_c} \leq 0.2 \quad (3.48)$$

where CFL_c is the *CFL* number in cell c , f is the index of the cell faces, A_f the surface area of face f , \vec{n}_f its surface unit normal vector and V_c is the volume of the cell.

For spatial discretization, a fourth order interpolation scheme is employed (see appendix F for more information). The coupling of pressure, density and velocity is done with the PIMPLE algorithm, which combines the PISO [148] and SIMPLE [149] algorithms.

The method used for solving the Navier–Stokes equations together with the balance equations of energy and species masses in this work is generally known as direct numerical simulation (DNS). This means, that no sub-grid models are required to describe the small-scale effect of turbulence. Instead, all length and time scales of all relevant physical processes are fully resolved. This specifically means the full

resolution of the reaction layer inside the flame front and the resolution of the smallest turbulent length scale, the Kolmogorov length.¹

3.1.6 Structure of the DNS Solver

The in-house DNS solver [169, 170] improved in this work is based on OpenFOAM® [171]. OpenFOAM® is an open-source fluid dynamics library, providing many solvers for different multi-physics applications. It provides a full implementation of the finite volume method but lacks the ability to compute detailed transport coefficients from kinetic gas theory, which play an important role in flames. Because of this, OpenFOAM®’s capabilities for solving the balance equations numerically are combined with Cantera’s implementation for computing detailed transport coefficients. Cantera [46] is also an open-source library, providing routines for computing thermo-physical and transport properties, chemical reaction rates and reaction mechanism parsers.

The working principle of the in-house solver is shown in Fig. 3.1. The balance equations are implemented in the OpenFOAM® framework and species properties are provided by the routines of Cantera. In this work, the in-house code has been heavily modified to reduce overall simulation times by up to 70 % compared with OpenFOAM®’s standard implementation, without reducing the accuracy. The details of the new performance optimization strategies are given in appendix E.

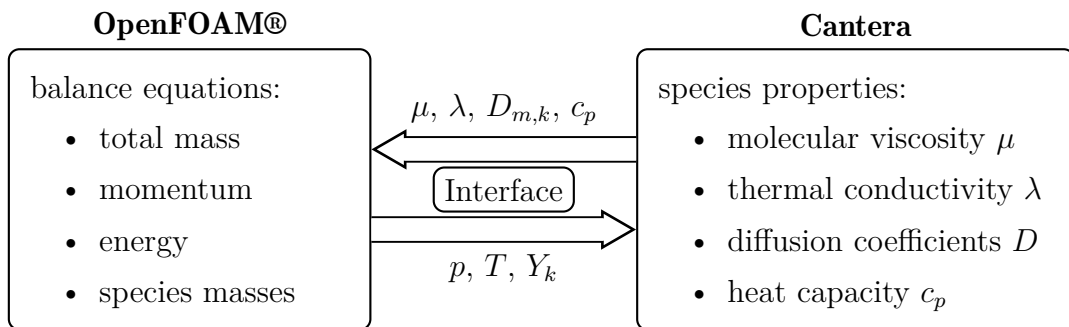


Figure 3.1: Working principle of the in-house DNS solver. OpenFOAM®’s capabilities for solving the balance equations with the finite volume method are combined with Cantera’s abilities to compute detailed thermo-physical properties and transport coefficients.

¹ Because the simulation tool used in this work, OpenFOAM®, employs the finite volume method on unstructured grids, spatial and temporal accuracy are generally limited to second order. Therefore, some authors prefer to use the term quasi-DNS [150–168]. In this work, the terms DNS and quasi-DNS are used synonymously and additional discussion of the numerical accuracy is provided in appendix F.

3.2 Flame Particle Tracking

To reveal the memory effect that affects the local flame dynamics in turbulent flames, time histories of points tracked on the flame front have to be recorded during the simulation. In this section, the recently developed flame particle tracking method is introduced and its relevancy for understanding local flame dynamics is highlighted. However, the flame particle tracking method, as introduced in the literature, has some important limitations, that have been addressed with a novel tracking method developed in this work. The description of the new tracking algorithm, as well as its implementation and validation are presented in this section, too.

3.2.1 Theoretical Background

Instead of looking at instantaneous snapshots of flames in an Eulerian viewpoint, which considers the flame to be frozen in time and therefore obscures the time dependence between different processes, a Lagrangian approach can be employed to extract additional information from direct numerical simulations of flames. By tracking specific points on the flame, the time history effect can be incorporated into the investigation of local flame dynamics by recording the time signals of e.g. flame speed and flame stretch. These points on the flame surface are known as material points and the Lagrangian particles tracking these points are known as flame particles (FP) [45]. Flame particles are virtual tracer particles or markers that have no interaction with the flow or flame and can therefore be regarded as massless and sizeless Lagrangian particles. Their trajectories reveal the temporal evolution of local quantities and represent the thermo-physical trajectories of flame surface elements. In contrast to *fluid* particles, which move with the fluid velocity \vec{u} and follow the flow pathlines, *flame* particles co-move with an iso-surface representing the flame and therefore move with the flame's total velocity \vec{w} (see chapter 2).

Pope [172] first discussed the Lagrangian equations governing the movement of flame surface area elements, that are the basis of the flame particle tracking [45] (FPT) method. The movement of the flame front can be described by the movement of a representative iso-surface, e.g. an iso-surface of a species mass fraction or temperature inside the reaction zone. This iso-surface represents a

material surface², which is made up by an infinite number of material points. Material surfaces can generate their own movement velocity (in the case of flames the displacement speed s_d) and are convected by a vector field (in the case of flames by the fluid flow). Any point that co-moves with an iso-surface, called a material point, has to stay on that iso-surface. Therefore, any point on an iso-surface of φ must fulfill the following condition:

$$\frac{d\varphi}{dt} = 0 \quad (3.49)$$

This is the Lagrangian viewpoint which ensures that a point of the iso-surface stays on that iso-surface. The total derivative d/dt is taken with respect to the movement velocity of that iso-surface, \vec{w} . In convective form, Eq. (3.49) reads:

$$\frac{\partial\varphi}{\partial t} + \vec{w} \cdot \nabla\varphi = 0 \quad (3.50)$$

\vec{w} is the instantaneous velocity of any point on that iso-surface. This is the Eulerian viewpoint, which shows that in a stationary reference frame, points have to move with \vec{w} to stay on the iso-surface.

As derived in section 2.1.3, the movement of the flame is composed by two effects: the convection by the fluid flow and the burning velocity of the flame. Therefore, \vec{w} can be decomposed into:

$$\vec{w} = \vec{u} + s_d\vec{n} \quad (3.51)$$

\vec{u} is the fluid velocity and s_d is the displacement speed of that iso-surface. Here, it is assumed that the flame propagates as a wave and therefore the displacement speed only creates movement in the flame normal direction \vec{n} .

² Some authors prefer the term *non-material surface*, if the movement of the surface is not purely caused by convection but is additionally affected by diffusion and reaction [82].

By substituting Eq. (3.51) into Eq. (3.50) and using the definition of the normal vector from Eq. (2.7), the basic movement equation for flame particles can be derived:

$$\begin{aligned}
\frac{\partial \varphi}{\partial t} + (\vec{u} + s_d \vec{n}) \cdot \nabla \varphi &= 0 \\
\frac{\partial \varphi}{\partial t} + \vec{u} \cdot \nabla \varphi &= -s_d \vec{n} \cdot \nabla \varphi \\
\frac{\partial \varphi}{\partial t} + \vec{u} \cdot \nabla \varphi &= -s_d \underbrace{\left(\pm \frac{\nabla \varphi}{|\nabla \varphi|} \right)}_{\substack{\equiv \vec{n} \\ = |\nabla \varphi|}} \cdot \nabla \varphi \\
\frac{\partial \varphi}{\partial t} + \vec{u} \cdot \nabla \varphi &= \mp s_d |\nabla \varphi|
\end{aligned} \tag{3.52}$$

For more information about the sign convention, see section 2.1.3. Substituting the material derivative with respect to the fluid velocity $D/Dt \equiv \partial/\partial t + \vec{u} \cdot \nabla$ on the l.h.s. yields an equation for the computation of the displacement speed (compare also with Eq. (2.22)):

$$s_d = \mp \frac{1}{|\nabla \varphi|} \frac{D\varphi}{Dt} \tag{3.53}$$

Computing s_d from the equation above has many advantages: First, the formulation is exact, meaning that it describes exactly the displacement speed of any iso-surface without simplifying assumptions. It is also applicable to any type of iso-surface, not just in the context of flames. Second, all terms are readily available in a DNS. Third, from a numerical point of view, computing s_d is cheap if a balance equation for φ is solved. For example, if φ is a species mass fraction, then D/Dt is already known in the solver.

Because flame particles follow material points, their movement is intrinsically related to flame stretch, which measures the relative change of the surface area of Lagrangian flame surface elements, spanned by material points (see section 2.3 for a comprehensive discussion of flame stretch). The movement velocity \vec{w} of each material point on the flame front is the same as the one in the definition of flame stretch in Eq. (2.53). Figure 3.2 illustrates this relation. It shows two flame particles on an iso-surface of an arbitrary scalar quantity φ at a time $t = t_0$. At the next time step $t = t_1$, the iso-surface has moved and the flame particles have tracked their material points, thus co-moving with and staying on the iso-surface. This movement is created by the flame's displacement speed as well as convection with the fluid velocity. At $t = t_1$, the two flame particles are further apart than

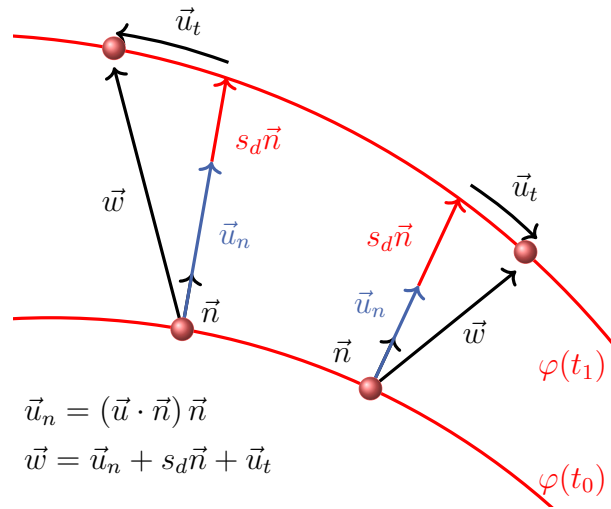


Figure 3.2: Movement of two flame particles \bullet located on an iso-surface of φ at $t = t_0$. Both particles move with the velocity \vec{w} , which is a superposition of the fluid velocity \vec{u} and the displacement velocity $s_d \vec{n}$. Since the distance between the two flame particles on the new flame surface $\varphi(t_1)$ is larger than at t_0 , this is a situation where the flame stretch is positive.

at $t = t_0$, showing that a flame surface area element spanned by the two points has increased in surface area. Therefore, in the situation given in Fig. 3.2, the local value of flame stretch is positive. In general, flame particles starting out close together, will move away from each other in regions with positive flame stretch and cluster in regions with negative flame stretch. Because of this, flame particles tend to move from regions with positive flame stretch and generation of flame surface area toward regions with negative flame stretch and flame surface destruction over time. This means, tracking clusters of flame particles and their distribution over time is a direct measure for flame surface creation or destruction.

3.2.2 Literature Overview

Analyses of flames from a Lagrangian viewpoint other than the flame particle tracking method have been performed in recent works with various approaches. For example, Hamlington et al. [173] used fluid particles to study the path lengths and residence times in turbulent flame fronts. Towery et al. [174] utilized fluid particles to track chemical modes and thermo-chemical trajectories in highly turbulent hydrogen-air flames. Lagrangian particles have been employed by Scholtissek et al. [34] to investigate flamelet histories in turbulent flames. Other works are based on the tracking of flame surface area elements, which is closely related to the flame particle tracking method: Zheng et al. [175] studied the evolution of flame

surface elements and explored the statistics of principle curvature in turbulent flames. Yang et al. [176] performed a similar analysis and looked at the evolution of Lagrangian surface area elements in turbulent flows. Oster et al. [177] developed visualization tools for flame surface area elements. Sripakagorn et al. [178] used flame element tracking to study ignition and re-ignition events.

The term flame particle tracking method has been recently introduced by Chaudhuri [45]. It has been applied to study the correlation between flame displacement speed with strain and curvature on different iso-surfaces of temperature in turbulent methane-air and hydrogen-air flames and ignition kernels [45, 179–181]. Flame particles have also been used to investigate the applicability of Bachelor's pair dispersion law for flame particles [182]. Dave et al. [183] uniformly seeded flame particles on temperature iso-surfaces of turbulent flames and tracked them backward in time. They found that the flame particles originate from leading points of the flame and cluster at the positively curved flame parts at an earlier time. Over time, the strongly positively curved leading points align with the turbulent flow and become tangentially stretched. They conclude that leading points of the flame are the main source of flame surface area. However, since the movement of flame particles is intrinsically connected to flame stretch (see section 3.2.1), and leading points of the flame exhibit strong positive curvature and therewith positive flame stretch, flame particles move away from these points over time. When tracked backward in time, they will statistically end up in regions with previously high positive flame stretch rates. Likewise, flame particles will statistically end up in regions with strong negative flame stretch, which act as a sink for flame surface area and therefore also for flame particles. This leads to a characteristic evolution of displacement speed over the lifetime of a flame particle. Two phases can be identified [41, 45]. In phase one, the flame particle starts out with moderate values of flame displacement speed in regions of statistically positive flame stretch and then transitions to regions with tangential straining. In phase two, the flame displacement speed rapidly increases as the flame particle gets annihilated in regions with strong negative curvature [41, 180, 181, 184]. There is also ongoing work on developing an on-the-fly tracking method in the original FPT framework [185].

3.2.3 Novel Tracking Method based on Barycentric Coordinates

Even though the flame particle tracking method has been shown to be a useful tool for studying turbulent flames, there are some important limitations in the original method [45]. First, the method has been implemented as a post-processing

step. This means, that full three-dimensional data sets from DNS have to be stored with a high time frequency to perform the tracking after the simulation has finished. This requires the storage of large amounts of data. Secondly, the tracking has been implemented with MATLAB [186]. This limits the potential for utilizing large parallel computer systems and ultimately limits the number of concurrently tracked flame particles. Lastly, the tracking algorithm includes expensive operations like ray-tracing to find the intersection of the particle tracks with the tracked iso-surface, so that it can be ensured that the flame particles always end up on the iso-surface. This also requires the reconstruction of the iso-surface globally, which is another expensive operation. Therefore, the goal of this work is to develop a novel flame particle tracking algorithm that overcomes the aforementioned limitations. The newly developed tracking method fulfills the following main properties:

1. The flame particles are tracked in situ during the simulation, so that there is no need to store large amounts of simulation data.
2. This means that the tracking algorithm has to be fully parallelized.
3. The tracking algorithm avoids expensive operations like ray-tracing and global iso-surface reconstruction.
4. The new method can handle tens of millions of flame particles without significantly affecting the simulation times.
5. The algorithm is applicable for the tracking of general iso-surfaces, not just in the context of reacting flows.

To achieve these goals, a new tracking algorithm [187–190] has been developed in this work. Because the method should be applied to large scale parallel simulations, computational performance is an important factor. The new tracking method is based on barycentric coordinates which enables a computationally efficient tracking. Due to the use of barycentric coordinates, fast interpolation methods can be used to find the flame properties at the particle positions and the tracking is compatible with any type of cell shape, making it applicable to unstructured meshes. An analytic expression for finding the intersection of flame particle trajectories and the iso-surface is formulated, which makes ray-tracing and global iso-surface reconstruction unnecessary. The implementation has been done in the DNS solver described in section 3.1.6 in the OpenFOAM® framework and is the first fully parallelized realization of the flame particle tracking method. In addition, the flame particle tracking method from the literature has been limited to study the flame speed in terms of the flame displacement speed. However, in many situations,

the flame consumption speed constitutes a physically more meaningful quantity. Computing the consumption speed is, however, computationally expensive due to the need of evaluating a line integral at each position on the flame front. Because of this, a fully parallelized implementation for computing the flame consumption speed has been developed in conjunction with the new flame particle tracking method, making the study of flame consumption speeds in this work possible.

In order to track material points on the flame front and gather information in the Lagrangian frame of reference, the first step of the flame particle method is to seed the flame particles (FP) onto the flame surface and consequently track them over time. After seeding the flame particles on an initial iso-surface, usually of temperature or species mass fraction, the new tracking algorithm is comprised of the following steps:

1. compute the flame's movement velocity \vec{w} and interpolate it to each FP position;
2. compute the position of each flame particle at the next time step based on \vec{w} ;
3. move the flame particles toward the new position;
4. if the particle crosses a domain boundary between different parallel processes, move the particle to the neighboring process;
5. after the tracking, find the intersection of the flame particle trajectory with the iso-surface to ensure that it is located exactly on the flame surface.

Figure 3.3 illustrates steps 1–3 of the new tracking algorithm. It shows two cells in the computational domain, here shown as hexahedral cells. A flame particle (FP) is located in the right hand side cell at the time $t = t_0$. At that time step, the flame particle was located on the iso-surface that it tracks. At the next time step $t = t_1$, the flame and therewith the iso-surface has moved so that the flame particle is no longer located on the iso-surface. To find the material point on the new iso-surface at t_1 , that corresponds to the material point tracked by the flame particle, the movement velocity \vec{w} of that point is calculated from Eq. (3.51), with the displacement speed calculated from Eq. (3.53) in the three dimensional Eulerian field and interpolated to the flame particle position. In the most simple case, the new position of the flame particle \vec{x}_{FP} at $t = t_1$ can be computed from

$$\vec{x}_{\text{FP}}(t_1) \approx \vec{x}_{\text{FP}}(t_0) + \vec{w}\Delta t \quad (3.54)$$

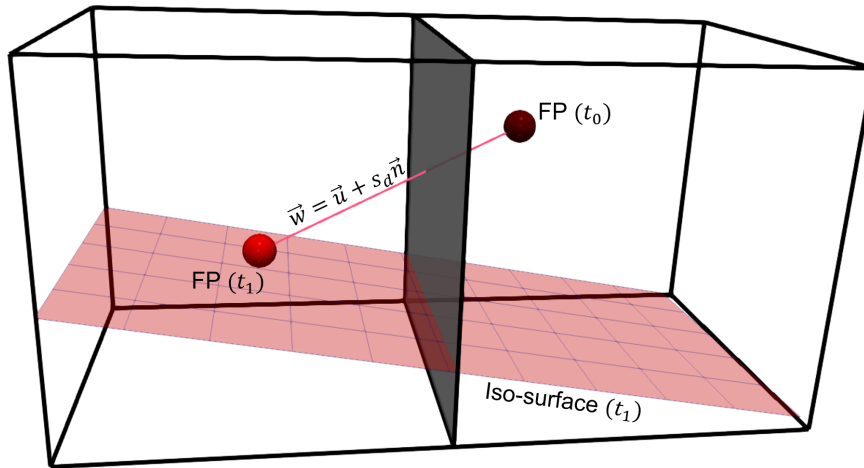


Figure 3.3: Illustration of the first steps from the new flame particle tracking method. The movement velocity \vec{w} of the material point tracked by the flame particle (FP), shown as red sphere, is computed from Eq. (3.51) and interpolated to the FP position. The FP is then moved to its new location, which lies on the tracked iso-surface at $t = t_1$. In this example, the FP position at $t = t_0$ is located in a different cell than its position at $t = t_1$. These two cells might be on two physically different computers or parallel processes in a simulation.

where Δt is the simulation time step. The accuracy of this step can be improved by utilizing a predictor-corrector approach, high order integration [45] or high order interpolation methods [191, 192].

In the example given in Fig. 3.3, the FP position at $t = t_0$ is located in a different cell than its position at $t = t_1$. These two cells might be on two physically different computers in a parallel simulation. Because the new tracking method is implemented in OpenFOAM®, its infrastructure can be used to implement the parallel handling of the flame particle tracking method. In OpenFOAM®, the computational domain is split into sub-domains at the beginning of the simulation. Each sub-domain is assigned to a parallel process. Each time the flame particle crosses a cell face, the tracking algorithm checks if this is a face between two cells that are located on the same process. If not, the flame particle is deleted on the current process and its information is sent to the process that owns the target cell. This step is done concurrently by batching all flame particles together to minimize the number of parallel communications. There is also another option, where the cell face is a physical boundary of the domain. In this case, the flame particle is removed from the simulation, unless the boundary is a cyclic or periodic boundary condition.

After the flame particle has been moved to its new position with Eq. (3.54), the flame particle should be located on the iso-surface at $t = t_1$. However, due to numerical errors, the particle might not be exactly located on that iso-surface. This is usually not a problem directly, but as the numerical errors add up over many time steps, the particle will drift away from the iso-surface over time. To avoid this, an additional correction step is employed. Here, barycentric coordinates are used to efficiently find the intersection of the particle trajectory with the iso-surface. To do this, the computational cell is split into tetrahedra and the particle position is expressed as its normalized distance to the corners of the tetrahedron. This also has the advantage that any polyhedral shape can be uniquely split into tetrahedra so that the tracking method is applicable to any cell shape and therefore also to arbitrary unstructured meshes.

In the correction step, the tetrahedron in the decomposed cell is identified where the flame particle is located in. The goal is to find the intersection of the particle trajectory with the iso-surface. However, the movement due to the fluid velocity \vec{u} can be considered exact as the values are taken directly from the DNS. The displacement speed from Eq. (2.26), on the other hand, is a derived property and therefore subject to more numerical errors. Therefore, the correction step corrects the movement of the flame particle due to the flame's displacement speed, which is directed in the flame's normal direction. This means, that correcting the position due to the displacement speed is the same as finding the shortest distance ΔC between the new particle position and the iso-surface.

Figure 3.4 illustrates the correction step. The particle position is stored in barycentric coordinates. To distinguish between Cartesian and barycentric coordinates, the $\hat{\cdot}$ symbol is used to represent barycentric coordinates. In this notation, the flame particle position is $\hat{\lambda}_{FP}$. The vector $\hat{\lambda}_{FP}$ contains the normalized distances to the four corner points of the tetrahedron within the cell and is therefore a 4×1 column vector. When decomposing the cell into tetrahedra, one of the corners is always the cell center (blue sphere in Fig. 3.4), and the other three corner points of the tetrahedron are formed by three corner points of the cell (green spheres in Fig. 3.4). For a hexahedral cell, this means that the cell is split into 12 tetrahedra (two tetrahedra per cell face). The components of the barycentric coordinates of the corner points of the tetrahedron are all zero, except for one component which is unity. For example, $\hat{\lambda}_1 = (1, 0, 0, 0)^T$ is the position of the cell center in barycentric coordinates, because it has the shortest possible distance to the first corner point of the tetrahedron (itself) and the maximum distance to

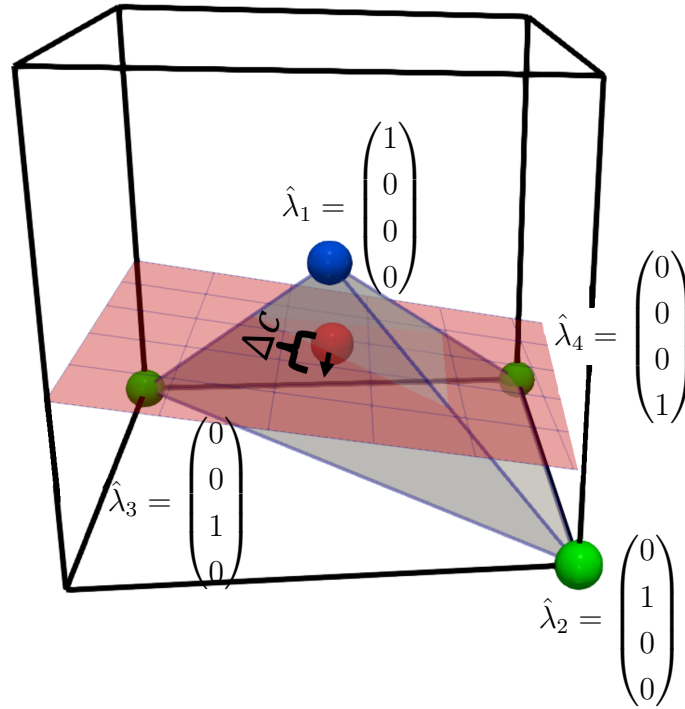


Figure 3.4: After moving the flame particle (red sphere) to its new position, the shortest distance between the particle and the iso-surface ΔC is computed to correct the particle position. This is done using barycentric coordinates relative to the cell tetrahedron the flame particle is located in, comprised of three corner points of the cell and the cell center.

the three other corner points. Because the barycentric coordinates are normalized, $\hat{\lambda} = (\lambda_1, \lambda_2, \lambda_3, \lambda_4)^\top$ fulfills the property

$$\sum_{i=1}^4 \lambda_i = 1, \quad \lambda_i \geq 0 \quad (3.55)$$

The use of barycentric coordinates also allows the formulation for computationally efficient interpolation. For any barycentric coordinate $\hat{\lambda}$ inside that tetrahedron, the value of an arbitrary quantity φ can be found by:

$$\varphi(\hat{\lambda}) = \sum_{i=1}^4 \lambda_i \varphi_i \quad (3.56)$$

φ_i is the value of φ at the corner point i of the tetrahedron known from the simulation. Equation (3.56) can also be used to express the part of the iso-surface cutting through this tetrahedron:

$$\varphi_{\text{iso}} = \sum_{i=1}^4 \lambda_i \varphi_i \quad (3.57)$$

Any point $\hat{\lambda}$ that fulfills this condition lies on the iso-surface. In previous works from literature [45], the intersection of the particle trajectory with the iso-surface was found by reconstructing the whole iso-surface and performing ray-tracing. This is avoided entirely by using the barycentric coordinate approach. The shortest distance d between a point \vec{p} and a plane can be generally computed from

$$d = (\vec{p} - \vec{q}) \cdot \vec{n} = \vec{p} \cdot \vec{n} - \vec{q} \cdot \vec{n} \quad (3.58)$$

where \vec{q} is an arbitrary point that lies on the plane. In the context of the FPT method, the point \vec{p} represents the position of the flame particle \vec{p}_{FP} . However, this position is stored in barycentric coordinates $\hat{\lambda}_{\text{FP}}$. The conversion from barycentric to Cartesian coordinates is given by

$$\vec{p}(\hat{\lambda}) = \lambda_1 \vec{x}_1 + \lambda_2 \vec{x}_2 + \lambda_3 \vec{x}_3 + \lambda_4 \vec{x}_4 = \underline{\underline{\mathbf{T}}} \hat{\lambda}, \quad \underline{\underline{\mathbf{T}}} = (\vec{x}_1 \ \vec{x}_2 \ \vec{x}_3 \ \vec{x}_4) \quad (3.59)$$

\vec{x}_i are the Cartesian coordinates of the four corner points of the tetrahedron. $\underline{\underline{\mathbf{T}}}$ is the 3×4 transformation matrix whose columns are the Cartesian position vectors of the corner points. Combining Eq. (3.58) and Eq. (3.59) for finding the shortest distance between the flame particle and the iso-surface yields

$$d = \left(\underline{\underline{\mathbf{T}}} \hat{\lambda}_{\text{FP}} \right) \cdot \vec{n} - \vec{q} \cdot \vec{n} \quad (3.60)$$

A very efficient method of finding a point \vec{q} that lies on the iso-surface is identifying any edge of the tetrahedron that is cut by the iso-surface. Any point on that edge expressed in barycentric coordinates will have two components that are zero, which correspond to the two points that are not part of that edge. For example, assume the edge from the corner point 1 at $\hat{\lambda}_1$ to the corner point 3 at $\hat{\lambda}_3$ is cut by the iso-surface (Fig. 3.4). The point on that edge which also lies on the iso-surface must have the form $\hat{\lambda}_{\text{edge}} = (\lambda_1, 0, \lambda_3, 0)$. Because of Eq. (3.57), this point also has to fulfill $\varphi_{\text{iso}} = \sum_{i=1}^4 \lambda_i \varphi_i$, which for this example reduces to

$$\varphi_{\text{iso}} = \lambda_1 \varphi_1 + \lambda_3 \varphi_3 \quad (3.61)$$

And because of Eq. (3.55), the sum of the components of the barycentric coordinate vector $\hat{\lambda}$ has to be unity. In this example, this yields

$$\lambda_1 + \lambda_3 = 1, \quad \lambda_1, \lambda_3 \geq 0 \quad (3.62)$$

The two unknowns λ_1 and λ_3 can be found with Eq. (3.61) and Eq. (3.62). In this way, a point on the iso-surface can be found efficiently by choosing an edge and finding the point of that edge that is cut by iso-surface $\hat{\lambda}_{\text{edge}}$. The Cartesian coordinate of that point is found by Eq. (3.59) as $\vec{q} = \underline{\underline{\mathbf{T}}} \hat{\lambda}_{\text{edge}}$. Substituting this back into Eq. (3.58) finally yields the equation for efficiently finding the shortest distance between the flame particle and the iso-surface:

$$\Delta C = (\underline{\underline{\mathbf{T}}} \hat{\lambda}_{\text{FP}}) \cdot \vec{n} - (\underline{\underline{\mathbf{T}}} \hat{\lambda}_{\text{edge}}) \cdot \vec{n} = \left(\underline{\underline{\mathbf{T}}} \left(\hat{\lambda}_{\text{FP}} - \hat{\lambda}_{\text{edge}} \right) \right) \cdot \vec{n} \quad (3.63)$$

After correcting the flame particle position by $\Delta C \vec{n}$, it exactly lies on the iso-surface within the numerical precision of the simulation.

It is possible that the intersection point of the flame particle trajectory and the iso-surface lies in another tetrahedron than the flame particle itself. If this is the case, the flame particle is iteratively moved toward the iso-surface until it is located in the correct tetrahedron. The distance Δx between the flame particle and the iso-surface can be approximated by using the relation

$$\frac{\partial \varphi}{\partial n} \approx \frac{\varphi_{\text{iso}} - \varphi_{\text{FP}}}{\Delta x} \rightarrow \Delta x \approx \frac{\varphi_{\text{iso}} - \varphi_{\text{FP}}}{\left(\frac{\partial \varphi}{\partial n} \right)} \quad (3.64)$$

This correction is done iteratively in the direction of the local normal vector $\Delta x \vec{n}$. With the definition of the directional derivative $\partial \varphi / \partial n \equiv \nabla \varphi \cdot \vec{n}$ and the definition of \vec{n} from Eq. (2.7), the correction becomes:

$$\begin{aligned} \Delta x \vec{n} &\approx \frac{\varphi_{\text{iso}} - \varphi_{\text{FP}}}{\frac{\partial \varphi}{\partial n}} \vec{n} = \frac{\varphi_{\text{iso}} - \varphi_{\text{FP}}}{\nabla \varphi_{\text{FP}} \cdot \vec{n}} \vec{n} = \frac{\varphi_{\text{iso}} - \varphi_{\text{FP}}}{\nabla \varphi_{\text{FP}} \cdot \frac{\nabla \varphi_{\text{FP}}}{|\nabla \varphi_{\text{FP}}|}} \frac{\nabla \varphi_{\text{FP}}}{|\nabla \varphi_{\text{FP}}|} \\ &= \epsilon (\varphi_{\text{iso}} - \varphi_{\text{FP}}) \frac{\nabla \varphi_{\text{FP}}}{|\nabla \varphi_{\text{FP}}|^2} \end{aligned} \quad (3.65)$$

φ_{FP} is the value of φ interpolated at the particle position and $\nabla \varphi_{\text{FP}}$ its gradient at the particle position. ϵ in the last step is introduced as a numerical underrelaxation factor, which is usually set to a value of 0.9 for practical applications. In this way, computing the exact location on the iso-surface can be done without the need of reconstructing large portions of the iso-surface or performing ray-tracing.

As part of the new tracking approach, a fully parallel method for computing the flame consumption speed has been implemented as well. As shown in Eq. (2.4), the evaluation of the consumption speed requires the computation of a line integral normal to the flame front. Assume there is a total number of 1 million flame particles in the simulation, and each line integral is performed over 50 points for the numerical integration, 50 million values of the fuel reaction rate have to be interpolated from the numerical simulation mesh to the integration points. Because of this, the evaluation of the consumption speed is computationally expensive and therefore often not considered in the literature when DNS results are analyzed. In the context of the flame particles, the consumption speed can be computed fully parallel as well. This is achieved by creating two new virtual particles, here called consumption speed particles, at each flame particle location. The two particles are then tracked in positive and negative normal direction to the flame front over a distance sufficiently large to include the whole reaction layer. Again, while moving along the integration path, the consumption speed particles can cross process boundaries and are automatically distributed among the parallel processes. When they reach the end of their integration path, they send the accumulated reaction rates back to the flame particle, which can then

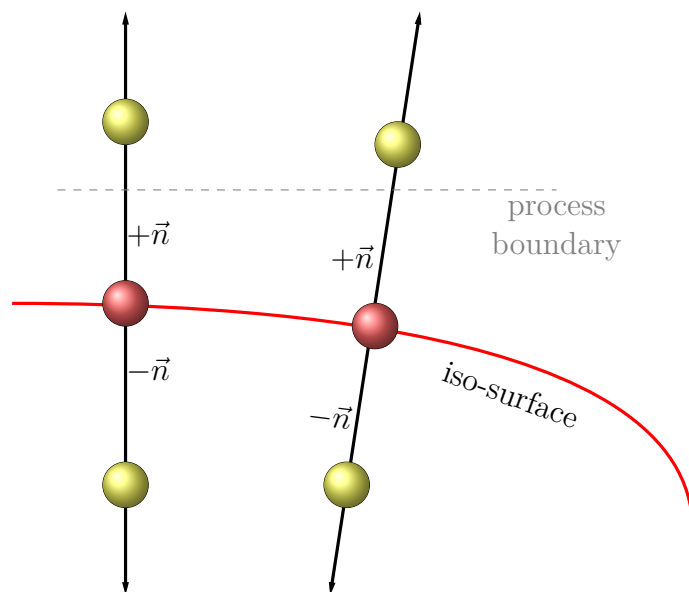


Figure 3.5: Two flame consumption speed particles \bullet are generated at each flame particle \bullet position in each time step of the simulation. They are moved in positive and negative normal direction to the flame front and integrate the chemical reaction rate of the fuel according to Eq. (2.4). Like the flame particles, the transfer of consumption speed particles between the parallel processes is handled automatically.

compute the flame consumption speed. This method is visualized in Fig. 3.5. For more information about the consumption speed computation, see also [188].

3.2.4 Computational Performance

Because the flame particle tracking method is used in large-scale parallel simulations, it is paramount that the new tracking method is able to handle a large number of Lagrangian particles without affecting the total simulation times significantly. To evaluate the performance of the new tracking code, a simplified version of the three-dimensional flames in section 4.3 is used. The computational domain is a cube with side length of 1 cm and a total of 64 million cells. The turbulent flame is a hydrogen-air flame, computed with the reaction mechanism by Li et al. [51], which consists of 9 species and 19 chemical reactions.

First, the memory required for the flame particle tracking is estimated. Table 3.1 lists the memory required to store each flame particle. Depending on the compiler settings, a single flame particle requires about 100 bytes of information. Other Lagrangian particle types, which might represent physical objects like liquid droplets and therefore require the computation of forces or thermo-chemical effects, have to store much more data. As the trend of modern supercomputers goes toward more parallel CPU cores and less memory per core, it is important that the memory overhead stays minimal when using FPT. By definition, flame particles only exist on a two-dimensional iso-surface. Also, a typical case assumes that there is on average one flame particle per cell that is cut by the iso-surface. Using more flame particles is usually not beneficial, since this would exceed the accuracy the simulation can provide. Because of this, the number of flame

Table 3.1: Memory required to store one flame particle (assuming 64 bit floating points and 32 bit integers).

Information	Size (bytes)
barycentric coordinates	32
tetrahedron point IDs	24
MPI rank of original process	4
unique particle ID	4
coordinate of new FP position	24
additional bookkeeping	24
	112

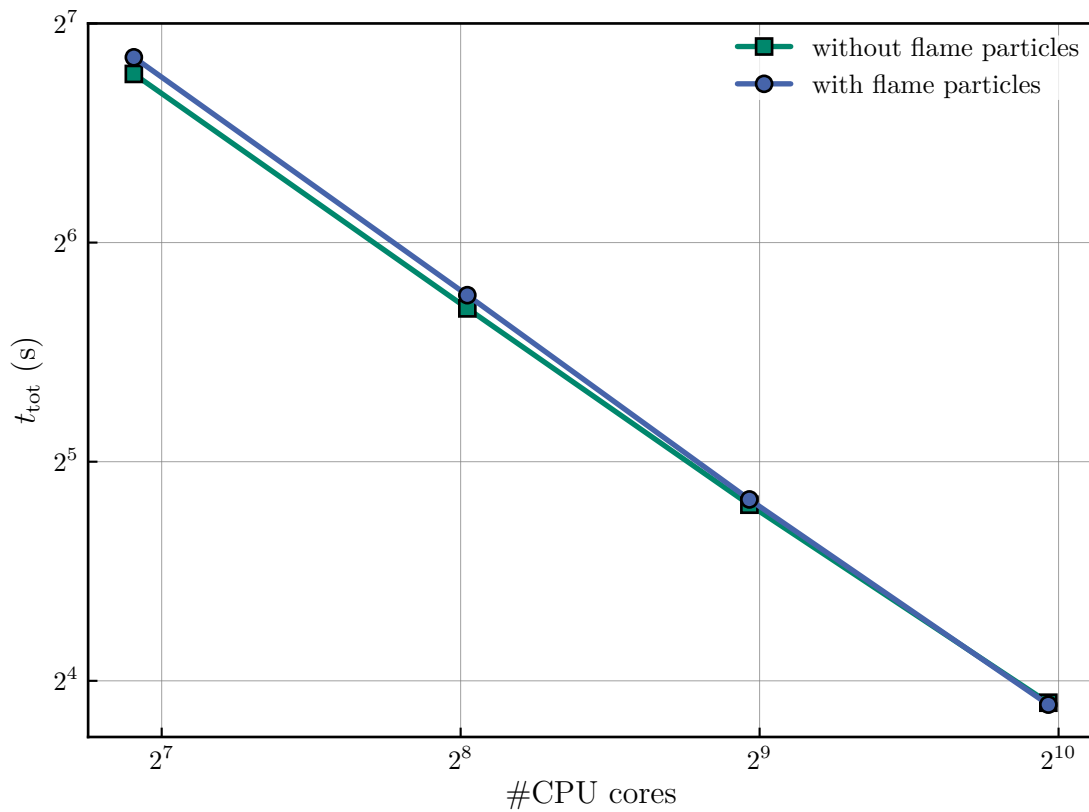


Figure 3.6: Time for one simulation time step t_{tot} at varying number of parallel processes without particle tracking and with 500 000 flame particles.

particles is much lower than the total number of cells in the three-dimensional computational domain. However, each cell has to store the information about species mass fractions, enthalpy, fluid velocity, transport coefficients and thermo-physical properties in addition to topological information. Because of this, the amount of data added by the flame particle method is negligible compared to the total memory requirement of the simulation itself.

Figure 3.6 shows performance measurements, starting with one flame particle per cell that is cut by the iso-surface of the turbulent flame. In this way, the total number of cells is 64 million and the total number of flame particles is 500 000. The measurements have been performed on the ForHLR II cluster at the Steinbuch Centre for Computing at the Karlsruhe Institute of Technology with 120 CPU cores up to 1000 CPU cores. For more information on the cluster hardware, see appendix E.

First, the results in Fig. 3.6 show that the code has very good parallel scaling, both with and without flame particle tracking. The parallel efficiency at 1000 CPU cores is more than 90 % (for more information, see appendix E.4). Also, the

Table 3.2: Time for one simulation time step t_{tot} with 1000 CPU cores and different numbers of flame particles.

Particles	Time per time step t_{tot} (s)
0	14.8
500 000	14.9
5 000 000	15.0
50 000 000	18.5

overhead introduced by using the FPT method becomes smaller when using more parallel processes, because the interpolation step from Eq. (3.56) can be done more efficiently once the mesh fits into the CPU cache. One consequence of having particles tracking a flame iso-surface is, that the particles only exist on processes where the flame is located. In theory, this can lead to load imbalances between the processes. However, in practice, the load imbalance due to the computation of chemical reaction rates is much more severe and is addressed in appendix E.3.

Although the case with 500 000 particles constitutes the usual use-case, where on average one flame particle is placed in each cell that is part of the iso-surface, simulations with much larger numbers of particles have been measured as well. Table 3.2 shows the overhead for the total simulation time with different numbers of flame particles. In the usual use-case, the total simulation time is increased by about 0.7%. Increasing the number of particles by a factor of 10 does not affect the overall simulation time significantly. With this amount of particles, the tracking itself is not the limiting factor, but the computation of \vec{w} . Even using 100 times as many particles as in a reasonable use-case, the simulation time increases by less than 30%. Therefore, the implementation is able to handle a large number of particles efficiently on highly parallel systems.

3.2.5 Validation

For the validation of the flame particle tracking implementation and the computation of additional quantities like flame stretch, a simple one-dimensional setup of a spherically expanding flame is used. The computational domain is formally a prism shaped block, where the only physical boundary is the outlet on the right. All other boundaries employ OpenFOAM®'s wedge boundary condition to evaluate spatial derivatives in spherical coordinates. The setup is shown in Fig. 3.7. The domain is initially filled with the unburnt fuel-air mixture. At the origin, the flame is ignited at the start of the simulation and propagates to the

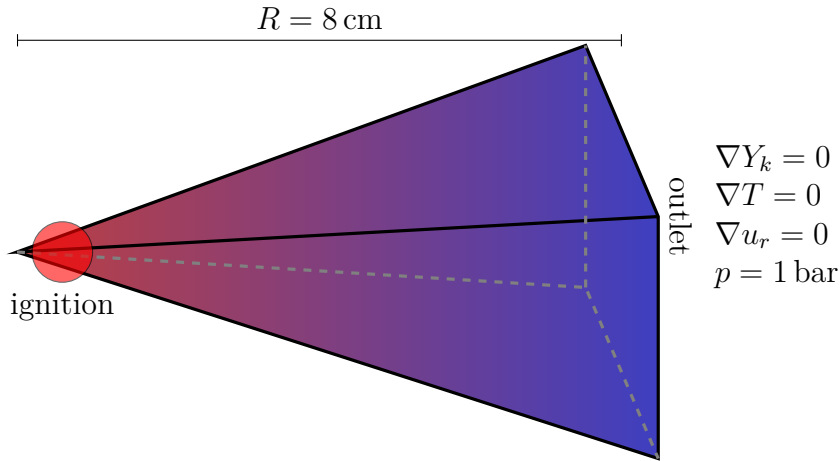


Figure 3.7: One-dimensional domain for spherical symmetry, which is formally represented by a prism shaped block. The domain is initially filled with the unburnt fuel-air mixture. At the origin, the flame is ignited at the start of the simulation and propagates to the right. The case represents a constant pressure spherically expanding flame.

right. The outlet is an open boundary, so that the case represents a constant pressure spherically expanding flame. The radius of the domain is 8 cm and the mesh is equidistantly spaced with cells of 10^{-5} m in radial direction. The *CFL* number is set to 0.1. The premixed gas is a hydrogen-air mixture at $\phi = 0.5$ at atmospheric conditions. The reaction mechanism by Li et al. [51] is employed.

Once the flame has established, a single flame particle is put onto the flame front. As the flame expands spherically, this flame particle tracks the iso-surface of $T_{\text{iso}} = 1050 \text{ K}$, which corresponds to the temperature at the position of maximum heat release rate in a freely propagating flame. The use of the one-dimensional spherical setup has the advantage, that different important quantities can be evaluated simply from the flame's position. Because the origin of the coordinate

Table 3.3: For validation, the evaluation of different quantities within the flame particle code with their general expressions can be compared with the analytic expression for one-dimensional, spherically expanding flames [129].

Quantity	General Expression	Spherical Flame
position	\vec{x}_{FP}	r
total speed \vec{w}	$\vec{u} + s_d \vec{n}$	$\frac{dr}{dt}$
curvature κ	$\nabla \cdot \vec{n}$	$\frac{2}{r}$
flame stretch K	$\nabla_t \cdot \vec{w}$	$\frac{2}{r} \frac{dr}{dt}$
aerodynamic strain K_s	$\nabla_t \cdot \vec{u}$	$\frac{2u_r}{r}$

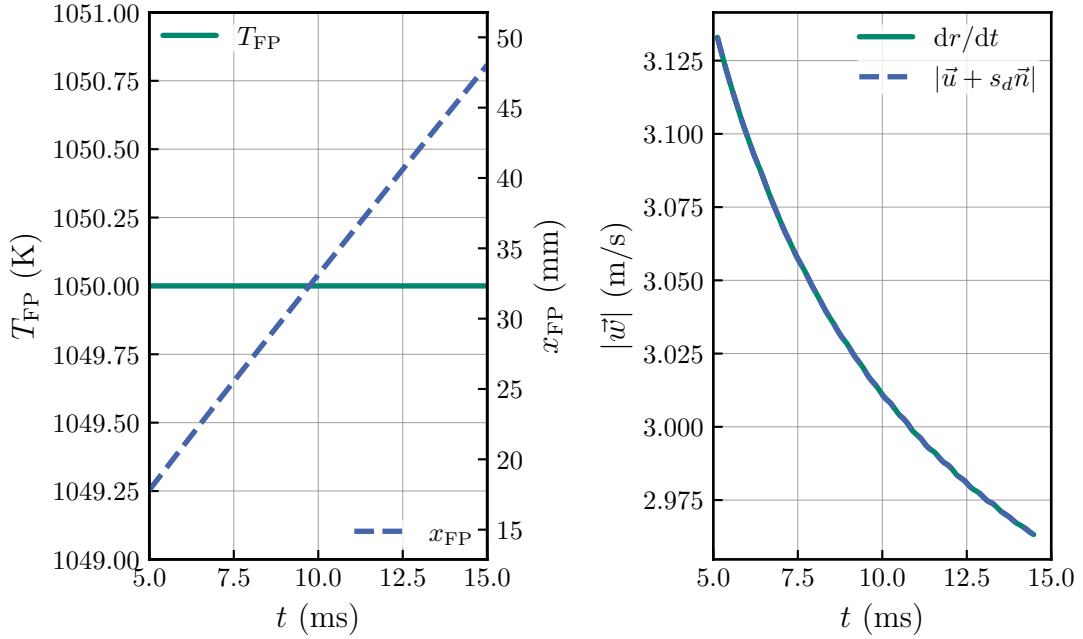


Figure 3.8: Left: position of the flame particle x_{FP} and temperature at the flame particle position over time as the flame propagates and expands spherically. Right: total movement velocity \vec{w} evaluated with the general implementation in the flame particle tracking code compared against the simplified evaluation valid for a one-dimensional spherical flame.

system is at $r = 0$, the flame particle's position \vec{x}_{FP} is the same as the flame radius r . With this, the implemented routines for computing the total flame movement velocity \vec{w} , curvature and flame speed can be compared with the simplified expressions for the spherically expanding flame. For example, the curvature $\kappa = \nabla \cdot \vec{n}$ reduces for the spherical flame to $\kappa = 2/r$. A comparison of the implemented, general expressions and the simplified forms for the spherical flame are given in Table 3.3.

Figure 3.8 on the left shows the value of the temperature T over time at the flame particle position. Because the flame particle co-moves with the iso-surface, the value of T at \vec{x}_{FP} is $T_{FP} = T_{iso}$ at every time instance. Additionally, Fig. 3.8 on the left shows the flame radius or particle position over time, showing that the flame propagates with a nearly constant velocity. On the right of Fig. 3.8, the total flame speed is compared between the general implementation in the code ($\vec{u} + s_d \vec{n}$) and the recorded flame radius over time. The comparison shows that both methods yield the same result for \vec{w} as expected.

Figure 3.9 on the left shows the flame's curvature over the flame radius. On the right, the total flame stretch and aerodynamic strain rate is recorded over the flame radius. Again, the general evaluation routines implemented for the flame

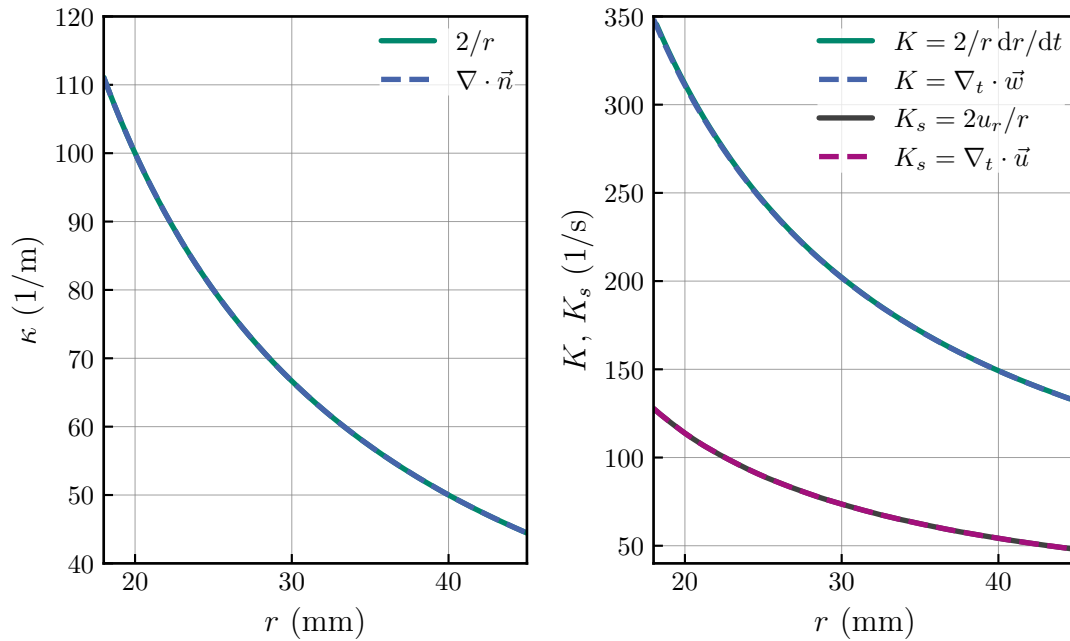


Figure 3.9: Validation of the routines computing the curvature (left) as well as total flame stretch K and aerodynamic strain rate K_s (right) for the spherically expanding flame.

particle tracking method are compared against the corresponding expressions valid for a spherically expanding flames. The comparison shows very good agreement, thus validating the implementation.

3.2.6 Application to Other Physical Setups

Because the implementation of the flame particle tracking algorithm is done in a general way, it is not limited to reacting flow simulations. In any simulation, where an iso-surface and its movement velocity \vec{w} can be expressed in a closed form, the particle tracking method developed in this work can be applied. As an outlook to future work, one such example is briefly discussed here.

In previous works [193, 194], the breakup of a liquid jet has been numerically investigated in the context of fuel atomization. Simulating the breakup behavior of the jet is challenging due to the large range of length scales, from the diameter of the nozzle to the smallest droplets created during secondary breakup. To study the breakup behavior in more detail and to collect statistical data about the time-dependent interaction of the jet with the gas flow, the droplets and the turbulent flow field around the jet, the particle tracking method can be applied. Figure 3.10 shows a snapshot from a volume-of-fluid (VoF) [195, 196] simulation of the jet breakup based on the setup described in [193, 194]. The yellow region

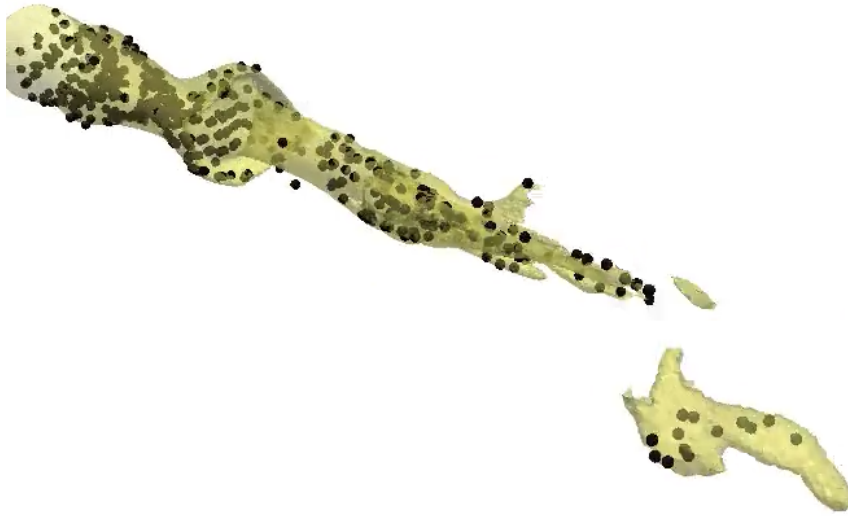


Figure 3.10: Breakup of a liquid jet (yellow region) embedded in a turbulent gas flow from [193, 194]. The black dots are particles being tracked using the same code as for the flame particles, but here the interface between the liquid and gas phase is tracked.

marks the water column and water droplets. The black points are particles that track the iso-surface of the volume fraction 0.5 and therefore track the interface between the liquid phase and the surrounding gas phase.

3.2.7 Summary

In this section, the development and implementation of the first fully parallel tracking algorithm for flame particles on high performance computing systems has been presented. Flame particles (FP) are virtual particles that follow material points on the flame front and thereby reveal the thermo-physical trajectories of the flames and allow to investigate the time-resolved local flame dynamics. Their movement is intrinsically tied to the flame stretch. Because of this, flame particles will move away from each other in regions of positive stretch and move closer to each other in regions with negative stretch, eventually leading to the destruction of the flame surface area and deletion of the flame particles. The novel tracking algorithm is based on barycentric coordinates, which enables fast interpolation to the FP location and efficient position correction of the FP to the iso-surface. The methodology can also be used on unstructured meshes due to the decomposition of computational cells into tetrahedra. The computation of the particles' movement velocity \vec{w} involves quantities that are already known in the simulation so that the computational overhead introduced by the tracking is low. In contrast to previous works from the literature, the new method is able to

handle millions of flame particles in large-scale parallel simulations with negligible impact on total simulation times and therefore enables the gathering of large statistical data sets from turbulent flames, which has not been possible before. In addition, two performance optimization techniques have been developed to speed up the computation of chemical reaction rates in the in-house DNS solver, which reduce total simulation times by up to 70%.

The key points from this section are summarized as follows:

- i.** Employing a Lagrangian viewpoint by tracking material points on flame surfaces with flame particles allows to consider the time history of local quantities and reveal the thermo-physical trajectories of the flame.
- ii.** A novel tracking algorithm based on barycentric coordinates has been devised which incorporates an analytic method for correcting the flame particle position to the flame surface in an efficient manner and avoids expensive ray-tracing and global iso-surface reconstruction.
- iii.** Even with tens of millions of particles, computational overhead of typical simulation cases is below 1%, the memory overhead is negligible as well.
- iv.** Fully parallel evaluation of the flame consumption speed is included as well, which is often neglected in the literature due to its expensive computation.
- v.** The implementation is done in a general way and not limited to reacting flows but can be applied to the tracking of any iso-surface.

4

Results and Discussion

To assess the effect of flow fluctuations with different time scales on the local flame dynamics, direct numerical simulations of different flame setups are performed. However, before the complex relations in turbulent flames are discussed, low-dimensional laminar flame cases are considered first. Section 4.1 presents one-dimensional flames, that are subjected to transient changes of the equivalence ratio without the influence of flame stretch. The simulations provide important qualitative insights into the flame's response in terms of the flame speed amplitude to oscillations of the upstream equivalence ratio with a wide range of frequencies, as well as the dependence of the flame relaxation time on equivalence ratio. Oscillating two-dimensional Bunsen flames are discussed in section 4.2. They provide a convenient way for determining frequency dependent, averaged Markstein numbers by having the flames oscillate with isolated frequencies. Lastly, section 4.3 considers three-dimensional turbulent flames that are subjected to the full turbulent frequency spectrum. The application of the flame particle tracking method allows to record the time histories of local flame speed and flame stretch values by tracking material points on the flame front. From this, a flame relaxation time is determined that recovers a quasi-linear correlation from the otherwise weakly correlated instantaneous flame speed and flame stretch. Together with the averaged turbulent Markstein number, a model for predicting local flame speeds is formulated.

4.1 Equivalence Ratio Fluctuations in One-dimensional Flames

In turbulent flows, flames are subjected to transient stretching. Especially for fuel-oxidizer mixtures with a Lewis number below unity, i.e. flames where the dynamics are diffusion controlled, the main effect of flame stretch on local flame speeds is altering the local equivalence ratio ϕ (see section 2.3.3 for the physical mechanism). At the same time, the flame speed in terms of the consumption speed directly depends on the local equivalence ratio because it is computed directly from the chemical reaction rates. For unstretched, steady-state planar flames, there is a unique correlation between the equivalence ratio and the flame speed. Figure 4.1 shows the laminar flame speed $s_{L,0}$ in dependence on the equivalence ratio of the unburnt gas for hydrogen and methane flames. The calculations have been performed with Cantera, using freely propagating 1D flames. The temperature of the unburnt mixture is 300 K and the pressure is constant at 1 bar. The reaction mechanism for hydrogen is a detailed mechanism by Li et al. [51] containing 9 species and 19 elementary reactions, and the reaction mechanism for methane oxidation is a reduced mechanism by Kee [52] with 18 species and 52 reactions. For hydrogen, the flammability limits are much wider than for methane and likewise flame speeds are much higher for the hydrogen flames, due to the high diffusivity of the light species H and H₂. The maximum of the flame

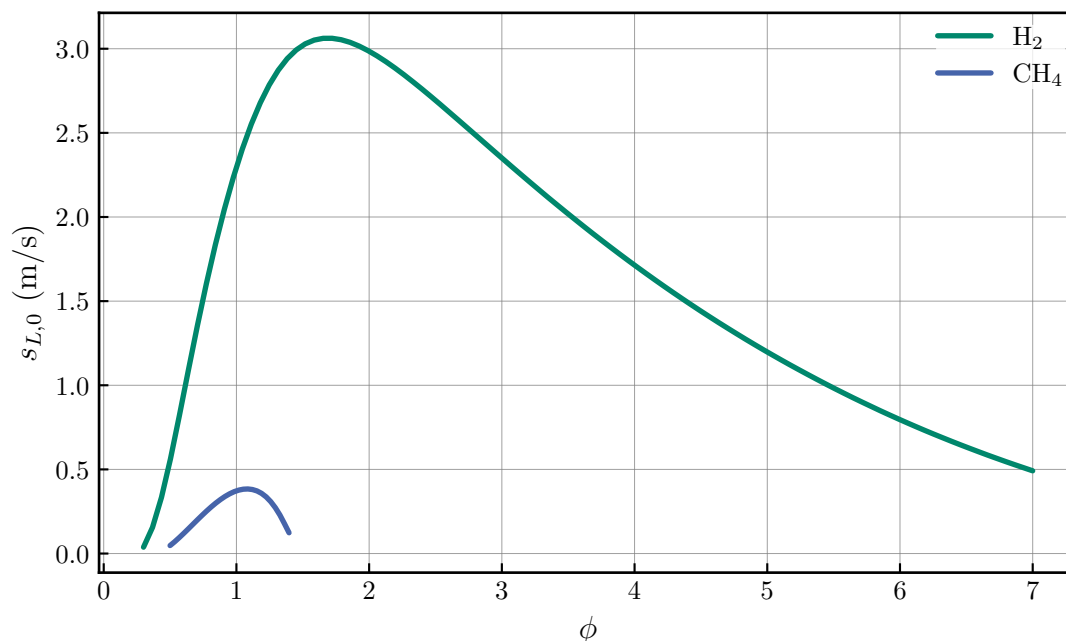


Figure 4.1: Laminar flame speed $s_{L,0}$ from unstretched 1D calculations in dependence on the equivalence ratio ϕ for hydrogen-air and methane-air flames at atmospheric conditions.

speed is shifted toward slightly rich conditions in both cases. The settings for these 1D flames, in terms of unburnt mixture conditions and reaction mechanisms, correspond to the flames investigated in the later sections.

For stretched flames, the equivalence ratio is altered locally, so that the observed local flame speeds do not correspond to the equivalence ratio of the unburnt mixture anymore, but to the locally present equivalence ratio. Even though the flame speed is a direct function of the equivalence ratio for steady-state unstretched flames, this correlation is only valid for steady-state flames. For transient flow with unsteady fluctuations, the flame cannot adjust instantaneously to the local equivalence ratios. Instead, it requires a relaxation time to adjust its thickness, temperature and species profiles if the equivalence ratio is changed. If the fluctuations have a smaller time scale than this relaxation time, the flame cannot fully relax to a quasi-steady state, resulting in a damped amplitude response of the flame in terms of the local flame speeds. However, in turbulent flows, the flame interacts with a full frequency spectrum of velocity fluctuations and therewith flame stretch fluctuations, which makes studying the flame's response to isolated frequencies a difficult task.

Therefore, two setups are employed in this section that are based on one-dimensional flames and allow to study the flame's response to isolated frequencies and to measure the relaxation time: The first setup prescribes a harmonically oscillating equivalence ratio for the unburnt gases at the inlet. The second setup instantaneously changes the species concentrations to the ones corresponding to another equivalence ratio. This allows to measure the relaxation time required by the flame to adjust its thickness and temperature as well as species profiles to the new equivalence ratio.

4.1.1 Harmonically Oscillating Upstream Equivalence Ratio

The first setup investigates the flame's response to harmonic oscillations of the upstream equivalence ratio with specific frequencies and amplitudes. This allows to assess the amplitude of the flame speed oscillation. There are experimental [197–199] and numerical [121, 200–204] investigations. However, the focus of these works lies mainly on heat release rates, which are influenced by the flame's change in surface area, acoustic properties of the flame and the effect on (thermo-acoustic) combustion instabilities, not the response of the local flame speed itself.

The simulations are performed with the DNS solver implemented in OpenFOAM® described in section 3.1.6. In this way, the transient flame dynamics can be fully

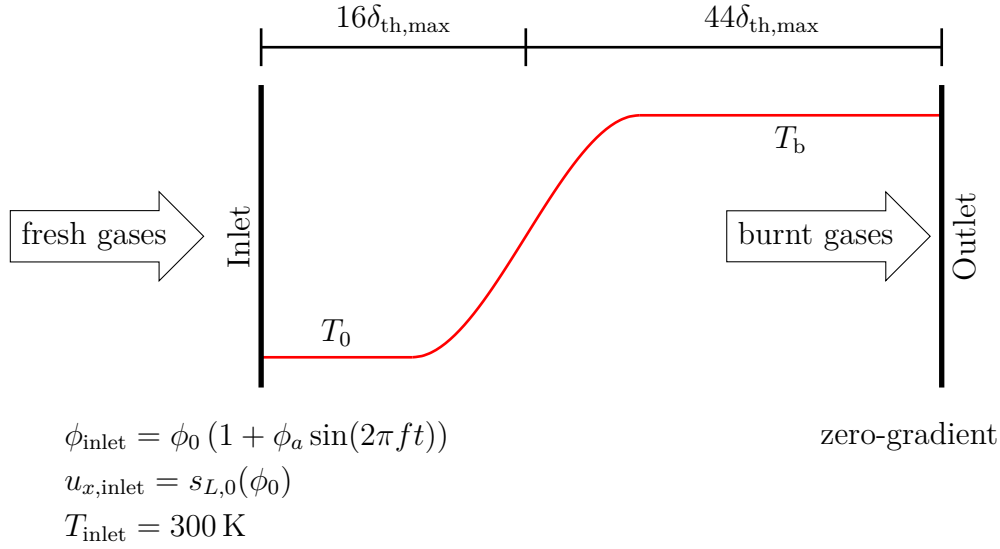


Figure 4.2: Initial state of the harmonically oscillating equivalence ratio simulations. The domain has a total length of $60 \delta_{\text{th,max}}$. On the left, the composition of fresh gases oscillates harmonically in time with a fixed temperature and flow velocity. At the outlet, zero gradients are prescribed. Initially, the flame starts from a steady-state solution at $\phi = \phi_0$, here shown as the profile of temperature in red.

captured including the computation of the detailed molecular diffusive fluxes for each species and considering the Arrhenius-based finite rate chemistry model from the detailed reaction mechanisms.

The computational domain has a total length of $60 \delta_{\text{th,max}}$, where $\delta_{\text{th,max}}$ is the maximum thermal flame thickness of a steady-state flame, which is either the flame thickness at the lowest or highest equivalence ratio during the oscillation. Similarly, the numerical resolution is equidistantly set to $\delta_{\text{th,min}}/20$, where $\delta_{\text{th,min}}$ is the minimum flame thickness corresponding to a steady-state flame at either the maximum or minimum equivalence ratio during the oscillation. In this way, different flames can be compared with a consistent resolution. This setup is shown schematically in Fig. 4.2.

As initial condition, the profiles of temperature, species mass fractions and velocity are taken from a 1D steady-state flame computed with Cantera at $\phi = \phi_0$. The flame is positioned inside the domain so that the distance between the inlet and the position with the highest heat release rate is $16\delta_{\text{th,max}}$. This allows the flame to move when adjusting to the changing equivalence ratios and not propagate into the inlet. The remaining part of the domain with a length of $44\delta_{\text{th,max}}$ is sufficient to ensure zero gradients at the outlet. Temperature and velocity are fixed at the inlet as shown in Fig. 4.2 and zero gradients are prescribed at the outlet. At the

start of the simulation, the composition of the fresh gases at the inlet oscillates according to

$$\phi_{\text{inlet}} = \phi_0 (1 + \phi_a \sin(2\pi ft)) \quad (4.1)$$

where ϕ_0 is the mean equivalence ratio, ϕ_a the relative equivalence ratio amplitude and f the frequency. More specifically, each species mass fraction is prescribed at the inlet. First, the mixture composition is computed for the current value of ϕ , assuming an oxidizer composition of $X_{\text{O}_2} = 0.21$, $X_{\text{N}_2} = 0.79$ and pure fuel, where X are the mole fractions. The implementation for this boundary condition is written in a general way and can handle arbitrary oxidizer and fuel compositions. First, the oxygen required to fully oxidize a given gas mixture and the amount of oxygen present is computed from the elemental compositions:

$$\beta_{\text{O}_2, \text{required}} = \sum_k \frac{Y_k}{M_k} \left(a_{\text{C},k} + a_{\text{S},k} + \frac{1}{4} a_{\text{H},k} \right) \quad (4.2)$$

where the sum considers all species k and $a_{e,k}$ is the number of atoms of element e in species k . Likewise, the amount of oxygen present can be computed from:

$$\beta_{\text{O}_2, \text{present}} = \frac{1}{2} \sum_k \frac{Y_k}{M_k} a_{\text{O},k} \quad (4.3)$$

With these quantities, the stoichiometric air to fuel ratio AFR_{st} can be computed as:

$$AFR_{\text{st}} = - \frac{\beta_{\text{O}_2, \text{required}}(\text{Fuel}) - \beta_{\text{O}_2, \text{present}}(\text{Fuel})}{\beta_{\text{O}_2, \text{required}}(\text{Oxidizer}) - \beta_{\text{O}_2, \text{present}}(\text{Oxidizer})} \quad (4.4)$$

and the mass fraction of species k for a given ϕ can be computed from

$$Y_k = \frac{\phi Y_k(\text{Fuel}) + AFR_{\text{st}} Y_k(\text{Oxidizer})}{\phi + AFR_{\text{st}}} \quad (4.5)$$

where $Y_k(\text{Fuel})$ and $Y_k(\text{Oxidizer})$ are the mass fractions of species k in the fuel and oxidizer compositions.

It should, however, be noted, that the flame speed does not linearly depend on ϕ (see e.g. Fig. 4.1). Because of this, the movement of the flame back and forth during the oscillation is generally not symmetric and the mean flame position can move away or toward the inlet over time. Also, the permissible amplitudes are limited on one hand by the size of the domain, limiting the amount the flame can freely move, and on the other hand by the flammability limits. If the flame extinguishes at some point in time, it will stay extinguished. Another

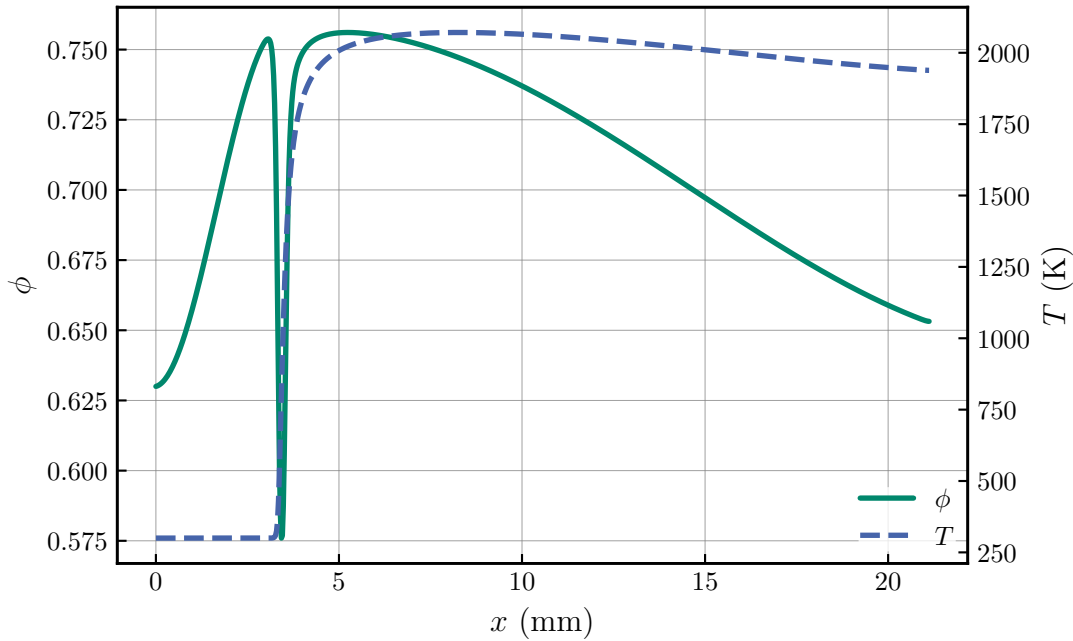


Figure 4.3: Snapshot of the spatial profile of equivalence ratio and temperature at the time $t \cdot f = 1.75$ for a hydrogen-air flame oscillating with $f = 1/(20\tau_c)$ and relative amplitude of $\phi_a = 0.1$.

effect that is different from the steady-state flames is commonly known as back-supporting [9, 205, 206]. During the oscillation period where ϕ increases for the lean flames, the adiabatic flame temperature and therewith the temperature of the burnt gases is higher than at the mean equivalence ratio ϕ_0 . Therefore, when ϕ decreases again, the temperature of the hot exhaust gases is higher than the adiabatic flame temperature at the current ϕ and more heat is conducted back into the reaction zone than at a steady-state flame with the same equivalence ratio, thus supporting the flame from the back. These effects lead to the flame speed signal to be not symmetric around the flame speed corresponding to $\phi = \phi_0$.

First, a set of lean hydrogen flames subjected to the oscillating upstream equivalence ratio is studied. Lean hydrogen flames are chosen because of their technical relevancy, because they have a Lewis number below unity, meaning that they are diffusion controlled due to $Le < 1$, and they correspond to the turbulent flames later discussed in section 4.3. Figure 4.3 shows a snapshot from the simulation of hydrogen-air at $\phi_0 = 0.7$ with a frequency of $1/(20\tau_c)$ or 190 Hz and relative amplitude of $\phi_a = 0.1$. The flame transit time τ_c is evaluated for a steady-state flame at $\phi = \phi_0$. The snapshot is taken at the time $t = 9.24$ ms or $f \cdot t = 1.75$. This is the time when the equivalence ratio at the inlet is at its minimum value of $\phi(t) = 0.63$.

Table 4.1: Flame transit time and flame thickness for the lean hydrogen flames used in the harmonically oscillating equivalence ratio cases.

ϕ_0	$s_{L,0}$ (m/s)	τ_c (ms)	δ_{th} (mm)
0.5	0.56	0.75	0.42
0.7	1.3	0.26	0.35
0.9	2.0	0.18	0.35

The oscillation of ϕ can be seen from its spatial profile in Fig. 4.3, which is at its lowest point at the inlet ($x = 0$) and then increases up to the flame front at $x \approx 4$ mm and decreases again after the flame front. Inside the flame front, the local equivalence ratio drops significantly due to preferential diffusion: in the hydrogen flame, hydrogen radicals and hydrogen gas diffuse much faster than other species due to their size and therefore diffuse faster into the reaction zone, leaving behind a locally lowered equivalence ratio. The same effect is present in steady-state flames. The local equivalence ϕ_{loc} ratio is computed based on Eq. (4.2) and Eq. (4.3) from

$$\phi_{loc} = \frac{\beta_{O_2,required}(\text{gas mixture})}{\beta_{O_2,present}(\text{gas mixture})} \quad (4.6)$$

The temperature profile in Fig. 4.3 shows the back-supporting effect. At $x = 5$ mm, the temperature is higher than at the outlet. This effect is not present in lean, steady-state hydrogen flames but a consequence of the equivalence ratio oscillation.

For the hydrogen flames, the following oscillation parameters have been applied:

- frequencies f : $1/(40\tau_c)$, $1/(20\tau_c)$, $1/(10\tau_c)$, $1/(5\tau_c)$, $1/(2.5\tau_c)$
- relative amplitudes ϕ_a : 0.025, 0.05, 0.1
- mean equivalence ratios ϕ_0 : 0.5, 0.7, 0.9

The flame properties at the mean equivalence ratios ϕ_0 of steady-state flames are summarized in Table 4.1.

Figure 4.4 shows the flame response in terms of its global consumption speed over time for different oscillation frequencies. The displayed results are obtained from a hydrogen-air flame with a mean equivalence ratio $\phi_0 = 0.7$ and a relative oscillation amplitude of $\phi_a = 0.05$. At every time step, the consumption speed s_c

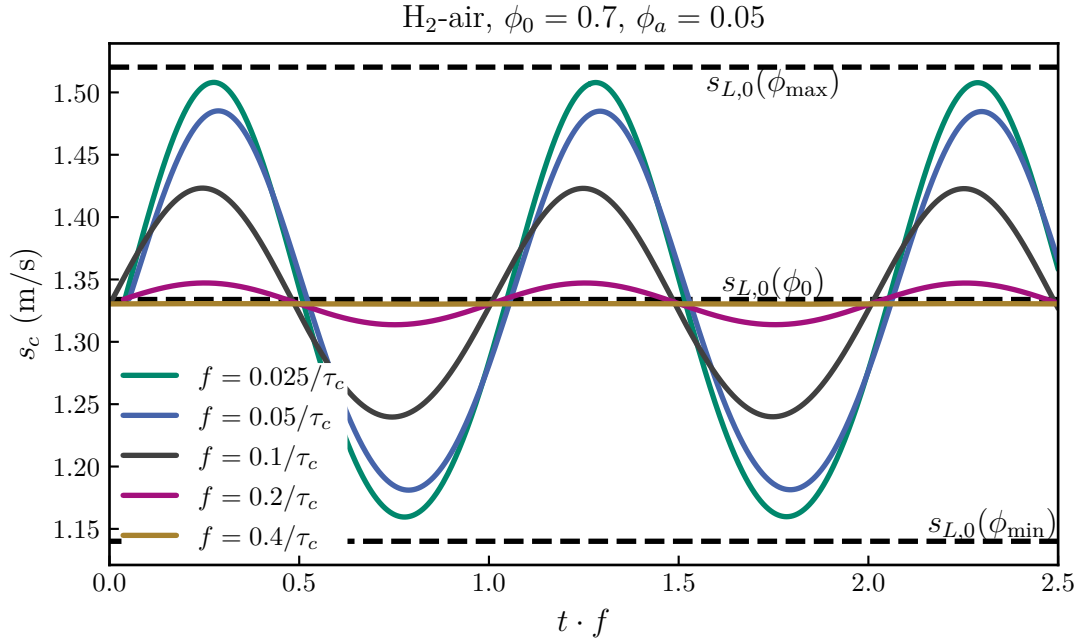


Figure 4.4: Global consumption speed computed at every time point during the oscillation of the upstream equivalence ratio for different frequencies f and constant relative amplitude $\phi_a = 0.05$ around $\phi_0 = 0.7$.

is computed by integration of the fuel reaction rate $\dot{\omega}_F$ along the one-dimensional domain:

$$s_c \equiv \frac{1}{\rho_0 (Y_{F,b} - Y_{F,0})} \int_{-\infty}^{+\infty} \dot{\omega}_F dx \quad (4.7)$$

At high frequencies, e.g. $f = 0.4/\tau_c$ which corresponds to a physical frequency of 1538 Hz, the flame does not react to the equivalence ratio oscillation. The black dashed lines show the flame speed of a steady-state flame $s_{L,0}$ corresponding to ϕ_0 (dashed line in the center) and the minimum and maximum equivalence ratio during the oscillation. With decreasing frequency, the amplitude of the consumption speed increases. At $f = 0.025/\tau_c$ or 96 Hz, the flame can almost relax to the steady-state flame speed $s_{L,0}(\phi_{\max})$ and $s_{L,0}(\phi_{\min})$ during the oscillation. It is therefore evident that the frequency of the equivalence ratio oscillation plays an important role for the flame dynamics.

The dependence of the flame dynamics on the amplitude of the oscillation is not as pronounced as the dependence on frequency. Figure 4.5 compares the flame response in terms of the global consumption speed for two different oscillation amplitudes. In the case on the left, the equivalence ratio varies between 0.6875–0.7125, which is a difference of 1.24 m/s–1.43 m/s in the steady-state flame speed. On the right, the equivalence ratio varies between 0.63–0.77 or a difference of the steady-state flame speed of 0.94 m/s–1.70 m/s. However, even though

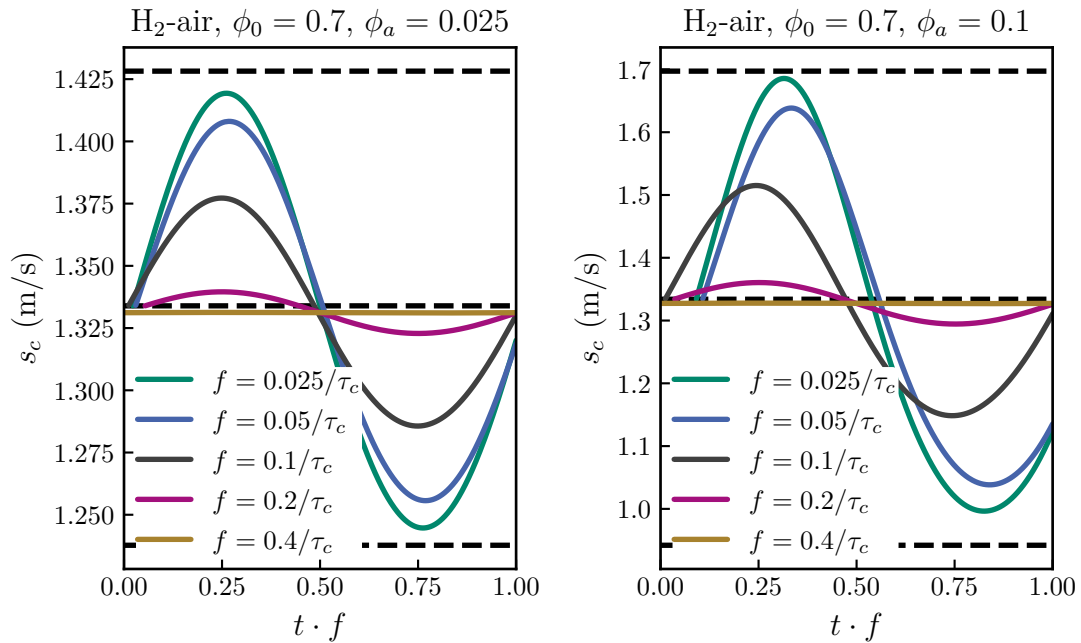


Figure 4.5: Comparison of the flame's response in terms of the global consumption speed for different oscillation amplitudes.

there is a significant discrepancy in the flame speed range, both cases have a comparable effect on the flame response. A quantitative analysis of this is given in section 4.1.2.

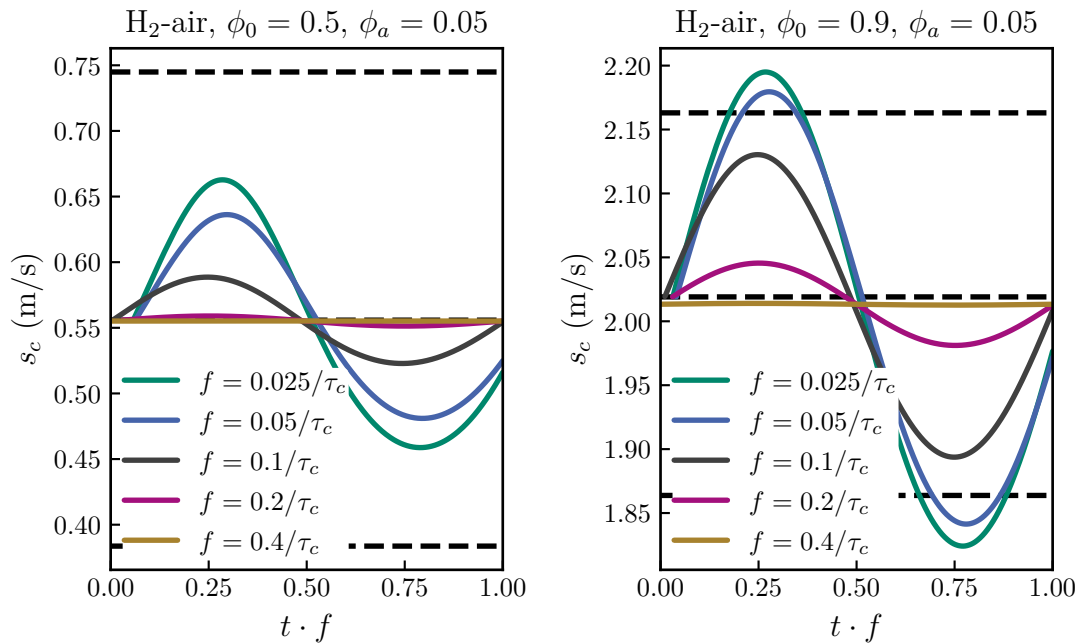


Figure 4.6: Comparison of the flame's response in terms of the global consumption speed for different ϕ_0 and same ϕ_a .

Lastly, the influence of the equivalence ratio itself is discussed. As shown in Fig. 4.4 and Fig. 4.5, at a frequency of $f = 0.025/\tau_c$, the flames with $\phi_0 = 0.7$ reach peak flame speeds that are within a few percent of the steady-state flame speed at ϕ_{\max} independent of amplitude. However, this behavior depends on ϕ_0 itself. The consumption speed amplitude shown in Fig. 4.6 for flames with $\phi_0 = 0.5$ on the left and $\phi_0 = 0.9$ on the right demonstrates that the time normalized by the flame transit time required to relax to a quasi-steady state is much longer for slower, leaner flames than faster flames, which are closer to stoichiometry. While for frequencies of $f = 0.025/\tau_c$, the flames with $\phi_0 = 0.7$ almost reach the quasi-steady state, the flames with $\phi_0 = 0.5$ at the same normalized frequency only reach half of the amplitude required to have the instantaneous consumption speed match the steady-state flame speed. On the other hand, the much faster flames at $\phi_0 = 0.9$ slightly exceed the steady-state flame speeds at ϕ_{\max} and ϕ_{\min} already at $f = 0.05/\tau_c$. The reason why the flame speed can be higher (or lower) than the corresponding steady-state flame speed for the $\phi_0 = 0.9$ case lies in the back-supporting. Similar results have been recently found by Tomidokoro et al. [206] for premixed counterflow flames.

Because a turbulent methane flame with a global equivalence ratio of $\phi = 0.909$ is considered in section 4.3, results for this flame are briefly presented here. The flame parameters are $s_{L,0} = 0.28$ m/s, $\delta_{\text{th}} = 0.49$ mm and $\tau_c = 1.5$ ms. The flame response in Fig. 4.7 is qualitatively similar to the results of the hydrogen-air flame at $\phi_0 = 0.9$ in Fig. 4.6 on the right.

4.1.2 Evaluation of the Amplitude Response

In order to quantify and combine the previous results, the consumption speed amplitude is evaluated relative to the steady-state values as:

$$s_{c,a} \equiv \frac{\max(s_c) - \min(s_c)}{s_{L,0}(\phi_{\max}) - s_{L,0}(\phi_{\min})} \quad (4.8)$$

This is shown in Fig. 4.8 for the hydrogen flames, where the normalized amplitude of the flame speed response $s_{c,a}$ is plotted over the Damköhler number $Da = 1/(f\tau_c)$ ¹, where τ_c is the flame transit time of the steady-state flame at $\phi = \phi_0$. It is clear that different lines corresponding to different amplitudes ϕ_a collapse. Therefore,

¹ Some authors prefer to use the Strouhal number St to characterize the flame dynamics. As these results are related to the study of turbulent flames in section 4.3, the Damköhler number is used here to express the dimensionless frequency.

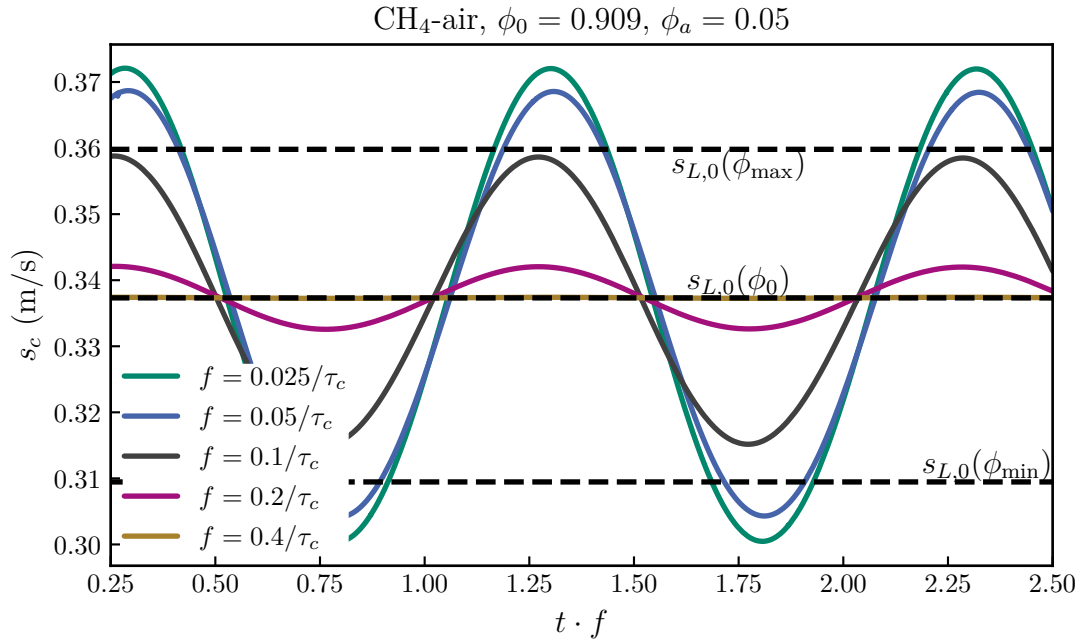


Figure 4.7: Response of a methane-air flame at $\phi_0 = 0.909$ to upstream equivalence ratio oscillations with $\phi_a = 0.05$ and different frequencies.

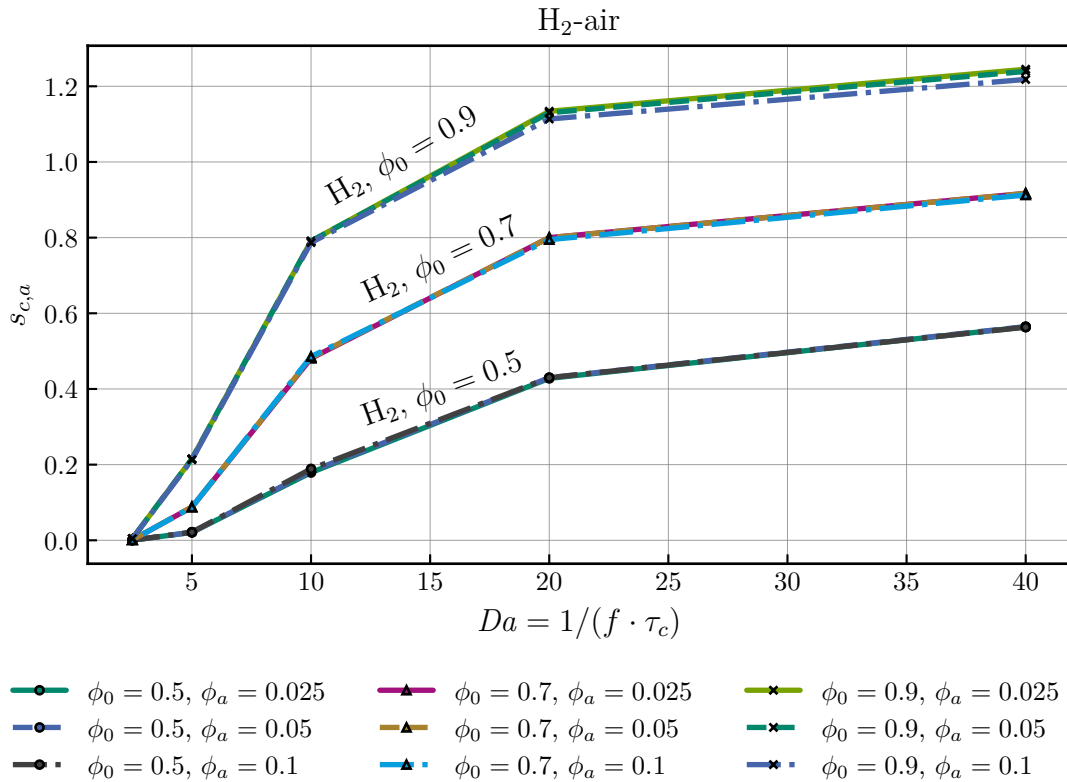


Figure 4.8: Summary of the consumption speed amplitude response of the hydrogen flames to different frequencies and amplitudes of equivalence ratio oscillations.

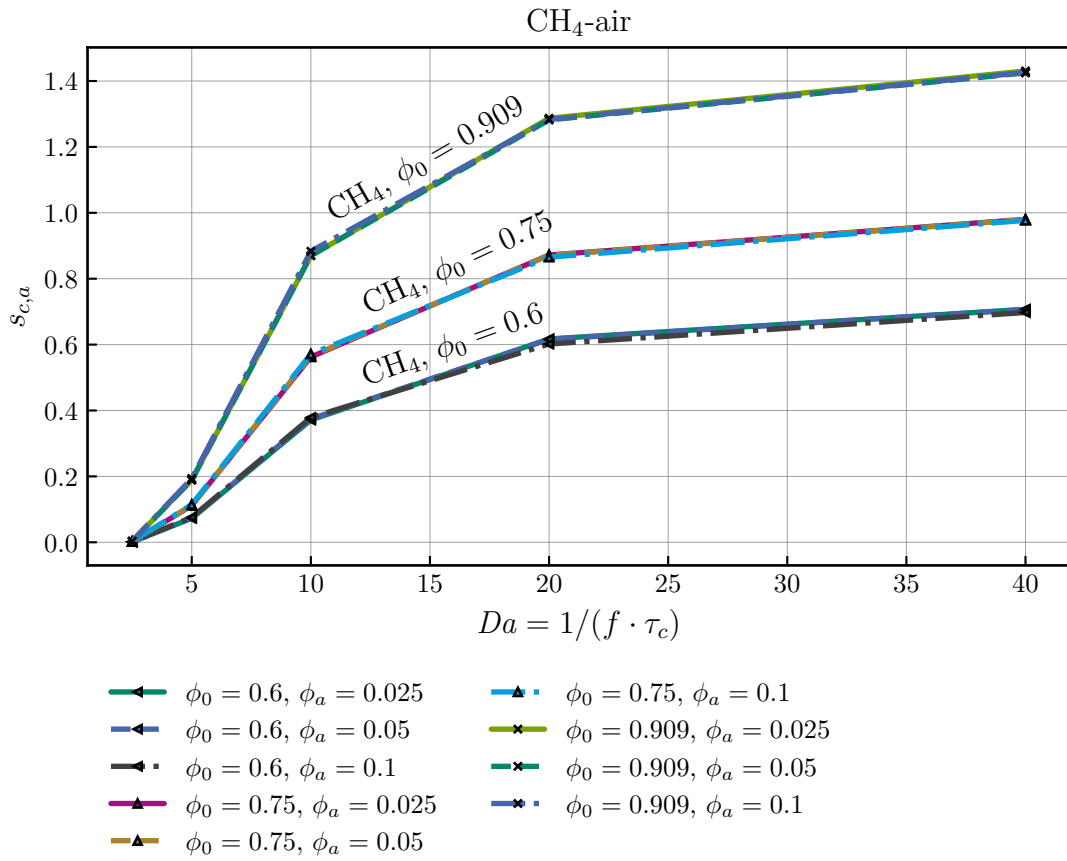


Figure 4.9: Summary of the consumption speed amplitude response of methane flames to different frequencies and amplitudes of equivalence ratio oscillations.

the flame dynamics are mostly determined by ϕ_0 and the frequency. The values of $s_{c,a} > 1$ are a result of the back-supporting present in the harmonically oscillating upstream equivalence ratio setup. The same trend is found for methane flames in Fig. 4.9

This setup of one-dimensional flames subjected to upstream equivalence ratio oscillation still has some limitations: as mentioned before, the amplitude and frequencies are limited by a certain extend. If the frequencies are too low, the flame will eventually propagate to the inlet or leave the domain through the outlet. Lower frequencies would therefore require much larger computational domains, which drastically increases the computational effort. Additionally, if frequencies are too high, the wavelength of the equivalence ratio oscillation inside the domain becomes very low. As the equivalence ratio disturbance is convected with the unburnt flow speed $s_{L,0}$, for frequencies of $f = 1/\tau_c$ the wavelength is the same as the flame thickness. Because of this, the equivalence ratio profile is flattened over time due to diffusion before it can reach the flame front, leading to a more damped response. However, in practical applications, such fluctuations are rapidly

destroyed by diffusion. To overcome these limitations, a new setup for studying flame relaxation times in the limit of instantaneously changing equivalence ratios is used in the next section, which also avoids the back-supporting effect.

4.1.3 Sudden Change of Equivalence Ratio

To overcome the shortcomings of the previous setup and to quantify the flame's relaxation time, a novel numerical setup is used. Instead of having a transiently changing equivalence ratio field, the species concentrations are instantaneously changed and the flame has to adapt its temperature as well as thickness of species profiles. In this way, there is no back-supporting, diffusive flattening of the equivalence ratio amplitude, limitation to the difference in equivalence ratio or stratification throughout the flame stemming from upstream equivalence ratio changes. Of course, such a setup is only possible in the context of numerical simulations. Nonetheless, the time it takes for the flame to adapt to the new equivalence ratio is a measure for the flame relaxation time in the limit of instantaneous changes in ϕ .

The computational setup is similar to the one described in section 4.1.1. It is one-dimensional with fixed values of temperature, mass fraction and velocity at the inlet. What differs is the generation of the initial conditions. To measure the flame relaxation time for instantaneously changing equivalence ratio from ϕ_1 to ϕ_2 , two steady-state simulations are performed with Cantera. First, for a flame with the equivalence ratio $\phi = \phi_1$, which represents the “previous” equivalence ratio from which the flame starts, and a steady-state simulation with Cantera at $\phi = \phi_2$, which represents the “new” equivalence ratio after the sudden change. Based on these two preliminary steady-state flame results, the initial conditions for the new setup can be generated.

Figure 4.10 gives an overview how the initial conditions for the transient simulation with the DNS solver in OpenFOAM® are generated. The two pictures in the top row show an example of a progress variable θ for the two steady-state flames at ϕ_1 and ϕ_2 :

$$\theta \equiv \frac{T - \min(T)}{\max(T) - \min(T)} \quad (4.9)$$

In this example, ϕ_1 has a much broader profile and the flame at ϕ_2 is much thinner, because ϕ_2 is closer to unity than ϕ_1 . In this way, the flames can be expressed as a function of $\theta(x)$. Using θ based on the temperature can be done in these cases, because for lean flames, the temperature rises strictly monotonically. The two pictures in the second row of Fig. 4.10 show schematically the mass fraction profile

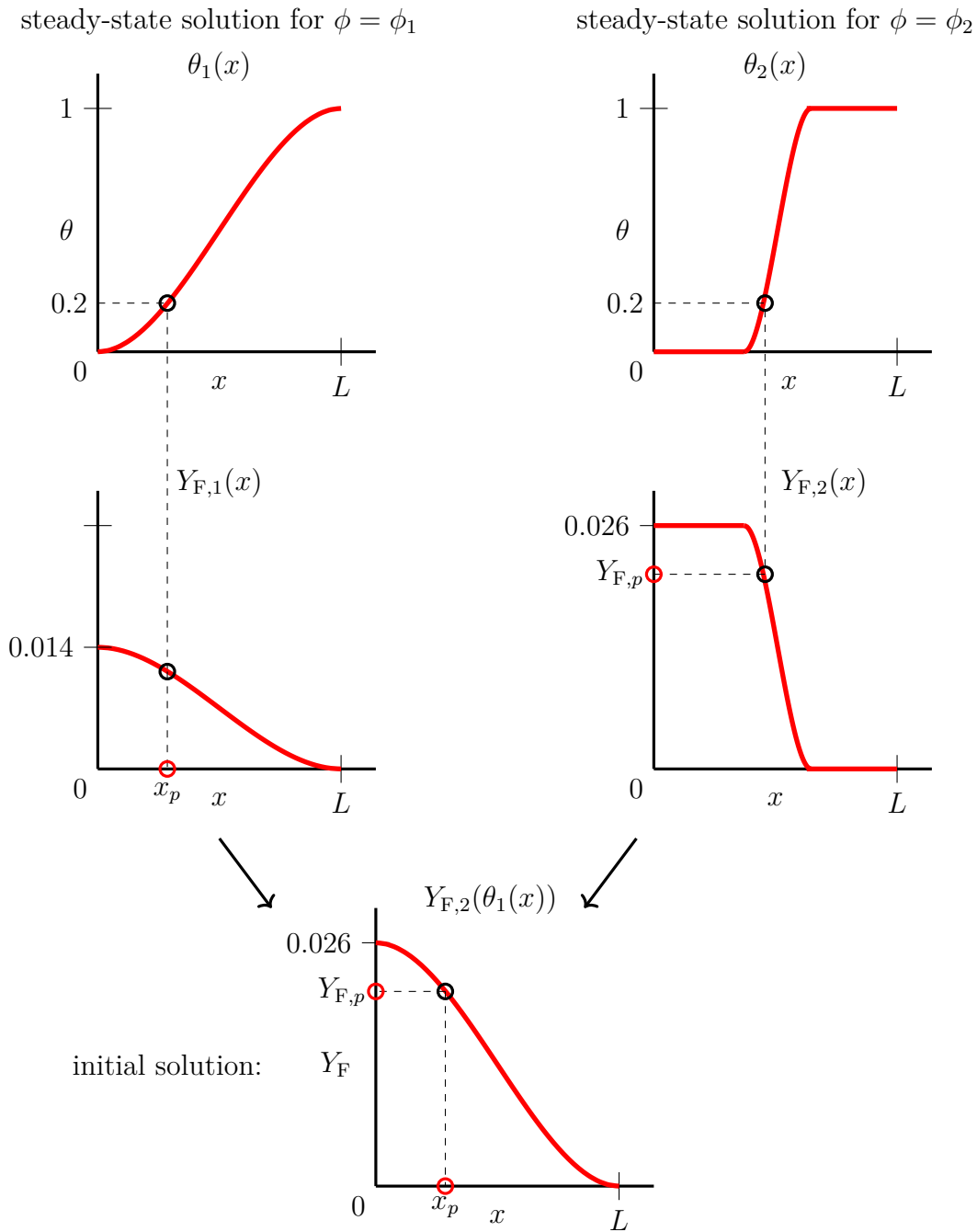


Figure 4.10: Generation of the initial solution: First, simulate two steady-state flames at $\phi = \phi_1$ and $\phi = \phi_2$. Then, map the mass fractions of each species and the velocity profile of the solution for ϕ_2 as a function of θ to the spatial profile of θ_1 . In this way, the local equivalence ratio is set to the case for ϕ_2 but the profile thickness and temperature is taken from the solution at ϕ_1 .

of the fuel species Y_F . In this case, the example is given for a hydrogen-air flame at $\phi_1 = 0.5$, where the mass fraction of H_2 in the fresh gas is 0.014, and $\phi_2 = 0.9$, where the mass fraction of H_2 in the fresh gas is 0.026. The initial conditions can now be created by mapping the species profiles of $Y_{k,2}(\theta)$ to the spatial profile of $\theta_1(x)$. In Fig. 4.10 at the bottom, the final profile used as initial condition for the simulation has the mass fraction value of $Y_{k,2}$ from the ϕ_2 case at the position of $\theta(x)$ from ϕ_1 . The physical meaning is, that the flame structure of ϕ_1 in terms of its flame thickness remains unchanged, but instantaneously at each position throughout the flame the local species concentrations now belong to the case for $\phi = \phi_2$. In order to reach a steady state at the end of the transient simulation, the gas velocity values are mapped from ϕ_2 as well.

When the simulation starts, chemical reaction rates are suddenly higher, due to the local equivalence ratio corresponding to $\phi_2 = 0.9$, but the diffusive fluxes have to adjust, because the flame thickness is too broad as it still follows the flame at $\phi_1 = 0.5$. Likewise, the temperature is taken from ϕ_1 , so that the flame first has to heat up to the adiabatic flame temperature corresponding to $\phi_2 = 0.9$. The adjustment of the flame thickness (becoming thinner) and adaptation of the diffusive fluxes to the increased reaction rates as well as the heating of the gas requires time, which can be measured with this setup. The computational domain is one-dimensional with a length of $L = 50 \max(\delta_{th}(\phi_1), \delta_{th}(\phi_2))$ and the resolution is $\Delta x = \min(\delta_{th}(\phi_1), \delta_{th}(\phi_2))/20$. The time step is adjusted to have a convective CFL number of 0.1.

4.1.4 Evaluation of Flame Relaxation Times

The temporal evolution of the flame's consumption speed s_c is shown in Fig. 4.11 for the case where the local equivalence ratio is instantaneously changed from $\phi_1 = 0.5$ to $\phi_2 = 0.9$ for a hydrogen-air flame at atmospheric conditions. It takes about 0.42 ms for the flame to adjust to the flame speed of the undisturbed steady-state flame at ϕ_2 , which is depicted as black dashed line. The relaxation time t_{relax} is defined as the time, when the consumption speed has reached a value within 1% of the final steady-state value:

$$t_{relax} \equiv t \left(\frac{|s_c(t) - s_{L,0}(\phi_2)|}{s_{L,0}(\phi_2)} = 0.01 \right) \quad (4.10)$$

Figure 4.11 on the right shows the reverse case, where the flame starts out at $\phi_1 = 0.9$ and then the species concentrations are instantaneously changed to the

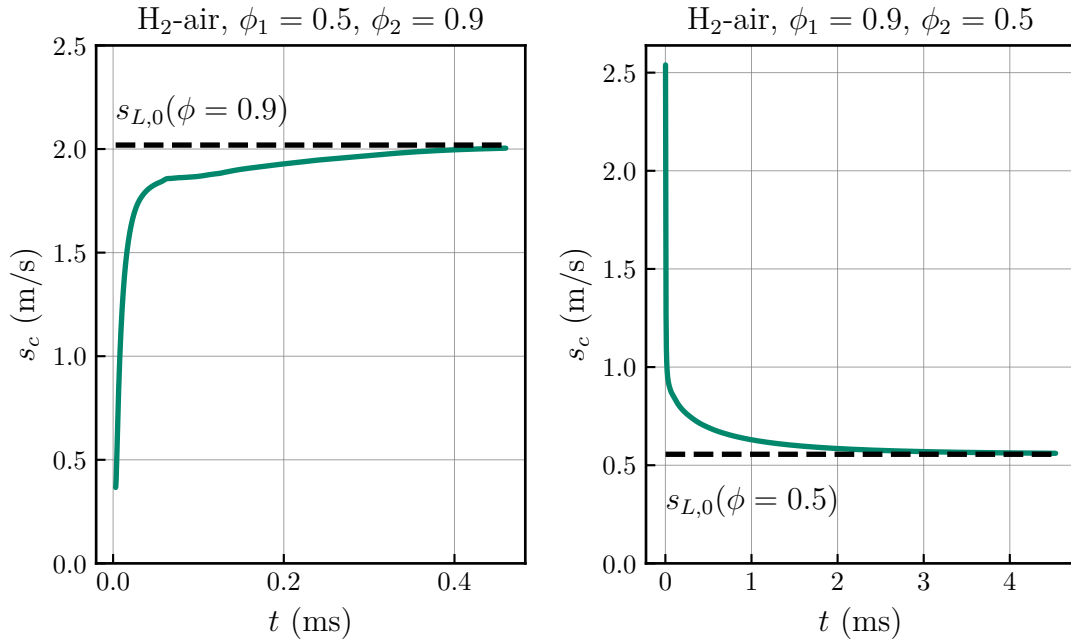


Figure 4.11: Temporal evolution of the flame's consumption speed s_c when changing the equivalence ratio instantaneously from $\phi_1 = 0.5$ to $\phi_2 = 0.9$ on the left and the other way around on the right. The black dashed line is the steady-state flame speed $s_{L,0}$ at $\phi = \phi_2$.

ones corresponding to $\phi_2 = 0.5$. In this case, the flame requires a relaxation time of $t_{\text{relax}} \approx 4.38$ ms to adapt to the new equivalence ratio.

The values of t_{relax} measured with this setup are summarized in Table 4.2. The two values in bold correspond to the cases shown in Fig. 4.11. Two observations can

Table 4.2: t_{relax} in ms for different hydrogen-air flames.

		ϕ_2						
		0.4	0.5	0.6	0.7	0.8	0.9	1.0
ϕ_1	0.4	—	7.19	3.01	1.62	1.04	0.73	0.36
	0.5	29.3	—	1.55	0.90	0.61	0.42	0.21
	0.6	31.1	3.91	—	0.54	0.41	0.29	0.12
	0.7	31.4	4.23	1.01	—	0.24	0.17	0.07
	0.8	31.6	4.33	1.17	0.36	—	0.07	0.04
	0.9	31.4	4.38	1.23	0.44	0.11	—	0.02
	1.0	31.6	4.41	1.26	0.47	0.141	0.02	—

be made from these absolute relaxation times: when starting with any equivalence ratio ϕ_1 , the relaxation time is mostly dependent on the final equivalence ratio ϕ_2 . And secondly, the faster the flame is at ϕ_2 , the lower the flame relaxation time is. The difference $\phi_1 - \phi_2$ is less important, since the initial adaption phase is very fast, see Fig. 4.11.

The flame relaxation times can be correlated by defining a dimensionless flame relaxation time:

$$\hat{t}_{\text{relax}} \equiv \frac{t_{\text{relax}}}{\max(\tau_c(\phi_1), \tau_c(\phi_2))} \quad (4.11)$$

Plotting values of \hat{t}_{relax} as a function of ϕ_2 shows that the results collapse for different ϕ_1 , as shown in Fig. 4.12. Additionally, the trend is valid for both hydrogen and methane flames. In real turbulent flames, the deviation of local equivalence ratio caused by flame stretch is usually moderate $\Delta\phi \approx 0.1$, unless strong thermo-diffusive instabilities or flame quenching occur. Therefore, in a first order approximation, $\phi_1 \approx \phi_2$ and $\tau_c(\phi_1) \approx \tau_c(\phi_2)$, so that the flame relaxation time Eq. (4.11) can be expressed from the general equivalence ratio as (black dashed line from Fig. 4.12):

$$\frac{t_{\text{relax}}}{\tau_c} = 160 \exp(-7\phi) \quad (4.12)$$

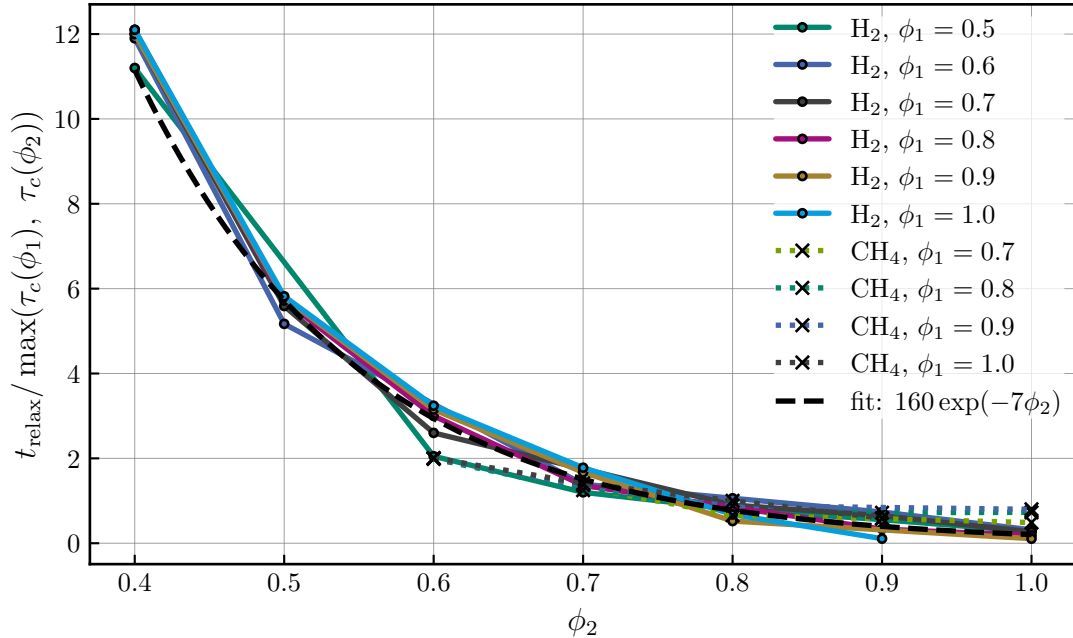


Figure 4.12: Normalized flame relaxation time \hat{t}_{relax} as a function of ϕ_2 for different ϕ_1 , valid for both lean hydrogen and methane flames at atmospheric conditions. The black dashed line is a fit of the form $\hat{t}_{\text{relax}} = a \exp(b\phi_2)$.

This result from Eq. (4.12) has several consequences. First, it explains the finding from section 4.1.1 that the response of the flame in terms of the consumption speed amplitude depends much more strongly on the frequency of the upstream equivalence ratio oscillation than on the amplitude. Secondly, it explains why at the same normalized frequency, faster flames with ϕ closer to unity can reach a quasi-steady state during oscillation, while slower flames require lower normalized frequencies. The reason is that t_{relax}/τ_c is faster for flames closer to stoichiometry than for slower flames so that the normalized frequency at which the flame can reach a quasi-steady state $f \cdot \tau_c$ depends on the global equivalence ratio, as slower frequencies are required for the flame to have enough time to adapt the flame thickness and diffusive fluxes to the changing local equivalence ratio. If the frequencies are too high, the flame has not enough time to reach a quasi-steady state, which results in an attenuated flame response in terms of the consumption speed amplitude to the equivalence ratio oscillation.

4.1.5 Conclusions

Turbulent flames are subjected to transient flame stretch which leads to locally altered flame speeds. For flames with $Le < 1$, this is caused mainly by the change in local equivalence ratio due to focused or defocused diffusive fluxes of the fuel and oxidizer. In order to study the effect of this transient behavior in a clearly defined and controlled manner while taking preferential diffusion and complex reaction mechanisms into account, two one-dimensional flame setups have been presented. In this way, the effect of transient change in equivalence ratio can be studied isolated from flame stretch itself and without any flame instability mechanisms.

In the first setup, the upstream equivalence ratio of the unburnt fuel-oxidizer mixture oscillates harmonically with a specified frequency and amplitude. The flame's response is evaluated in terms of the amplitude of the consumption speed. The simulations show that the flame's response is damped with increasing frequency. This means that the flame becomes less sensitive to the equivalence ratio changes. This result is further discussed in the next section, where the flame's sensitivity to flame stretch reduces with increasing frequency. If the frequencies become too high, the flame does not respond at all. For very low frequencies, the flame has enough time to relax to a quasi-steady state during the oscillation. The specific frequencies at which the flame can relax to a steady state depend on the mean equivalence ratio. Faster flames, meaning flames closer to $\phi = 1$ with small τ_c , can adapt at lower values of $f \cdot \tau_c$ or higher values of Da to a quasi-steady

state compared to slower flames. The results are consistent for both hydrogen and methane flames and yield a characteristic trend when plotted non-dimensionalized.

The second setup allows to quantify the relaxation time. Instead of having a periodic oscillation, the underlying species composition is instantaneously changed to the one for a flame at a different equivalence ratio. However, the thickness of the flame as well as the temperature profile is left unchanged. In this way, chemical reaction rates are instantly changed due to the new species concentrations, but diffusive fluxes have to adapt by changing the flame thickness and heating up or cooling down the burnt gases. This relaxation time explains the amplitude response of the consumption speed from the previous setup: oscillations with time scales lower than the relaxation time do not allow the flame to relax to a quasi-steady state. By normalizing the relaxation time with the flame transit time, results for different equivalence ratios collapse and allow for a simple correlation. The normalized relaxation time is higher for slow flames farther away from stoichiometry than for fast flames.

The key points from this section are summarized as follows:

- i.** The flame's response in terms of flame speed to transient equivalence ratio fluctuations depends strongly on the frequency.
- ii.** This response is much less dependent on the amplitude of the fluctuation.
- iii.** At same non-dimensionalized frequency $f \cdot \tau_c$, the amplitude response depends on mean equivalence ratio: the slower the flame in terms of τ_c , the lower the frequency has to be for the flame to be able to relax to a quasi-steady state. These results hold for both lean hydrogen and methane flames.
- iv.** A new setup is proposed that realizes a sudden change of the underlying equivalence ratio to evaluate relaxation times.
- v.** The normalized relaxation times depend on ϕ and are higher for slower flames, which explains the previous results and the decreasing sensitivity of flames to flame stretch with increasing frequency.
- vi.** This effect can be modeled with $t_{\text{relax}}/\tau_c = 160 \exp(-7\phi)$, which is valid for both hydrogen and methane flames and is the flame's relaxation time in the limit of instantaneous equivalence ratio changes.

4.2 Oscillating Laminar Bunsen Flames

In the last section, the response of one-dimensional model flames to changes in local equivalence ratio have been investigated. In turbulent flames, however, the flame dynamics are determined by the flame's interaction with a three-dimensional turbulent flow field. This means, that the flame is subjected to unsteady flame stretching. Isolating the effect of transient flame stretch on the flame's properties in turbulent flows is not an easy task, because turbulent fluctuations are characterized by a broad frequency spectrum.

Therefore, in this section, axisymmetric two-dimensional Bunsen flames with harmonically oscillating inflow conditions are considered. Compared to other model flames, i.e. counterflow or spherically expanding flames, which are limited in the type of flame stretch that appears, the pulsating Bunsen flames are subjected to both positive and negative flame stretch as well as stretching due to curvature and aerodynamic straining. Because of this, they can be used to study flame-flow interaction in a more realistic manner and allow to use single frequency disturbances to investigate the influence of transient effects. The results are then applied to the turbulent flames in section 4.3.

4.2.1 Computational Setup

The computational setup is shown in Fig. 4.13. It represents a two-dimensional axisymmetric case by applying OpenFOAM®'s wedge boundary conditions. Therefore, the domain is built with a wedge angle of 5° . The dimensions of the domain are adapted to the properties of the fresh gas mixture. Based on prior freely propagating one-dimensional flame simulations, the flame thickness δ_{th} and flame speed $s_{L,0}$ are determined. The fresh gas enters the domain from an inlet with a radius of $8\delta_{th}$, having a parabolic velocity profile with a bulk velocity of $u_{bulk} = 3s_{L,0}$. On the outside, a pilot flow consisting of the fully burnt gas at chemical equilibrium enters from an annular area with a width of $6.5\delta_{th}$. The length of the domain is approximately three flame heights h_f , assuming a conical flame. On the right, a slip-wall is prescribed to ensure mass conservation within the domain and to avoid additional velocity gradients on the outer boundary. The gas leaves the domain through an outlet on the top. The resolution of the domain is set equidistantly to $\delta_{th}/20$ to ensure a sufficient resolution of the flame. This results in about 350 000 cells in the computational domain. The time step is set to a *CFL* number of 0.2, which corresponds to time steps of $2.5 \cdot 10^{-5}$ s to $5 \cdot 10^{-5}$ s. Since the dimensions of the domain scale with the flame properties, the Reynolds numbers

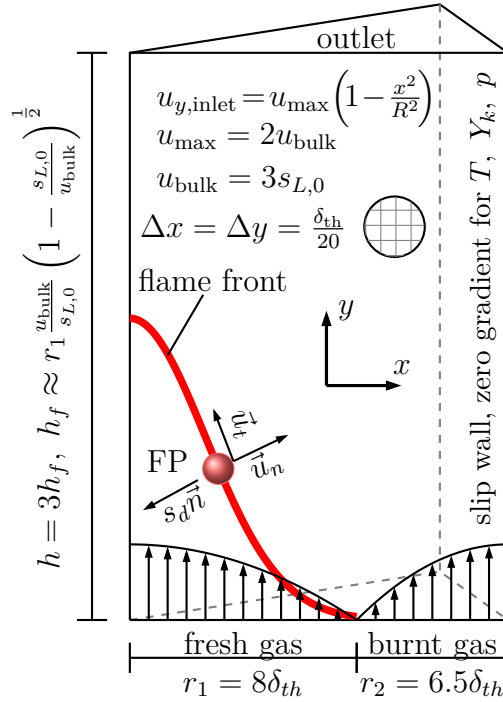


Figure 4.13: Computational domain and boundary conditions for the oscillating Bunsen flames. The red line represents the flame front. The velocity components of a flame particle \bullet on the flame front are indicated as well.

are between 500 and 1000 and therewith in the laminar flow regime. In this way, all flames experience comparable flame stretch in terms of the non-dimensional Karlovitz number Ka .

For all considered cases, the fresh gas enters the domain with $T_0 = 300$ K and $p_0 = 1$ bar. The equivalence ratio ϕ varies, but focus in this section is put on hydrogen-air flames with $\phi = 0.5$ and $\phi = 4$ to include lean and rich conditions as well as positive and negative Markstein numbers (see Table 4.3). In the case of lean hydrogen flames, strong thermo-diffusive instabilities occur due to the low Lewis

Table 4.3: Properties of the freely propagating lean and rich hydrogen flames at atmospheric conditions. The Lewis number $Le = a_0/D_{m,\text{deficient},0}$ is computed from the diffusion coefficient of the deficient species (hydrogen for the lean case and oxygen for the rich case). The flame frequency is $f_c = 1/\tau_c$. The Markstein numbers Ma are determined in Fig. 4.14.

ϕ	$s_{L,0}$ (m/s)	δ_{th} (mm)	ρ_0 (kg/m ³)	τ_c (ms)	f_c (Hz)	Le	Ma
0.5	0.56	0.42	0.97	0.75	1334	0.46	-0.8
4.0	1.71	0.44	0.48	0.26	3901	1.98	0.1

number. The oxidation of hydrogen in air is described by the detailed reaction mechanism by Li et al. [51]. In a previous work [117], periodic slot-burner flames were considered. The new setup in this work improves the previous setup by only including half the flame in the computational domain, thereby saving computing time, having an additional circumferential stretch component to achieve higher stretch rates and including the hot pilot flow to stabilize the flame.

For the oscillating flame cases, the parabolic velocity profiles of the fresh gas inlet and pilot flow oscillate harmonically with a prescribed frequency f and amplitude a :

$$u_y = 2u_{\text{bulk}} \left(1 - \frac{x^2}{R^2} \right) (1 + a \sin(2\pi ft)) \quad (4.13)$$

R is the radius of the respective inlet, $u_{\text{bulk}} = 3s_{L,0}$ and $a = 0.5$ for all considered cases. Because the flame time scales are on the order of milliseconds, frequencies can become high when oscillations with $f > 1/\tau_c$ are considered. Because of this, appendix D presents simulations of high-frequency pulsating flows to show that even at high frequencies, the induced variations in thermo-physical properties in terms of pressure variations, density or temperature are negligible.

4.2.2 Steady-state Bunsen Flames

Figure 4.14 shows the relation between flame speed and flame stretch for the lean and rich Bunsen flames. Because the lean hydrogen flame has $Le \ll 1$, the mass flux of oxygen is being defocused slower at the positively stretched base of the flame, leading to higher heat release rates and therewith consumption speeds near the base of the flame. A tip opening occurs for the lean flame at the negatively stretched flame tip, where the flame locally quenches because the radial diffusion of the fuel is so strong, that the local equivalence ratio at the tip is below the ignition limit. For the rich hydrogen flame on the right of Fig. 4.14, $Le > 1$ and therefore the flame speed and flame stretch correlation reverses: the maximum heat release rate and flame speed is located at the negatively curved flame tip and the minima at the slightly positively curved base of the flame. The steady-state Markstein number Ma from Table 4.3 is determined from a linear fit of $s_c/s_{L,0}$ and Ka in the range of $-0.5 < Ka < 0.5$.

4.2.3 Dynamics of Oscillating Bunsen Flames

The effect of the oscillating inflow on the flame is depicted in Fig. 4.15. Shown are iso-surfaces of the hydrogen mass fraction, which correspond to the hydrogen

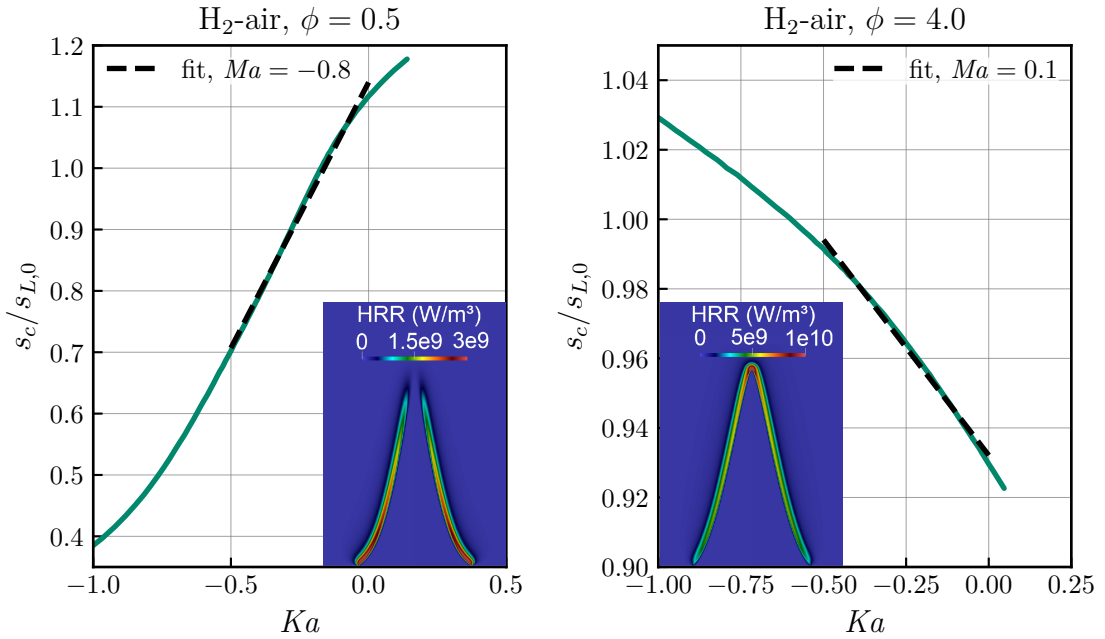


Figure 4.14: Correlation of normalized flame consumption speed $s_c/s_{L,0}$ and normalized flame stretch Ka along the steady-state Bunsen flame for the lean (left) and rich (right) case. The heat release rate (HRR) is depicted for each flame on the bottom. Due to the thermo-diffusive instability of the lean flame, tip opening occurs.

mass fraction at the position of maximum heat release rate in a freely propagating flame. In the background, the heat release rate is depicted on a two-dimensional cutting plane through the flame. At $f = 0$, the flame is in steady-state, as shown in section 4.2.2. The second flame from the left shows the case of a low frequency oscillation, in this case with $f = 0.1/\tau_c$ or $Da = 1/(f\tau_c) = 10$. For $Da \gg 1$, the flame oscillates as a whole. This is illustrated by the two heat release rate profiles in the background of this case, which correspond to the time instances with the minimum and maximum flame height. As the frequency increases, the amplitude of the flame movement is continually attenuated.

The third flame from the left shows the case with $f = 1/\tau_c$ or $Da = 1$. In this frequency range, the response of the flame changes from an oscillation of the whole flame to a pulsating mode, where the flame front becomes wrinkled. This is also demonstrated by the gray-scale temperature on the iso-surfaces in Fig. 4.15, which illustrates the wrinkles on the flame front. The last flame on the right shows the high frequency case with $f = 10/\tau_c$ or $Da = 0.1$. For $Da \ll 1$, the time scales of the flow are so small, that the flame cannot respond to the oscillations. Therefore, the flame in the high frequency case is the same as the steady-state

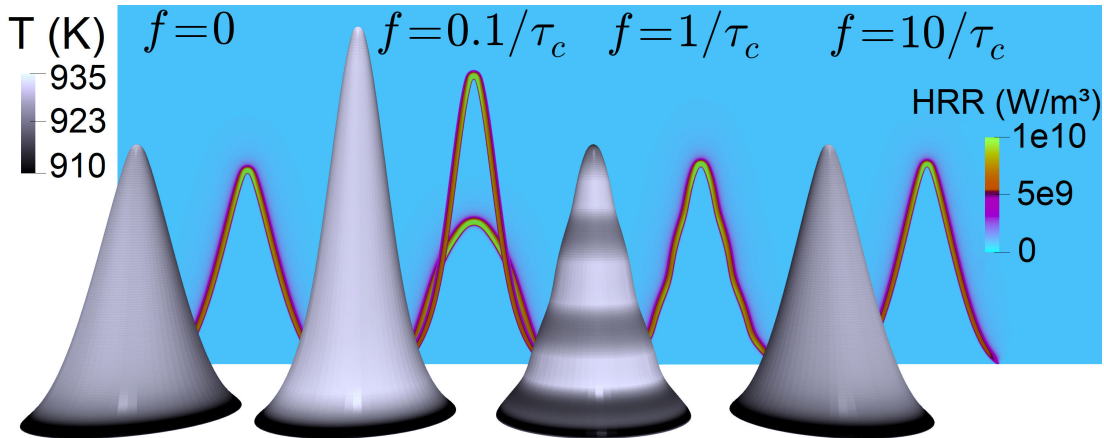


Figure 4.15: Response of the hydrogen-air Bunsen flame at $\phi = 4$ to flow oscillations with different frequencies f . In the foreground, iso-surfaces of the hydrogen mass fraction colored by temperature show the shape of the flame, while the background shows the heat release rate on a two-dimensional cutting plane.

flame. This is consistent with the results presented in section 4.1.1, where the amplitude response of one-dimensional flames has been shown to go toward zero for high Da fluctuations.

Figure 4.16 shows the details of the flame structure at $Da = 1$ for the lean (left) and rich (right) flames. Both flames exhibit the corrugated flame front structure as described above. However, the wrinkles are much more pronounced for the lean flame due to the strong thermo-diffusive instability and the heat release rate

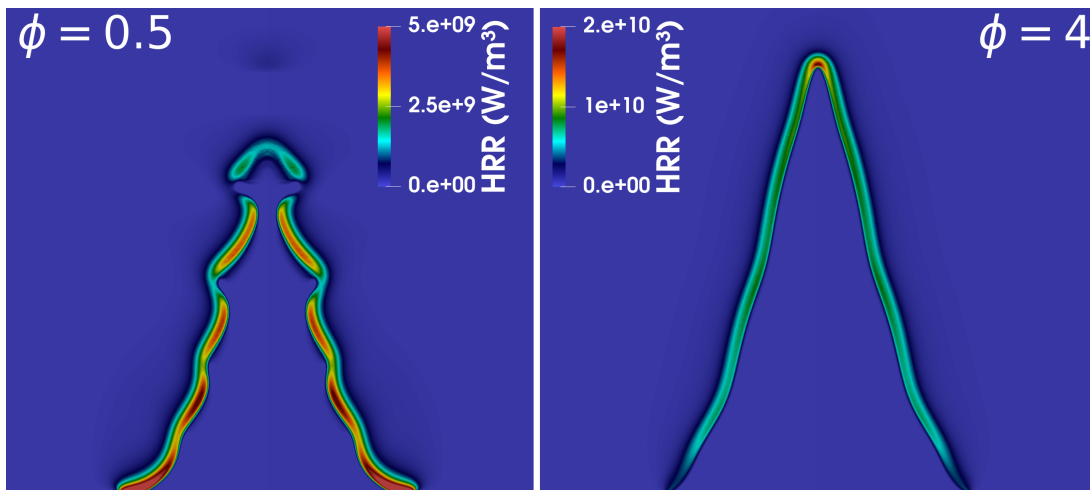


Figure 4.16: Instantaneous heat release rate field on a two-dimensional cutting plane through the flames at $f = 1/\tau_c$ or $Da = 1$. Lean flame on the left, rich flame on the right.

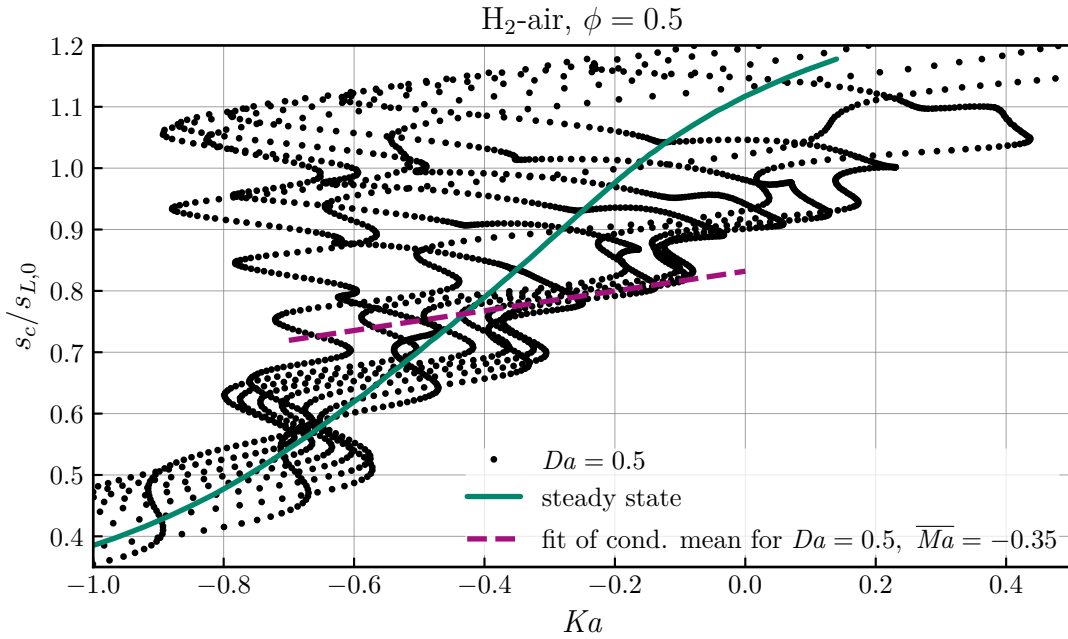


Figure 4.17: Example of computing the averaged Markstein number \overline{Ma} from eight time instances based on the conditional mean of flame speed and flame stretch for the lean flame at $Da = 0.5$.

varies strongly along the flame front. At negatively curved parts of the flame, there is even local extinction.

Not only the flame's response in terms of the amplitude of the flame height attenuates with increasing frequency, the flame's sensitivity to flame stretch is affected as well. This can be expressed as a frequency dependent averaged Markstein number \overline{Ma} [129, 130], which represents the flame as a whole. To determine this Markstein number, the method from [117] is used, where eight time instances within the oscillation period are used to determine an averaged Markstein number. Figure 4.17 shows an example of this procedure for the lean flame at $Da = 0.5$. Although the general trend of the steady-state case remains valid, i.e. negative stretch generally corresponds to low flame speed and positive stretch corresponds to high flame speed, points on the flame surface do not lie on the steady-state correlation. Therefore, to capture the response of the flame as a whole, the conditional mean of all flame speed values of points on the oscillating flame fronts with respect to flame stretch is computed and the averaged Markstein number is determined from a linear fit over the conditional mean from $-0.5 < Ka < 0.5$. These results are later used to describe the global response of turbulent flames in section 4.3 to the turbulent flow.

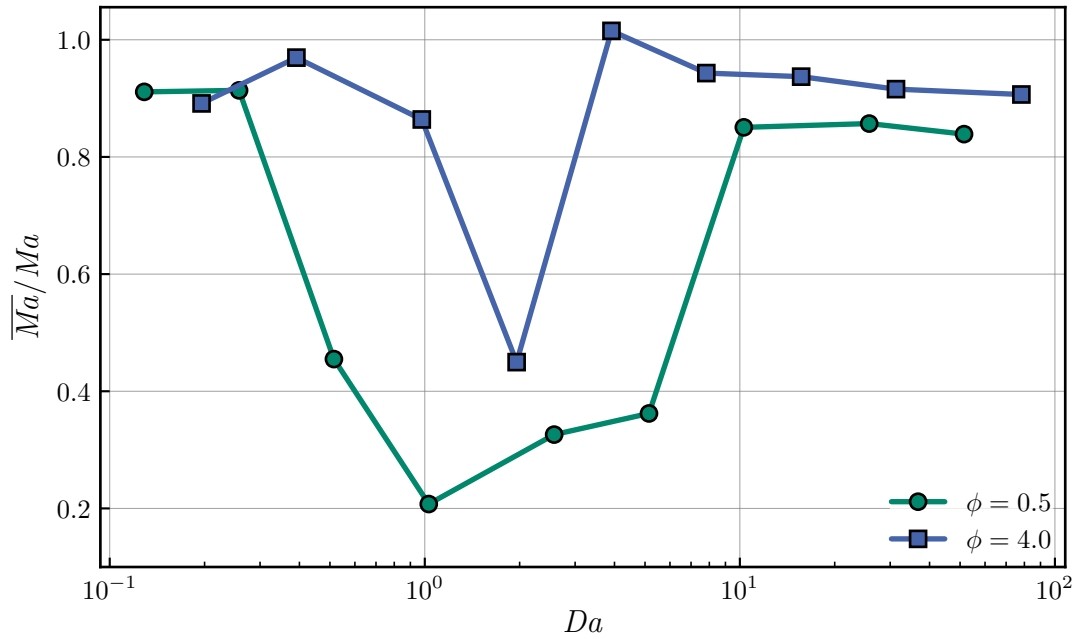


Figure 4.18: Ratio of averaged Markstein number \overline{Ma} to the steady-state Markstein number Ma for the lean and rich flames for different Damköhler numbers Da .

Figure 4.18 shows the frequency dependent averaged Markstein numbers \overline{Ma} normalized by the steady-state Markstein number Ma for the lean and rich flames at different frequencies or Damköhler numbers Da . For low frequencies ($Da > 10$), the averaged Markstein number is approximately the same as the steady-state Markstein number. As the frequency increases to values of the inverse flame time scale at $Da = 1$, the averaged Markstein number becomes lower, meaning that the sensitivity of flame speed to flame stretch decreases. For very high frequencies ($Da \ll 1$), the flame has the same shape as the steady-state flame, so that the averaged Markstein number is close to the steady-state one. It should be noted, however, that this regime of $Da \ll 1$ is not necessarily representative for a turbulent flame, as the interaction with the broad-band frequency spectrum and length scales generally means that flame speed to flame stretch sensitivity of a steady-state flame is not recovered in this limit. This is further discussed in section 4.3.

4.2.4 Global Flame Properties

Instead of considering the local flame properties by evaluating local flame speed and flame stretch on points on the flame surface, the effect of flow transients on global flame properties can be evaluated as well with the oscillating Bunsen flame setup. Figure 4.19 shows the global flame speed, which can be considered as an

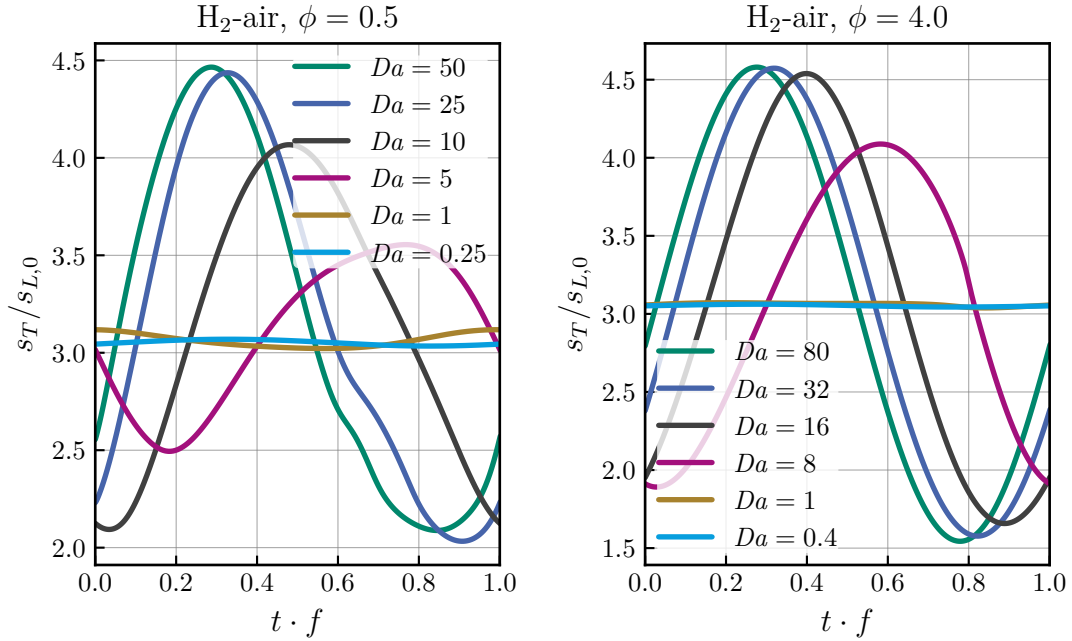


Figure 4.19: Normalized global flame speed s_T for different Da for the lean (left) and rich (right) flames.

analogue to the turbulent flame speed, over one oscillation period for different Da . The global flame speed is computed from the global fuel consumption rate:

$$s_T \equiv \frac{1}{\rho_0 A_0 (Y_{F,b} - Y_{F,0})} \int \dot{\omega}_F dV \quad (4.14)$$

where A_0 is the surface area of the steady-state flame and the subscript 0 denotes the fresh gas state and b the burnt gas. From Fig. 4.19, two important effects of the flow transients on the global flame properties can be seen. On the one hand, for very high Damköhler numbers, the amplitude of s_T stays nearly constant. For $Da < 10$, the amplitude of s_T decreases with decreasing Damköhler number. This behavior corresponds to the averaged, frequency dependent Markstein numbers from Fig. 4.18, as the amplitude of the global flame speed oscillation can be considered as the flame's response or sensitivity to global flame stretch, given by the amplitude of the flow oscillation. For high frequencies or $Da \ll 1$, the amplitude of s_T becomes zero as the flame cannot respond to the flow transients anymore. Note that the mean value of $s_T/s_{L,0}$ lies at 3, because the bulk flow velocity is prescribed as $u_{\text{bulk}} = 3s_{L,0}$.

The second effect of the flow transients is a time delay between the flame response and the flow oscillations. This can be seen in Fig. 4.19 from the peak locations moving to later phase angles compared to the oscillation of the bulk flow, which for all graphs is the same. Another common way of visualizing this is to plot

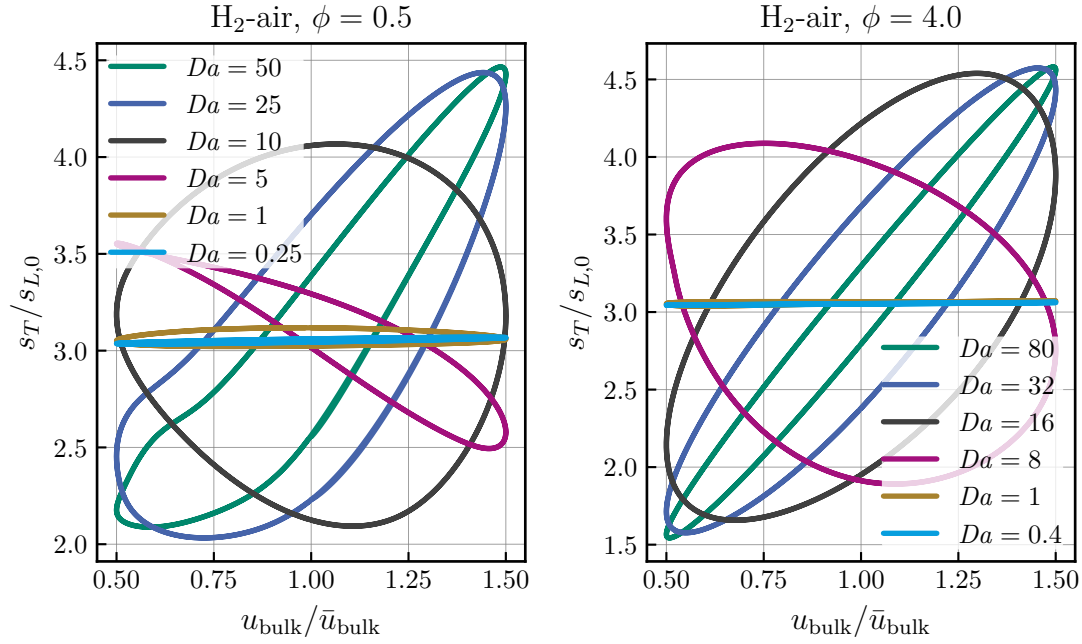


Figure 4.20: Global flame speed plotted against the bulk flow for the lean flame (left) and rich flame (right) at different Damköhler numbers.

the global flame speed against the bulk flow, as shown in Fig. 4.20. In addition of showing the amplitude of s_T , the time shift can be seen from the different orientations of the ellipses. The ratio of instantaneous bulk flow to mean bulk flow is:

$$\frac{u_{\text{bulk}}}{\bar{u}_{\text{bulk}}} = 1 + a \sin(2\pi ft) \quad (4.15)$$

In section 2.2, Eq. (2.50), the turbulent flame speed closure model by Schmid [66, 67] has been introduced. It expresses the turbulent flame speed as a function of the turbulent Damköhler number. The shape function for the term containing the Damköhler number has been chosen to ensure the correct behavior at $Da_t \rightarrow 0$ and $Da_t \rightarrow \infty$. However, an exact definition of the shape function remains an open question. By defining a turbulent flame speed variation $s'_T = s_T - s_{L,0}$, the Schmid model can be rewritten to:

$$\frac{s'_T}{u'} = (1 + Da_t^{-2})^{-\frac{1}{4}} \quad (4.16)$$

These quantities can be determined from the oscillating Bunsen setup as well. s'_T is computed from the standard deviation of s_T during an oscillation period, and likewise u' is the standard deviation of the bulk flow oscillation.

Figure 4.21 plots s'_T/u' from the two-dimensional Bunsen flame simulations for different Da along with the prediction by the Schmid model. It should be noted

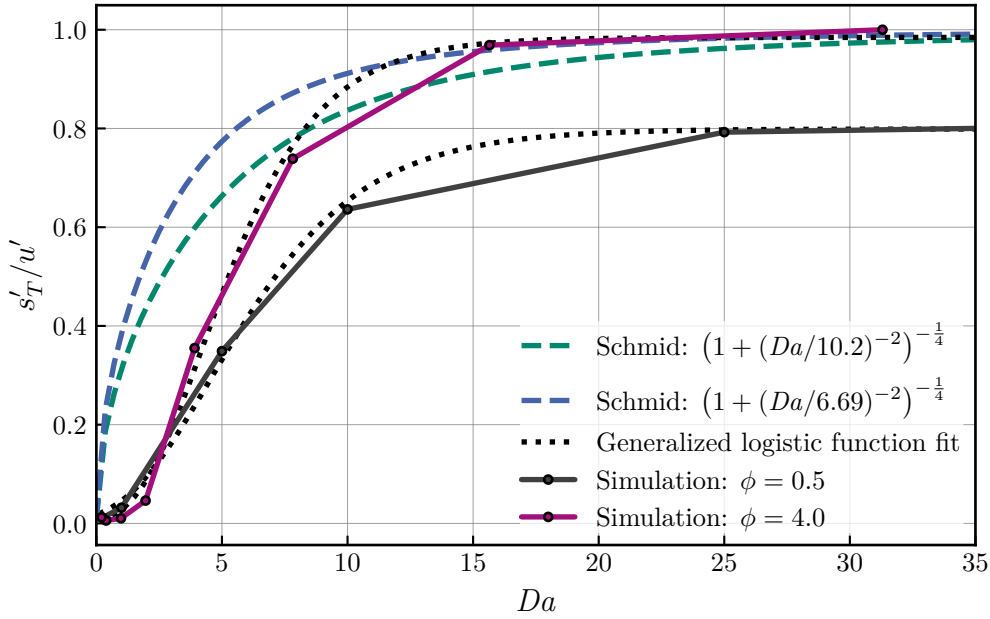


Figure 4.21: Global flame speed fluctuation s'_T divided by the characteristic flow fluctuation u' for different Damköhler numbers from the two-dimensional Bunsen flame simulations and the Schmid model.

that in the derivation of Da_t for the Schmid model, model constants have to be accounted for. In order to compare the Damköhler number in the Schmid model with the definition used in this thesis, the flame time scale has to be converted:

$$\tau_{c,\text{Schmid}} = \frac{C_w^2 a_0}{s_{L,0}^2 C_e}, \quad C_w = 2.4, \quad C_e = 0.09 \quad (4.17)$$

where a_0 is the thermal diffusivity of the fresh gas. With this, the flame time scales and hence the Damköhler numbers can be converted with the factor $\tau_c/\tau_{c,\text{Schmid}} = 10.2$ for $\phi = 0.5$ and $\tau_c/\tau_{c,\text{Schmid}} = 6.69$ for $\phi = 4$. For low Damköhler numbers ($Da < 10$), the shape function of the Schmid model does not capture the trend from the Bunsen flame simulations. Instead, a sigmoid function is more appropriate. The dotted black lines in Fig. 4.21 show a fit of the generalized logistic function, which better describes the trend from the simulations. It is defined as:

$$y(x) = A + \frac{B - A}{(C + D \exp(-Ex))^{\frac{1}{F}}} \quad (4.18)$$

Due to the tip opening and strong thermo-diffusive instability at $\phi = 0.5$, the lean hydrogen flame is not representative for the general cases covered by the Schmid model. The flame at $\phi = 4$ is a better comparison due to its Markstein number

being close to zero. The generalized logistic function from Eq. (4.18) in the case of $\phi = 4$ reduces to the simpler form

$$\frac{s'_T}{u'} \approx (1 + \exp(c_1 Da))^{c_2} \quad (4.19)$$

with $c_1 = -0.4$ and $c_2 = -6.6$. The dependence of the flame's global response in terms of the flame speed fluctuation s'_T to the flow fluctuations shows the same qualitative behavior as the response of the flame consumption speed of one-dimensional flames to equivalence ratio oscillations from section 4.1.2. In both cases, the sigmoid shaped dependence is visible, as the flame cannot respond to high frequency oscillations or $Da \ll 1$ and approaches a quasi-steady state independent of the fluctuations, and can attain a quasi-steady state to the changing flow or equivalence ratio conditions for low frequency excitations or $Da \gg 1$.

4.2.5 Application of Flame Particles

Before applying the flame particle tracking method from section 3.2 to turbulent flames, the method is first used for the oscillating Bunsen flames. This is the first time, that the FPT method is used in the context of laminar flames. Applying FPT to laminar flames constitutes another validation case for the implemented method but also demonstrates how the local flame speed and flame stretch characteristics can be better described in a Lagrangian frame of reference.

During the simulation, flame particles are continually seeded on the flame surface. They track the iso-surface of the fuel mass fraction, corresponding to the fuel mass fraction at the location of the maximum heat release rate in a freely propagating flame. Figure 4.22 shows schematically the behavior of flame particles on a steady-state Bunsen flame. A flame particle seeded on any point of the steady-state flame surface will move toward the tip of the flame over time. This can be explained by the definition of flame particles from section 3.2. Because flame particles track material points on the flame surface, they co-move with the iso-surface. Even though the flame is in steady-state, there is a tangential movement along the flame surface. Any point on the flame surface does not move in the normal direction, because the flame is in steady state. Therefore, $\vec{u}_n = -s_d \vec{n}$ at any flame position. Otherwise, there would be a movement in normal direction and the flame would no longer be in steady state. However, there is still a component of the fluid velocity tangential to the flame front. Because of this, the movement velocity of a flame particle reduces to $\vec{w} = \vec{u}_t$, which moves the flame particles toward the flame tip.

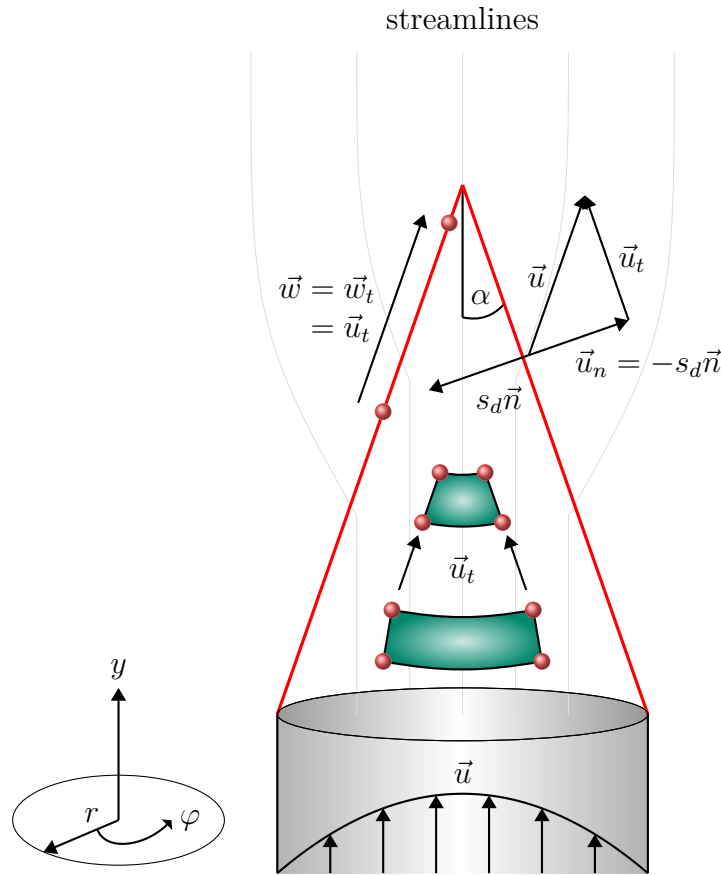


Figure 4.22: Schematic view of flame particles \bullet on a steady-state Bunsen flame.

Another way of looking at this is given by the flame stretch. As explained in section 3.2, the movement of flame particles is intrinsically connected to flame stretch. Even though the flame is in steady state, it still experiences flame stretch. Therefore, it can be stated, that the flame particles move along the flame surface *because* the flame is stretched. This can be visualized by considering a surface element on the flame surface (green patch in Fig. 4.22). Because the flame is negatively stretched due to the circumferential curvature, flame particles have to move closer together. As the flame particles move toward the tip, which in real flames is the part with the largest negative flame stretch, they move closer together and the surface area spanned by the four flame particles in Fig. 4.22 shrinks, so that $K = 1/A \, dA/dt < 0$. This behavior is also present in turbulent flames discussed in section 4.3, where the flame particles will generally move from areas with positive stretch to areas with negative stretch.

A visual example of flame particles tracking the flame front is given in Fig. 4.23 for the case $\phi = 0.5$ and $Da = 1$. The flame particles are continually seeded near the base of the flame. Over time, they move toward the tip, co-moving with the flame

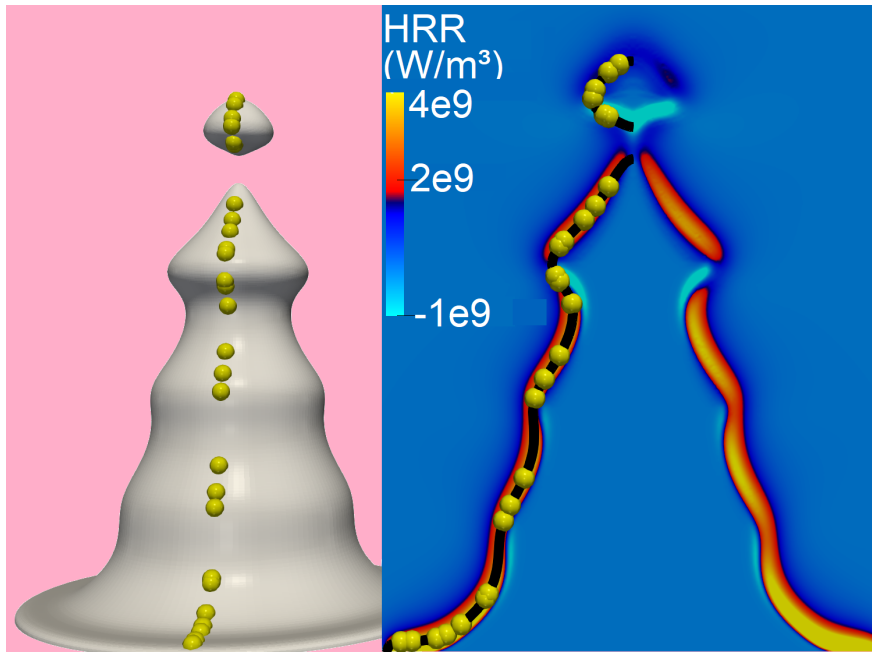


Figure 4.23: Flame particles, shown as yellow spheres \bullet , tracking a fuel mass fraction iso-surface (shown as gray surface on the left and black line in the heat release rate field on the right) during the oscillation. The case is hydrogen-air at $\phi = 0.5$ and $Da = 1$.

front. During the pulsating mode of the thermo-diffusively unstable flame, island formation can be observed at the top. The pocket of hot gas that is continually shed from the flame quickly extinguishes, as shown by the heat release rates in Fig. 4.23 on the top right.

Figure 4.24 shows an example for the type of analysis possible by employing flame particles. Shown are the recorded time signals of the balance terms of the balance equation of the fuel species (see Eq. (3.4)) from a single flame particle. The flame particle is seeded near the base of the flame and over time moves to the tip of the flame. On the left of Fig. 4.24, the trajectory of a flame particle on the steady-state Bunsen flame is shown. The sub-plot on the bottom right shows the y -coordinate of the particle over time, showing that it moves along the flame surface to the tip of the flame. As the particle gets closer to the flame tip, the stretch rate becomes more negative. As this is the lean flame with $\phi = 0.5$, the flame is locally extinguished at the flame tip due to the strong negative curvature and therewith flame stretch. This can be seen from the signal of the reaction rate $\dot{\omega}_{\text{H}_2}$, which has its largest negative value at the beginning of the trajectory near the flame base and reaches approximately zero near the flame tip. As the flame depicted on the left of Fig. 4.24 is in steady state, the sum of the three balance terms equals $\partial Y_{\text{H}_2} / \partial t = 0$ in the Eulerian reference frame, which must be

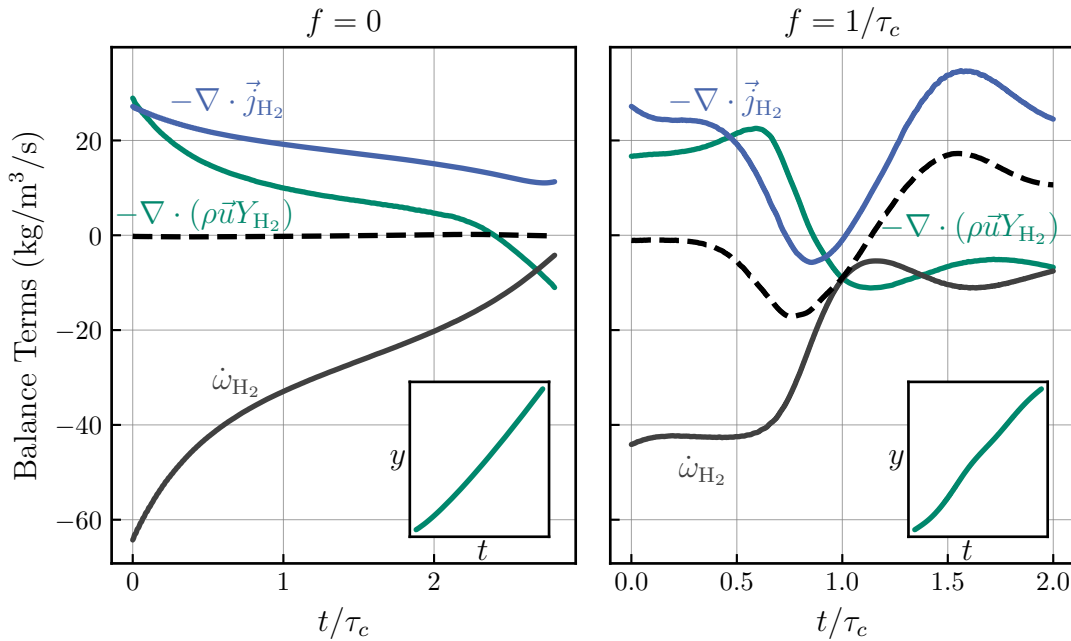


Figure 4.24: Recorded time signals of the balance terms of the fuel species balance equation from a single flame particle, moving from the base of the flame to the tip of the flame with $\phi = 0.5$. Left: steady-state case. Right: oscillation with $f = 1/\tau_c$.

zero. This is shown by the black dashed line, which can therefore be regarded as another validation case for the implemented flame particle tracking method and the evaluation of local flame properties.

On the right of Fig. 4.24, the time signals of the balance terms of a single flame particle are shown for the oscillating flame with $Da = 1$. In this case, due to the unsteady nature of the flame, the sum of the balance terms is not zero (black dashed line on the right). The complex interplay of convection, diffusion and chemical source term can be revealed by the flame particle. This type of analysis is only possible by employing flame particles that track material points on the flame front. For example, in a previous work [117], only the movement of the flame tip of oscillating laminar flames could be tracked, as the flame tip only moves along the y -direction. With the flame particle tracking method, any point on the flame surface can be tracked.

Another powerful analysis enabled by the flame particle tracking method is the study of the time dependent correlation of local flame speed and local flame stretch. Figure 4.25 again shows the recorded time signals of local properties from a single flame particle, in this case for the $\phi = 4$ and $Da = 1$ flame. In Fig. 4.25a, the time histories of the flame speed, both as consumption speed s_c and density weighted displacement speed s_d^* , are plotted together with the normalized flame

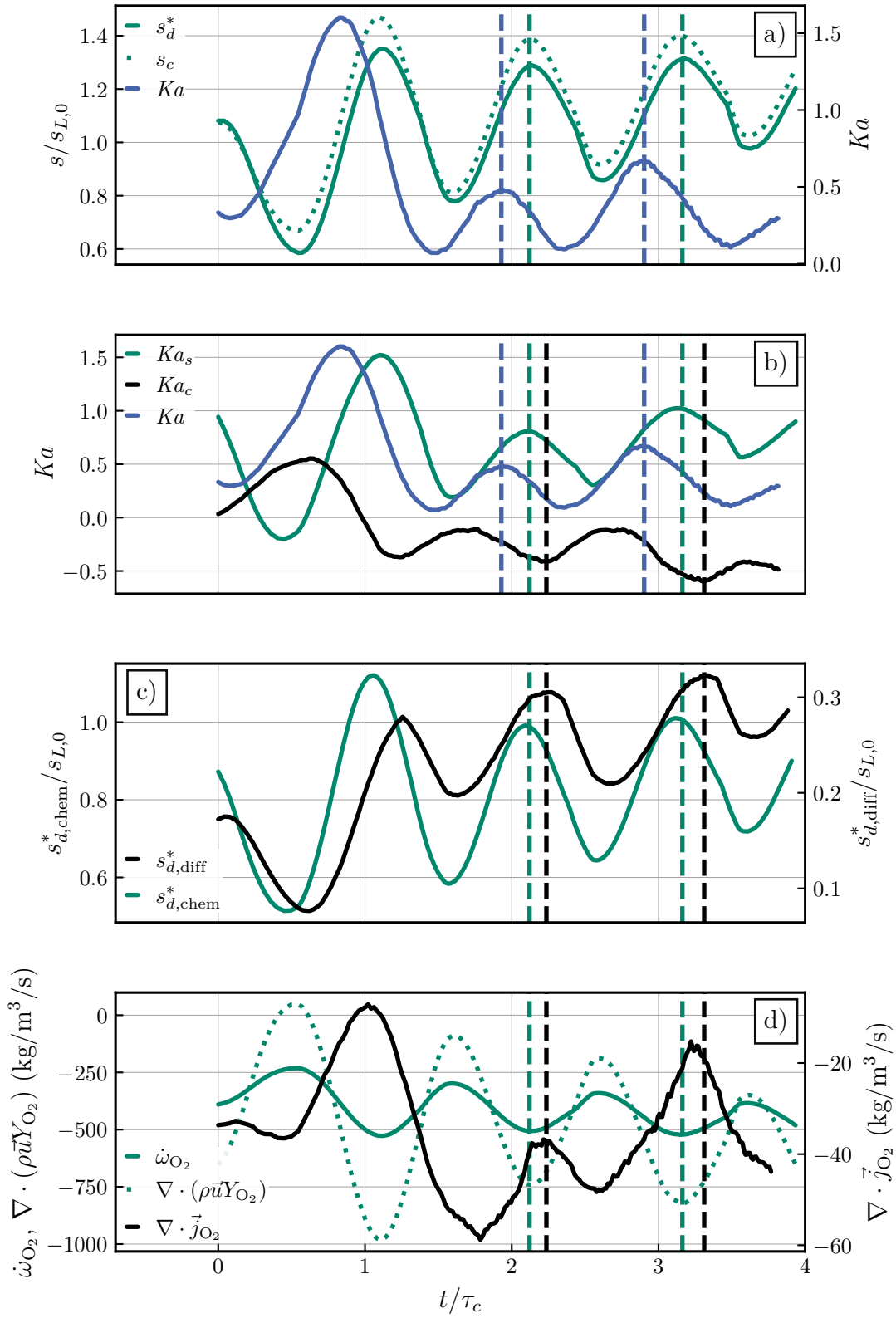


Figure 4.25: Recorded time signals of flame speed, flame stretch and balance terms of the fuel species balance equation for the flame with $\phi = 4$ and $Da = 1$.

stretch Ka . Because this flame is transiently stretched, s_c and s_d^* are not the same. However, they have the same behavior in time, meaning that their peaks occur at the same time instance, which is marked by the vertical dashed green line in all plots. However, the signal of the flame stretch is shifted in time. The peaks of the flame stretch are marked by the vertical dashed blue line. The observed time delay is of the order of $0.25\tau_c-0.3\tau_c$, which is comparable to results found in [117].

Figure 4.25b breaks down the flame stretch in its components, $Ka = Ka_c + Ka_s$ (see section 2.3). Although the flame stretch signal is shifted in time relative to the flame speed, the time signal of the aerodynamic straining Ka_s matches with the time signal of the flame speed. However, the curvature component Ka_c has a different behavior in time, leading to the apparent shift between total flame stretch and flame speed. Figure 4.25c breaks down the displacement speed in its contributions from chemical reactions and diffusion (see section 2.1.3). In this case, the flame stretch is moderate and the chemical contribution to s_d^* correlates with the time signal of Ka_s , while the time signal of the diffusive contribution to s_d^* correlates with Ka_c . Because $s_{d,\text{chem}}^* > s_{d,\text{diff}}^*$ in this case, the overall dynamic is determined by the time signal of Ka_s .

The same trend is recovered when looking at the balance terms of the fuel mass fraction equation in Fig. 4.25d. The diffusive mass flux term corresponds most closely to the Ka_c signal, due to the focusing and defocusing effect of curvature, while the chemical source term follows the time signal of Ka_s . Since the contribution of the chemical source term is higher than that of the diffusion terms, the convective term mostly balances the chemical source term, therewith having the same time behavior. It should be noted that these results are only applicable to the chosen flame setup and not valid in general. However, it demonstrates that the flame particle tracking method is able to break down the time dependent correlation of flame speed and flame stretch into its underlying causes. A more comprehensive study of the time history effects is done in the next section for turbulent flames.

4.2.6 Conclusions

Direct numerical simulations of two-dimensional lean and rich oscillating laminar hydrogen-air Bunsen flames have been performed. These flames are subjected to both positive and negative tangential and normal straining, and can therefore be used to study the effect of transient flow oscillations on local flame dynamics in a realistic manner. Compared to turbulent flames, which are characterized by a wide frequency spectrum, single frequency oscillations are used for the oscillating

flames to systemically study the effect of flow transients on flame dynamics. For the first time ever, the flame particle tracking method has been applied to a laminar flame setup to reveal the time dependent correlation of flame speed and flame stretch as well as its underlying causes.

The key points from this section are summarized as follows:

- i.** The flame's response in terms of the amplitude of flame height is attenuated with increasing frequency. At $Da \approx 1$, the flame goes into a pulsating mode. For $Da \ll 1$, the flame cannot respond to the flow oscillations.
- ii.** The local flame consumption speed becomes less sensitive to local flame stretch with increasing frequency. The averaged Markstein number \overline{Ma} decreases with Da and reaches its lowest value at $Da \approx 1$. For high frequencies at $Da \ll 1$, the averaged Markstein number increases again to its steady-state value.
- iii.** With increasing frequency, the global flame speed s_T shows an increased phase shift relative to the oscillation of the inflow and a decreased amplitude, which is consistent with the findings from section 4.1.
- iv.** Based on these results, a new shape function for the turbulent flame speed closure model by Schmid is proposed: $\frac{s_T}{s_0} \approx 1 + \frac{u'}{s_{L,0}} (1 + \exp(c_1 Da))^{c_2}$, with $c_1 = -0.4$ and $c_2 = -6.6$ valid for the rich hydrogen flame.
- v.** The application of the flame particle tracking method to the unsteady flames enables to identify causes for the time shift of flame speed and flame stretch. In case of the rich flame at $\phi = 4$, the flame speed correlates more closely with aerodynamic straining, which in term correlates with the chemical source term. The curvature correlates in time with the diffusive contribution, which is smaller than the chemical one. Although these results are not general, they showcase the type of analysis enabled by the flame particle tracking method, which is applied to turbulent flames in the next section.

4.3 Memory Effects in Turbulent Flames

While the last section discussed the effect of flow transients on laminar flames, this section presents three-dimensional simulations of premixed turbulent flames in the flamelet regime. By using the flame particle tracking (FPT) method, the local flame dynamics in terms of flame speed and flame stretch can be analyzed by taking their time histories into account.

4.3.1 Computational Setup

To study time dependent local flame dynamics of turbulent flames with the flame particle tracking method, direct numerical simulations of flames, also known as flame-in-a-box, are conducted. The computational setup is shown in Fig. 4.26. A turbulence generator [207] based on the digital filter by Klein et al. [208] generates turbulent inflow conditions with a prescribed mean flow velocity \bar{u}_x , fluctuation scale u' and turbulent length scale L_t . The four lateral boundaries are periodic. On the right, the burnt gases leave the domain through an outlet. The flame

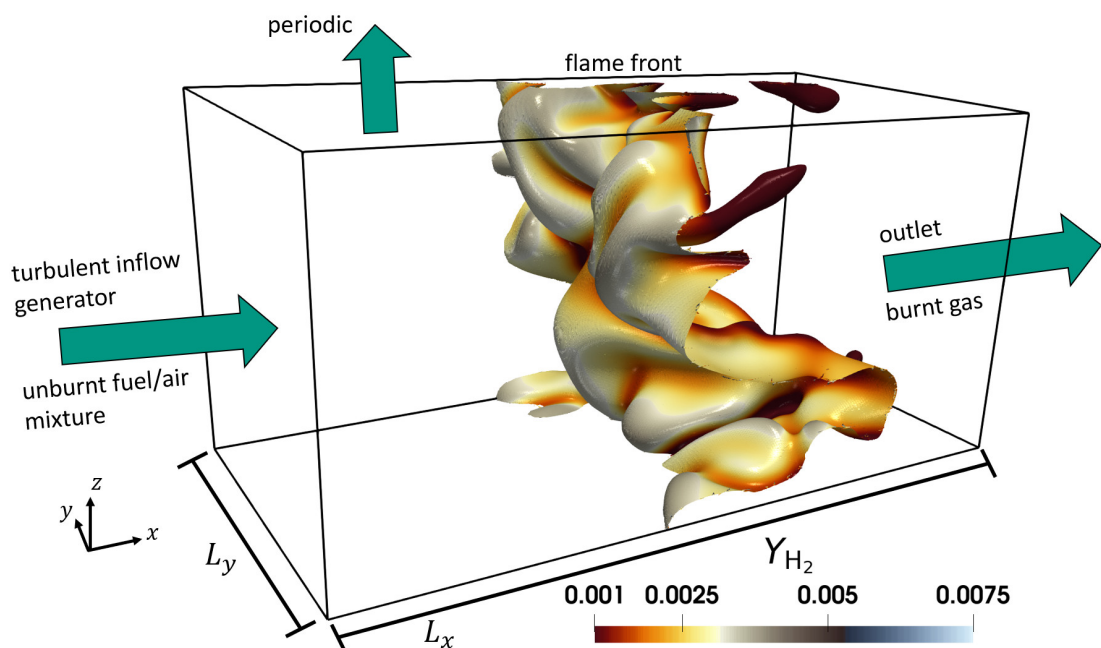


Figure 4.26: Computational setup for the simulation of turbulent flames. A turbulence generator creates turbulent inflow conditions at the inlet on the left. The sides of the box are periodic boundary conditions. On the right, the burnt gases leave the domain through the outlet. The flame starts as a planar flame front and then interacts with the turbulent flow, here shown by the temperature iso-surface $T = 1050$ K of a hydrogen-air flame.

is initialized with the one-dimensional solution of a freely propagating flame computed beforehand with Cantera. The planar flame then starts to interact with the turbulent flow once the simulation is started.

Three cases of flames at atmospheric conditions are considered, which are summarized in Table 4.4. Case a is a lean hydrogen-air flame at $\phi = 0.5$ with low turbulent fluctuations of $u'/s_{L,0} = 1.3$. Case b is the same flame, but stronger turbulent fluctuations at $u'/s_{L,0} = 3.4$. Case c is a methane-air flame at $\phi = 0.909$ and $u'/s_{L,0} = 6$. Based on u' , L_t , $s_{L,0}$ and δ , all flames are located in the flamelet regime (see Fig. 2.2 in section 2.2). The computational domains consist of $N_x \times N_y \times N_z = 400^3 = 64$ million cells for the methane flame and $N_x \times N_y \times N_z = 719 \times 359 \times 359 = 92$ million cells for the hydrogen flames, resolving the flame fronts with about 20 cells. The simulation time step is adjusted so that $CFL = 0.1$. The simulations have been performed on one of Germany's fastest supercomputers HPE Apollo Hawk at the High Performance Computing Center Stuttgart [209] as well as HoreKa [210] at the Karlsruhe Institute of Technology (see also appendix E for more information about the performance of different high performance computing systems).

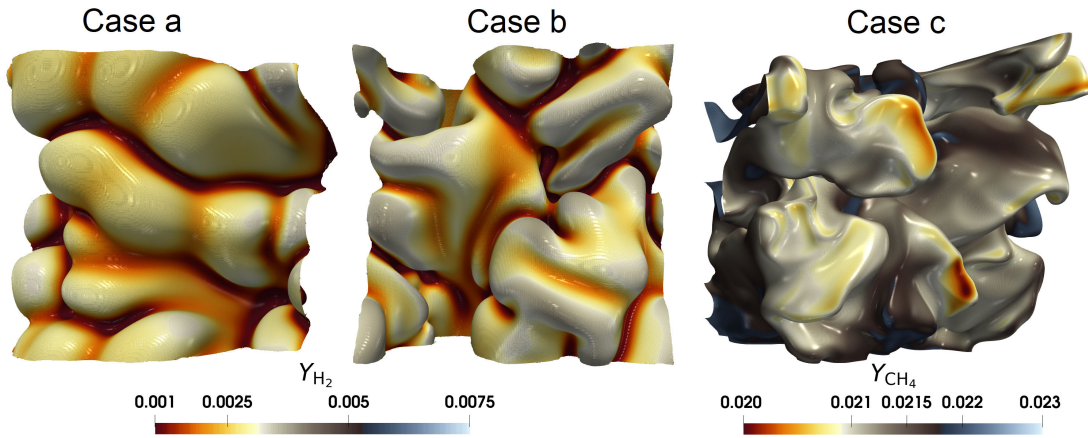


Figure 4.27: Instantaneous snapshot of temperature iso-surfaces colored by fuel mass fraction of the three cases from Table 4.4. Viewing direction is in the direction of the inflow, so the inlet is in the front and outlet in the back.

Table 4.4: Properties of the corresponding freely propagating flames, turbulence parameters and mesh settings.

Case	Fuel	ϕ	τ_c (ms)	$\bar{u}_x/s_{L,0}$	$u'/s_{L,0}$	L_t/δ	$L_x \times L_y \times L_z$	$N_x \times N_y \times N_z$
a	H ₂	0.5	0.75	2.7	1.3	30	2 cm \times 1 cm \times 1 cm	719 \times 359 \times 359
b	H ₂	0.5	0.75	4.5	3.4	30	2 cm \times 1 cm \times 1 cm	719 \times 359 \times 359
c	CH ₄	0.9	1.45	6.0	6.0	30	1 cm \times 1 cm \times 1 cm	400 \times 400 \times 400

Figure 4.27 shows instantaneous snapshots of the temperature iso-surface ($T = 1050$ K for the hydrogen flames and $T = 1592$ K for the methane flame, which correspond to the temperature at the location of maximum heat release rate in the respective freely propagating flames), colored by the mass fraction of the fuel species. The effect of the different u' can be seen by comparing the flame from case a and case b. The wrinkles on the flame for case a are larger and less deep than the ones in case b. However, in both cases, the effect of the thermo-diffusive instability for the lean hydrogen cases becomes visible by the strongly negatively curved folds arching toward the back with low local equivalence ratio.

4.3.2 Turbulent Flame Speed

Before analyzing the local flame dynamics with the flame particle tracking method, the global flame properties in terms of the turbulent flame speed are evaluated first. Figure 4.28 shows the turbulent flame speed s_T computed from

$$s_T = \frac{1}{\rho_0 A_0 (Y_{F,b} - Y_{F,0})} \int \dot{\omega}_F dV \quad (4.20)$$

with $A_0 = L_y L_z = 1 \text{ cm}^2$, together with the turbulent flame surface area A_t , defined as the surface area of the fuel mass fraction iso-surface $Y_{F,iso}$, which corresponds to the value of the mass fraction at the location of the maximum

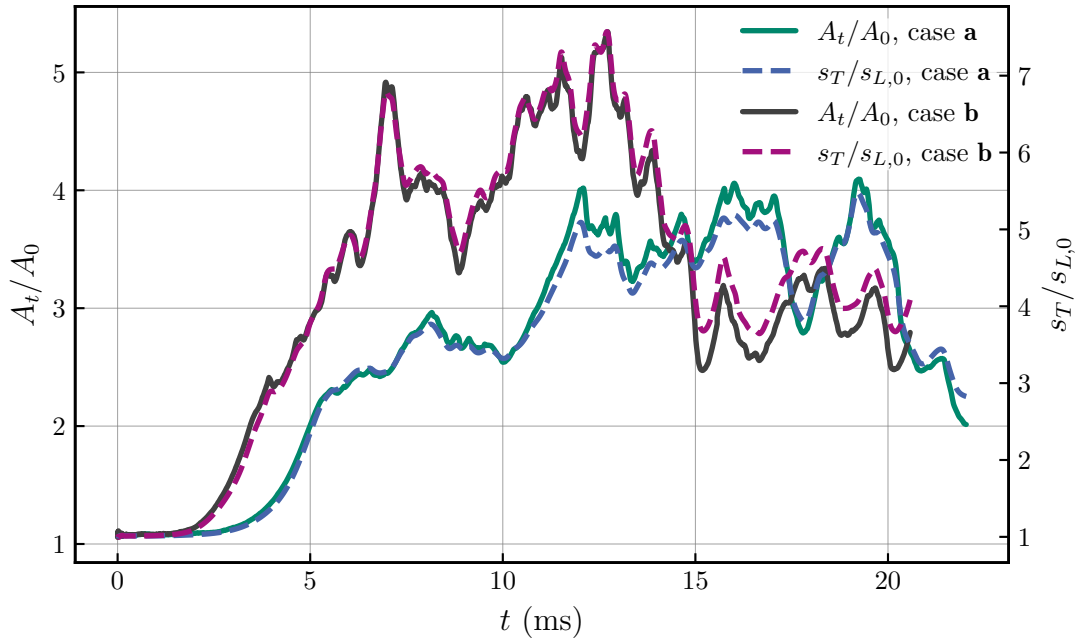


Figure 4.28: Turbulent flame speed s_T and surface area of the turbulent flame front A_t over time for the two hydrogen flames.

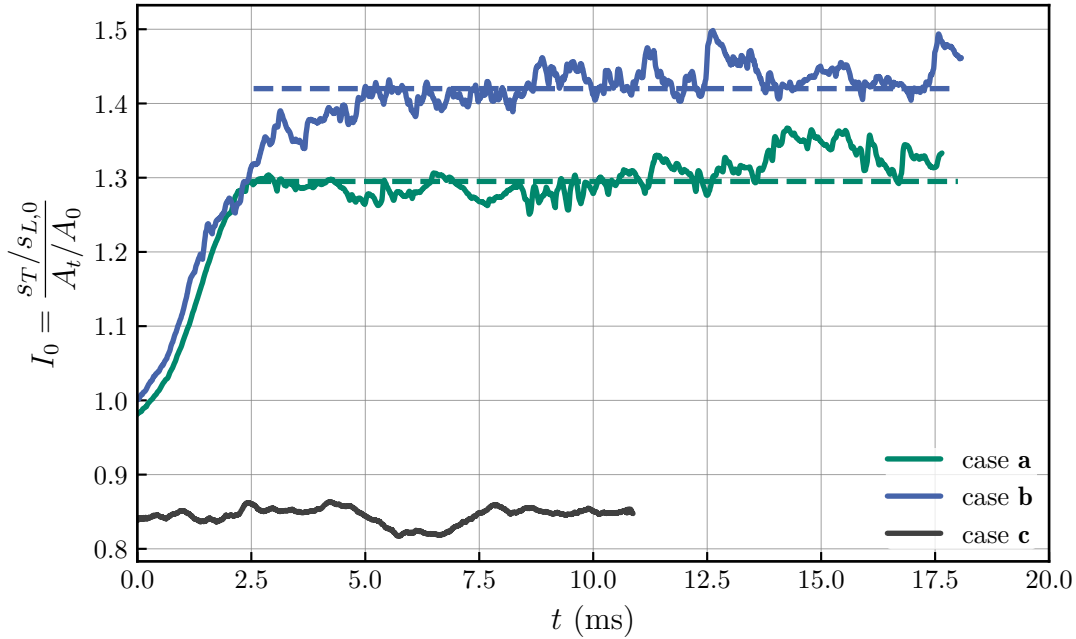


Figure 4.29: Efficiency factor I_0 over time for the three turbulent flame cases.

heat release rate in the respective freely propagating flame, over time. As the flames start with an initial solution from a laminar planar flame, both $s_T/s_{L,0}$ and A_t/A_0 start at unity. For case b, the flame surface increases more rapidly at the start of the simulation due to the larger \bar{u}_x and u' . However, in both cases, the correlation of turbulent flame speed and turbulent flame surface area is very strong, confirming that the flames are located in the flamelet regime, where Damköhler's first hypothesis from Eq. (2.46) is approximately valid.

The efficiency factor $I_0 = (s_T/s_{L,0})/(A_t/A_0)$ is plotted over time for all three cases in Fig. 4.29. Note that for the methane flame, the simulation starts with an already turbulent flame, not a planar laminar flame. In general, turbulent flow will lead to an increase in flame surface area so that the global flame stretch is positive. The methane flame in case c has a positive Markstein number, and therefore local flame speeds reduce with increasing flame stretch, leading to an $I_0 < 1$. On the contrary, the lean hydrogen flames from cases a and b have a strongly negative Markstein number and hence a $I_0 > 1$, which is higher for the more strongly stretched flame in case b. However, at higher u' , I_0 is expected to reduce again due to the bending effect [211, 212]. Nonetheless, the efficiency factor approaches a constant value for a specific set of turbulence parameters u' and L_t .

4.3.3 Simulation of Flame Particles

Flame particles are tracked during the simulation of the turbulent flames with the new tracking algorithm described in section 3.2. At the beginning of the simulation, one flame particle is seeded onto the flame front for every tenth cell that is cut by the iso-surface, resulting in approximately 50 000 flame particles. Every 0.5 ms, flame particles are reseeded to ensure that enough particles are present during the simulation to record sufficient data.

Figure 4.30 shows a visualization of flame particles on the iso-surface $Y_{F,iso}$ of the methane flame (case c), colored by the magnitude of the fluid velocity. On the left of Fig. 4.30, the initial state after seeding the particles is shown. On the right of Fig. 4.30, the distribution of flame particles at a later time instance is shown. As explained in section 3.2.1, flame particles will move away from each other in regions of positive flame stretch and cluster together in regions with negative flame stretch. Here, an accumulation of flame particles in a part of the flame curved toward the burnt cases is highlighted. Flame particles are removed from the simulation if the flame becomes locally quenched, i.e. if the heat release rate is below 0.1 % of the maximum heat release rate in a freely propagating flame, or

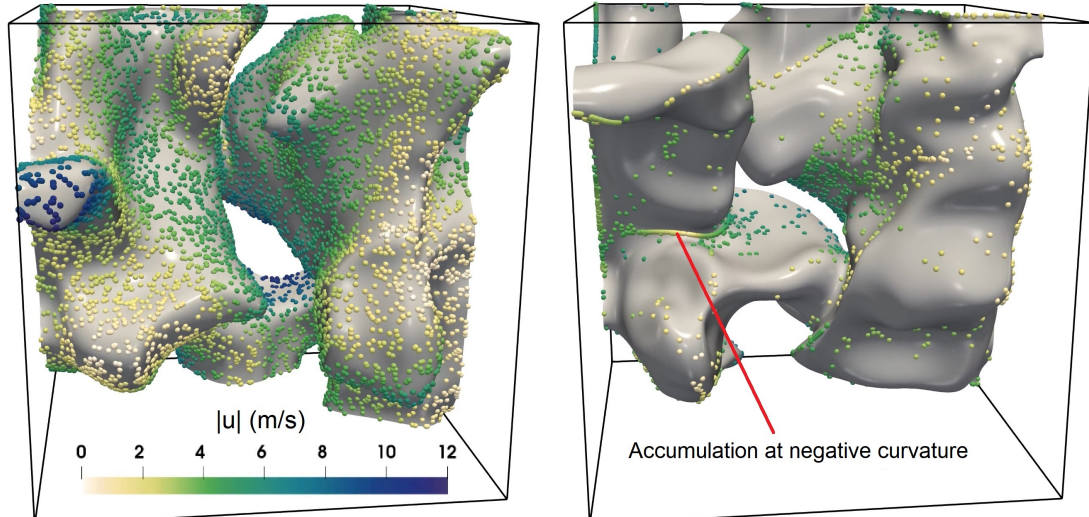


Figure 4.30: Left: Flame particles (FP) randomly seeded on an iso-surface of $Y_{F,iso}$ for the flame in case c. FPs are colored by the magnitude of the fluid velocity. Right: Distribution of FPs at a later time step without re-seeding the particles. FPs tend to move to regions with negative flame stretch, e.g. folds in the flame surface, and are eventually removed from the simulation when the tracked flame surface area elements are annihilated. The inlet is in the front, the outlet in the back.

when the local flame area is annihilated, e.g. when a flame island detaches from the flame, propagates inward and finally disappears.

4.3.4 Moderate Flame Stretch Regime

During the simulation of the turbulent flames, the flame particles record the time signals of local flame properties like flame speeds, flame stretch and its components as well as the contributions of the diffusion and convection terms as well as chemical reaction rates to the balance equations for the species mass fractions. The following analysis is based on classifying the flame particles on the flame stretch into a moderate flame stretch regime and a high flame stretch regime. First, the moderate flame stretch regime is discussed. The flame dynamics in the following are presented using results obtained from the turbulent hydrogen flame from case b.

As shown in the introduction in Fig. 1.1, there is a strong correlation between local flame stretch and local flame speed in laminar flames, but a strong scattering is observed for the same correlation in turbulent flames. To explore this further

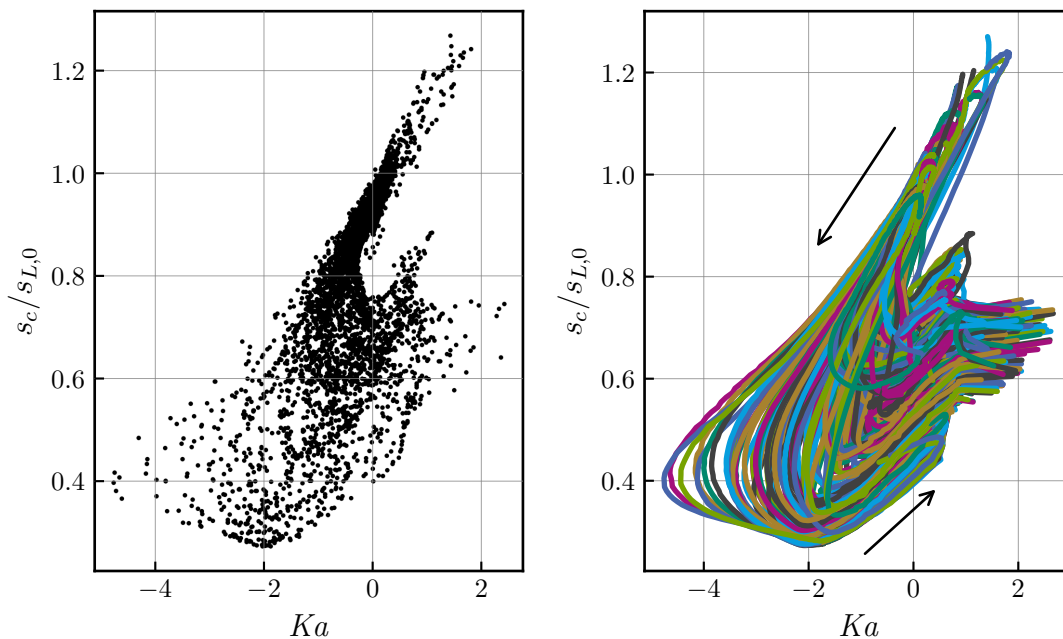


Figure 4.31: Flame speed to flame stretch correlation from the flame in case b. Depicted on the left are several time instances showing the instantaneous correlation of a small part of the flame in a moderate stretch regime. On the right, trajectories of flame particles in the flame speed and flame stretch space tracking that part of the flame are shown. Each colored line represents a different flame particle trajectory.

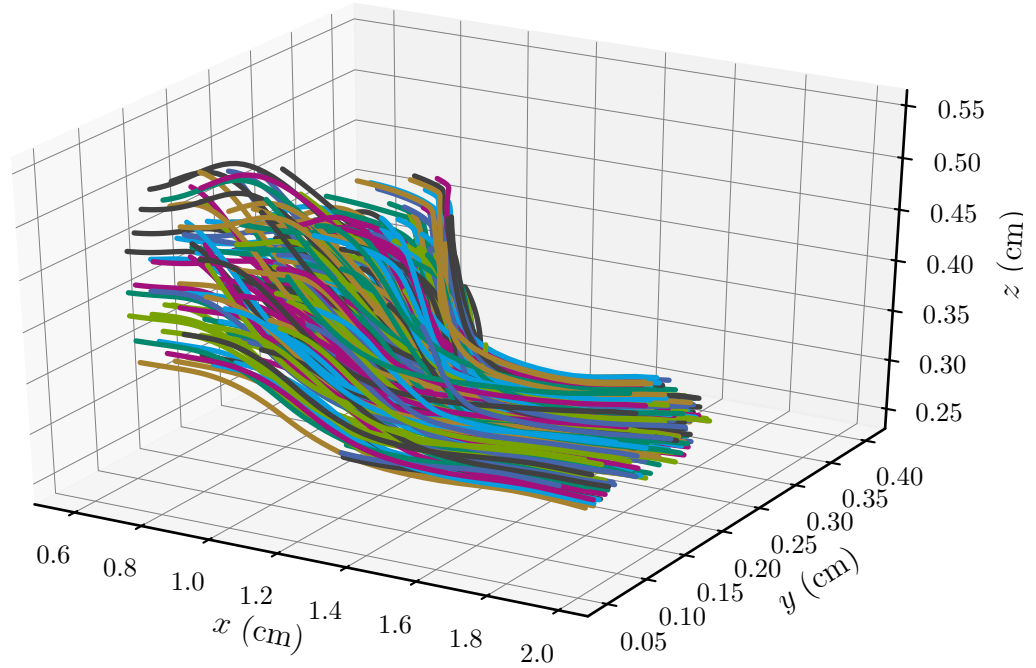


Figure 4.32: Trajectories of the flame particle cluster in space from Fig. 4.31 for the flame of case b.

and to investigate the impact of memory effects, the time histories recorded by the flame particles are studied in the following sections.

Figure 4.31 on the left shows the instantaneous correlation between flame speed and flame stretch at several time instances, evaluated on a small part of the flame from case b that experiences moderate flame stretch. The use of flame particles allows to consider the flame speed to flame stretch correlation not just statistically as in the picture on the left, but also with temporal causation. Figure 4.31 on the right shows the trajectories of flame particles that track the same small part of the flame depicted on the left. However, their tracks reveal that the flame at that position and at that time instance undergoes a hysteresis. In fact, this part of the flame has been specifically chosen because it starts out in the positive stretch regime, which generally means that the flame particles stay alive for a long time (see also section 4.3.8). The hysteresis undergone by the flame at that position in terms of the temporal flame speed and flame stretch dynamics allows to analyze the influence of the time history effect in section 4.3.5 and to quantify the time shift between flame speed and flame stretch. Figure 4.32 shows the trajectories of the flame particle cluster from Fig. 4.31 on the right in physical space. In total, the cluster consists of about 300 flame particles.

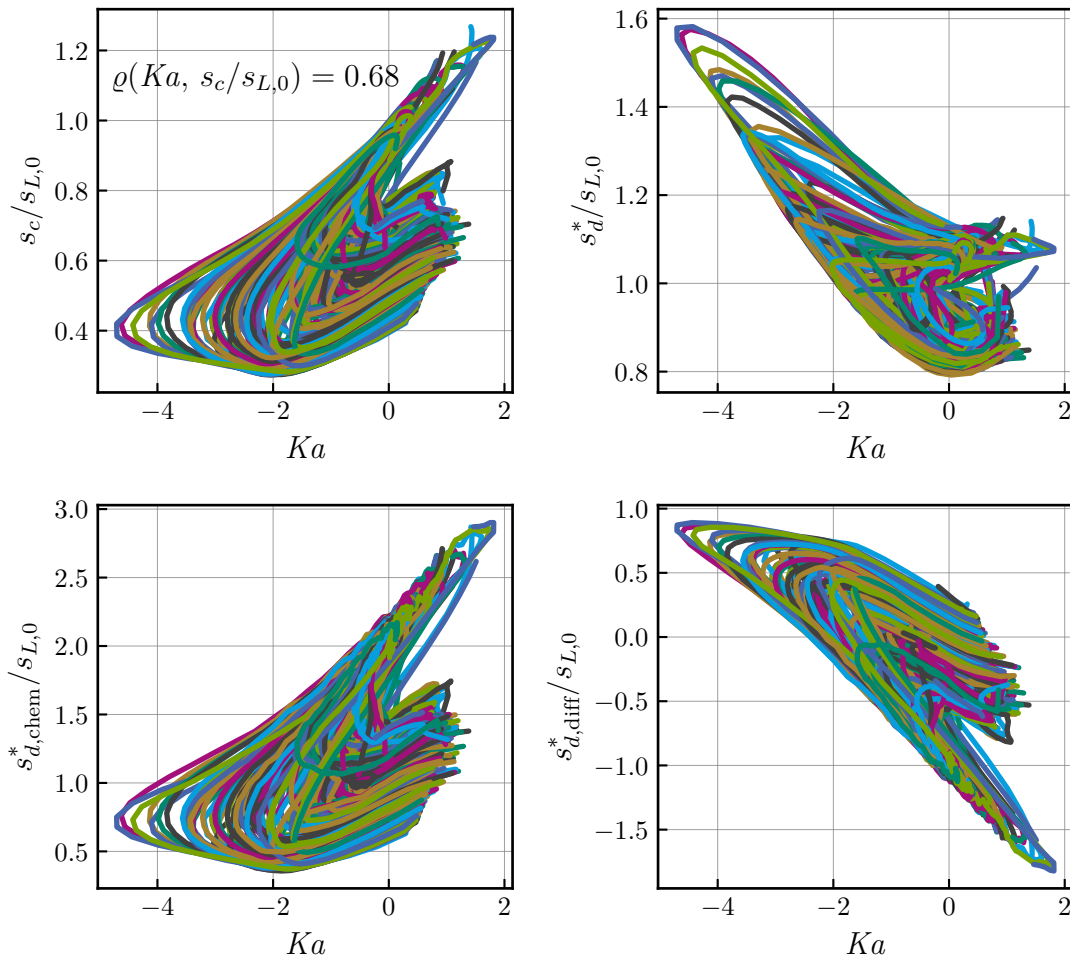


Figure 4.33: Particle trajectories in the flame speed and flame stretch space for the consumption speed, displacement speed and the components of displacement speed.

In addition to considering the flame speed and flame stretch correlation in terms of the consumption speed s_c , the flame speed can also be expressed as the density weighted displacement speed s_d^* and its components $s_{d,diff}^*$ and $s_{d,chem}^*$ from Eq. (2.33). Figure 4.33 therefore shows the flame particle tracks of the cluster from Fig. 4.32 in the consumption speed/displacement speed and flame stretch space. The general trend of consumption speed follows the expected behavior due to the lean hydrogen flame having a negative Markstein number, so that s_c increases with flame stretch (top left of Fig. 4.33). The Pearson correlation coefficient ρ in the top left corner for the consumption speed with flame stretch is $\rho = 0.68$, which is discussed further in the next section. For the displacement speed (top right of Fig. 4.33), the trend of flame speed to flame stretch is reversed. The reason for this is shown in the bottom two graphs of Fig. 4.33. The contribution of the chemical source term to the displacement speed $s_{d,chem}^*$ behaves the same as the

consumption speed s_c . Both flame speeds, s_c and $s_{d,\text{chem}}^*$, are directly computed from the chemical reaction rate of the fuel species, $s_{d,\text{chem}}^*$ from the local values (see Eq. (2.33)) and s_c from line integration (see Eq. (2.4)) and therefore follow the same trend. The diffusive contribution to the displacement speed $s_{d,\text{diff}}^*$ on the bottom right of Fig. 4.33 shows the reversed trend. As the flame experiences more and more negative flame stretch, the local equivalence ratio becomes leaner, leading to lower local flame speeds and eventual extinction. However, the iso-surface of the fuel mass fraction continues to move, even if the flame is locally extinguished. This movement is caused by the diffusive contribution, leading to high apparent displacement velocities of the iso-surface in regions where the contribution from chemical reaction rates is low. A similar effect has been found for laminar hydrogen flames with cellular instabilities [98]. This is achieved by having an increased contribution of the diffusive flux to the mass fraction balance equation. This also serves as an example to show that the flame consumption speed often is a more physically meaningful representation of the flame, while the displacement speed is a purely abstract movement speed of an iso-surface. It is therefore useful to evaluate the consumption speed in DNS of turbulent flames, even though it is computationally more expensive than the computation of the displacement speed.

A strong correlation of the flame speed can be found by considering the particle trajectories in the flame speed and local equivalence ratio ϕ_{loc} (see Eq. (4.6)) space, shown in Fig. 4.34. Although the flame particles track an iso-surface of the fuel mass fraction, the local equivalence ratio changes due to the flame being subjected to flame stretch. Because the flame consumption speed and chemical reaction contribution of the displacement speed are directly computed from the chemical reaction rates, they directly depend on the local equivalence ratio. Because of this, s_c and $s_{d,\text{chem}}^*$ correlate well with ϕ_{loc} . This relation can be approximated by performing one-dimensional freely propagating flame simulations at varying equivalence ratio and plotting the flame speed $s_{L,0}$ against the value of ϕ_{loc} present at the location of $Y_{\text{F,iso}}$. This is shown as dashed black line on the top left of Fig. 4.34 and again shows that the turbulent flame is located in the flamelet regime.

Similarly to $s_{d,\text{chem}}^*$, $s_{d,\text{diff}}^*$ also correlates strongly with ϕ_{loc} , as explained above. Because of this, the total displacement speed s_d^* does not correlate well with ϕ_{loc} due to the opposite trend of $s_{d,\text{chem}}^*$ and $s_{d,\text{diff}}^*$. Because consumption speed and the two components of the displacement speed show a strong direct correlation with the local equivalence ratio, a good correlation with flame stretch should be expected as well. However, as shown before in section 4.1 and section 4.2, the

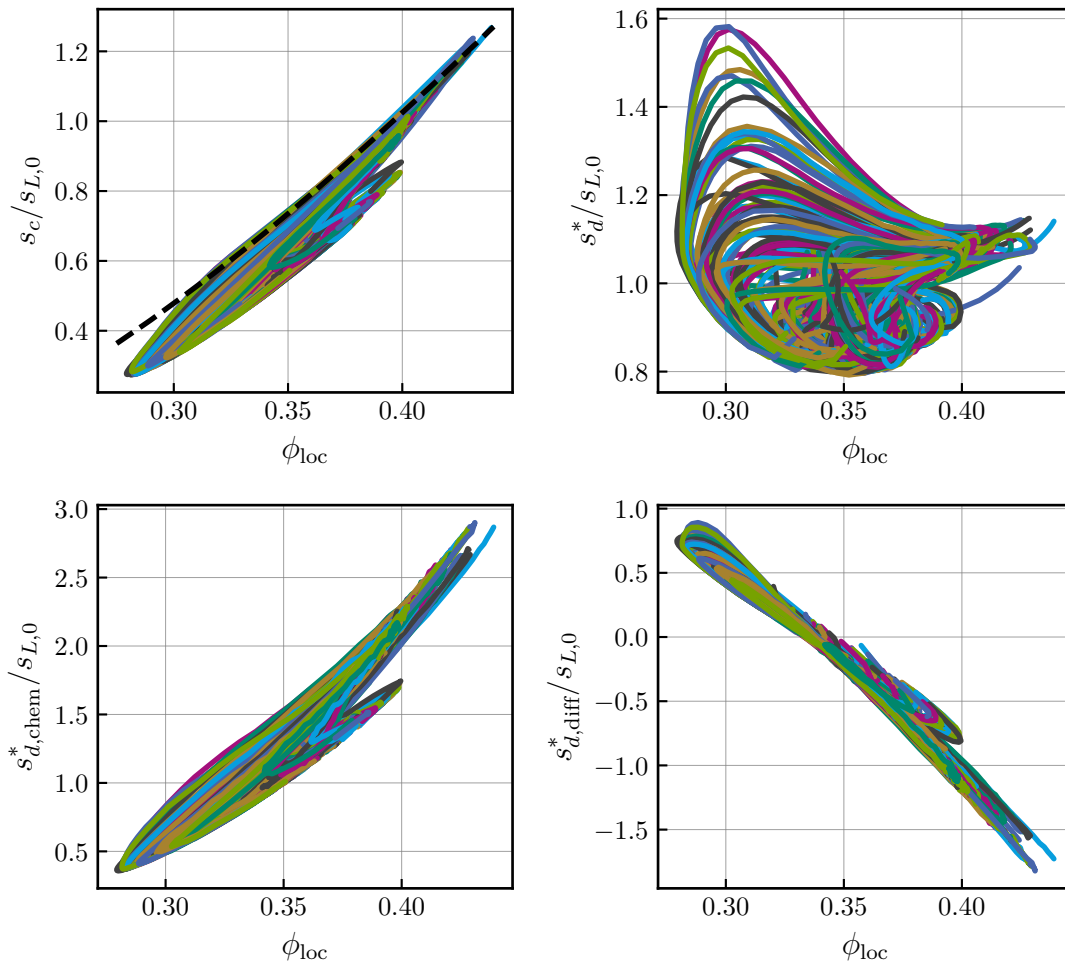


Figure 4.34: Particle trajectories in the flame speed and local equivalence ratio space for the consumption speed, displacement speed and the components of displacement speed. The dashed line shows the flame speed from freely propagating flames.

flame cannot adapt instantaneously to changing flow conditions. Because of this, a flame subjected to instantaneous flame stretch rates requires a relaxation time to adapt its inner structure to the new stretch conditions. In this way, a time delay between the flame stretch and the resulting flame speed is expected, which is quantified in the next section.

4.3.5 Effect of Time Histories on Local Correlations

As described in the previous section, the effect of flame stretch on local equivalence ratios and therefore flame speeds is not instantaneous, but instead requires a certain relaxation time. Due to the flame particle trajectories, it is possible to analyze the time histories of local flame speed and flame stretch and use them to determine

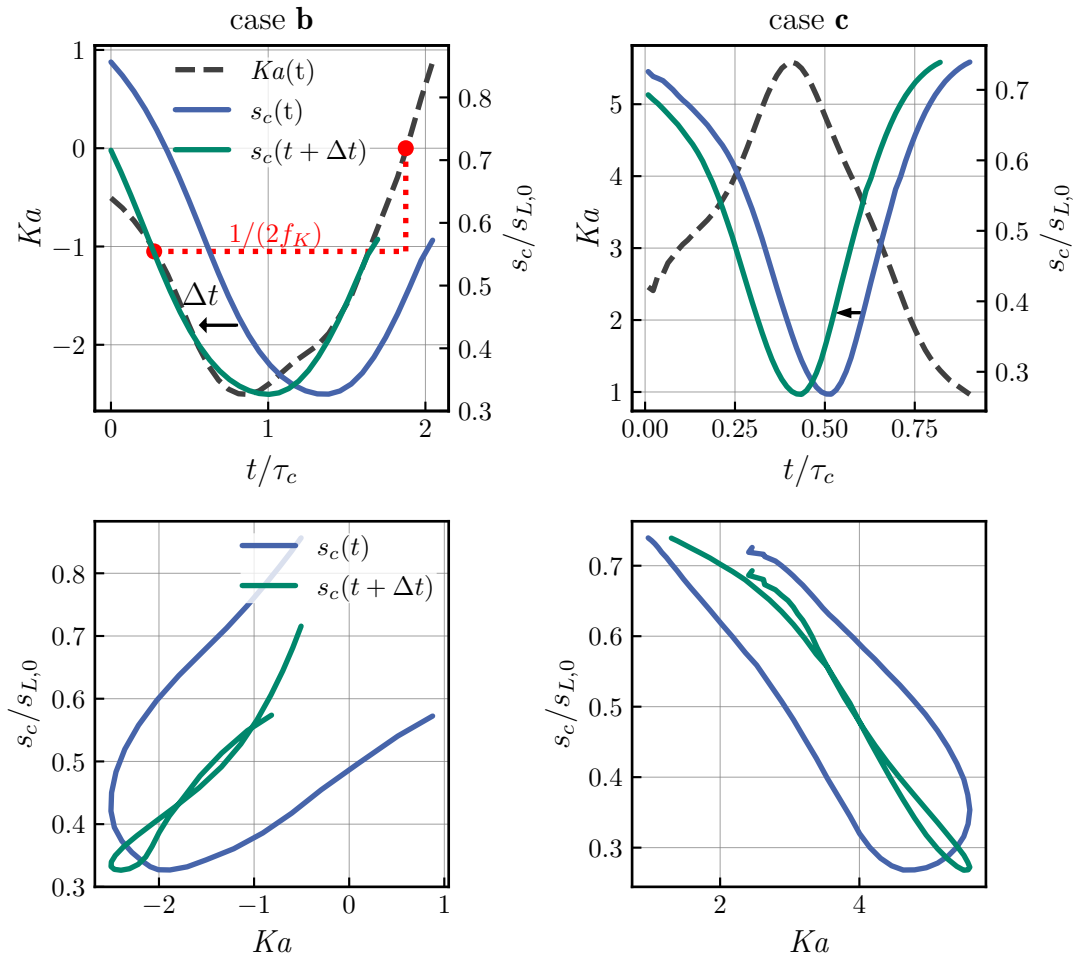


Figure 4.35: Time signal of $Ka(t)$ and $s_c(t)$ (top) for a single flame particle on the lean hydrogen flame (left) and methane flame (right). The green line shows the time signal of s_c moved backward in time relative to the flame stretch signal. Bottom: resulting flame speed and shifted flame speed signal plotted against flame stretch from the pictures at the top.

the local flame relaxation times. In this way, the linear correlation between flame speed and flame stretch found in steady-state flames can be recovered by moving the time signals of flame speed backward in time relative to the flame stretch time signal. Figure 4.35 on the top shows the time signals of normalized total flame stretch and the time signal of the flame consumption speed for a single particle on the turbulent hydrogen (top left) and methane flame (top right). On the top of Fig. 4.35, the time signal of s_c is shifted backward in time (green line) by a flame relaxation time Δt to overlap with the time signal of the normalized flame stretch Ka (dashed black line). On the bottom of Fig. 4.35, the corresponding correlation in the flame speed and flame stretch space is shown. Plotting the instantaneous values of flame speed and flame stretch against each other results in the hysteresis, while a quasi-linear correlation is recovered by shifting the flame

speed and flame stretch signals against each other in time by the local flame relaxation time Δt .

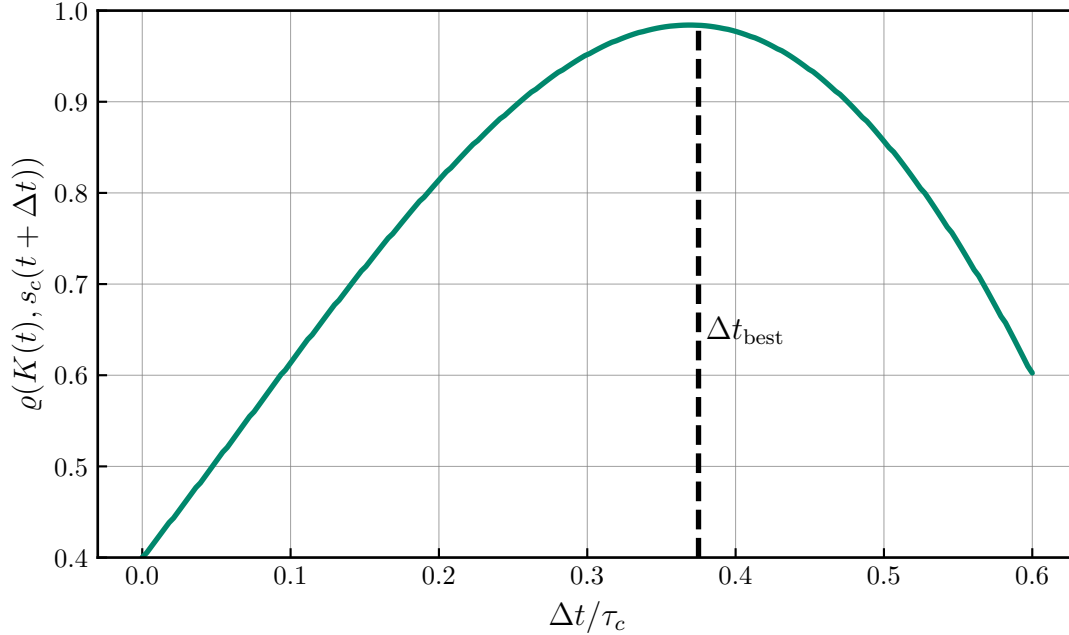


Figure 4.36: Pearson correlation coefficient $\rho(Ka(t), s_c(t + \Delta t) / s_{L,0})$ for different values of Δt for the particle depicted on the left of Fig. 4.35.

Because the particle cluster discussed here has been chosen for its hysteresis in terms of the flame stretch, the flame relaxation time can be determined by successively shifting the flame speed signal backward in time until a maximum of the correlation coefficient $\rho(Ka(t), s_c(t + \Delta t) / s_{L,0})$ is reached. This procedure is shown in Fig. 4.36 for the particle on the left of Fig. 4.35.

When applying this methodology for finding the flame relaxation time by maximizing $\rho(Ka(t), s_c(t + \Delta t) / s_{L,0})$ to all flame particles from the cluster in Fig. 4.32 and shifting the flame stretch signal backward in time, a quasi-linear correlation between flame stretch and flame speed is successfully recovered, as shown in Fig. 4.37. This is the same figure as Fig. 4.33 showing the strong scattering by correlating the instantaneous values of flame speed and flame stretch, except that the time signal of the flame speed is shifted in time by Δt . This leads to an improvement of the correlation, from $\rho(Ka(t), s_c(t) / s_{L,0}) = 0.68$ to $\rho(Ka(t), s_c(t + \Delta t) / s_{L,0}) = 0.92$, because the underlying physical connection between flame stretch and flame speed has been recovered by taking the flame relaxation time into account. This methodology is valid for the consumption speed as well as the two components of flame displacement speed (compare Fig. 4.37 and Fig. 4.33). The total flame

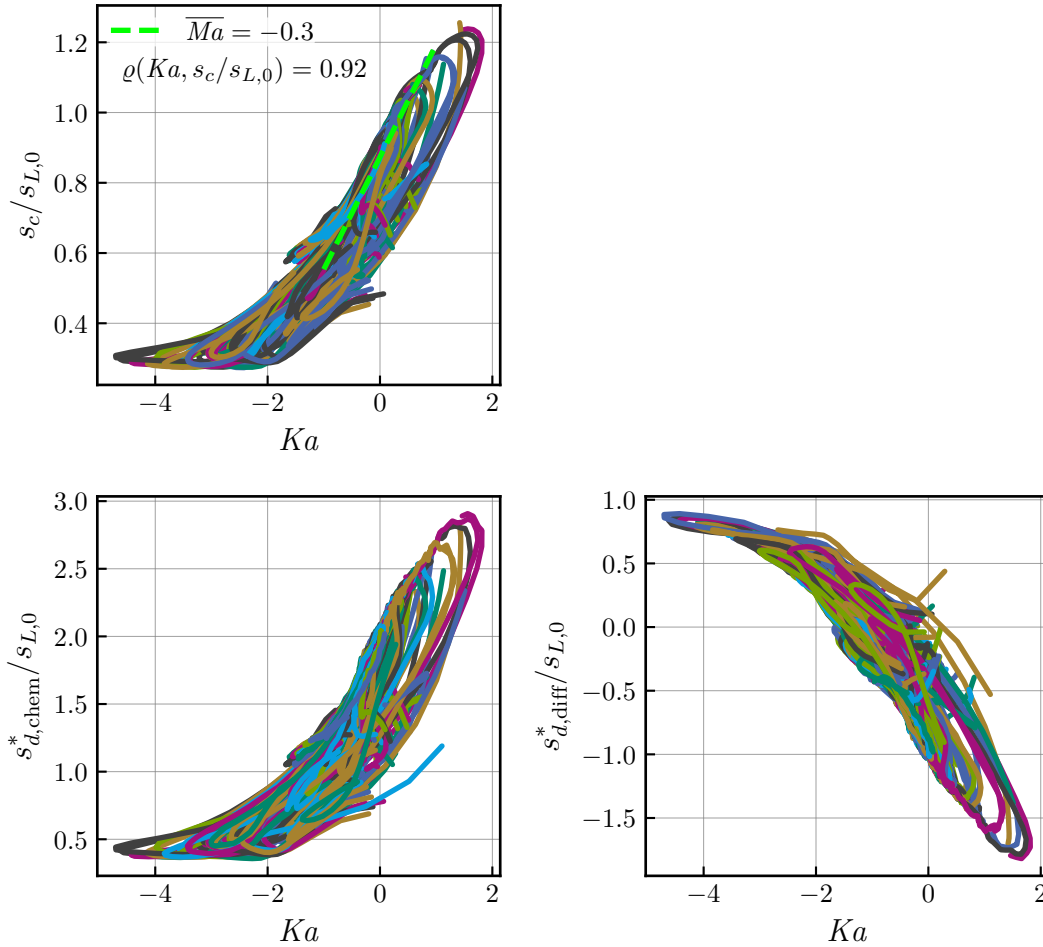


Figure 4.37: Correlation of consumption speed and the two components of displacement speed with flame stretch from the same particle cluster as before, where each particle's flame speed time signal is shifted in time following Fig. 4.36. The green dashed line is the averaged Markstein number obtained from a linear fit.

displacement speed is omitted in Fig. 4.37, due to the generally poor correlation with the local equivalence ratio, shown in Fig. 4.34.

The green dashed line in the top left of Fig. 4.37 shows a linear fit for the Markstein number from $-1 < Ka < 1$, which yields $\overline{Ma} = -0.3$. As this Markstein number is determined by the conditional mean over all flame particles, it represents an averaged or turbulent Markstein number. This Markstein number is further discussed in section 4.3.6 by comparing it to the results from the oscillating Bunsen flames. At more negative flame stretch values near $Ka \leq -4$ in Fig. 4.37, the linear correlation is not valid anymore as the correlation deviates from the quasi-linear trend. This is further discussed in section 4.3.7.

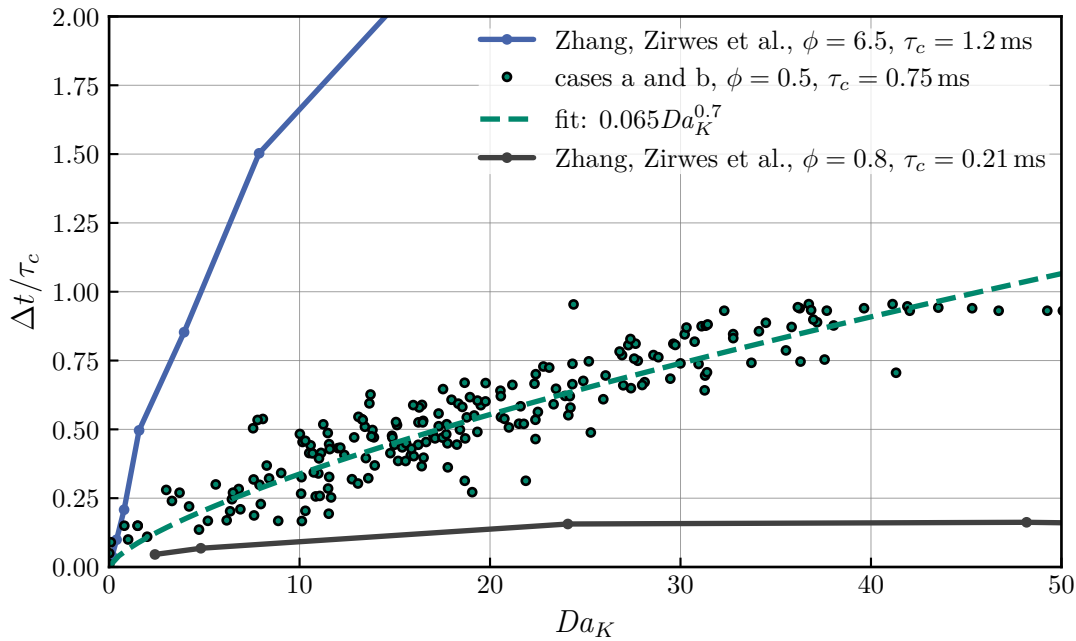


Figure 4.38: Flame relaxation time Δt as a function of local frequencies or local Damköhler number $Da_K = 1/(f_K\tau_c)$ for the hydrogen flames. Additionally, previous results from oscillating hydrogen slot burner flames from Zhang, Zirwes et al. [117] are shown as well.

The local flame relaxation time Δt depends on the local flow timescales, which are expressed as a local Damköhler number Da_K . Δt determined from each flame particle trajectory is plotted against the local time scale experienced by each flame particle or more specifically the rate of change of the local flame stretch in Fig. 4.38. This is done by determining the inflection points of the flame stretch time signal, which are depicted as red points in Fig. 4.35. Twice the time difference between the two inflection points is assumed to represent the inverse frequency of the flame stretch change f_K . In this way, a time scale of the local flame stretch rate of change can be attributed to each flame particle as a local Damköhler number $Da_K = 1/(f_K\tau_c)$. This type of analysis is possible because the chosen flame particles experience the hysteresis evolution of flame stretch with a dominant single frequency. Of course, the correlation still shows a low amount of scattering, as this part of the flame is also affected by low amplitude oscillations with other frequencies due to the turbulent nature of the flow.

The local flame relaxation time Δt dependence on the local Damköhler number can be expressed from a power-law relation. The dashed green line in Fig. 4.38 shows a fit of the form

$$\Delta t/\tau_c = c_1 (Da_K)^{c_2} \quad (4.21)$$

Similar results have been found in oscillating laminar slot Burner flames from a previous work of Zhang, Zirwes et al. [117], where the time delay between the local flow field and the movement of the flame tip has been studied. The general trend of Δt agrees with the results from section 4.1, where flame relaxation times are exponentially higher at the same Da for flames with higher time scales τ_c (see Fig. 4.12). However, these types of time dependent flame dynamics data are very spare and generally not available in the literature, as the flame particle tracking method is new and full simulations of three-dimensional turbulent flames are computationally very expensive.

The new findings allow to describe the local flame speed to flame stretch correlation in a more precise way, which helps to improve future models that depend on an accurate time-resolved modeling of local flame speeds and constitutes a new method of tabulating flame speed to flame stretch correlations as a function of local flow time scales. In the moderate flame stretch regime, where the flamelet assumption is valid, an analogous way to the laminar linear Markstein model is possible:

$$\frac{s(t)}{s_{L,0}} = 1 - \overline{Ma}(Da_t) Ka(t - \Delta t) \quad (4.22)$$

s is either the consumption or one of the components of displacement speed and Δt is computed from Eq. (4.21) based on the Damköhler number $Da_K = 1/(f_K \tau_c)$, which represents the local rate of change of flame stretch. The averaged, global or turbulent Markstein number \overline{Ma} depends on the turbulent Damköhler number Da_t and is discussed in the next section. The normalized flame stretch values Ka can be determined from the local flow properties and are shifted in time by $\Delta t/\tau_c = c_1 Da_K^{c_2}$, with $c_1 = 0.065$ and $c_2 = 0.7$ for the studied hydrogen flames. In this way, a strong, quasi-linear correlation of local flame speeds and local flame stretch values corresponding to the oscillating laminar flames can be successfully recovered from the otherwise strongly scattered correlation of instantaneous local flame speed and flame stretch.

4.3.6 Connection to Oscillating Laminar Flames

The averaged Markstein number $\overline{Ma}(Da_t)$ from the turbulent Markstein correlation in Eq. (4.22) can be expressed as a function the global turbulent Damköhler number $Da_t = (L_t/u')/(\delta_{th}/s_{L,0})$ and corresponds well to the ones obtained from low-dimensional flames, e.g. the oscillating Bunsen flames in section 4.2. The averaged Markstein number describes, how sensitive the flame as a whole is to flame stretch based on global flame and flow properties. When shifting the time

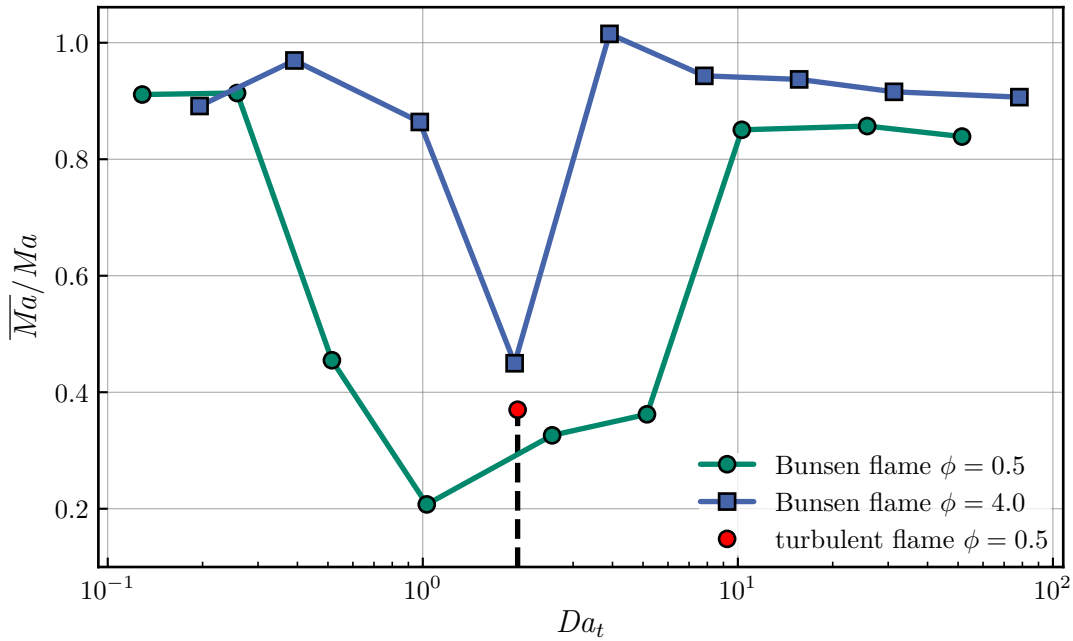


Figure 4.39: Ratio of averaged Markstein number \bar{Ma} to the steady-state Markstein number Ma for the oscillating laminar Bunsen flames from section 4.2.3. The red dot shows the turbulent Markstein number from Fig. 4.37 of the turbulent hydrogen-air flame from case b with $Da_t = 2$ and $\phi = 0.5$.

signals of $s_c(t)$ and $Ka(t)$ by the local flame relaxation time Δt for each point on the flame front to obtain the quasi-linear correlation in Fig. 4.37, the resulting averaged Markstein number shows a good agreement with the averaged Markstein number obtained from the oscillating Bunsen flames in Fig. 4.18 from section 4.2.3 with $\bar{Ma} \approx -0.3$ or $\bar{Ma}/Ma \approx 0.38$. The red point in Fig. 4.39 plots the turbulent Markstein number from Fig. 4.37 for the hydrogen flame in case b with $Da_t \approx 2$, together with the averaged Markstein numbers from the Bunsen flames oscillating with isolated frequencies or time scales Da discussed in section 4.2.3. In this way, the same effect of attenuated flame sensitivity at Damköhler numbers near unity is present both in the oscillating laminar and turbulent flames.

4.3.7 High Flame Stretch Regime

The previously described methodology of using a linear Markstein correlation with a global Damköhler number dependent Markstein number and a time shifted flame stretch rate depending on the local Damköhler number in Eq. (4.22) is valid in the flamelet regime and therefore the moderate flame stretch regime. Because of this, the high stretch rate regime is discussed next.

For the high flame stretch regime with $|Ka \gg 1|$, the linear Markstein correlation is no longer valid [213]. High stretch rates also coincide with large local rates of change of the flame stretch. Figure 4.40 shows trajectories of 5000 flame particles, randomly sampled from the simulation, in the consumption speed and flame stretch space for the flame in case b, starting in regions with positive flame stretch and moving to regions with large negative flame stretch. The particle tracks are colored by the instantaneous normalized rate of change of the local flame stretch. For $Ka < -2$, the rates of change of the flame stretch become very large, which means that the associated frequencies with the local rates of change become very large as well. In this regime, the flame speed stays nearly constant for each particle entering the high flame stretch regime. This is consistent with the findings in section 4.1 and section 4.2, where the flame cannot respond to high frequency oscillations. As a consequence, the sensitivity of flame speed to flame stretch goes toward zero, which means that locally $Ma \rightarrow 0$ in the high flame stretch regime, and thus there is a decoupling between flame speed and flame stretch.

This high flame stretch regime is only present on very small parts of the flame surface and thus not dominant for the flame dynamics, because the investigated flames are in the flamelet regime. Figure 4.41 shows the probability density

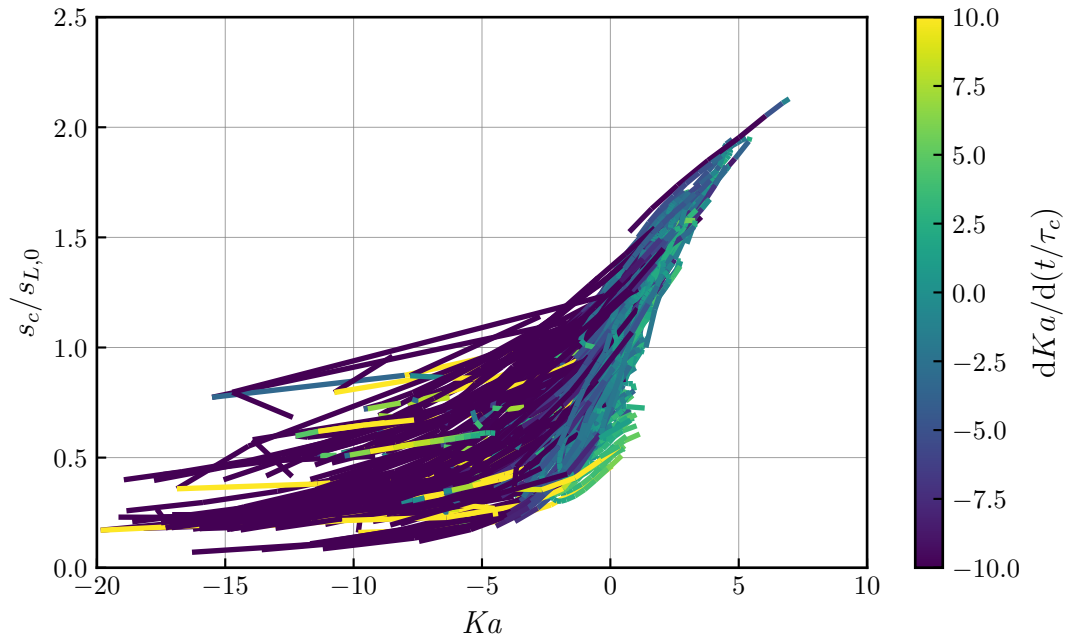


Figure 4.40: Trajectories of 5000 flame particles in the consumption speed and flame stretch space for the flame in case b, starting in regions with positive flame stretch and moving to regions with large negative flame stretch. Particle tracks are colored by the instantaneous normalized rate of change of the local flame stretch.

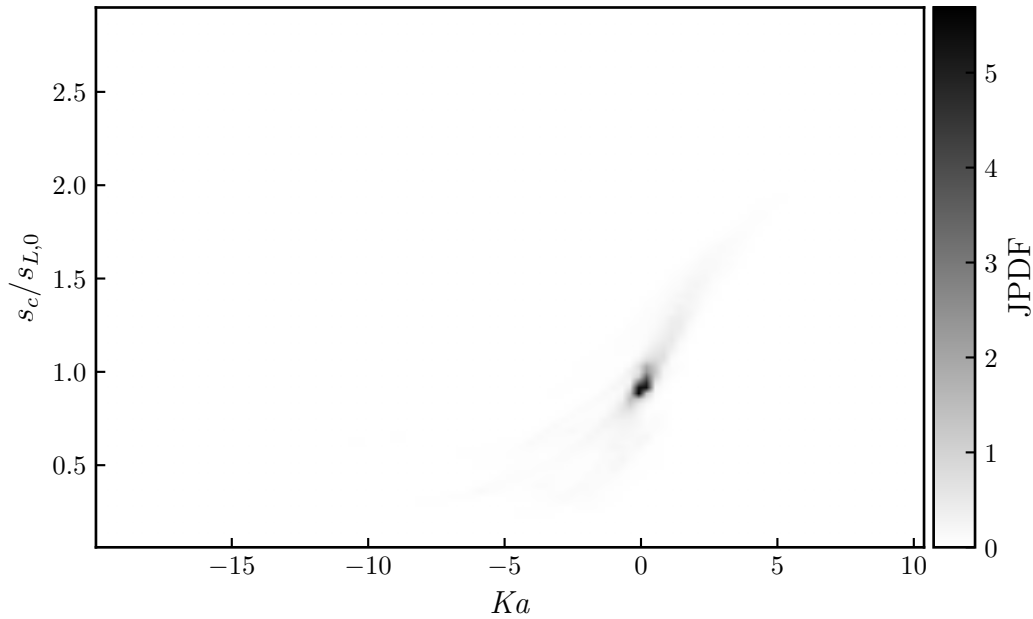


Figure 4.41: Joint probability density function (JPDF) of flame speed and flame stretch obtained from 10 000 flame particles. For the considered flames, the high flame stretch regions only make up a negligible portion of the total flame surface area.

function (JPDF) of flame speed and flame stretch obtained from 10 000 flame particles from the hydrogen-air flame from case b. It is evident that most of the flame surface area experiences moderate flame stretching. Additionally, for many practical turbulent flames, the surface averaged value of curvature is close to zero [27] so that it tends not to affect the global flame properties significantly.

4.3.8 Characteristic Flame Particle Trajectories

As explained in section 3.2, the movement of flame particles is related to flame stretch and therefore flame particles will on average move toward regions with more negative flame stretch, which, by definition, are regions where flame surface area is annihilated. Figure 4.42 shows an ensemble average of different quantities over 50 000 flame particles. The average is taken with respect to the flame particle's residence time t_{FP} , which starts at $t_{FP} = 0$ when the particle is seeded onto the flame front and ends at $t_{FP} = t_{Lifetime}$, when the flame particle is removed from the simulation.

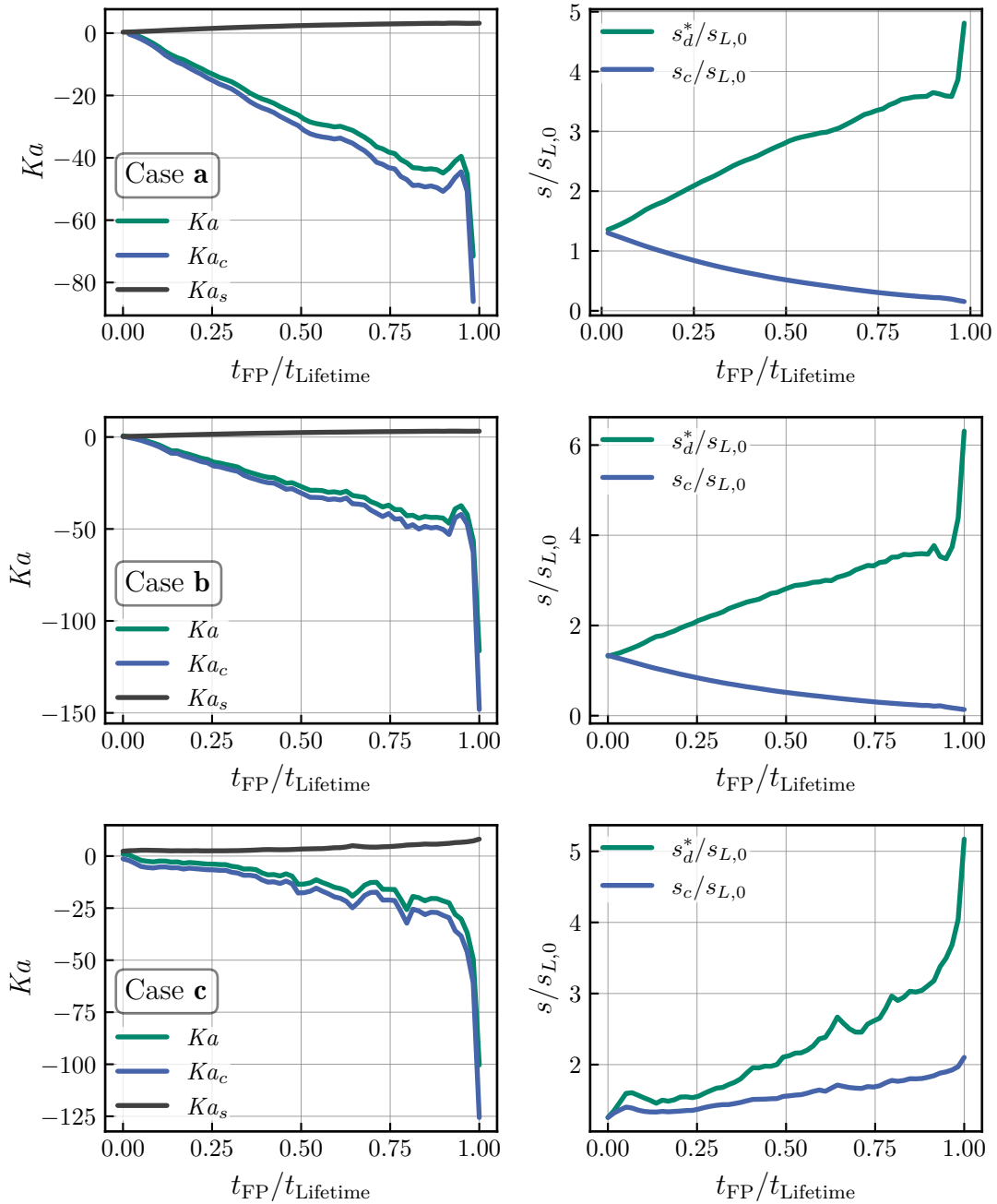


Figure 4.42: Ensemble average of 50 000 particles for different quantities over the flame particle's lifetime for the three turbulent flame cases.

In this way, the flame particles have a universal characteristic trend, first noted by Chaudhuri [45]. In Fig. 4.42, the ensemble averages are performed for all three cases, which include a methane flame and two hydrogen flames. In all cases, the local flame stretch at the flame particle's position decreases to more negative values over time. In this way, the contribution of curvature determines the flame stretch, so that Ka and Ka_c have the same trend. For the lean hydrogen flames with a generally negative Markstein number, the flame consumption speed decreases as the flame stretch becomes more negative. For the methane flame with positive Markstein number, the consumption speed increases. However, at about $t_{FP}/t_{Lifetime} \approx 0.9$, a strong decrease of the flame stretch toward large negative values is observed, which coincides with a strong increase of the flame displacement speed. This regime has been called interaction regime, as the annihilation of flame surface area can occur due to flame-flame interaction [214] or island formation [41]. The large negative flame stretch rates correspond to large negative curvature, where the curvature radius is on the order of the flame thickness, so that the flame cannot be considered as a flamelet anymore but more resembles a flame kernel.

A more detailed description of what happens when a flame particle enters the high stretch range is shown in Fig. 4.43 for a single flame particle on the flame of case b. On the top left, the flame speed in terms of consumption and displacement speed is shown. At first, both flame speeds stay relatively constant in the moderate flame stretch regime. As the flame stretch reaches high negative values, the flame extinguishes locally ($s_c \approx 0$) while the displacement speed becomes very high. The decrease of the flame stretch is caused by more negative curvatures, that cause a decrease of the local equivalence ratio (top right), making the flame locally even leaner. The increase of Ka_s cannot compensate the strong negative curvature in Ka_c . It can be observed that the effective normal strain $a_{e,N}$ from Eq. (2.73) is generally positively correlated with the total displacement speed s_d^* . However, the best correlation is achieved by considering the diffusive and chemical contribution to the displacement speed separately and correlating them with the flame stretch or local equivalence ratio, as shown previously in Fig. 4.34 and Fig. 4.37. The large positive value of $a_{e,N}$ shows an increase in flame thickness, however, at the extreme curvatures, the local structure does not resemble a flamelet anymore.

Another interesting aspect is the change of normal and tangential diffusive fluxes as well as the chemical source term and convection during the transition from moderate flame stretch to high flame stretch, shown in the bottom two graphs of Fig. 4.43. In the moderate flame stretch regime, the diffusive mass flux is mostly caused by normal diffusion, which has a negative contribution to the displacement speed. As the flame stretch becomes more negative and the flame

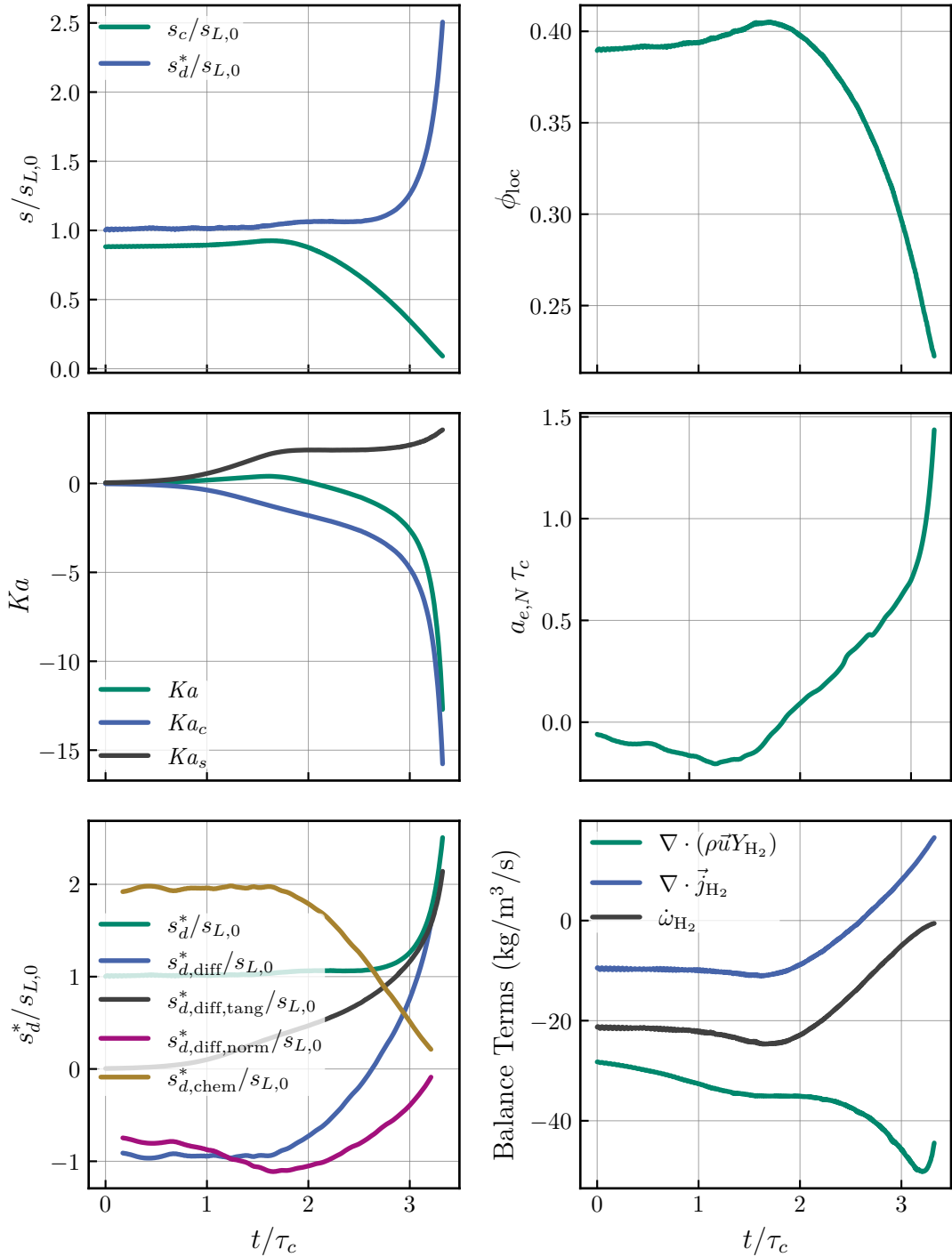


Figure 4.43: Time signals of different quantities for a single flame particle on the flame of case b.

becomes more strongly curved, the normal diffusive contribution vanishes and the chemical reaction rates go to zero as the flame locally extinguishes. The tangential mass flux, which depends directly on the curvature (see Eq. (2.33)) and was close to zero in the moderate flame stretch range, causes strong positive displacement speeds. At the same time, the convective term balances this change in the tangential diffusive flux and the diffusive flux contribution to the balance equation $\nabla \cdot \vec{j}_{\text{H}_2}$ reverses its sign as the total flame stretch reaches large negative values.

4.3.9 Regime Overview

Figure 4.44 summarizes the previous findings by plotting instantaneous consumption speed and instantaneous flame stretch from 10 000 flame particles for the flame in case b. Two flame stretch regimes can be identified: a moderate flame stretch regime for $-4 < Ka < 4$ and a high flame stretch regime, here for $Ka \ll -4$. Additionally, due to the flame being a lean hydrogen-air flame, flame quenching can be observed as well.

In the moderate flame stretch regime, local flame speed can be expressed as a linear Markstein correlation from Eq. (4.22), where the turbulent Markstein number is

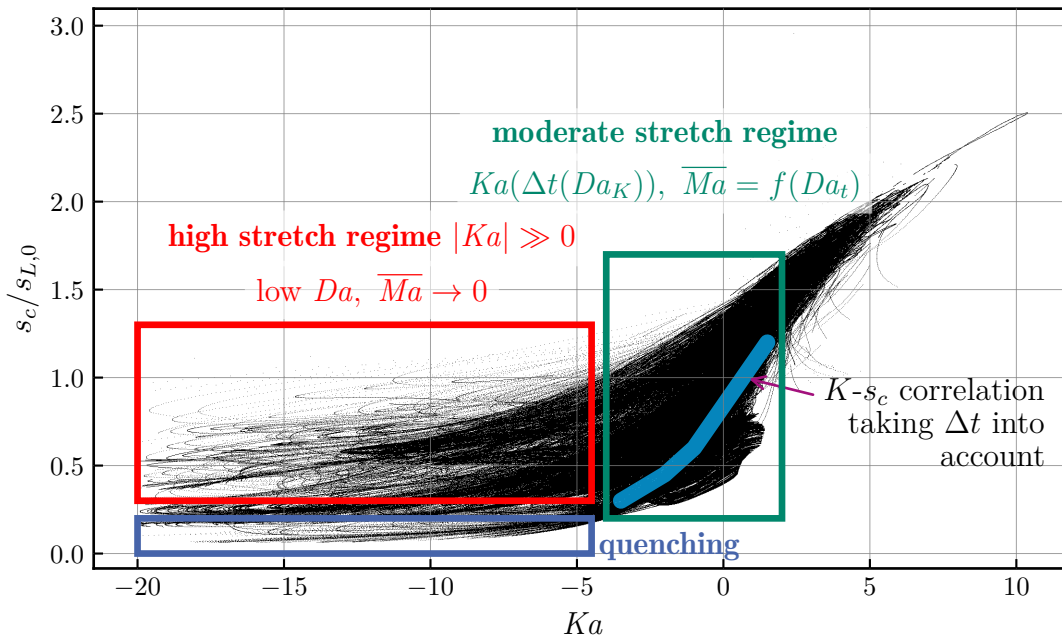


Figure 4.44: Scatterplot of instantaneous consumption speed and instantaneous flame stretch from 10 000 flame particles for the flame in case b. In the moderate flame stretch regime, the scattered data collapse to the blue region when adjusted by the local flame relaxation time Δt .

a function of the global turbulent Damköhler number $\overline{Ma}(Da_t)$ and the Karlovitz number is computed from the local flame stretch shifted in time based on the local rates of change of flame stretch $\Delta t(Da_K)$, or more specifically $\Delta t/\tau_c = c_1 Da_K^{c_2}$. Taking this relaxation time into account can recover the quasi-linear correlation. The blue region in Fig. 4.44 shows the time-shifted flame speed and flame speed correlation spanned by the particle tracks from the top left of Fig. 4.37. In the high flame stretch regime, the apparent sensitivity of the flame to flame stretch goes toward zero, which can be expressed as a Markstein number of zero, as the local rates of change become very high (very low local Damköhler numbers) so that the flame cannot follow the unsteady conditions. This is evident by the near-horizontal lines of the particle tracks in the flame speed and flame stretch space on the left of Fig. 4.44. It should be noted, that the high flame stretch regime may account for a significant portion of the total global flame stretch, but it covers only a small part of the total flame surface area. This can also be seen in Fig. 4.28, where Damköhler's first hypothesis is fulfilled despite the existence of the high stretch regime.

4.3.10 Conclusions

Direct numerical simulations of three turbulent flame cases in the flamelet regime have been performed. During the simulation, flame particles are seeded onto an iso-surface of the fuel mass fraction and tracked over time. The new flame particle tracking implementation allows the tracking of a large number of flame particles and for the first time a concurrent evaluation of the flame consumption speed. The flame particles' trajectories in the flame speed and flame stretch space reveal the underlying connection of the flame dynamics to the memory effect. Two regimes have been identified: A moderate flame stretch regime where a new Markstein correlation can successfully recover a linear correlation by taking the time relaxation time into account. And a high flame stretch regime where apparent stretch sensitivities go toward zero. This regime covers, however, only a negligible portion of the total flame surface area. The inclusion of time history effects in the correlation of flame speed and flame stretch opens new possibilities of modeling local flame speeds in a more accurate way in the future.

The key points from this section are summarized as follows:

- i. The investigated turbulent flame cases are located in the flamelet regime. Because of this, Damköhler's first hypothesis is valid and the turbulent flame speed s_T correlates well with the turbulent flame surface area.

- ii. The efficiency factor I_0 is shown to reach a constant value which is a function of u' , and takes values above unity for lean hydrogen flames and below unity for the methane flame.
- iii. A cluster of flame particles has been chosen for analysis which undergoes a hysteresis of the flame stretch. This allows to determine local flame relaxation times by finding the maximum correlation coefficient between flame speed and flame stretch for each flame particle.
- iv. The local flame relaxation time is a function of the local Damköhler number Da_K for each flame particle or each point on the flame surface as $\Delta t/\tau_c = c_1 Da_K^{c_2}$, with $c_1 = 0.065$ and $c_2 = 0.7$ for the hydrogen flames. These results are consistent with previous findings in laminar flames.
- v. Taking the relaxation time into account, the flame speed and flame stretch correlation can be improved from $\varrho = 0.68$ to $\varrho = 0.92$ for the studied flame case because instantaneous values of flame speed are determined from previous values of flame stretch due to the memory effect of the flame. In the new linear Markstein approach, a turbulent Markstein number that depends on the global Damköhler number Da_t can be modeled from the low-dimensional Bunsen flames in section 4.2. In this way, a quasi-linear correlation can be used for the prediction of local flame speeds as a function of the turbulence conditions and local flow time scales as $s(t)/s_{L,0} = 1 - \overline{Ma}(Da_t)Ka(t - \Delta t)$. This improved prediction is possible for the consumption speed as well as the two components of the displacement speed, but in general not for the displacement speed.
- vi. In the high flame stretch regime, curvatures become generally very negative and eventually lead to annihilation of flame surface area together with the flame particles. Taking the ensemble average over all flame particles shows a characteristic trend for all three flame cases, which ends with a sudden drop of flame stretch to very large negative values and an increase of flame displacement speed. In that case, the tangential contribution from mass diffusion drives the flame, while normal diffusion and chemical source terms become less important, until the local flame surface area is annihilated.

Summary

Combustion will remain a key technology for providing the world's energy in the foreseeable future. It is therefore mandatory to improve current combustion devices and aid the design of new concepts to reduce pollutant emissions and improve efficiencies. This, however, relies on a better understanding of the underlying physics that govern turbulent combustion processes.

With the increase in computing power, high-fidelity simulations become feasible where parts of the flame are resolved. This, however, requires an accurate modeling of local flame speeds, which is a fundamental quantity to describe the fuel consumption rate. For steady-state laminar flames, a well-known modeling approach can be used by expressing the flame speed as a function of the flame stretch. Flame stretch is a measure of how strongly the flame is disturbed by an inhomogeneous flow field and subsequent flame deformation. In a moderate flame stretch range, a linear correlation, known as the Markstein model, can be applied in laminar steady-state flames. Despite this, the correlation of local flame speeds and flame stretch in turbulent flames is much less pronounced and characterized by a large scattering. As turbulent flames are subjected to transient stretching in a wide range of length and time scales, the time histories or memory effects influence the temporal correlation of flame speed and flame stretch. The flame cannot adapt instantaneously to changing stretch rates, but instead requires a relaxation time to reach a quasi-steady state. However, there is no comprehensive study of the effect of flow transients on flame dynamics in the literature and the influence of time histories on flame dynamics is mostly unknown. Detailed simulations of

turbulent flames are mostly analyzed from instantaneous flame snapshots in an Eulerian reference frame, thus prohibiting the study of the memory effect and its influence on the flame speed.

The goal of this work is to investigate the memory effect of flames in unsteady flows. The focus lies on studying the impact of flame relaxation times on the local dynamics of premixed flames, more specifically on the correlation between local flame speeds and flame stretch. The aim is to recover a strong quasi-linear correlation from the scattered flame speed and flame stretch data by considering the relaxation time that the flame requires to adjust its local flame speed to the changing flame stretch conditions.

Because fluctuations in turbulent flows occur in a wide range of time scales which mutually interact, the numerical investigations in this work start systematically with low-dimensional, laminar flames with isolated time scales to assess the flame's response to unsteady effects. From the laminar flame simulations, frequency dependent, global Markstein numbers can be computed that are directly applicable to turbulent flames. Then, turbulent flames are simulated that experience complex, three-dimensional and unsteady stretching and are subjected to the full frequency spectrum of the turbulence. The flame relaxation times are evaluated by tracking the time histories of flame speed and flame stretch of every point on the flame surface of turbulent flames with the recently developed flame particle tracking method. In this way, a new model for predicting local flame speeds in turbulent flames based on turbulent Markstein numbers and flame relaxation times is formulated that successfully recovers a quasi-linear flame speed and flame stretch correlation.

Development of Numerical Tools

To evaluate the local time histories and record the thermo-physical trajectories of points on the flame surface, a Lagrangian viewpoint has to be employed. The recently developed flame particle tracking (FPT) method is applied in this work to evaluate the flame relaxation times in turbulent flames. In this method, virtual tracer particles, called flame particles (FP), that represent material points on the flame surface, are tracked during the simulation. These material points move as a superposition of the flow velocity and the flame's displacement speed, and thus co-move with an iso-surface of the flame. Flame particles are also intrinsically connected to flame stretch. In regions of positive flame stretch, flame particles

move away from each other and in regions of negative flame stretch, they cluster together.

The current practice of the flame particle tracking method has some shortcomings. In the literature, the method has been introduced as a post-processing operation. This limits the number of concurrently tracked particles and requires to store large amounts of simulation data. Additionally, the original tracking implementation requires ray-tracing of the particle trajectory to a global iso-surface, which is an expensive operation. Therefore, a new tracking method has been developed in this work that allows to use the flame particle tracking method for the first time in a fully parallelized manner during the simulation, including the computation of flame consumption speeds which is often neglected in the literature due to the high computational cost. One key feature of the new method is the representation of the flame particle positions in barycentric coordinates. This allows fast interpolation of quantities to the particle position, can be applied to any mesh cell shapes and uses an analytic expression for finding the particle trajectory intersection with the iso-surface, thereby avoiding ray-tracing and other expensive operations.

All flames studied in this work are simulated with the direct numerical simulation (DNS) method, including detailed molecular diffusion and the finite rate chemistry model with detailed reaction mechanisms. The simulation of three-dimensional flames in this way requires large computational resources, so that the DNS of turbulent flames has been conducted on Germany's fastest national supercomputers. To enable the analyses carried out in this work, two new performance optimizations have been developed for the in-house DNS code, which is based on the open-source framework OpenFOAM®: an automated code generation approach that creates highly optimized source code for the computation of chemical reaction rates; and a new load balancing method for sharing parallel workload caused by the computation of chemical reaction rates. Together, these new optimization techniques can reduce total simulation times by 70 % compared to OpenFOAM®'s standard implementation, without reducing the accuracy of the simulation.

Global Flame Speed Dependence on the Damköhler Number

To quantify the impact of unsteady flame stretching on the global flame speed or integral fuel consumption speed s_T , oscillating laminar Bunsen flames are simulated. These flames are excited by a harmonically oscillating inflow and allow a systematic study of transient flame stretching with isolated frequencies f or time

scales. They are subjected to both aerodynamic straining and curvature, including positive and negative stretch rates, and can therefore be used to interpret the complex behavior of turbulent flames. In the context of turbulent flames, the global flame speed s_T represents the turbulent flame speed. The turbulent flame speed closure model by Schmid can be used to predict the turbulent flame speed as a function of the Damköhler number $Da = 1/(f\tau_c)$, where τ_c is the characteristic time scale of the flame. However, for Damköhler numbers near unity, the shape function assumed in the Schmid model does not predict the resulting trend from this work. Based on the simulation results, a different sigmoid-shaped form function is proposed for the prediction of turbulent flame speed fluctuation s'_T depending on flow fluctuation u' and Da as $s'_T/u' = (1 + \exp(c_1 Da))^{c_2}$. The new shape function captures the physical effect of flow transients on the flame's response. Because the flame requires a certain relaxation time to adapt to changing flow conditions, it cannot follow high frequency fluctuations (low Da), so that s'_T is attenuated with decreasing Da until $s'_T/u' \rightarrow 0$ for $Da \rightarrow 0$. On the other hand, for large Da , the flame relaxation time is faster than the fluctuation time scale so that the flame can relax to a quasi-steady state at $Da \gg 1$.

Impact of the Memory Effect on Local Flame Speeds

There is a linear dependence between normalized flame stretch Ka and flame speed in laminar, steady-state flames, but a strong scattering is observed in turbulent flames. In analogy to the classical Markstein model, a new unsteady or turbulent Markstein model has been devised: $s(t)/s_{L,0} = 1 - \overline{Ma} Ka(t - \Delta t)$, where $s(t)$ is the local flame speed of a point on the flame surface, either in terms of the consumption speed or a component of the displacement speed, and $s_{L,0}$ is the laminar flame speed. The global sensitivity of the normalized flame speed to normalized flame stretch Ka is expressed by the averaged Markstein number \overline{Ma} . To unravel the scattering in the flame speed and flame stretch correlation under turbulent conditions, a local flame relaxation time Δt is introduced to consider the memory effect of the flame and to correlate instantaneous values of flame speed with previous values of flame stretch.

The oscillating laminar Bunsen flames are used to determine the flame's global sensitivity to flame stretch in terms of a frequency dependent, averaged Markstein number \overline{Ma} . The correlation of local flame speed and flame stretch in the oscillating Bunsen flames does not show the linear correlation from steady-state flames, but exhibits a scattering similar to turbulent flames. By taking the conditional mean

of the instantaneous local flame speed and flame stretch data collected from each point of the Bunsen flame surface at different time instances, \overline{Ma} can be computed as the negative slope of the averaged flame speed and flame stretch correlation. This is done for each flame, oscillating with a specific frequency, to obtain \overline{Ma} as a function of the frequency or Damköhler number. As the frequencies approach the characteristic time scale of the flame τ_c ($Da \rightarrow 1$), the global sensitivity of the flame speed to flame stretch, which is the Markstein number, is attenuated. For higher frequencies, there is no flame response to the fluctuations and the steady-state Markstein number is recovered. The impact of unsteady flame stretch can therefore be regarded as the competition of the flow's time scale with the flame's relaxation time scale. The same trend has also been identified in turbulent flames.

Full three-dimensional turbulent hydrogen and methane flames are simulated to determine the local flame relaxation times Δt . Turbulent flames interact with the turbulent flow in a wide range of time scales. To evaluate the flame relaxation times Δt , the simulations are conducted together with the flame particle tracking method (FPT). By seeding flame particles (FP) onto the surface of the turbulent flame, the local values of flame speed and flame stretch on each point of the flame surface can be tracked over time. There is a time lag between the flame speed and flame stretch signal. The flame relaxation time can be computed by shifting the time signals of flame speed and flame stretch against each other until they overlap.

The local flame relaxation time Δt itself depends on the unsteadiness of the underlying turbulent flow. Because of this, to model Δt , the rate of change of the local flame stretch has to be considered. The time scale of the local flame stretch is expressed as a local Damköhler number Da_K . In this work, the time scale of the local flame stretch is computed from two inflection points of the flame stretch time signal, which corresponds to the stretch time scale $1/f_K$ or $Da_K = 1/(f_K\tau_c)$. In this way, the influence of the memory effect can be modeled by the local flame relaxation time Δt as a function of the local Damköhler number Da_K from the new relation $\Delta t/\tau_c = c_1 (Da_K)^{c_2}$.

By computing the flame relaxation time Δt for each flame particle and shifting the flame stretch time signal by that value, a quasi-linear correlation is recovered from the strongly scattered data in turbulent flames. For a particle cluster on a turbulent hydrogen flame simulated in this work, the correlation coefficient ρ between local flame stretch and flame speed improves from $\rho = 0.68$ to $\rho = 0.92$, because the underlying physical relation between the two quantities is restored in this way.

The associated averaged Markstein number \overline{Ma} of the quasi-linear correlation corresponds well to the one obtained from the laminar oscillating Bunsen flames, where the representative global Damköhler number of the turbulent flame is the turbulent Damköhler number $Da_t = (L_t/u')/\tau_c = 2$ instead of the single-frequency Damköhler number Da from the Bunsen flames. In this way, by taking the flame relaxation time into account, the local flame speed in turbulent flames can be modeled according to the new linear relation. Due to the quasi-linear nature of the new relation, it can be applied in a moderate flame stretch regime. For high stretch rates, local Damköhler numbers in turbulent flames typically become very low, leading to local Markstein numbers close to zero and a non-linear dependence of flame speed and flame stretch. However, the high flame stretch regime makes up only a negligible portion of the total flame surface area in the investigated turbulent flames, which are located in the flamelet regime.

In summary, the effect of unsteady flame stretching is characterized by an attenuation of the flame's response in terms of flame speed with increasing frequencies of the unsteady stretching. The results are consistent for both laminar and turbulent flames and allow to express both the global, turbulent flame speed as well as local flame speeds as a function of characteristic time scales. The quantification of the impact of unsteady stretching from both laminar and turbulent flames leads to the development of new methods to describe the flame dynamics. An extended model for the turbulent flame speed has been developed based on the global Damköhler number, which improves the prediction in the range of Damköhler numbers near unity. The large scattering of local flame speeds plotted against local flame stretch in turbulent flames is shown to be caused by the memory effect, where instantaneous flame speed values are determined by previous flame stretch rates. The flame speed and flame stretch correlation has been unraveled by introducing a flame relaxation time, which depends exponentially on the local flow time scales. The local relaxation times have been determined by tracking the time histories of material points on the flame surface with the flame particle tracking method. The quasi-linear correlation between local flame speed and flame stretch in turbulent flames is recovered by taking the new flame relaxation time into account, which is valid in the moderate flame stretch regime. For the first time, the flame consumption speed could be evaluated together with the flame particle tracking method in a fully parallel manner due to the new flame particle tracking algorithm, which made the analyses from this work possible. The new model for the local flame speed based on a turbulent Markstein number and the newly found local flame relaxation times enable a more accurate description of local flame dynamics for future simulations.

6

Zusammenfassung

Verbrennung wird in absehbarer Zukunft eine Schlüsseltechnologie für die Energieversorgung der Welt bleiben. Daher ist es zwingend erforderlich, die derzeit verfügbaren Technologien zu verbessern und die Entwicklung neuer Konzepte zu unterstützen, um Schadstoffemissionen zu verringern und Wirkungsgrade zu erhöhen. Dies setzt allerdings ein besseres Verständnis der physikalischen Vorgänge voraus, die turbulenten Verbrennungsprozessen zugrunde liegen.

Mit zunehmender Rechenleistung werden Simulationen möglich, bei denen Teile der Flamme aufgelöst werden. Dies erfordert jedoch eine genaue Modellierung der lokalen Flammengeschwindigkeiten, die eine grundlegende Größe zur Beschreibung des Brennstoffumsatzes darstellen. Für stationäre, laminare Flammen kann ein Modellierungsansatz verwendet werden, bei dem die Flammengeschwindigkeit als Funktion der Flammenstreckung ausgedrückt wird. Die Flammenstreckung ist ein Maß dafür, wie stark die Flamme durch ein inhomogenes Strömungsfeld und die daraus resultierende Flammenverformung gestört wird. In einem moderaten Bereich von Flammenstreckung kann bei laminaren, stationären Flammen eine lineare Korrelation, das lineare Markstein Modell, angewendet werden. In turbulenten Flammen ist die Korrelation zwischen lokalen Flammengeschwindigkeiten und Flammenstreckung jedoch weit weniger ausgeprägt und durch eine große Streuung gekennzeichnet. Da turbulente Flammen in einem weiten Bereich von Längen- und Zeitskalen einer instationären Streckung unterworfen sind, beeinflussen Gedächtniseffekte (Memory-Effekte) die zeitliche Korrelation von Flammengeschwindigkeit und Flammenstreckung. Die Flamme kann nicht instantan auf sich ändernde

Streckungsraten reagieren, sondern benötigt eine Relaxationszeit, um einen quasi-stationären Zustand zu erreichen. In der Literatur gibt es jedoch keine umfassenden Studien über die Auswirkungen von transienten Strömungseffekten auf die Flammendynamik, und der Einfluss von Memory-Effekten auf die Flammendynamik ist weitgehend unbekannt. Detaillierte Simulationen von turbulenten Flammen werden meist anhand von Momentaufnahmen der Flamme in einem Eulerschen Bezugssystem analysiert, wodurch die Untersuchung des Memory-Effekts und seines Einflusses auf die Flammengeschwindigkeit nicht möglich ist.

Ziel dieser Arbeit ist es daher, den Memory-Effekt von Flammen in instationären Strömungen zu untersuchen. Der Schwerpunkt liegt auf der Untersuchung des Einflusses von Flammenrelaxationszeiten auf die lokale Dynamik von vorge-mischten Flammen, genauer gesagt auf der Korrelation zwischen lokalen Flammengeschwindigkeiten und Flammenstreckung. Ziel ist es, aus den gestreuten Flammengeschwindigkeits- und Flammenstreckungsdaten in turbulenten Flammen eine quasi-lineare Korrelation zurückzugewinnen, indem die Relaxationszeit berücksichtigt wird, die die Flamme benötigt, um ihre lokale Flammengeschwindigkeit an die wechselnden Flammenstreckungsraten anzupassen.

Da Fluktuationen in turbulenten Strömungen in einem breiten Spektrum von Zeitskalen auftreten, die sich gegenseitig beeinflussen, beginnen die numerischen Untersuchungen in dieser Arbeit systematisch mit niedrigdimensionalen, laminaren Flammen mit isolierten Zeitmaßen, um die Reaktion der Flamme auf instationäre Effekte auszuwerten. Aus den laminaren Flammensimulationen können frequenz-abhängige, globale Markstein-Zahlen berechnet werden, die direkt auf turbulente Flammen anwendbar sind. Anschließend werden turbulente Flammen simuliert, die komplexe, dreidimensionale und instationäre Streckungen erfahren und dem gesamten Frequenzspektrum der Turbulenz ausgesetzt sind. Die Flammenrelaxationszeiten werden ermittelt, indem die Zeitverläufe der Flammengeschwindigkeit und der Flammenstreckung jedes Punktes auf der Flammenoberfläche von turbulenten Flammen mit der kürzlich entwickelten Flammenpartikelverfolgungsmethode (flame particle tracking method) verfolgt werden. Auf diese Weise wurde ein neues Modell für die Vorhersage lokaler Flammengeschwindigkeiten in turbulenten Flammen auf der Grundlage der turbulenten Markstein-Zahlen und der Flammenrelaxationszeiten formuliert, das erfolgreich eine quasi-lineare Korrelation zwischen Flammengeschwindigkeit und Flammenstreckung aus den turbulenten Flammen wiederherstellt.

Numerische Methodenentwicklung

Um die lokalen Zeitverläufe auszuwerten und die thermophysikalischen Trajektorien von Punkten auf der Flammenoberfläche zu erfassen, muss ein lagrangescher Ansatz verwendet werden. Die kürzlich entwickelte Flammenpartikelverfolgungsmethode (FPT) wird in dieser Arbeit angewandt, um die Flammenrelaxationszeiten in turbulenten Flammen auszuwerten. Bei dieser Methode werden virtuelle Tracerpartikel, sogenannte Flammenpartikel (FP), die materielle Punkte auf der Flammenoberfläche darstellen, während der Simulation verfolgt. Diese materiellen Punkte bewegen sich als Überlagerung der Strömungsgeschwindigkeit und der Verdrängungsgeschwindigkeit der Flamme und bewegen sich somit gemeinsam mit einer Isofläche der Flamme. Die Flammenpartikel sind intrinsisch mit der Flammenstreckung verbunden. In Bereichen mit positiver Flammenstreckung entfernen sich die Flammenpartikel voneinander, und in Bereichen mit negativer Flammenstreckung laufen sie zusammen.

In der Praxis hat die Methode der Flammenpartikelverfolgung einige Einschränkungen. In der Literatur wurde die Methode als Post-Processing Schritt eingeführt. Dadurch ist die Anzahl der gleichzeitig verfolgten Partikel begrenzt und es müssen große Mengen an Daten der Simulationsergebnisse gespeichert werden. Darüber hinaus erfordert die ursprüngliche Implementierung Ray-Tracing der Partikeltrajektorien zu einer globalen Isofläche, was eine rechenintensive Operation ist. Daher wurde in dieser Arbeit eine neue Verfolgungsmethode entwickelt, die es erstmals ermöglicht, die Flammenpartikelverfolgungsmethode während der Simulation vollständig zu parallelisieren, einschließlich der Berechnung der Flammenumsatzgeschwindigkeit (flame consumption speed), die in der Literatur aufgrund der hohen Rechenkosten oft vernachlässigt wird. Ein wesentliches Merkmal der neuen Methode ist die Darstellung der Flammenpartikelpositionen in baryzentrischen Koordinaten. Dies ermöglicht eine schnelle Interpolation von beliebigen Größen auf die Partikelposition, kann auf beliebige Netzzellenformen angewandt werden und verwendet einen analytischen Ausdruck für die Ermittlung des Schnittpunkts der Partikeltrajektorien mit der Isofläche, wodurch Ray-Tracing und andere teure Rechenoperationen vermieden werden können.

Alle in dieser Arbeit untersuchten Flammen werden mit der Direkten Numerischen Simulations-Methode (DNS) berechnet, einschließlich detaillierter molekularer Diffusion und des finite rate chemistry Ansatzes zusammen mit detaillierten Reaktionsmechanismen. Die Simulation von dreidimensionalen Flammen auf diese Weise erfordert große Rechenressourcen, sodass die Direkte Numerische Simulation von turbulenten Flammen in dieser Arbeit auf den schnellsten nationalen

Supercomputern Deutschlands ausgeführt wurden. Um die in dieser Arbeit durchgeführten Analysen zu ermöglichen, wurden zwei neue Leistungsoptimierungen für den in-house DNS-Code entwickelt, der auf dem Open-Source-Framework OpenFOAM® basiert: ein automatischer Codegenerierungsansatz, der hochoptimierten Quellcode für die Berechnung chemischer Reaktionsraten erzeugt, und eine neue Lastausgleichsmethode zur Verteilung der parallelen Arbeitslast, die durch die Berechnung chemischer Reaktionsraten verursacht wird. Zusammen können diese neuen Optimierungstechniken die Gesamtsimulationszeiten im Vergleich zur Standardimplementierung von OpenFOAM® um 70 % reduzieren, ohne die Genauigkeit der Simulation zu verringern.

Abhängigkeit der globalen Flammengeschwindigkeit von der Damköhler-Zahl

Um die Auswirkungen der instationären Flammenstreckung auf die globale Flammengeschwindigkeit oder die integrale Brennstoffumsatzgeschwindigkeit s_T zu quantifizieren, werden oszillierende laminare Bunsen-Flammen simuliert. Diese Flammen werden durch eine harmonisch oszillierende Anströmung angeregt und ermöglichen eine systematische Untersuchung der instationären Flammenstreckung mit isolierten Frequenzen f oder Zeitmaßen. Sie sind sowohl aerodynamischer Dehnung als auch Krümmung unterworfen, einschließlich positiver und negativer Streckungsraten, und können daher zur Interpretation des komplexen Verhaltens turbulenter Flammen verwendet werden. Im Zusammenhang mit turbulenten Flammen stellt die globale Flammengeschwindigkeit s_T die turbulente Flammengeschwindigkeit dar. Mit Hilfe des Modells für die Schließung der turbulenten Flammengeschwindigkeit von Schmid lässt sich die turbulente Flammengeschwindigkeit in Abhängigkeit der Damköhler-Zahl $Da = 1/(f\tau_c)$ vorhersagen, wobei τ_c das charakteristische Zeitmaß der Flamme ist. Für Damköhler-Zahlen nahe Eins sagt die im Schmid-Modell angenommene Formfunktion jedoch nicht den in dieser Arbeit berechneten Trend voraus. Auf der Grundlage der Simulationsergebnisse wird eine andere sigmoid-förmige Formfunktion für die Vorhersage der turbulenten Flammengeschwindigkeitsschwankung s'_T in Abhängigkeit der Strömungsschwankung u' und Da als $s'_T/u' = (1 + \exp(c_1 Da))^{c_2}$ vorgeschlagen. Die neue Formfunktion erfasst die physikalische Wirkung von Strömungsfluktuationen auf das Verhalten der Flamme. Da die Flamme eine Relaxationszeit benötigt, um sich an veränderte Strömungsbedingungen anzupassen, kann sie hochfrequenten Schwankungen (niedrigen Da) nicht folgen, sodass s'_T mit abnehmender Da gedämpft wird, bis $s'_T/u' \rightarrow 0$ für $Da \rightarrow 0$. Andererseits ist für

große Da die Relaxationszeit der Flamme kleiner als das Fluktuationszeitmaß, sodass die Flamme bei $Da \gg 1$ einen quasi-stationären Zustand erreichen kann.

Einfluss des Memory-Effekts auf lokale Flammengeschwindigkeiten

In laminaren, stationären Flammen gibt es eine lineare Abhängigkeit zwischen der normalisierten Flammenstreckung Ka und der Flammengeschwindigkeit. In turbulenten Flammen weist diese Korrelation eine starke Streuung auf. In Analogie zum klassischen Markstein-Modell wurde ein neues instationäres oder turbulentes Markstein-Modell entwickelt, das dargestellt werden kann als $s(t)/s_{L,0} = 1 - \overline{Ma} Ka(t - \Delta t)$, wobei $s(t)$ die lokale Flammengeschwindigkeit eines Punktes auf der Flammenoberfläche ist, entweder in Form der Umsatzgeschwindigkeit oder einer Komponente der Verdrängungsgeschwindigkeit, und $s_{L,0}$ die laminare Flammengeschwindigkeit ist. Die globale Sensitivität der normierten Flammengeschwindigkeit gegenüber der normierten Flammenstreckung Ka wird durch die gemittelte Markstein-Zahl \overline{Ma} ausgedrückt. Um die Streuung in der Korrelation von Flammengeschwindigkeit und Flammenstreckung unter turbulenten Bedingungen zu entschlüsseln, wird eine lokale Flammenrelaxationszeit Δt eingeführt, um den Memory-Effekt der Flamme zu berücksichtigen und die momentanen Werte der Flammengeschwindigkeit mit vorherigen Werten der Flammenstreckung zu korrelieren.

Die oszillierenden laminaren Bunsen-Flammen werden verwendet, um die globale Sensitivität der Flamme gegenüber der Flammenstreckung in Form einer frequenzabhängigen, gemittelten Markstein-Zahl zu bestimmen. Die Korrelation von lokaler Flammengeschwindigkeit und Flammenstreckung in den oszillierenden Bunsen-Flammen zeigt nicht die lineare Korrelation von stationären Flammen, sondern weist eine Streuung ähnlich wie bei turbulenten Flammen auf. Durch Bildung des bedingten Mittelwerts der momentanen lokalen Flammengeschwindigkeiten und Flammenstreckungen, die an jedem Punkt der Bunsen-Flammenoberfläche zu verschiedenen Zeitpunkten gemessen werden, kann \overline{Ma} als negative Steigung der gemittelten Korrelation von Flammengeschwindigkeit und Flammenstreckung berechnet werden. Dies wird für jede Bunsen-Flamme, die mit einer einzelnen Frequenzen oszilliert, durchgeführt, um \overline{Ma} als Funktion der Frequenz oder Damköhler-Zahl zu erhalten. Wenn sich die Frequenzen dem charakteristischen Zeitmaß der Flamme τ_c annähern ($Da \rightarrow 1$), wird die globale Sensitivität der Flammengeschwindigkeit gegenüber der Flammenstreckung abgeschwächt. Bei

höheren Frequenzen reagiert die Flamme nicht mehr auf die Fluktuationen, und die Markstein-Zahl nimmt den Wert vom stationären Zustand an. Die Auswirkungen der instationären Flammenstreckung können daher als Konkurrenz zwischen dem Zeitmaß der Strömung und der Relaxationszeit der Flamme betrachtet werden. Derselbe Trend wurde auch bei turbulenten Flammen festgestellt.

Zur Bestimmung der lokalen Flammenrelaxationszeiten Δt werden dreidimensionale turbulente Wasserstoff- und Methanflammen simuliert. Turbulente Flammen interagieren mit der turbulenten Strömung in einem weiten Bereich von Zeitskalen. Um die Flammenrelaxationszeiten Δt unter diesen Umständen zu ermitteln, werden die Simulationen zusammen mit der Flammenpartikelverfolgungsmethode (FPT) durchgeführt. Durch das Aufbringen von Flammenpartikeln (FP) auf die Oberfläche der turbulenten Flamme können die lokalen Werte der Flammengeschwindigkeit und der Flammenstreckung an jedem Punkt der Flammenoberfläche über die Zeit verfolgt werden. Zwischen dem Flammengeschwindigkeits- und dem Flammenstreckungssignal besteht eine zeitliche Verzögerung. Die Flammenrelaxationszeit kann berechnet werden, indem die Zeitsignale der Flammengeschwindigkeit und der Flammenstreckung gegeneinander verschoben werden, bis sie sich überlagern.

Die lokale Flammenrelaxationszeit Δt hängt von der Instationarität der zugrunde liegenden turbulenten Strömung ab. Aus diesem Grund muss zur Modellierung von Δt die Änderungsrate der lokalen Flammenstreckung berücksichtigt werden. Das Zeitmaß der lokalen Flammenstreckung wird als lokale Damköhler-Zahl Da_K ausgedrückt. In dieser Arbeit wird das Zeitmaß der lokalen Flammenstreckung aus zwei Wendepunkten des Zeitsignals der Flammenstreckung berechnet, was dem Streckungszeitmaß $1/f_K$ oder $Da_K = 1/(f_K\tau_c)$ entspricht. Auf diese Weise kann der Einfluss des Memory-Effekts durch die lokale Flammenrelaxationszeit Δt als Funktion der lokalen Damköhler-Zahl Da_K mit dem neuen Ansatz $\Delta t/\tau_c = c_1 (Da_K)^{c_2}$ modelliert werden.

Durch die Berechnung der Flammenrelaxationszeit Δt für jedes Flammenpartikel und die Verschiebung des Zeitsignals der Flammenstreckung um diesen Wert lässt sich aus den stark gestreuten Flammengeschwindigkeits- und Flammenstreckungsdaten eine quasi-lineare Korrelation zurückgewinnen. Für einen Partikelcluster auf einer in dieser Arbeit berechneten turbulenten Wasserstoffflamme verbessert sich dadurch der Korrelationskoeffizient ρ zwischen lokaler Flammenstreckung und Flammengeschwindigkeit von $\rho = 0,68$ auf $\rho = 0,92$, da die zugrunde liegende physikalische Beziehung zwischen den beiden Größen

durch den Zeitverzug um die Relaxationszeit wiederhergestellt wird. Die zugehörige gemittelte Markstein-Zahl \overline{Ma} der quasi-linearen Korrelation entspricht derjenigen, die aus den laminar oszillierenden Bunsen-Flammen ermittelt wurden, wobei die repräsentative globale Damköhler-Zahl der turbulenten Flamme die turbulente Damköhler-Zahl $Da_t = (L_t/u')/\tau_c$ ist. Auf diese Weise kann unter Berücksichtigung der Flammenrelaxationszeit die lokale Flammengeschwindigkeit in turbulenten Flammen nach der neuen linearen Beziehung modelliert werden. Da die neue Beziehung quasi-linear ist, kann sie bei moderaten Flammenstreckungen angewendet werden. Bei hohen Streckungsraten werden die lokalen Damköhler-Zahlen in turbulenten Flammen typischerweise sehr niedrig, was zu lokalen Markstein-Zahlen nahe Null und zu einer nichtlinearen Abhängigkeit von Flammengeschwindigkeit und Flammenstreckung führt. Der Bereich hoher Flammenstreckung macht jedoch nur einen vernachlässigbaren Teil der gesamten Flammenoberfläche in den untersuchten turbulenten Flammen aus, die sich im Flamelet Regime befinden.

Zusammenfassend lässt sich sagen, dass die Auswirkung der instationären Flammenstreckung durch eine Abschwächung der Flammenantwort in Bezug auf die Flammengeschwindigkeit mit zunehmender Frequenz der instationären Streckung gekennzeichnet ist. Die Ergebnisse sind sowohl für laminare als auch für turbulente Flammen gültig und erlauben es, die globale, turbulente Flammengeschwindigkeit sowie die lokalen Flammengeschwindigkeiten als Funktion charakteristischer Zeitmaße auszudrücken. Die Quantifizierung des Einflusses der instationären Streckung sowohl von laminaren als auch von turbulenten Flammen hat zur Entwicklung neuer Methoden zur Beschreibung der Flammendynamik geführt. Es wurde ein erweitertes Modell für die turbulente Flammengeschwindigkeit entwickelt, das auf der globalen Damköhler-Zahl basiert und die Vorhersage im Bereich der Damköhler-Zahlen nahe Eins verbessert. Die große Streuung der lokalen Flammengeschwindigkeiten, die gegen die lokale Flammenstreckung in turbulenten Flammen aufgetragen werden, wird durch den Memory-Effekt verursacht, da die momentanen Flammengeschwindigkeitswerte durch vorhergehende Flammenstreckungsraten bestimmt werden. Die Korrelation zwischen Flammengeschwindigkeit und Flammenstreckung wurde durch die Einführung einer Flammenrelaxationszeit entschlüsselt, die exponentiell von den lokalen Strömungszeitmaßen abhängt. Die lokalen Relaxationszeiten wurden durch Verfolgung der Zeitverläufe von materiellen Punkten auf der Flammenoberfläche mit der Flammenpartikelverfolgungsmethode bestimmt. Eine quasi-lineare Korrelation zwischen lokaler Flammengeschwindigkeit und Flammenstreckung in turbulenten Flammen kann durch die Berücksichtigung der neuen Flammenrelaxationszeit

wiederhergestellt werden, die im Bereich moderater Flammenstreckungen gültig ist. Erstmals konnte die Flammenumsatzgeschwindigkeit zusammen mit der Flammenpartikelverfolgungsmethode vollständig parallel ausgewertet werden, was durch den in dieser Arbeit neu entwickelten Verfolgungsalgorithmus ermöglicht wurde. Das neue Modell für die lokale Flammengeschwindigkeit basierend auf einer turbulenten Markstein-Zahl und den neu gefundenen lokalen Flammenrelaxationszeiten ermöglicht eine genauere Beschreibung der lokalen Flammendynamik für zukünftige Simulationen.

Appendix A

Scaling Laws for the Flame Speed

In section 2.2, results from thermal theory and the scaling laws for the laminar flame have been used. In this appendix, the scaling laws for flame speed are derived to give more context about their application.

The general balance equations for species mass fraction Y_k and temperature T for an ideal gas ($\left. \frac{\partial h_k}{\partial p} \right|_T = 0$) from continuum mechanics, assuming steady-state, are (compare also with section 3.1.1):

$$\underbrace{\frac{\partial \rho Y_k}{\partial t}}_{=0} + \nabla \cdot (\rho \vec{u} Y_k) = -\nabla \cdot \vec{j}_k + \dot{\omega}_k \quad (\text{A.1a})$$

$$\underbrace{c_p \frac{\partial \rho T}{\partial t}}_{=0} + c_p \nabla \cdot (\rho \vec{u} T) = -\nabla \cdot \vec{q} + \dot{q} + \underbrace{\frac{Dp}{Dt} + \sum_k \vec{f}_k \cdot \vec{j}_k}_{=0, \text{ assume no external forces and } p \approx \text{const}} + \underbrace{\underline{\underline{\tau}} : \nabla \vec{u}}_{\text{neglected}} + \underbrace{\sum_k h_{s,k} \nabla \cdot \vec{j}_k}_{\text{neglected for discussion}} \quad (\text{A.1b})$$

\vec{u} is the mass-averaged bulk fluid velocity, $\dot{\omega}_k$ the reaction rate of species k (in kg/m³/s), c_p the mass-specific isobaric heat capacity of the mixture, $\dot{q} =$

$-\sum_k h_k \dot{\omega}_k$ the heat release rate, h_k the mass-specific absolute enthalpy of species k , \vec{f}_k external forces (e.g. gravity, magnetic forces, ...), $\underline{\tau}$ the stress tensor, \dot{q}_{rad} heat transfer through radiation and $h_{s,k} = h_k - h_k^0$ the mass-specific sensible enthalpy of species k . Expressing the diffusion terms \vec{j}_k and \vec{q} with the Curtiss-Hirschfelder approximation for an ideal gas mixture yields:

$$\vec{j}_k = -\rho D_{m,k} \nabla Y_k - \underbrace{D_k^T \frac{1}{T} \nabla T}_{\text{neglected}} \quad (\text{A.2a})$$

$$\vec{q} = -\lambda \nabla T + \underbrace{\sum_k \vec{j}_k h_{s,k}}_{\text{neglected for discussion}} - \mathcal{R}T \underbrace{\sum_k \frac{D_k^T}{M_k} \left(\frac{1}{p} \nabla p + \frac{1}{\bar{M}} \nabla \bar{M} + \frac{1}{Y_k} \nabla Y_k \right)}_{\text{neglected}} \quad (\text{A.2b})$$

For a freely propagating one-dimensional planar, steady-state, constant pressure flame, the balance equations reduce with the simplifications introduced in the equations above to:

$$\rho u_x \frac{\partial Y_k}{\partial x} = \frac{\partial}{\partial x} \left(\rho D_k \frac{\partial Y_k}{\partial x} \right) + \dot{\omega}_k \quad (\text{A.3a})$$

$$\rho u_x \frac{\partial T}{\partial x} = \frac{1}{c_p} \frac{\partial}{\partial x} \left(\lambda \frac{\partial T}{\partial x} \right) + \frac{\dot{q}}{c_p} \quad (\text{A.3b})$$

Note that $\rho u_x \equiv \rho_0 s_{L,0} = \text{const}$ for this planar flame. In the following discussion, the species diffusion coefficients are simply denoted as D_k .

To derive scaling laws for the flame speed, Eq. (A.3a) or Eq. (A.3b) are integrated from $x = -\infty$ to $x = +\infty$:

$$\int_{-\infty}^{+\infty} \rho u_x \frac{\partial Y_k}{\partial x} dx = \int_{-\infty}^{+\infty} \frac{\partial}{\partial x} \left(\rho D_k \frac{\partial Y_k}{\partial x} \right) + \dot{\omega}_k dx \quad (\text{A.4})$$

$$\Rightarrow \rho_0 s_{L,0} [Y_k]_{-\infty}^{+\infty} = \cancel{\left[\rho D_k \frac{\partial Y_k}{\partial x} \right]_{-\infty}^{+\infty}} + \int_{-\infty}^{+\infty} \dot{\omega}_k dx \quad (\text{A.5})$$

$$\Rightarrow \rho_0 s_{L,0} (Y_{k,b} - Y_{k,0}) = \int_{-\infty}^{+\infty} \dot{\omega}_k dx \quad (\text{A.6})$$

$$\int_{-\infty}^{+\infty} \rho u_x \frac{\partial T}{\partial x} dx = \int_{-\infty}^{+\infty} \frac{1}{c_p} \frac{\partial}{\partial x} \left(\lambda \frac{\partial T}{\partial x} \right) + \frac{\dot{q}}{c_p} dx \quad (\text{A.7})$$

$$\Rightarrow \rho_0 s_{L,0} [T]_{-\infty}^{+\infty} = \frac{1}{\bar{c}_p} \left[\lambda \frac{\partial T}{\partial x} \right]_{-\infty}^{+\infty} + \int_{-\infty}^{+\infty} \frac{\dot{q}}{c_p} dx \quad (\text{A.8})$$

$$\Rightarrow \rho_0 s_{L,0} (T_b - T_0) = \int_{-\infty}^{+\infty} \frac{\dot{q}}{c_p} dx \quad (\text{A.9})$$

Here, the heat capacity c_p in the diffusion term is formally assumed to be a (constant) effective heat capacity \bar{c}_p . With this, the laminar flame speed, or consumption speed, becomes:

$$s_{L,0} \equiv \frac{1}{\rho_0 (Y_{k,b} - Y_{k,0})} \int_{-\infty}^{\infty} \dot{\omega}_k dx \quad (\text{A.10a})$$

$$s_{L,0} \approx \frac{1}{\rho_0 (T_b - T_0)} \int_{-\infty}^{\infty} \frac{\dot{q}}{c_p} dx \quad (\text{A.10b})$$

Equation (A.10a) is exact and does not contain any simplification for the steady-state 1D Cartesian flame setup, except for the exclusion of external forces and thermo-diffusion. Equation (A.10b) on the other hand contains a number of simplifications, like the assumed constant heat capacity and the neglected multi-component enthalpy flux in the $s_{L,0}$ definition from the energy equation in Eq. (A.1). Introducing $\Delta Y_k \equiv Y_{k,b} - Y_{k,0}$, $\Delta T \equiv T_b - T_0$, $\bar{\dot{\omega}}_k \Delta x \equiv \int_{-\infty}^{\infty} \dot{\omega}_k dx$, $\frac{\bar{\dot{q}}}{\bar{c}_p} \Delta x \equiv \int_{-\infty}^{\infty} \frac{\dot{q}}{c_p} dx$, where Δx is the flame thickness of the flame, Eq. (A.10a) and Eq. (A.10b) become:

$$\rho_0 s_{L,0} = \frac{\bar{\dot{\omega}}_k \Delta x}{\Delta Y_k} \quad (\text{A.11a})$$

$$\rho_0 s_{L,0} = \frac{\bar{\dot{q}} \Delta x}{\bar{c}_p \Delta T} \quad (\text{A.11b})$$

In a second step, Eq. (A.3a) or Eq. (A.3b) are integrated from $x = -\infty$ to $x = x_p$, where x_p is the position where the preheat zone ends and the reaction zone starts. It is assumed that there are no chemical reactions in the preheat zone:

$$\rho_0 s_{L,0} \int_{-\infty}^{x_p} \frac{\partial Y_k}{\partial x} dx = \int_{-\infty}^{x_p} \left(\frac{\partial}{\partial x} \left(\rho D_k \frac{\partial Y_k}{\partial x} \right) + \dot{\omega}_k \right) dx \quad (\text{A.12})$$

$$\rho_0 s_{L,0} \int_{-\infty}^{x_p} \frac{\partial T}{\partial x} dx = \int_{-\infty}^{x_p} \left(\frac{1}{c_p} \frac{\partial}{\partial x} \left(\lambda \frac{\partial T}{\partial x} \right) + \frac{\dot{q}}{c_p} \right) dx \quad (\text{A.13})$$

The integrals for the species equations can be evaluated as

$$\int_{-\infty}^{x_p} \frac{\partial Y_k}{\partial x} dx = Y_k(x = x_p) - Y_k(x = -\infty) \equiv \Delta_{x_p} Y_k \quad (\text{A.14})$$

and

$$\int_{-\infty}^{x_p} \frac{\partial}{\partial x} \left(\rho D_k \frac{\partial Y_k}{\partial x} \right) dx = \rho D_k \frac{\partial Y_k}{\partial x} \Big|_{x=x_p} - \underbrace{\rho D_k \frac{\partial Y_k}{\partial x}}_{=0} \Big|_{x=-\infty} = \rho D_k \frac{\partial Y_k}{\partial x} \Big|_{x=x_p} \quad (\text{A.15})$$

Linearizing the equation with $\frac{\partial Y_k}{\partial x} \approx \frac{\Delta Y_k}{\Delta x_p}$, where Δx_p is the thickness of the preheat zone, introducing the ratio $c = \frac{\Delta x}{\Delta x_p}$ of the preheat zone thickness to the total flame thickness and using a representative value for the heat capacity \bar{c}_p yields:

$$\rho_0 s_{L,0} \Delta_{x_p} Y_k = \rho D_k \frac{\partial Y_k}{\partial x} \Big|_{x=x_p} \quad (\text{A.16}) \quad \left| \quad \rho_0 s_{L,0} \Delta_{x_p} T = \frac{1}{\bar{c}_p} \lambda \frac{\partial T}{\partial x} \Big|_{x=x_p} \quad (\text{A.17}) \right.$$

$$\rho_0 s_{L,0} \Delta_{x_p} Y_k = \rho_{x_p} D_{k,x_p} \frac{\Delta_{x_p} Y_k}{c \Delta x} \quad (\text{A.18}) \quad \left| \quad \rho_0 s_{L,0} \Delta_{x_p} T = \frac{1}{\bar{c}_p} \lambda_{x_p} \frac{\Delta_{x_p} T}{c \Delta x} \quad (\text{A.19}) \right.$$

where the density and transport coefficients on the right hand side are evaluated at $x = x_p$. The results from the second step can be summarized as:

$$\rho_0 s_{L,0} = \frac{\rho_{x_p} D_{k,x_p}}{c \Delta x} \quad (\text{A.20a})$$

$$\rho_0 s_{L,0} = \frac{\lambda_{x_p}}{\bar{c}_p c \Delta x} \quad (\text{A.20b})$$

Combining Eq. (A.11a) and Eq. (A.20a) or Eq. (A.11b) and Eq. (A.20b) and dropping the overbar notation as well as dropping the notation specifying where density and transport coefficients are evaluated (which is another simplification) yields:

$$\left. \begin{aligned} \frac{\dot{\omega}_k \Delta x}{\Delta Y_k} &= \frac{\rho D_k}{c \Delta x} & (\text{A.21a}) \\ \Rightarrow \Delta x^2 &= \frac{\Delta Y_k \rho D_k}{c \dot{\omega}_k} & (\text{A.21b}) \end{aligned} \right| \begin{aligned} \frac{\dot{q} \Delta x}{c_p \Delta T} &= \frac{\lambda}{c_p c \Delta x} & (\text{A.22a}) \\ \Rightarrow \Delta x^2 &= \frac{\Delta T \lambda}{c \dot{q}} & (\text{A.22b}) \end{aligned}$$

Assuming that the ratio of preheat zone thickness to total flame thickness stays approximately constant, the first set of scaling laws, relating the flame thickness to the transport coefficients, density and chemical source terms can be derived:

$$\Delta x = \Delta Y_k^{\frac{1}{2}} \rho^{\frac{1}{2}} D_k^{\frac{1}{2}} \dot{\omega}_k^{-\frac{1}{2}} \quad (\text{A.23a})$$

$$\Delta x = \Delta T^{\frac{1}{2}} \lambda^{\frac{1}{2}} \dot{q}^{-\frac{1}{2}} \quad (\text{A.23b})$$

Substituting Eq. (A.23a) and Eq. (A.23b) back into Eq. (A.20a) and Eq. (A.20b) yields:

$$s_{L,0} = \rho_0^{-1} \Delta Y_k^{-\frac{1}{2}} (\rho D_k)^{\frac{1}{2}} \dot{\omega}_k^{\frac{1}{2}} \quad (\text{A.24a})$$

$$s_{L,0} = \rho_0^{-1} c_p^{-1} \Delta T^{-\frac{1}{2}} \lambda^{\frac{1}{2}} \dot{q}^{\frac{1}{2}} \quad (\text{A.24b})$$

The classical result from thermal theory can be recovered from Eq. (A.24b). The heat release rate \dot{q} (W/m³) is defined as $\dot{q} \equiv -\sum h_k \dot{\omega}_k$, where h_k are the (absolute) mass specific pure species enthalpies (assuming perfect mixture). Simplifying this to $-\sum h_k \dot{\omega}_k \approx \bar{h} \bar{\omega}$, where \bar{h} is a representative enthalpy and $\bar{\omega}$ a representative reaction rate, approximating $\bar{h} \approx \bar{c}_p \Delta T$ and dropping the overbar notation, Eq. (A.24b) yields:

$$s_{L,0} \approx \rho_0^{-1} c_p^{-1} \Delta T^{-\frac{1}{2}} \lambda^{\frac{1}{2}} (c_p \Delta T \dot{\omega})^{\frac{1}{2}} \quad (\text{A.25})$$

Using a reaction time scale $\hat{\omega} \equiv \dot{\omega}/\rho_0$ (s⁻¹), one obtains:

$$s_{L,0} = \sqrt{\frac{\lambda}{\rho_0 c_p} \hat{\omega}} = \sqrt{a \hat{\omega}} \quad (\text{A.26})$$

where $a = \lambda/(\rho_0 c_p)$ is the thermal diffusivity.

To find the dependence of $s_{L,0}$ on pressure, it is assumed that the adiabatic flame temperature $T_{\text{ad}} = T_b$ stays approximately constant for varying pressure at the same T_0 . Therefore, the pressure dependence of ΔT can be neglected. Similarly, the composition of the burnt gas is approximately constant for varying pressure, so that the pressure dependence of ΔY_k is negligible, too. Lastly, for an ideal gas, the heat capacity is not a function of pressure but only temperature and gas composition. Therefore, the pressure dependence of c_p in the scaling laws will

be omitted as well. Finally, in terms of pressure dependence, the laminar flame speed scales with

$$s_{L,0} \stackrel{\text{pressure dep.}}{\propto} \rho_0^{-1} (\rho D_k)^{\frac{1}{2}} \dot{\omega}_k^{\frac{1}{2}} \quad (\text{A.27a})$$

$$s_{L,0} \stackrel{\text{pressure dep.}}{\propto} \rho_0^{-1} \lambda^{\frac{1}{2}} \dot{q}^{\frac{1}{2}} \quad (\text{A.27b})$$

The mass diffusion coefficient D_k for an ideal gas depends inversely proportional on pressure and heat conductivity is independent of pressure. The pressure dependence of the reaction rates or heat release rate can be expressed with the overall reaction order n ($\dot{q} \propto p^n$). Using these assumptions, the pressure dependence of $s_{L,0}$ can be expressed as:

$$\left. \begin{aligned}
 s_{L,0} &\propto \underbrace{\rho_0^{-1}}_{p^{-1}} \underbrace{\dot{q}^{\frac{1}{2}}}_{(p^n)^{\frac{1}{2}}} \underbrace{\lambda^{\frac{1}{2}}}_{\neq f(p)} \\
 s_{L,0} &\propto \underbrace{\rho_0^{-1}}_{p^{-1}} \underbrace{\dot{\omega}_k^{\frac{1}{2}}}_{(p^n)^{\frac{1}{2}}} \underbrace{(\rho D_k)^{\frac{1}{2}}}_{\neq f(p)}
 \end{aligned} \right\} \begin{aligned}
 &\text{pressure dependence} \\
 &\text{from density} \\
 &\propto \underbrace{p^{-1}}_{\text{pressure dependence}} \underbrace{p^{\frac{1}{2}n}}_{\text{from chemistry}} = p^{\frac{1}{2}n-1}
 \end{aligned} \quad (\text{A.28})$$

Appendix B

Tensor Notation and Conventions

B.1 OpenFOAM®'s Notation

The mathematical description of flame stretch in section 2.3 relies on tensor notation. However, there are different conventions for tensor calculus. The tensor notation and conventions used in this work follow the one from OpenFOAM®. Because of this, the mathematical notation is presented together with examples analogous to OpenFOAM®'s C++ syntax in this appendix.

Vectors in OpenFOAM® are always column vectors. They are expressed in vector notation as

$$\vec{v} = \begin{pmatrix} v_1 \\ v_2 \\ v_3 \end{pmatrix} \quad (\text{B.1})$$

or in tensor notation as

$$v_i = \begin{pmatrix} v_{i=1} \\ v_{i=2} \\ v_{i=3} \end{pmatrix} \quad (\text{B.2})$$

The convention for naming the entries of tensors is expressed as

$$\underline{\underline{\mathbf{T}}} = \begin{pmatrix} T_{xx} & T_{xy} & T_{xz} \\ T_{yx} & T_{yy} & T_{yz} \\ T_{zx} & T_{zy} & T_{zz} \end{pmatrix} \quad (\text{B.3})$$

or in tensor notation

$$T_{i,j} = \begin{pmatrix} T_{i=1,j=1} & T_{i=1,j=2} & T_{i=1,j=3} \\ T_{i=2,j=1} & T_{i=2,j=2} & T_{i=2,j=3} \\ T_{i=3,j=1} & T_{i=3,j=2} & T_{i=3,j=3} \end{pmatrix} \quad (\text{B.4})$$

A more verbose notation specifies explicitly which index in tensor notation corresponds to rows and columns. For example, the tensor $\underline{\underline{\mathbf{T}}} = T_{i,j}$ or $T_{i,j}$ can be transposed $\underline{\underline{\mathbf{T}}}^T$. In tensor notation, this can be expressed as $(T_{j,i})_{i,j}$, where the indices at the parenthesis show which variables denote the rows and columns. Likewise, the tensor $\underline{\underline{\mathbf{T}}}$ itself could be written as $(T_{i,j})_{i,j}$, but this verbose notation is usually dropped.

B.1.1 Dyadic Product

The outer product of two vectors is commonly known as the dyadic product. The result is a tensor. The symbol for dyadic product \otimes is usually omitted. For example, the outer product of the vectors \vec{u} and \vec{v} can be written as:

$$\vec{u}\vec{v} = \vec{u} \otimes \vec{v} = \vec{u}\vec{v}^T = \begin{pmatrix} u_1 \\ u_2 \\ u_3 \end{pmatrix} \begin{pmatrix} v_1 & v_2 & v_3 \end{pmatrix} = \begin{pmatrix} u_1v_1 & u_1v_2 & u_1v_3 \\ u_2v_1 & u_2v_2 & u_2v_3 \\ u_3v_1 & u_3v_2 & u_3v_3 \end{pmatrix} \quad (\text{B.5})$$

or

$$(u_iv_j)_{i,j} = T_{ij} \quad (\text{B.6})$$

B.1.2 Dot Product

The inner product between tensors and/or vectors is also known as the dot product. The dot product between two vectors is a scalar and can be written in either vector, tensor or component notation as:

$$\vec{v} \cdot \vec{u} = \vec{v}^T \vec{u} = \begin{pmatrix} v_1 & v_2 & v_3 \end{pmatrix} \begin{pmatrix} u_1 \\ u_2 \\ u_3 \end{pmatrix} = v_i u_i = v_x u_x + v_y u_y + v_z u_z \quad (\text{B.7})$$

For the special case that $\vec{v} = \vec{u}$, this inner product is related to the magnitude of the vector:

$$\text{mag}(\vec{u}) = |\vec{u}| = \sqrt{\vec{u} \cdot \vec{u}} = \sqrt{u_i u_i} = \sqrt{u_x u_x + u_y u_y + u_z u_z} \quad (\text{B.8})$$

$$\text{magSqr}(\vec{u}) = |\vec{u}|^2 = \vec{u} \cdot \vec{u} = u_i u_i = u_x u_x + u_y u_y + u_z u_z \quad (\text{B.9})$$

mag and magSqr are the names of the corresponding functions in OpenFOAM®.

The inner product between two tensors results in a tensor. The convention followed by OpenFOAM® is:

$$\begin{aligned} \underline{\underline{\mathbf{T}}} \cdot \underline{\underline{\mathbf{S}}} &= (T_{ki} S_{il})_{k,l} \quad (\text{B.10}) \\ &= \begin{pmatrix} (T_{xx} S_{xx} + T_{xy} S_{yx} + T_{xz} S_{zx}) & (T_{xx} S_{xy} + T_{xy} S_{yy} + T_{xz} S_{zy}) & (T_{xx} S_{xz} + T_{xy} S_{yz} + T_{xz} S_{zz}) \\ (T_{yx} S_{xx} + T_{yy} S_{yx} + T_{yz} S_{zx}) & (T_{yx} S_{xy} + T_{yy} S_{yy} + T_{yz} S_{zy}) & (T_{yx} S_{xz} + T_{yy} S_{yz} + T_{yz} S_{zz}) \\ (T_{zx} S_{xx} + T_{zy} S_{yx} + T_{zz} S_{zx}) & (T_{zx} S_{xy} + T_{zy} S_{yy} + T_{zz} S_{zy}) & (T_{zx} S_{xz} + T_{zy} S_{yz} + T_{zz} S_{zz}) \end{pmatrix} \end{aligned}$$

The inner product of a tensor and a vector results in a vector:

$$\underline{\underline{\mathbf{T}}} \cdot \vec{v} = \underline{\underline{\mathbf{T}}} \vec{v} = \begin{pmatrix} T_{1,1} v_1 + T_{1,2} v_2 + T_{1,3} v_3 \\ T_{2,1} v_1 + T_{2,2} v_2 + T_{2,3} v_3 \\ T_{3,1} v_1 + T_{3,2} v_2 + T_{3,3} v_3 \end{pmatrix} = (T_{j,i})_{i,j} v_i = v_i T_{j,i} = T_{i,j} v_j \quad (\text{B.11})$$

The inner product of a vector with a tensor also results in a vector:

$$\begin{aligned} \vec{v} \cdot \underline{\underline{\mathbf{T}}} &= (\vec{v}^T \underline{\underline{\mathbf{T}}})^T = \underline{\underline{\mathbf{T}}}^T \vec{v} = \underline{\underline{\mathbf{T}}}^T \cdot \vec{v} = \begin{pmatrix} v_1 T_{1,1} + v_2 T_{2,1} + v_3 T_{3,1} \\ v_1 T_{1,2} + v_2 T_{2,2} + v_3 T_{3,2} \\ v_1 T_{1,3} + v_2 T_{2,3} + v_3 T_{3,3} \end{pmatrix} \\ &= v_i (T_{i,j})_{i,j} = v_i T_{i,j} \quad (\text{B.12}) \end{aligned}$$

As indicated above, the order of operation matters. The identities are:

$$\vec{v} \cdot \underline{\underline{\mathbf{T}}}^\top = \underline{\underline{\mathbf{T}}} \cdot \vec{v}, \quad \underline{\underline{\mathbf{T}}}^\top \cdot \vec{v} = \vec{v} \cdot \underline{\underline{\mathbf{T}}} \quad (\text{B.13})$$

Therefore, if $\underline{\underline{\mathbf{T}}}$ is symmetric, it follows that

$$\vec{v} \cdot \underline{\underline{\mathbf{T}}}^{\text{symm}} = \underline{\underline{\mathbf{T}}}^{\text{symm}} \cdot \vec{v} \quad (\text{B.14})$$

Another useful identity involving the dyadic product is:

$$(\vec{v}\vec{u}) \vec{w} = (\vec{v} \otimes \vec{u}) \vec{w} = (\vec{v}\vec{u}^\top) \vec{w} = (\vec{v}\vec{u}^\top) \cdot \vec{w} = \vec{v} (\vec{u} \cdot \vec{w}) = v_i u_j w_j \quad (\text{B.15})$$

B.1.3 Double Dot Product

The double dot product between two tensors results in a scalar:

$$\begin{aligned} \underline{\underline{\mathbf{T}}} : \underline{\underline{\mathbf{S}}} &= T_{ij} S_{ij} = \sum_i \sum_j T_{ij} S_{ij} = T_{xx} S_{xx} + T_{xy} S_{xy} + T_{xz} S_{xz} + T_{yx} S_{yx} \\ &\quad + T_{yy} S_{yy} + T_{yz} S_{yz} + T_{zx} S_{zx} + T_{zy} S_{zy} + T_{zz} S_{zz} \end{aligned} \quad (\text{B.16})$$

B.1.4 Other Tensor Operations

OpenFOAM® defines a number of additional tensor operations. They include the trace of a tensor:

$$\text{tr}(\underline{\underline{\mathbf{T}}}) = \text{tr}(\underline{\underline{\mathbf{T}}}^\top) = \underline{\underline{\mathbf{T}}} : \underline{\underline{\mathbf{I}}} = T_{ij} \delta_{ij} = T_{ii} = T_{xx} + T_{yy} + T_{zz} \quad (\text{B.17})$$

The symmetric part of a tensor:

$$\text{symm}(\underline{\underline{\mathbf{T}}}) = \frac{1}{2}(\underline{\underline{\mathbf{T}}} + \underline{\underline{\mathbf{T}}}^\top) = \frac{1}{2} \begin{pmatrix} 2T_{xx} & T_{xy} + T_{yx} & T_{xz} + T_{zx} \\ T_{xy} + T_{yx} & 2T_{yy} & T_{yz} + T_{zy} \\ T_{xz} + T_{zx} & T_{zy} + T_{yz} & 2T_{zz} \end{pmatrix} \quad (\text{B.18})$$

Two times the symmetric part of a tensor:

$$\begin{aligned} \text{twoSymm}(\underline{\underline{\mathbf{T}}}) &= 2\text{symm}(\underline{\underline{\mathbf{T}}}) \\ &= (\underline{\underline{\mathbf{T}}} + \underline{\underline{\mathbf{T}}}^\top) = \begin{pmatrix} 2T_{xx} & T_{xy} + T_{yx} & T_{xz} + T_{zx} \\ T_{xy} + T_{yx} & 2T_{yy} & T_{yz} + T_{zy} \\ T_{xz} + T_{zx} & T_{zy} + T_{yz} & 2T_{zz} \end{pmatrix} \end{aligned} \quad (\text{B.19})$$

The skew-symmetric part of a tensor:

$$\text{skew}(\underline{\underline{\mathbf{T}}}) = \frac{1}{2}(\underline{\underline{\mathbf{T}}} - \underline{\underline{\mathbf{T}}}^\top) = \frac{1}{2} \begin{pmatrix} 0 & T_{xy} - T_{yx} & T_{xz} - T_{zx} \\ T_{yx} - T_{xy} & 0 & T_{yz} - T_{zy} \\ T_{zx} - T_{xz} & T_{zy} - T_{yz} & 0 \end{pmatrix} \quad (\text{B.20})$$

Symmetric and skew-symmetric parts of a tensor are connected by:

$$\underline{\underline{\mathbf{T}}} = \text{symm}(\underline{\underline{\mathbf{T}}}) + \text{skew}(\underline{\underline{\mathbf{T}}}) \quad (\text{B.21})$$

The spherical part of a tensor:

$$\begin{aligned} \text{sph}(\underline{\underline{\mathbf{T}}}) &= \frac{1}{3}(\underline{\underline{\mathbf{T}}} : \underline{\underline{\mathbf{I}}})\underline{\underline{\mathbf{I}}} = \frac{1}{3}\text{tr}(\underline{\underline{\mathbf{T}}})\underline{\underline{\mathbf{I}}} \\ &= \frac{1}{3} \begin{pmatrix} T_{xx} + T_{yy} + T_{zz} & 0 & 0 \\ 0 & T_{xx} + T_{yy} + T_{zz} & 0 \\ 0 & 0 & T_{xx} + T_{yy} + T_{zz} \end{pmatrix} \end{aligned} \quad (\text{B.22})$$

where $\underline{\underline{\mathbf{I}}}$ is the unit tensor. The deviatoric part of a tensor is:

$$\begin{aligned} \text{dev}(\underline{\underline{\mathbf{T}}}) &= \underline{\underline{\mathbf{T}}} - \text{sph}(\underline{\underline{\mathbf{T}}}) = \underline{\underline{\mathbf{T}}} - \frac{1}{3}(\underline{\underline{\mathbf{T}}} : \underline{\underline{\mathbf{I}}})\underline{\underline{\mathbf{I}}} = \underline{\underline{\mathbf{T}}} - \frac{1}{3}\text{tr}(\underline{\underline{\mathbf{T}}})\underline{\underline{\mathbf{I}}} \\ &= \begin{pmatrix} T_{xx} - \frac{1}{3}(T_{xx} + T_{yy} + T_{zz}) & T_{xy} & T_{xz} \\ T_{yx} & T_{yy} - \frac{1}{3}(T_{xx} + T_{yy} + T_{zz}) & T_{yz} \\ T_{zx} & T_{zy} & T_{zz} - \frac{1}{3}(T_{xx} + T_{yy} + T_{zz}) \end{pmatrix} \end{aligned} \quad (\text{B.23})$$

Spherical and deviatoric part are connected by:

$$\underline{\underline{\mathbf{T}}} = \text{sph}(\underline{\underline{\mathbf{T}}}) + \text{dev}(\underline{\underline{\mathbf{T}}}) \quad (\text{B.24})$$

OpenFOAM® also defines a variant of the deviatoric part of a tensor as a separate function, which for example is used in the computation of the diffusive momentum flux:

$$\begin{aligned} \text{dev2}(\underline{\underline{\mathbf{T}}}) &= \underline{\underline{\mathbf{T}}} - 2\text{sph}(\underline{\underline{\mathbf{T}}}) = \underline{\underline{\mathbf{T}}} - \frac{2}{3}(\underline{\underline{\mathbf{T}}} : \underline{\underline{\mathbf{I}}})\underline{\underline{\mathbf{I}}} = \underline{\underline{\mathbf{T}}} - \frac{2}{3}\text{tr}(\underline{\underline{\mathbf{T}}})\underline{\underline{\mathbf{I}}} \\ &= \begin{pmatrix} T_{xx} - \frac{2}{3}(T_{xx} + T_{yy} + T_{zz}) & T_{xy} & T_{xz} \\ T_{yx} & T_{yy} - \frac{2}{3}(T_{xx} + T_{yy} + T_{zz}) & T_{yz} \\ T_{zx} & T_{zy} & T_{zz} - \frac{2}{3}(T_{xx} + T_{yy} + T_{zz}) \end{pmatrix} \end{aligned} \quad (\text{B.25})$$

The magnitude of a tensor can be expressed by the double dot product with itself:

$$|\underline{\mathbf{T}}|^2 = \text{magSq}(\underline{\mathbf{T}}) = \underline{\mathbf{T}} : \underline{\mathbf{T}} = T_{ij}T_{ij} = T_{xx}T_{xx} + T_{xy}T_{xy} + T_{xz}T_{xz} \\ + T_{yx}T_{yx} + T_{yy}T_{yy} + T_{yz}T_{yz} + T_{zx}T_{zx} + T_{zy}T_{zy} + T_{zz}T_{zz} \quad (\text{B.26})$$

$$|\underline{\mathbf{T}}| = \text{mag}(\underline{\mathbf{T}}) = \sqrt{\underline{\mathbf{T}} : \underline{\mathbf{T}}} = \sqrt{T_{ij}T_{ij}} \quad (\text{B.27})$$

B.2 Calculus Operators

B.2.1 Gradient

The gradient operator can formally be written as:

$$\nabla = \begin{pmatrix} \frac{\partial}{\partial x_1} \\ \frac{\partial}{\partial x_2} \\ \frac{\partial}{\partial x_3} \end{pmatrix} = \frac{\partial}{\partial x_i} \quad (\text{B.28})$$

Applied to a scalar s , the result is a vector:

$$\nabla s = \begin{pmatrix} \frac{\partial}{\partial x_1} \\ \frac{\partial}{\partial x_2} \\ \frac{\partial}{\partial x_3} \end{pmatrix} s = \begin{pmatrix} \frac{\partial s}{\partial x_1} \\ \frac{\partial s}{\partial x_2} \\ \frac{\partial s}{\partial x_3} \end{pmatrix} \quad (\text{B.29})$$

When applied to a vector, the result is a tensor:

$$\nabla \vec{u} = \nabla \otimes \vec{u} = \nabla (\vec{u}^T) = \begin{pmatrix} \frac{\partial}{\partial x_1} \\ \frac{\partial}{\partial x_2} \\ \frac{\partial}{\partial x_3} \end{pmatrix} \begin{pmatrix} u_1 & u_2 & u_3 \end{pmatrix} = \begin{pmatrix} \frac{\partial u_1}{\partial x_1} & \frac{\partial u_2}{\partial x_1} & \frac{\partial u_3}{\partial x_1} \\ \frac{\partial u_1}{\partial x_2} & \frac{\partial u_2}{\partial x_2} & \frac{\partial u_3}{\partial x_2} \\ \frac{\partial u_1}{\partial x_3} & \frac{\partial u_2}{\partial x_3} & \frac{\partial u_3}{\partial x_3} \end{pmatrix} \quad (\text{B.30})$$

or in tensor notation:

$$\nabla \vec{u} \equiv \left(\frac{\partial u_j}{\partial x_i} \right)_{i,j} = T_{ij} \quad (\text{B.31})$$

B.2.2 Divergence

The divergence of a vector is a scalar:

$$\begin{aligned}\nabla \cdot \vec{u} &= \nabla^T \vec{u} = \begin{pmatrix} \frac{\partial}{\partial x_1} & \frac{\partial}{\partial x_2} & \frac{\partial}{\partial x_3} \end{pmatrix} \begin{pmatrix} u_1 \\ u_2 \\ u_3 \end{pmatrix} \\ &= \text{tr}(\nabla \vec{u}) = \frac{\partial}{\partial x_i} u_i = \frac{\partial u_1}{\partial x_1} + \frac{\partial u_2}{\partial x_2} + \frac{\partial u_3}{\partial x_3}\end{aligned}\quad (\text{B.32})$$

Following Eq. (B.12) and setting \vec{v} informally to ∇ , the divergence of a tensor results in:

$$\nabla \cdot \underline{\underline{\mathbf{T}}} = \frac{\partial}{\partial x_i} T_{ij} = \begin{pmatrix} \frac{\partial}{\partial x_1} T_{1,1} + \frac{\partial}{\partial x_2} T_{2,1} + \frac{\partial}{\partial x_3} T_{3,1} \\ \frac{\partial}{\partial x_1} T_{1,2} + \frac{\partial}{\partial x_2} T_{2,2} + \frac{\partial}{\partial x_3} T_{3,2} \\ \frac{\partial}{\partial x_1} T_{1,3} + \frac{\partial}{\partial x_2} T_{2,3} + \frac{\partial}{\partial x_3} T_{3,3} \end{pmatrix}\quad (\text{B.33})$$

Note that

$$\nabla \cdot \underline{\underline{\mathbf{T}}} \neq \nabla \cdot \underline{\underline{\mathbf{T}}}^T\quad (\text{B.34})$$

B.2.3 Curl

The curl of a vector is computed in OpenFOAM® through the following expression:

$$\begin{aligned}\nabla \times \vec{u} &= 2(*(\text{skew}(\nabla \vec{u}))) = *(\nabla \vec{u} - (\nabla \vec{u})^T) \\ &= * \begin{pmatrix} \frac{\partial u_j}{\partial x_i} - \frac{\partial u_i}{\partial x_j} \end{pmatrix} = *T_{ij} = *\underline{\underline{\mathbf{T}}}\end{aligned}\quad (\text{B.35})$$

where $*$ is the Hodge dual:

$$*\underline{\underline{\mathbf{T}}} \equiv \begin{pmatrix} T_{yz} \\ -T_{xz} \\ T_{xy} \end{pmatrix}\quad (\text{B.36})$$

with this, the expression above becomes:

$$\nabla \times \vec{u} = *(\nabla \vec{u} - (\nabla \vec{u})^T) = \begin{pmatrix} \frac{\partial u_z}{\partial y} - \frac{\partial u_y}{\partial z} \\ -\frac{\partial u_z}{\partial x} + \frac{\partial u_x}{\partial z} \\ \frac{\partial u_y}{\partial x} - \frac{\partial u_x}{\partial y} \end{pmatrix}\quad (\text{B.37})$$

Or, using a different definition:

$$\vec{u} \times \vec{v} \equiv \begin{pmatrix} u_y v_z - u_z v_y \\ u_z v_x - u_x v_z \\ u_x v_y - u_y v_x \end{pmatrix} \rightarrow \nabla \times \vec{u} = \begin{pmatrix} \frac{\partial}{\partial x} \\ \frac{\partial}{\partial y} \\ \frac{\partial}{\partial z} \end{pmatrix} \times \begin{pmatrix} u_x \\ u_y \\ u_z \end{pmatrix} = \begin{pmatrix} \frac{\partial u_z}{\partial y} - \frac{\partial u_y}{\partial z} \\ -\frac{\partial u_z}{\partial x} + \frac{\partial u_x}{\partial z} \\ \frac{\partial u_y}{\partial x} - \frac{\partial u_x}{\partial y} \end{pmatrix} \quad (\text{B.38})$$

B.2.4 Special Cases

Mixing tensor and vector expressions requires that the notation given above is strictly followed as different conventions exist. Some useful examples are:

$$\begin{aligned} \vec{u} \cdot \nabla \vec{v} &\equiv \vec{u} \cdot (\nabla \vec{v}) = \begin{pmatrix} u_1 \\ u_2 \\ u_3 \end{pmatrix} \cdot \begin{pmatrix} \frac{\partial v_1}{\partial x_1} & \frac{\partial v_2}{\partial x_1} & \frac{\partial v_3}{\partial x_1} \\ \frac{\partial v_1}{\partial x_2} & \frac{\partial v_2}{\partial x_2} & \frac{\partial v_3}{\partial x_2} \\ \frac{\partial v_1}{\partial x_3} & \frac{\partial v_2}{\partial x_3} & \frac{\partial v_3}{\partial x_3} \end{pmatrix} \\ &= \begin{pmatrix} u_1 \frac{\partial v_1}{\partial x_1} + u_2 \frac{\partial v_1}{\partial x_2} + u_3 \frac{\partial v_1}{\partial x_3} \\ u_1 \frac{\partial v_2}{\partial x_1} + u_2 \frac{\partial v_2}{\partial x_2} + u_3 \frac{\partial v_2}{\partial x_3} \\ u_1 \frac{\partial v_3}{\partial x_1} + u_2 \frac{\partial v_3}{\partial x_2} + u_3 \frac{\partial v_3}{\partial x_3} \end{pmatrix} \end{aligned} \quad (\text{B.39})$$

or

$$\vec{u} \cdot \nabla \vec{v} = u_i \frac{\partial}{\partial x_i} v_j \quad (\text{B.40})$$

The gradient of the dot product of two vectors is:

$$\nabla(\vec{u} \cdot \vec{v}) = \nabla(u_1 v_1 + u_2 v_2 + u_3 v_3) = \begin{pmatrix} \frac{\partial(u_1 v_1 + u_2 v_2 + u_3 v_3)}{\partial x_1} \\ \frac{\partial(u_1 v_1 + u_2 v_2 + u_3 v_3)}{\partial x_2} \\ \frac{\partial(u_1 v_1 + u_2 v_2 + u_3 v_3)}{\partial x_3} \end{pmatrix} = \frac{\partial}{\partial x_j} u_i v_i \quad (\text{B.41})$$

Using a vector identity, this can be rewritten as:

$$\nabla(\vec{u} \cdot \vec{v}) = \vec{u} \cdot \nabla \vec{v} + \vec{v} \cdot \nabla \vec{u} + \vec{u} \times (\nabla \times \vec{v}) + \vec{v} \times (\nabla \times \vec{u}) \quad (\text{B.42})$$

where the notation assumes that $\vec{u} \times (\nabla \times \vec{v}) \equiv \vec{u} \times \nabla \times \vec{v}$. With this, an equivalent expression can be derived:

$$\nabla(\vec{u} \cdot \vec{v}) = \vec{u} \cdot (\nabla \vec{v})^\top + \vec{v} \cdot (\nabla \vec{u})^\top \quad (\text{B.43})$$

$$= (\nabla \vec{v}) \cdot \vec{u} + (\nabla \vec{u}) \cdot \vec{v} = u_i \frac{\partial v_i}{\partial x_j} + v_i \frac{\partial u_i}{\partial x_j} = \frac{\partial}{\partial x_j} u_i v_i \quad (\text{B.44})$$

Table B.1: Notation used by OpenFOAM® on the left compared to the numerator convention. The two expressions in each row are mathematically the same, as shown by the tensor notation, but the expression written in vector notation is different. For example, the two terms shown in green have a different meaning depending on which notation is used. In this work, the OpenFOAM® notation on the left is always used.

OpenFOAM®	Numerator layout
$\vec{u} \cdot \nabla \vec{v} \equiv \vec{u} \cdot (\nabla \vec{v}) = u_i \frac{\partial}{\partial x_i} v_j$	$(\vec{u} \cdot \nabla) \vec{v} = u_i \frac{\partial}{\partial x_i} v_j$
$\vec{u} \cdot (\nabla \vec{v})^\top = u_i \frac{\partial}{\partial x_j} v_i$	$\vec{u} \cdot \nabla \vec{v} = u_i \frac{\partial}{\partial x_j} v_i$

The second term from the above equation is expressed in component notation as:

$$\vec{u} \cdot (\nabla \vec{v})^\top = (\nabla \vec{v}) \cdot \vec{u} = u_i \frac{\partial}{\partial x_j} v_i = \begin{pmatrix} u_1 \frac{\partial v_1}{\partial x_1} + u_2 \frac{\partial v_2}{\partial x_1} + u_3 \frac{\partial v_3}{\partial x_1} \\ u_1 \frac{\partial v_1}{\partial x_2} + u_2 \frac{\partial v_2}{\partial x_2} + u_3 \frac{\partial v_3}{\partial x_2} \\ u_1 \frac{\partial v_1}{\partial x_3} + u_2 \frac{\partial v_2}{\partial x_3} + u_3 \frac{\partial v_3}{\partial x_3} \end{pmatrix} \quad (\text{B.45})$$

Note that the placement of parentheses is not arbitrary. The notation used in the code of OpenFOAM® and in this thesis differs from other conventions found in the literature. For example, some authors prefer to differentiate the gradient and the Jacobian matrix as [215]

$$\text{grad } \vec{u} \equiv (\nabla \vec{u})^\top \quad (\text{B.46})$$

Other authors use the nabla symbol (∇) to denote either *numerator layout* or *denominator layout* [216], where the notation in this work corresponds to the denominator convention. Because of this, different identities can be found in the literature, see Table B.1 for an example.

B.3 Identities

A list of commonly used identities is given below.

$$\text{symm}(\underline{\underline{\mathbf{T}}}) = (\text{symm}(\underline{\underline{\mathbf{T}}}))^\top \quad (\text{B.47})$$

$$\text{skew}(\underline{\underline{\mathbf{T}}}) = -(\text{skew}(\underline{\underline{\mathbf{T}}}))^\top \quad (\text{B.48})$$

$$\text{tr}(\text{sph}(\underline{\underline{\mathbf{T}}})) = \text{tr}(\underline{\underline{\mathbf{T}}}) \quad (\text{B.49})$$

$$\text{tr}(\text{dev}(\underline{\underline{\mathbf{T}}})) = 0 \quad (\text{B.50})$$

$$\text{tr}(\underline{\underline{\mathbf{T}}}) = \text{tr}(\underline{\underline{\mathbf{T}}}^\top) = \underline{\underline{\mathbf{T}}} : \underline{\underline{\mathbf{I}}} = T_{ii} \quad (\text{B.51})$$

$$\text{tr}(\underline{\underline{\mathbf{T}}} \cdot \underline{\underline{\mathbf{S}}}) = \text{tr}(\underline{\underline{\mathbf{S}}} \cdot \underline{\underline{\mathbf{T}}}) = \text{tr}(\underline{\underline{\mathbf{T}}}^\top \cdot \underline{\underline{\mathbf{S}}}^\top) \quad (\text{B.52})$$

$$\text{tr}(\vec{u} \otimes \vec{v}) = (\vec{u} \otimes \vec{v}) : \underline{\underline{\mathbf{I}}} = \vec{u} \cdot \vec{v} = u_i v_i \quad (\text{B.53})$$

$$\begin{aligned} \text{tr}(\underline{\underline{\mathbf{T}}} \cdot \underline{\underline{\mathbf{S}}}) = \text{tr}(\underline{\underline{\mathbf{S}}} \cdot \underline{\underline{\mathbf{T}}}) &= \delta_{kl} T_{ki} S_{il} = (T_{xx} S_{xx} + T_{xy} S_{yx} + T_{xz} S_{zx}) \\ &+ (T_{yx} S_{xy} + T_{yy} S_{yy} + T_{yz} S_{zy}) + (T_{zx} S_{xz} + T_{zy} S_{yz} + T_{zz} S_{zz}) \end{aligned} \quad (\text{B.54})$$

$$\text{tr}(\underline{\underline{\mathbf{T}}} \cdot \underline{\underline{\mathbf{S}}}^\top) = \underline{\underline{\mathbf{T}}} : \underline{\underline{\mathbf{S}}} \quad (\text{B.55})$$

$$\text{tr}(\underline{\underline{\mathbf{T}}} \cdot \underline{\underline{\mathbf{I}}}) = \underline{\underline{\mathbf{T}}} : \underline{\underline{\mathbf{I}}} = \text{tr}(\underline{\underline{\mathbf{T}}}) \quad (\text{B.56})$$

$$\underline{\underline{\mathbf{T}}} : \underline{\underline{\mathbf{I}}} = \underline{\underline{\mathbf{T}}}^\top : \underline{\underline{\mathbf{I}}} = \underline{\underline{\mathbf{T}}} : \underline{\underline{\mathbf{I}}}^\top = \underline{\underline{\mathbf{I}}} : \underline{\underline{\mathbf{T}}} = T_{ii} = \text{tr}(\underline{\underline{\mathbf{T}}}) = T_{xx} + T_{yy} + T_{zz} \quad (\text{B.57})$$

$$\underline{\underline{\mathbf{T}}} : \underline{\underline{\mathbf{S}}} = \underline{\underline{\mathbf{S}}} : \underline{\underline{\mathbf{T}}} = \underline{\underline{\mathbf{T}}}^\top : \underline{\underline{\mathbf{S}}}^\top \neq \underline{\underline{\mathbf{T}}}^\top : \underline{\underline{\mathbf{S}}} = \underline{\underline{\mathbf{T}}} : \underline{\underline{\mathbf{S}}}^\top \quad (\text{B.58})$$

$$\begin{aligned} (\vec{u}\vec{v}) : \underline{\underline{\mathbf{T}}} &= \vec{u} \cdot (\underline{\underline{\mathbf{T}}} \cdot \vec{v}) = (\vec{u}\vec{v})^\top : \underline{\underline{\mathbf{T}}} = \vec{v} \cdot (\vec{u} \cdot \underline{\underline{\mathbf{T}}}) \\ &\neq (\vec{v}\vec{u}) : \underline{\underline{\mathbf{T}}} = \vec{u} \cdot (\vec{v} \cdot \underline{\underline{\mathbf{T}}}) = \vec{v} \cdot (\vec{u} \cdot \underline{\underline{\mathbf{T}}}) \end{aligned} \quad (\text{B.59})$$

$$(\vec{u} \otimes \vec{v})^\top = \vec{v} \otimes \vec{u} \quad (\text{B.60})$$

$$(\vec{u} \otimes \vec{v}) \cdot \vec{w} = (\vec{v} \otimes \vec{u}) \cdot \vec{w} \quad (\text{B.61})$$

$$\underline{\underline{\mathbf{I}}} \cdot \vec{v} = \vec{v} \cdot \underline{\underline{\mathbf{I}}} = \vec{v} \quad (\text{B.62})$$

$$(\underline{\underline{\mathbf{T}}} \cdot \underline{\underline{\mathbf{S}}}) \cdot \vec{v} = \underline{\underline{\mathbf{T}}} \cdot \vec{v} + \underline{\underline{\mathbf{S}}} \cdot \vec{v} \quad (\text{B.63})$$

$$\vec{v} \cdot (\underline{\underline{\mathbf{T}}} \cdot \underline{\underline{\mathbf{S}}}) = \vec{v} \cdot \underline{\underline{\mathbf{T}}} + \vec{v} \cdot \underline{\underline{\mathbf{S}}} \quad (\text{B.64})$$

$$(\underline{\underline{\mathbf{T}}} + \underline{\underline{\mathbf{S}}})^\top = \underline{\underline{\mathbf{T}}}^\top + \underline{\underline{\mathbf{S}}}^\top \quad (\text{B.65})$$

$$(\underline{\underline{\mathbf{T}}} \cdot \underline{\underline{\mathbf{S}}})^\top \neq \underline{\underline{\mathbf{T}}}^\top \cdot \underline{\underline{\mathbf{S}}}^\top \quad (\text{B.66})$$

$$(\vec{u}\vec{v}) \cdot \vec{w} = (\vec{v} \cdot \vec{w})\vec{u} \quad (\text{B.67})$$

$$\underline{\underline{\mathbf{T}}} : (\underline{\underline{\mathbf{S}}} \cdot \underline{\underline{\mathbf{R}}}) = (\underline{\underline{\mathbf{R}}} \cdot \underline{\underline{\mathbf{T}}}^\top) : \underline{\underline{\mathbf{S}}}^\top = (\underline{\underline{\mathbf{S}}}^\top \cdot \underline{\underline{\mathbf{T}}}) : \underline{\underline{\mathbf{R}}} \quad (\text{B.68})$$

$$\begin{aligned} \nabla(s\vec{u}) &= (\vec{u}\nabla s)^\top + s\nabla\vec{u} = (\nabla s)\vec{u} + s\nabla\vec{u} \\ &= \left(\frac{\partial}{\partial x_i} s u_j \right)_{i,j} = \left(u_i \frac{\partial}{\partial x_j} s \right)^\top + s \left(\frac{\partial}{\partial x_i} u_j \right)_{i,j} \end{aligned} \quad (\text{B.69})$$

$$\begin{aligned}
\nabla(\vec{u} \cdot \vec{v}) &= \vec{u} \cdot \nabla \vec{v} + \vec{v} \cdot \nabla \vec{u} + \vec{u} \times (\nabla \times \vec{v}) + \vec{v} \times (\nabla \times \vec{u}) \\
&= \vec{u} \cdot (\nabla \vec{v})^\top + \vec{v} \cdot (\nabla \vec{u})^\top = u_i \frac{\partial v_i}{\partial x_j} + v_i \frac{\partial u_i}{\partial x_j} = \frac{\partial}{\partial x_j} u_i v_i
\end{aligned} \tag{B.70}$$

B.4 Applications

In this section, two examples are given for expressions corresponding to physical phenomena from fluid dynamics to demonstrate how to interpret OpenFOAM®'s code.

B.4.1 Dissipation Rate

The dissipation of turbulent kinetic energy is commonly expressed as

$$\epsilon = 2\nu S_{ij} S_{ij} \tag{B.71}$$

with the stress tensor

$$S_{ij} = \frac{1}{2} \left(\frac{\partial u_i}{\partial x_j} + \frac{\partial u_j}{\partial x_i} \right) \equiv \text{symm}(\nabla \vec{u}) \tag{B.72}$$

and the fluid velocity \vec{u} . In OpenFOAM®, this can be efficiently implemented as follows using the identities from the previous section:

$$\epsilon = 2\nu \underline{\underline{\mathbf{S}}} : \underline{\underline{\mathbf{S}}} = 2\nu |\underline{\underline{\mathbf{S}}}|^2 = \nu |\sqrt{2} \underline{\underline{\mathbf{S}}}|^2 = \nu \text{magSqr} \left(\sqrt{2} \text{symm}(\nabla \vec{u}) \right) \tag{B.73}$$

In this way, the gradient of \vec{u} only has to be evaluated once in the code.

B.4.2 Diffusive Momentum Flux

The diffusive momentum flux for a compressible, Newtonian fluid (neglecting volume viscosity) can be written as (see Eq. (3.3)):

$$\nabla \cdot \underline{\underline{\boldsymbol{\tau}}} = \nabla \cdot \left(\mu \left(\nabla \vec{u} + (\nabla \vec{u})^\top - \frac{2}{3} \nabla \cdot \vec{u} \underline{\underline{\mathbf{I}}} \right) \right) \tag{B.74}$$

In OpenFOAM®, it is implemented as:

$$\nabla \cdot \underline{\underline{\boldsymbol{\tau}}} = \nabla \cdot \left(\mu \text{dev2} \left((\nabla \vec{u})^\top \right) \right) + \nabla \cdot (\mu \nabla \vec{u}) \tag{B.75}$$

In this way, the first part can be discretized explicitly while the last term can be discretized implicitly. When applying the identities from above, both expressions can be shown to be equivalent. First, the deviatoric term can be rewritten with Eq. (B.25) to:

$$\text{dev}2 \left((\nabla \vec{u})^\top \right) = (\nabla \vec{u})^\top - \frac{2}{3} \text{tr} \left((\nabla \vec{u})^\top \right) \underline{\underline{\mathbf{I}}} \stackrel{(B.32)}{=} (\nabla \vec{u})^\top - \frac{2}{3} \nabla \cdot \vec{u} \underline{\underline{\mathbf{I}}} \quad (\text{B.76})$$

Substituting this back in Eq. (B.75) and combining all terms within the divergence yields Eq. (B.74).

B.4.3 Total Normal Stretch

A useful transformation for the total normal stretch from Eq. (2.58) is given in this section. The total normal stretch is

$$K_n = \nabla_t \cdot \vec{w}_n \quad (\text{B.77})$$

with $\vec{w}_n = (\vec{w} \cdot \vec{n}) \vec{n}$. Using $\nabla_t \cdot \equiv (\underline{\underline{\mathbf{I}}} - \vec{n}\vec{n}) :$, this becomes:

$$K_n = (\underline{\underline{\mathbf{I}}} - \vec{n}\vec{n}) : \nabla ((\vec{w} \cdot \vec{n}) \vec{n}) = \nabla \cdot ((\vec{w} \cdot \vec{n}) \vec{n}) - \vec{n}\vec{n} : \nabla ((\vec{w} \cdot \vec{n}) \vec{n}) \quad (\text{B.78})$$

The last term is rewritten with Eq. (B.69) to:

$$K_n = \nabla \cdot ((\vec{w} \cdot \vec{n}) \vec{n}) - \vec{n}\vec{n} : ((\nabla (\vec{w} \cdot \vec{n})) \vec{n}) - \vec{n}\vec{n} : ((\vec{w} \cdot \vec{n}) \nabla \vec{n}) \quad (\text{B.79})$$

Using the product rule for the first term and using $\vec{n} \cdot \vec{n} = |\vec{n}|^2 = 1$ and $\vec{n}\vec{n} : \nabla \vec{n} = 0$ for the second term, the expression becomes:

$$K_n = \vec{n} \cdot \nabla (\vec{w} \cdot \vec{n}) + (\vec{w} \cdot \vec{n}) \nabla \cdot \vec{n} - \vec{n} \cdot \nabla (\vec{w} \cdot \vec{n}) = (\vec{w} \cdot \vec{n}) \nabla \cdot \vec{n} \quad (\text{B.80})$$

Appendix C

Additional Equivalence Ratio Fluctuation Plots

In this appendix, additional plots of the flame response in terms of flame consumption speed amplitude to harmonic oscillations of the upstream equivalence ratio from section 4.1 are provided.

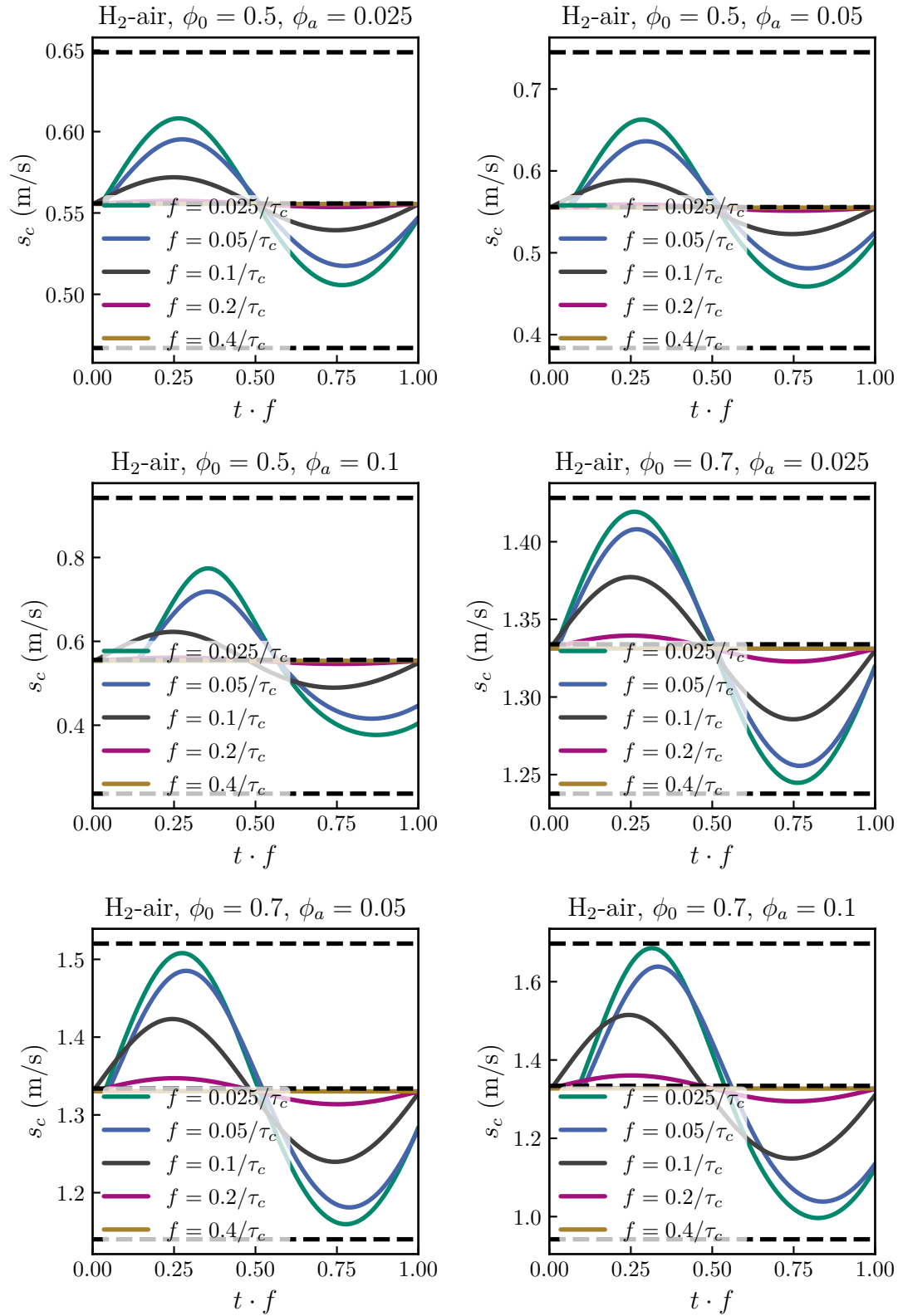


Figure C.1: Flame's response in terms of the global consumption speed for different mean equivalence ratios, oscillation amplitudes and frequencies.

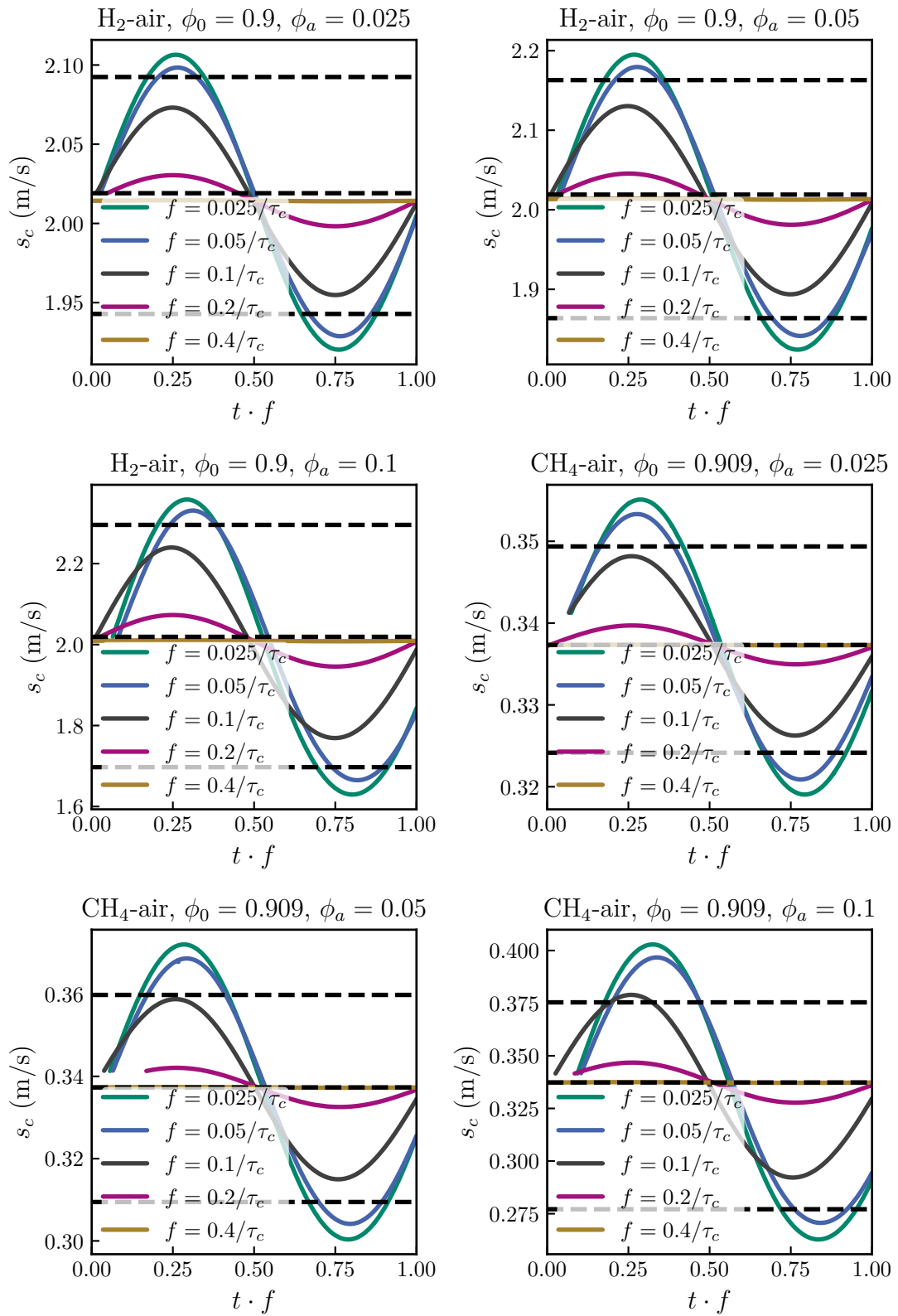


Figure C.2: Flame's response in terms of the global consumption speed for different mean equivalence ratios, oscillation amplitudes and frequencies.

Appendix D

High-frequency Pulsatile Flows

In section 4.2, oscillating Bunsen flames are discussed. These flames are excited by prescribing an oscillating mass flow rate of the unburnt gases at the domain inlet. For stoichiometric hydrogen/air flames at atmospheric conditions, the flame transit time $\tau_{\text{flame}} \equiv \delta_{\text{th}}/s_{L,0}$ is on the order of 0.1 ms and consequently, frequencies reach up to 10 000 Hz. Therefore, in this appendix, the numerical code is validated for these high frequencies by means of analytic solutions and experimental measurements for pulsatile pipe flows. Frictionless, one-dimensional flows are considered as well, because the oscillating Bunsen flames utilize frictionless slip-boundary conditions for the velocity. The dynamics of pressure, pressure gradient and mass flow rate for oscillating flows at high frequencies are derived and an estimate of the pressure differences expected for the high frequency flame simulations is provided.

D.1 Analytic Expressions for the Pressure Gradient

For the following analysis, analytic solutions for the pressure gradient are first derived for simplified flow configurations with and without oscillating mass flow

rates. The momentum balance equation from the general Navier–Stokes equations without body forces reads:

$$\frac{\partial \rho \vec{u}}{\partial t} + \nabla \cdot (\rho \vec{u} \vec{u}) = -\nabla p + \nabla \cdot \underline{\underline{\tau}} \quad (\text{D.1})$$

For an incompressible, Newtonian fluid, the stress tensor $\underline{\underline{\tau}}$ can be simplified to $\mu \Delta \vec{u}$.

First, the case of fully developed, steady-state pipe flow is discussed. Since the flow is in steady-state, the first term on the l.h.s. of Eq. (D.1) is zero and because the flow is fully developed, the convective term vanishes too. Therefore, the momentum equation reduces to:

$$0 = -\nabla p + \mu \Delta \vec{u} \quad (\text{D.2})$$

For fully developed pipe flow, the viscous term can be simplified in cylindrical coordinates to

$$(\nabla \cdot \underline{\underline{\tau}})_x = \mu \frac{1}{r} \frac{\partial}{\partial r} \left(r \frac{\partial u_x}{\partial r} \right) \quad (\text{D.3})$$

where x is the axial direction, because the pipe flow velocity profile is a parabola

$$u_x = 2\bar{u} \left(1 - \left(\frac{r}{R} \right)^2 \right) \quad (\text{D.4})$$

with R the pipe radius. Combining Eq. (D.2), Eq. (D.3) and Eq. (D.4) yields an expression for the pressure gradient for the steady-state pipe flow:

$$\frac{\partial p}{\partial x} = \mu \frac{1}{r} \frac{\partial}{\partial r} \left(r \frac{\partial}{\partial r} 2\bar{u} \left(1 - \left(\frac{r}{R} \right)^2 \right) \right) = -\frac{8\mu\bar{u}}{R^2} \quad (\text{D.5})$$

This will be denoted in the following as

$$P_{\text{pipe,steady}} \equiv \left| \frac{\partial p}{\partial x} \right| = \frac{8\mu\bar{u}}{R^2} \quad (\text{D.6})$$

where $P \equiv |\partial p / \partial x|$ is the pressure gradient, following the nomenclature from [217]. It is evident that the pressure gradient in this case scales linearly with the bulk flow velocity \bar{u} .

If instead the flow is one-dimensional (1D), that is $\partial / \partial r = 0$, which is realized by a slip-boundary condition instead of a no-slip boundary condition at the pipe

wall, the friction term becomes zero. In this case, no pressure gradient is required to drive the flow:

$$P_{1D,steady} \equiv \frac{\partial p}{\partial x} = 0 \quad (\text{D.7})$$

As in the case of the oscillating flames in section 4.2, the mass flow rate is now set to oscillate harmonically:

$$u_x = \bar{u} (1 + m_A^* \sin(2\pi ft)) \quad (\text{D.8})$$

m_A^* is the normalized amplitude of the velocity or mass flow rate oscillation. For the one-dimensional flow, the pressure gradient can be expressed as:

$$\frac{\partial \rho u_x}{\partial t} = -\frac{\partial p}{\partial x} \quad (\text{D.9})$$

Together with Eq. (D.8) and assuming constant density, the pressure gradient can be expressed as:

$$P_{1D,osc} \equiv \frac{\partial p}{\partial x} = -2\pi \rho \bar{u} f m_A^* \cos(2\pi ft) \quad (\text{D.10})$$

Therewith, the amplitude of the pressure gradient oscillation P_A is

$$P_{A,1D,osc} = 2\pi \rho \bar{u} f m_A^* \quad (\text{D.11})$$

For fully developed pipe flow with harmonically oscillating mass flow rate, an analytic solution is available, which is usually expressed in terms of the ratio of normalized mass flow rate amplitude \dot{m}_A^* and normalized pressure gradient amplitude $P_A^* = P/P_{\text{pipe,steady}}$ [217–221]:

$$\frac{\dot{m}_A^*}{P_A^*} = |\Psi| = \left| -\frac{4}{\pi F} \left(1 + \frac{2i^{1/2} J_1 \left[(2\pi F)^{1/2} i^{3/2} \right]}{(2\pi F)^{1/2} J_0 \left[(2\pi F)^{1/2} i^{3/2} \right]} \right) \right| \quad (\text{D.12})$$

F is the normalized frequency defined below in Eq. (D.17), i is the imaginary unit and J_n is the n -th Bessel function of the first kind. In the high frequency limit $F \gg 1$, the solution reduces to:

$$\frac{\dot{m}_A^*}{P_A^*} \rightarrow \frac{4}{\pi F} \quad (\text{D.13})$$

This relation is also shown in Fig. D.1.

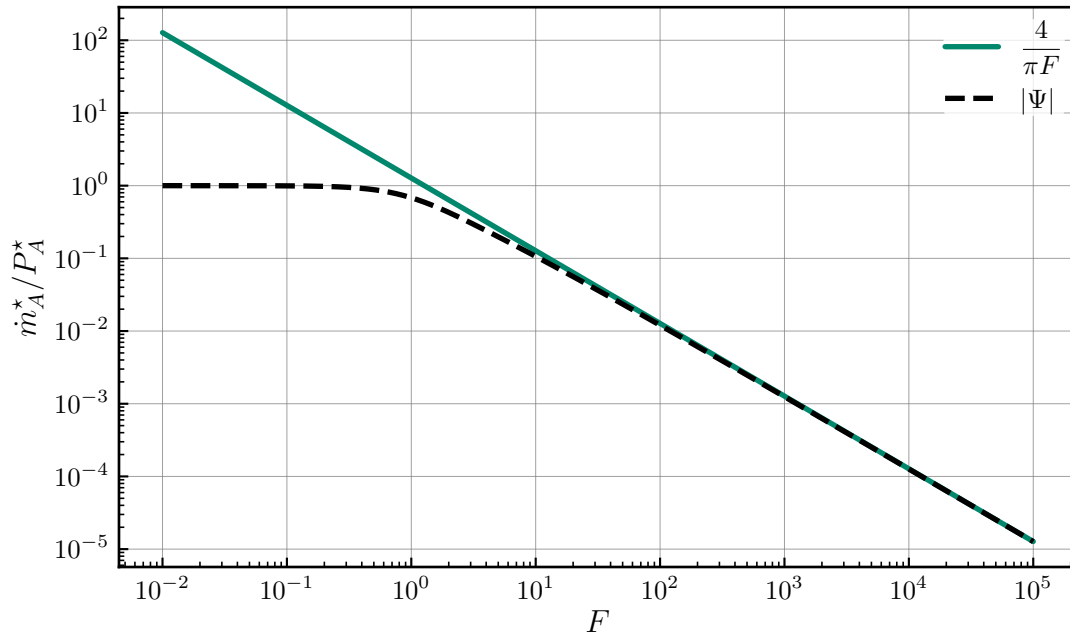


Figure D.1: Analytic solution and high frequency limit of $\frac{\dot{m}_A^*}{P_A^*}$ for pulsating pipe flows.

D.2 Computational Setup

The computational setup is built to resemble the experimental setup from [217, 222]. In the experiments, a pipe with a length of $L = 2$ m and radius of $R = 7$ mm is used. A mean mass flow rate of 35 g/min, or $Re = 2947$ to ensure laminar flow, enters the pipe and oscillates harmonically with prescribed amplitudes \dot{m}_A^* and frequencies f . Pressure gradient and mass flow rate are measured at the axial position $x = 1.75$ m. The fluid is air at room temperature.

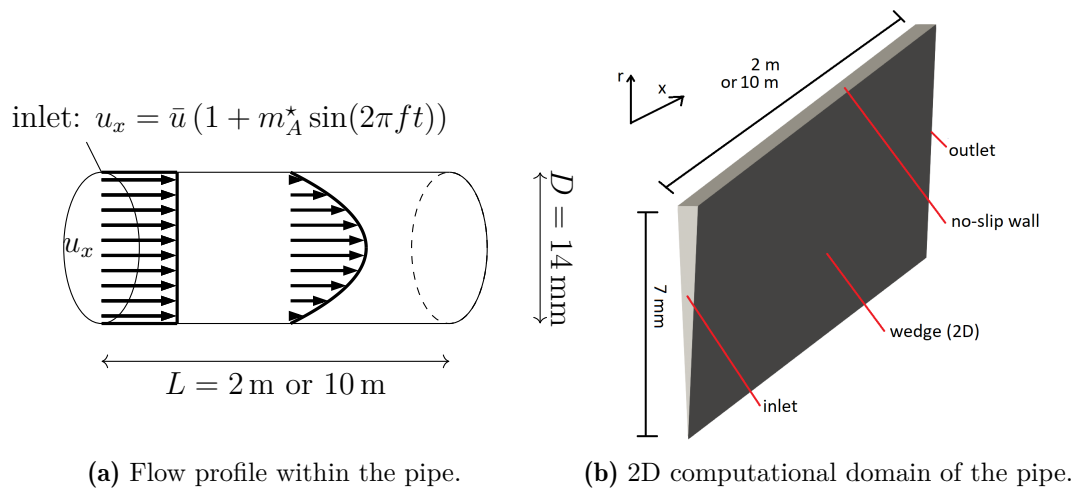


Figure D.2: Computational setup of the 2D pipe flow case.

In the simulations, a two-dimensional axisymmetric domain with length $L = 2$ m is used, as shown in Fig. D.2, with resolution $\Delta r = 0.14$ mm and $\Delta x = 1$ cm. For the frictionless flow, the domain is one-dimensional with the same axial resolution. In addition to the 2 m pipe used in the experiments, a pipe with $L = 10$ m is simulated as well.

At the inlet for the one-dimensional and pipe flow simulations, the velocity is prescribed as a block profile to resemble the experiments, with harmonic oscillation according to Eq. (D.8). For the compressible simulations, a partially non-reflecting boundary condition is applied for the pressure at the outlet to avoid reflection of pressure waves back into the domain. Initially, the pipe is uniformly initialized with $u_x = \bar{u}$. The parameters for the simulations are summarized in Table D.1. Note that the air for the simulations is assumed to be at 5 bar. However, for ideal gases, the choice of pressure does not affect the non-dimensionalized results, as shown below. Because the diameter and mass flow rate are fixed, the velocities vary with p but the Reynolds number, speed of sound and therefore the dynamics of the flow stay the same. All simulations are run with OpenFOAM® v2012, both incompressible (incomp) and fully compressible (comp). For a moderate range of frequencies, the incompressible and compressible solutions are the same, as explored later.

Table D.1: Numerical settings for the oscillating flows.

Fluid property	Value	Mesh/flow	Value
p_0	5 bar	L	2 m or 10 m
T_0	300 K	R	7 mm
μ_0	1.8×10^{-5} Pa s	Δr	0.14 mm
M_{air}	28.9 g/mol	Δx	10 mm
c_p	1007 J/kg/K	\bar{m}	35 g/min
Pr	0.7	\bar{u}	0.654 m/s
κ	1.4	$Re_{\bar{u}}$	2947
ρ_0	5.79 kg/m ³	m_A^*	0.82
c	347.6 m/s	f	0.0063 Hz–6300 Hz

D.3 Steady-state Pipe Flow

Before oscillating mass flows are considered, first the steady-state solution is obtained. To ensure that the steady-state solution is sufficiently reached, the simulations are run for 10 flow-through times.

$$t_{\text{end}} = 10t_{\text{flow through}} = 10\frac{L}{\bar{u}} \quad (\text{D.14})$$

Figure D.3 shows the temporal evolution of the centerline velocity for the $L = 10$ m case, measured at the position $x = 9.9$ m. As expected, the steady state solution is nearly reached after $\frac{1}{2}t_{\text{flow through}}$ since the center-line velocity is $2\bar{u}$ (analytic solution).

Since the fluid enters with a block profile for the velocity, it will require a certain length to fully develop. Figure D.4 shows the pressure distribution along the pipe length at the steady state. After the flow has fully developed, the pressure profile is linear with a pressure gradient of $P_{\text{pipe,steady}} \approx 2$ Pa/m. The deviation of the pressure profile from the linear profile at the beginning is a consequence of the flow still developing.

In the experimental setup, measurements are performed at the axial position $x = 1.75$ m. However, as shown in Fig. D.4, at that point the flow may not have been fully developed. Therefore, results of the radial velocity profile at $x = 1.75$ m

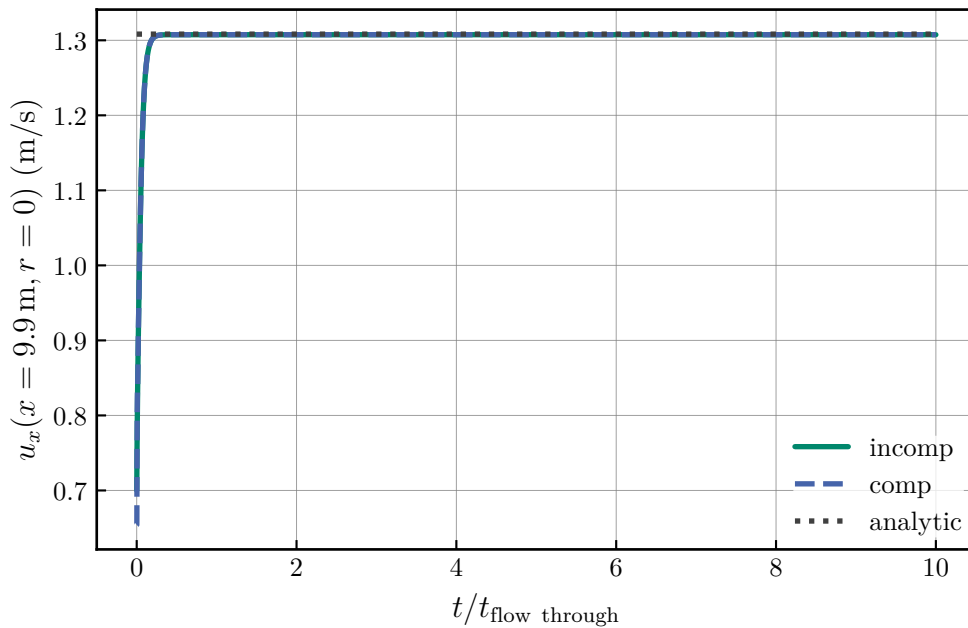


Figure D.3: Center-line velocity at $x = 9.9$ m over time.

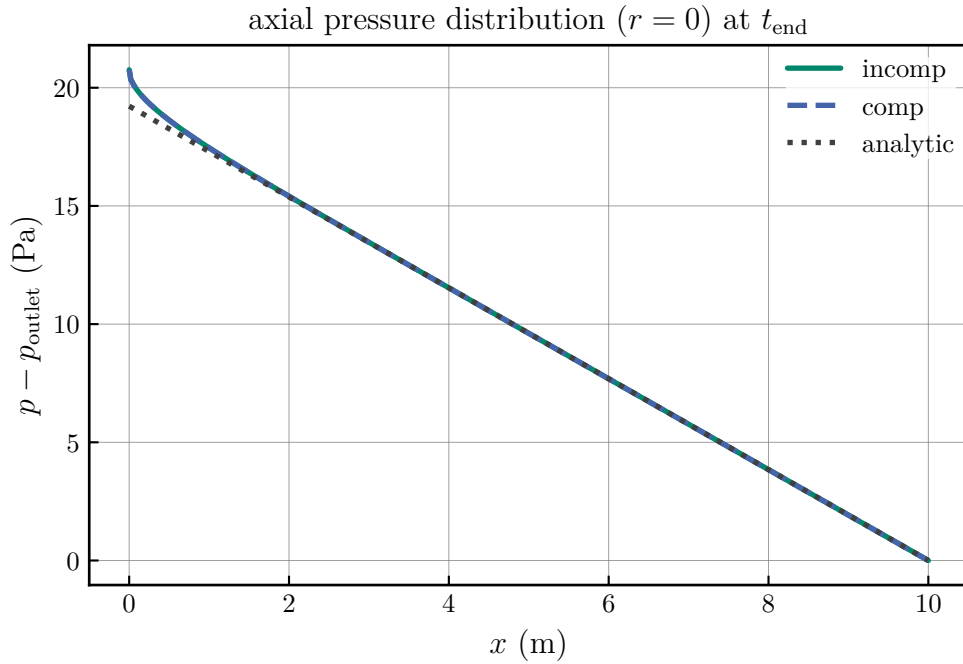


Figure D.4: Pressure distribution at the steady state.

and $x = 7.5$ are compared to the (analytic) parabolic profile from Eq. (D.4) in Fig. D.5. At $x = 1.75$ m, there are still deviations of the velocity profile in the center to the parabolic profile of the fully developed flow, while the simulation results match the analytic solution for $x = 7.5$ m.

The reason for this deviation is shown in Fig. D.6. Since the flow is still not fully developed at 1.75 m, there is a considerable contribution of the convective term. On the other hand, at $x = 7.5$, the convective term becomes zero and the friction term is fully balanced by the pressure gradient, as shown in Eq. (D.6).

Figure D.7 shows the contribution of the convective term along the center-line of the pipe. The vertical dashed black lines show the positions where pressure, pressure gradient and mass flow rate will be evaluated in the subsequent sections: at $x = 1.75$ m to compare results with the experiments and $x = 7.5$ m where the flow is fully developed for comparison with the analytic solution.

If the reference pressure is changed, the densities change as well. However, the Reynolds number stays constant due to the constant mass flow rate \dot{m} and diameter D :

$$Re = \frac{\bar{u}D}{\nu} = \frac{\dot{m}}{\rho\pi R^2} \frac{2R\rho}{\mu} \quad (\text{D.15})$$

as μ is not a function of pressure for ideal gases. Because of this, the flow behaves the same independent of pressure. Figure D.8 shows the centerline velocity along the pipe length for the steady state. At 1 bar, the velocities are five times as high

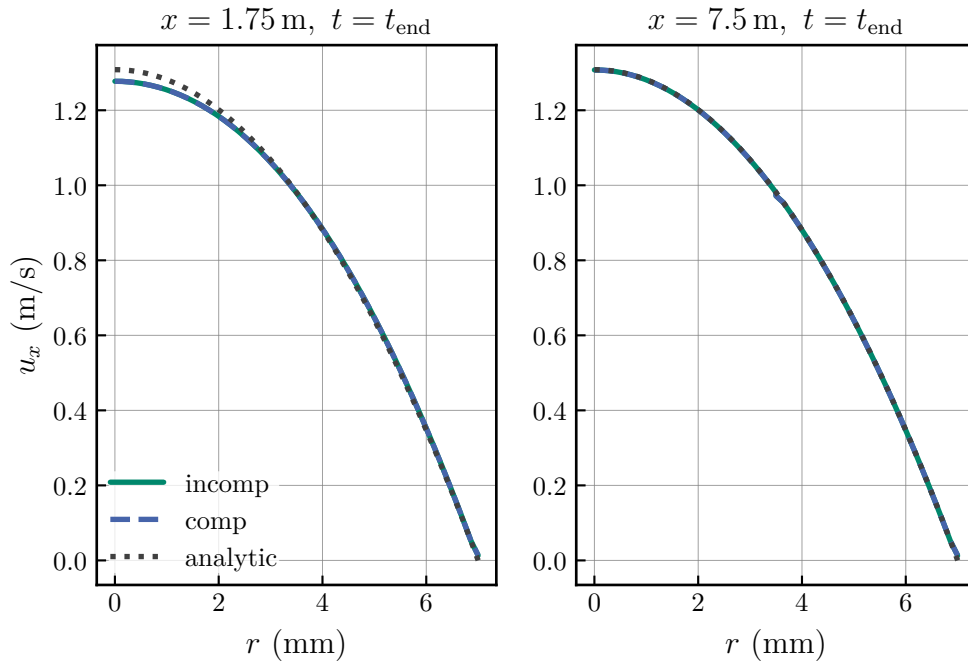


Figure D.5: Radial velocity profile of the steady-state solution taken at the same position as the experiments (left) and further downstream (right) compared to the analytic pipe flow solution. Colored lines are from the incompressible and compressible simulation, black dotted lines from the analytic solution.

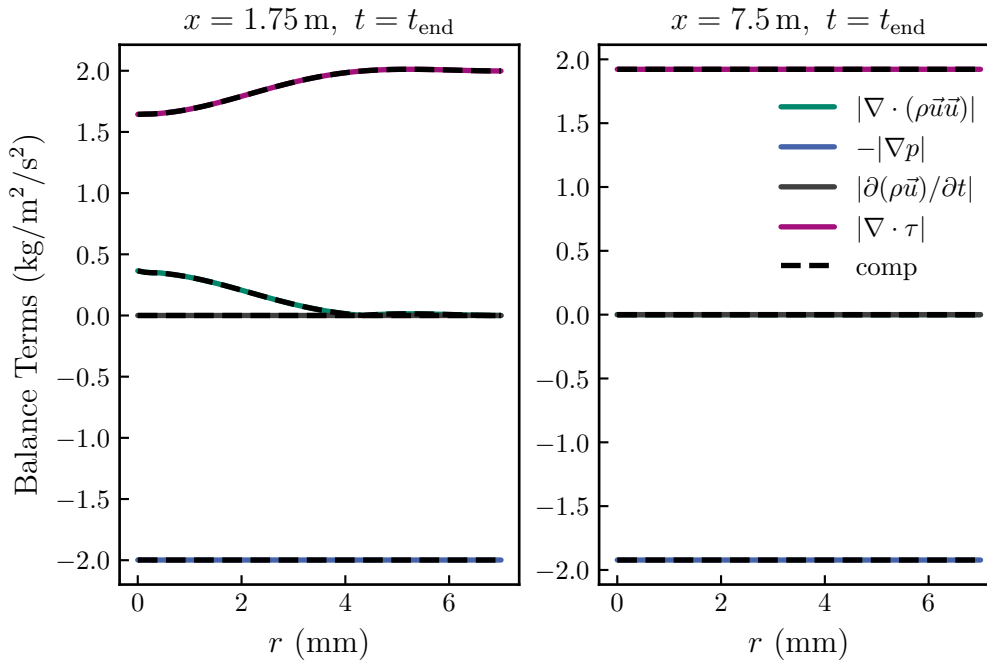


Figure D.6: Radial profiles of the balance terms from the momentum equation in Eq. (D.1) taken at the same position as the experiments (left) and further downstream (right). Colored lines show results from incompressible simulations and black dashed lines from compressible simulations.

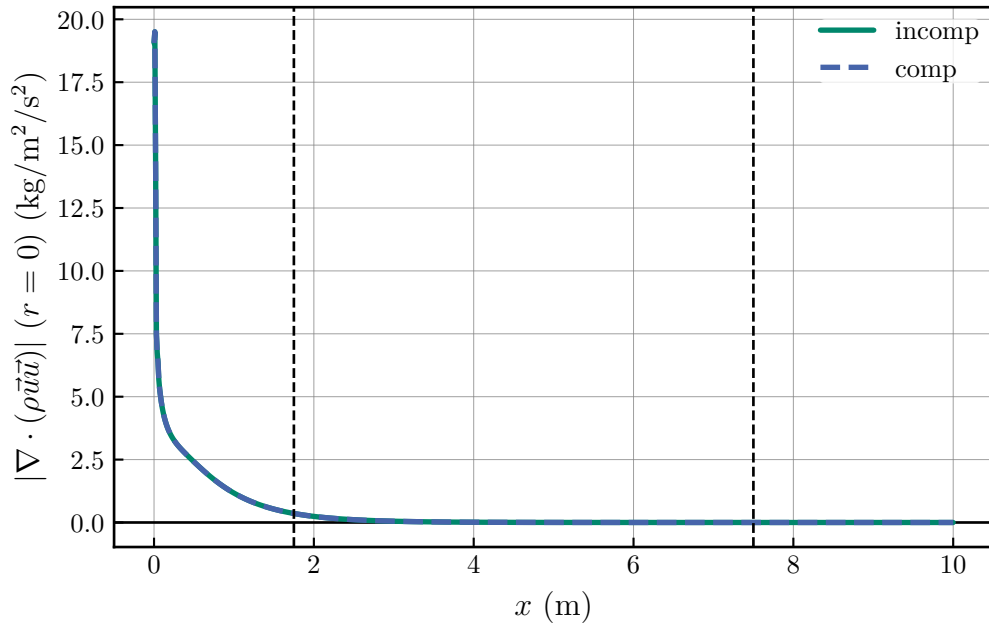


Figure D.7: Axial profile of the convective term of the momentum equation from the steady-state solution.

as at 5 bar. However, if plotted in normalized form, the inflow behavior in terms of the entrance length until the flow is fully developed stays the same.

D.4 Oscillating Flows

The characteristic dynamic of the relation between pressure and mass flow rate is expressed in normalized quantities: The normalized mass flow rate is $m^* = \dot{m}/\bar{m}$ and the normalized amplitude of the mass flow rate is m_A^* , which in the case of the simulations is prescribed at the inlet and is constant at $m_A^* = 0.82$. The mass flow rate \dot{m} is computed from

$$\dot{m} = \int \rho \vec{u} \cdot d\vec{A} \quad (\text{D.16})$$

Likewise, the normalized pressure gradient P^* is $P/P_{\text{pipe,steady}}$ (see Eq. (D.6)). The normalized frequency F is defined as

$$F = \frac{R^2 f}{\nu} \quad (\text{D.17})$$

In the chosen setup, $F = 1$ corresponds to a physical frequency of 0.063 Hz. Figure D.9 on the left shows an example of the axial pressure distribution during different phase angles θ of the oscillation period for an incompressible pipe flow

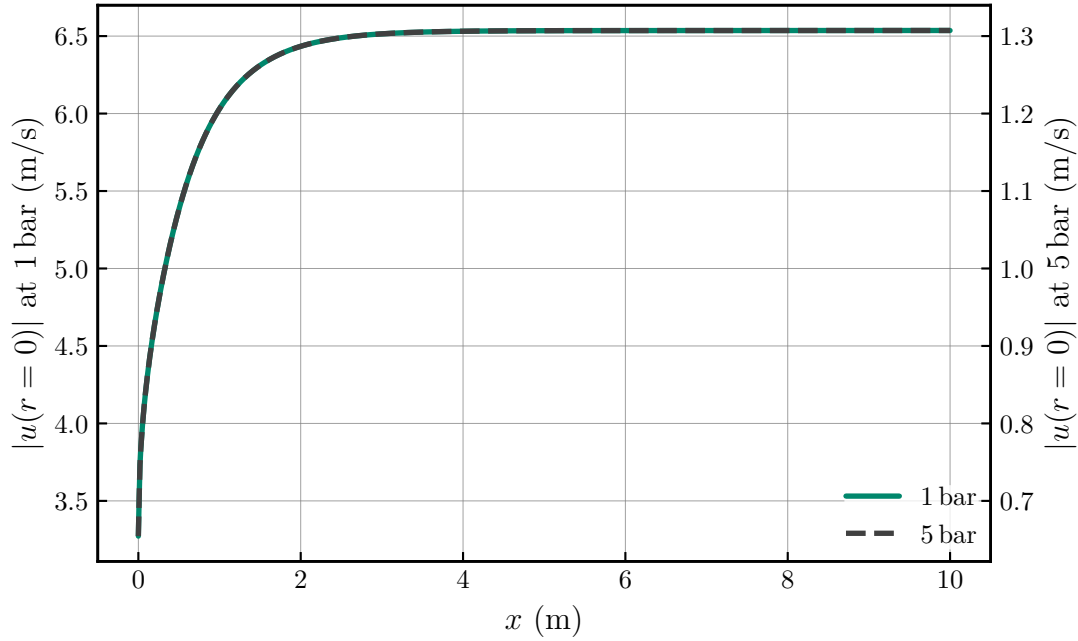


Figure D.8: Centerline velocity $|u(r = 0)|$ along the pipe length in the steady state. The inflow length required for the flow to fully develop is the same due to the same Reynolds number, even though the absolute velocities are different.

simulation at $F = 1$. The deviation from the linear profile at $x = 0$ stems from the block profile set for the velocity at the inlet. On the right of Fig. D.9, the time signal of the pressure at $x = 1.75$ m is shown.

Figure D.10 shows the time signals of the normalized mass flow rate $\dot{m}^* = \dot{m}/\bar{m}$ and normalized pressure gradient $P^* = P/P_{\text{pipe,steady}}$ for the same simulation as in Fig. D.9. A phase shift $\Delta\theta$ is visible between the pressure gradient and mass flow rate. The normalized amplitude of the mass flow rate is prescribed at the inlet as $m_A^* = 0.82$. The normalized amplitude of the pressure gradient P_A^* is computed from

$$P_A^* = \frac{1}{2} (\max(P^*) - \min(P^*)) \quad (\text{D.18})$$

Figure D.11 shows the ratio of m_A^* to P_A^* from the measurements and pipe flow simulations. The abscissa on the bottom shows the normalized frequency F and the abscissa on the top the corresponding physical frequencies. The black line is the analytic solution and the black symbols are experimental measurements from [217, 222, 223]. Colored symbols are the simulation results (both compressible and incompressible) for the 2 m pipe, where the time signals of pressure gradient and mass flow rate are evaluated at $x = 1.75$ m as in the experiments, and the 10 m pipe, where all signals are taken at $x = 7.5$ m.

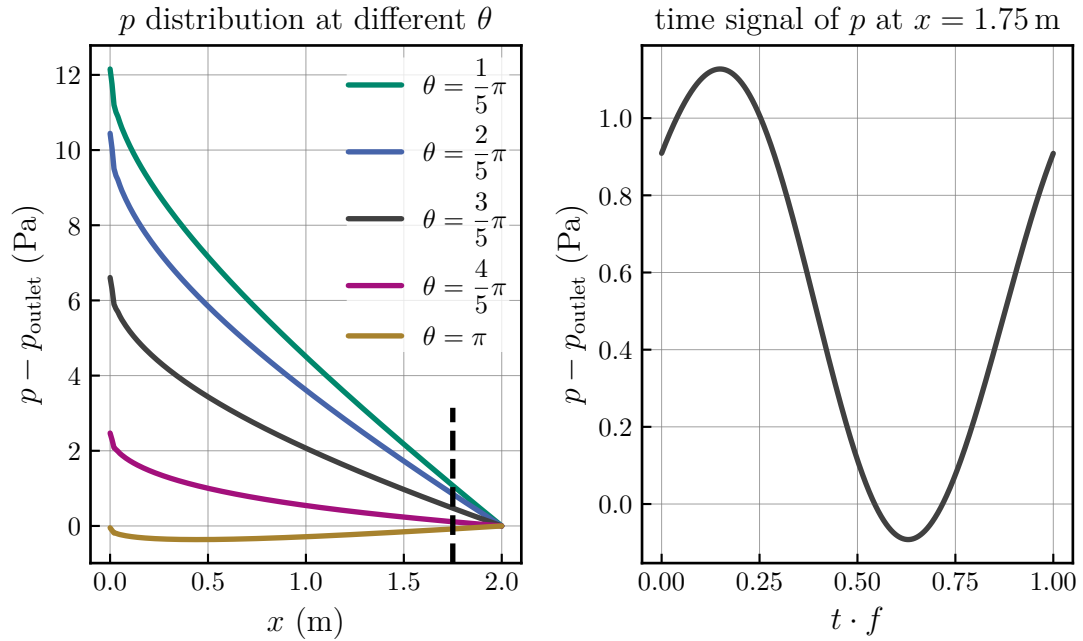


Figure D.9: Left: Axial pressure distribution at different phase angles θ during the first half of the oscillation period. Right: time signal of the pressure recorded at $x = 1.75$ m. Data from an incompressible pipe flow simulation with a 2 m pipe.

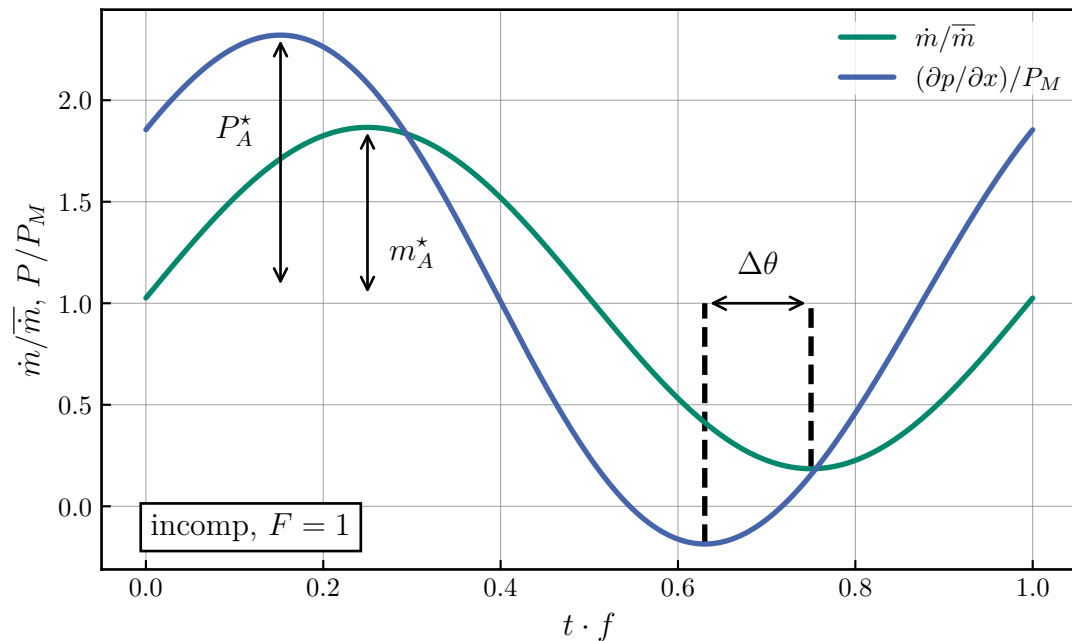


Figure D.10: Time signals of the normalized mass flow rate and normalized pressure gradient recorded at $x = 1.75$ m for the same simulation as in Fig. D.9.

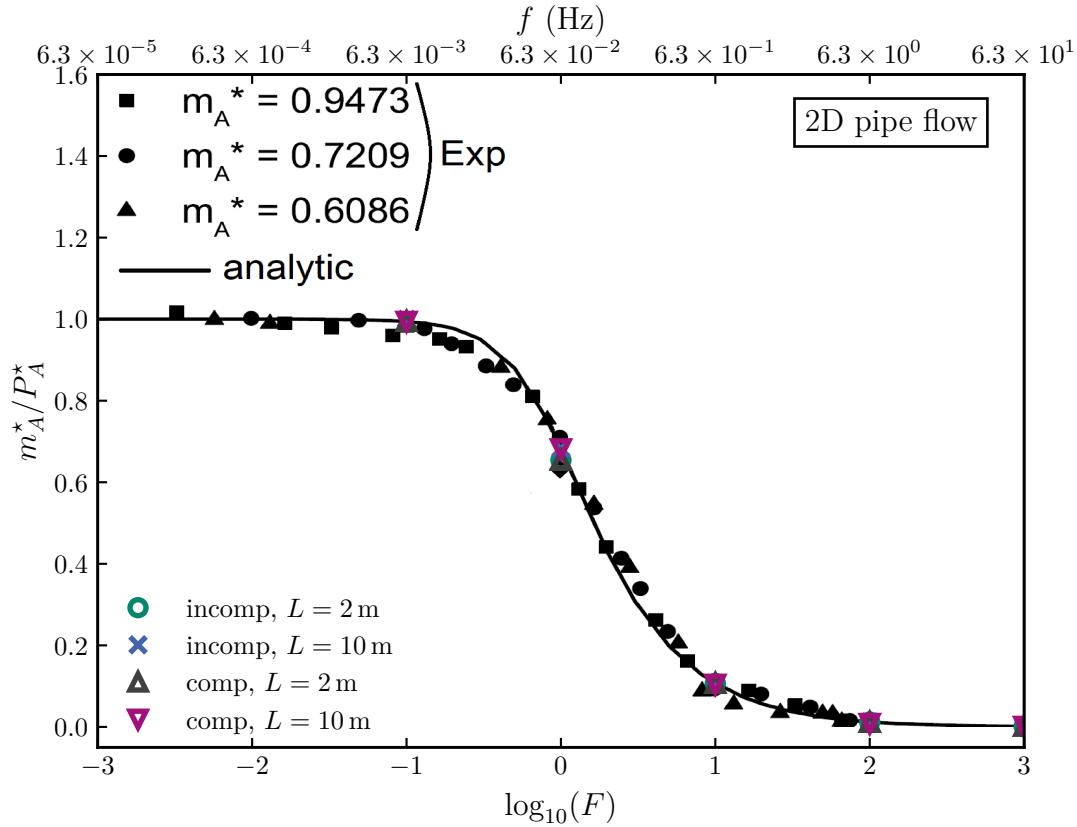


Figure D.11: Ratio of normalized mass flow rate amplitude and normalized pressure gradient amplitude from the analytic solution from Eq. (D.12) (black line), experimental measurements [217, 222] (black symbols) and pipe flow simulations (colored symbols).

For low frequencies ($F < 1$), the normalized pressure gradient amplitude stays comparable to the normalized mass flow rate amplitude. At higher frequencies of $F > 1$, however, the ratio of the two goes toward zero so that higher pressure gradients (and therewith absolute pressure differences) are required to keep the mass flow rate oscillating with a constant amplitude.

This behavior is further explained in Fig. D.12: For $F \gg 1$, the flow is dominated by the acceleration of the fluid $\partial(\rho\vec{u})/\partial t \gg \mu\Delta\vec{u}$. Because of this, the behavior in the high frequency pipe case approaches the solution of the oscillating frictionless 1D flow from Eq. (D.11), where the pressure gradient directly balances the time derivative term and therefore the pressure gradient amplitude $P_A \approx P_{A,1D,osc}$ scales linearly with f . The behavior in the high frequency range is showcased by

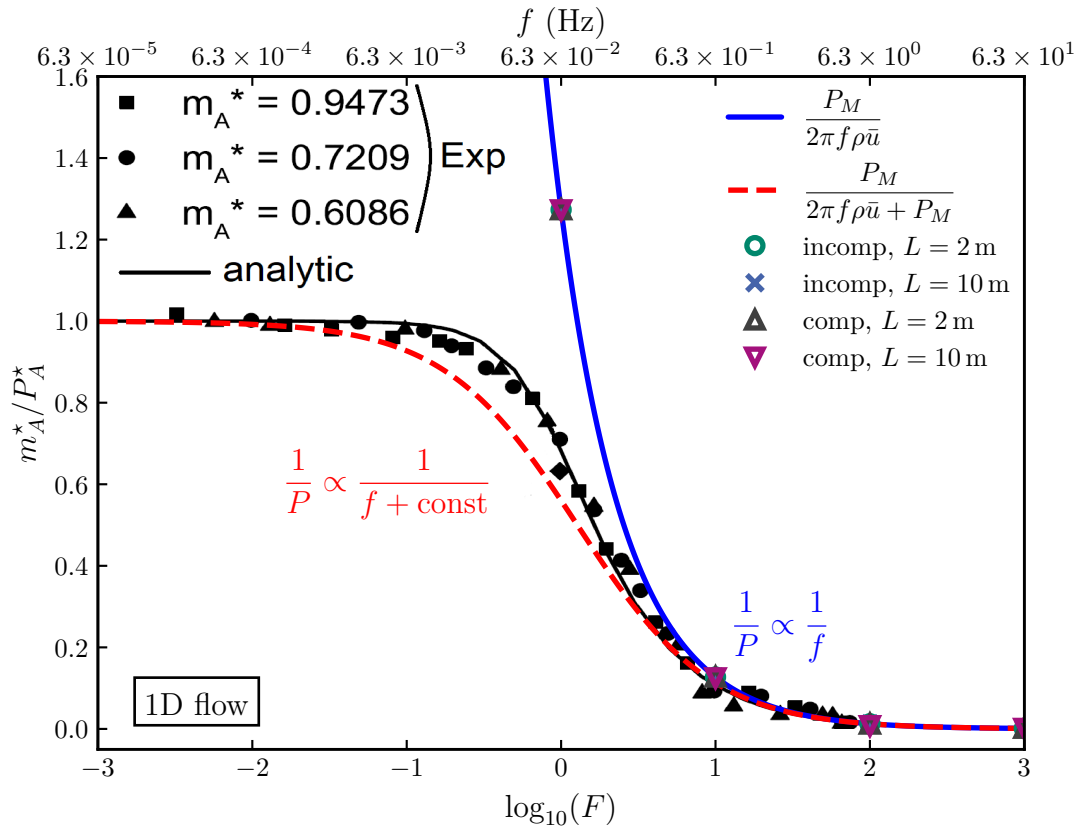


Figure D.12: Ratio of normalized mass flow rate amplitude and normalized pressure gradient amplitude from the analytic solution (black line), experimental measurements [217, 222] (black symbols) and 1D simulations (colored symbols).

the blue line in Fig. D.12. Since m_A^* and $P_{\text{pipe,steady}}$ are constant, the ratio in the figure can be simplified to:

$$\frac{m_A^*}{P_A^*} = \frac{m_A^*}{\frac{P_A}{P_M}} = \frac{m_A^*}{\frac{2\pi m_A^* f \rho \bar{u}}{P_{\text{pipe,steady}}}} = \frac{P_{\text{pipe,steady}}}{2\pi f \rho \bar{u}} \quad (\text{D.19})$$

Using the short hand notation $P_M \equiv P_{\text{pipe,steady}}$ and including Eq. (D.6), the ratio can be expressed as:

$$F \gg 1 : \quad \frac{m_A^*}{P_A^*} \rightarrow \frac{P_{\text{pipe,steady}}}{2\pi f \rho \bar{u}} = \frac{P_M}{2\pi f \rho \bar{u}} = \frac{\frac{8\mu \bar{u}}{R^2}}{2\pi f \rho \bar{u}} = \frac{4}{\pi} \frac{1}{F} \quad (\text{D.20})$$

To explain the behavior of m_A^*/P_A^* over the whole F range, a simplifying assumption can be made: The pressure gradient P has to balance two terms: the time derivative of the mass flow rate and the friction term. The pressure gradient that has to balance the time derivative term can be expressed with Eq. (D.10). To express

the pressure gradient required for the friction term, it is assumed that each point during the transient oscillation corresponds to a steady-state pipe flow with a mass flow rate of $\bar{m}(1 + m_A^* \sin(2\pi ft))$ at that time. In this way, the pressure gradient amplitude caused by the friction term during the simulation can be estimated by the pressure gradients in the steady state corresponding to a mass flow rate of the maximum and minimum mass flow rate during the oscillation:

$$\begin{aligned} P_{A,\text{friction}} &\approx \frac{1}{2} (P_{\text{pipe,steady}}(1 + m_A^*) - P_{\text{pipe,steady}}(1 - m_A^*)) \\ &= m_A^* P_{\text{pipe,steady}} = m_A^* P_M \end{aligned} \quad (\text{D.21})$$

since $P_{\text{pipe,steady}}$ scales linearly with \bar{u} (see appendix D.1). Therefore, the total pressure gradient amplitude can be estimated from the frequency dependent contribution due to the oscillating mass flow rate $P_{A,1\text{D,osc}}$ and the friction $P_{A,\text{friction}}$, which in this case is constant and not affected by f :

$$P_A \approx P_{A,1\text{D,osc}} + P_{A,\text{friction}} = 2\pi\rho\bar{u}fm_A^* + m_A^* \frac{8\mu\bar{u}}{R^2} \quad (\text{D.22})$$

Using this estimate in the expression for the amplitude ratio finally yields:

$$\begin{aligned} \frac{m_A^*}{P_A^*} &= \frac{m_A^*}{\frac{P_A}{P_M}} \approx \frac{m_A^* P_M}{P_{A,1\text{D,osc}} + P_{A,\text{friction}}} = \frac{P_M}{2\pi\rho f\bar{u} + P_M} \\ &= \frac{\frac{8\mu\bar{u}}{R^2}}{2\pi\rho\bar{u}f + \frac{8\mu\bar{u}}{R^2}} = \frac{1}{\frac{1}{4}\pi F + 1} \end{aligned} \quad (\text{D.23})$$

Thus, the characteristic curve of m_A^*/P_A^* is independent of the prescribed oscillation amplitude m_A^* . Plotting the normalized ratio m_A^*/P_A^* therefore has the following limiting behavior: as $F \rightarrow 0$, the ratio becomes unity since the pressure gradient caused by the oscillation is small compared to the steady-state pressure gradient balancing friction. At $F \rightarrow \infty$, $\partial(\rho u_x)/\partial t$ is much larger than the friction term and the pressure gradient scales with the frequency, as in the frictionless 1D case. The relation from Eq. (D.23) is shown in Fig. D.12 as red dashed line. The deviation from this simplified analysis (red dashed line) to the analytic solution (solid black line) is due to the simplification made in $P_{A,\text{friction}}$. During the oscillation, the velocity profile in reality is no longer parabolic. Therefore, the velocity field at a point during the oscillation cannot be directly compared to a steady-state pipe flow with the same mass flow rate.

The colored symbols in Fig. D.12 are simulation results from 1D simulations. For $F \gg 1$, the results coincide with the pipe flow cases. For lower frequencies, the amplitude ratio goes toward infinity because $1/P \propto 1/f$ as shown above. It

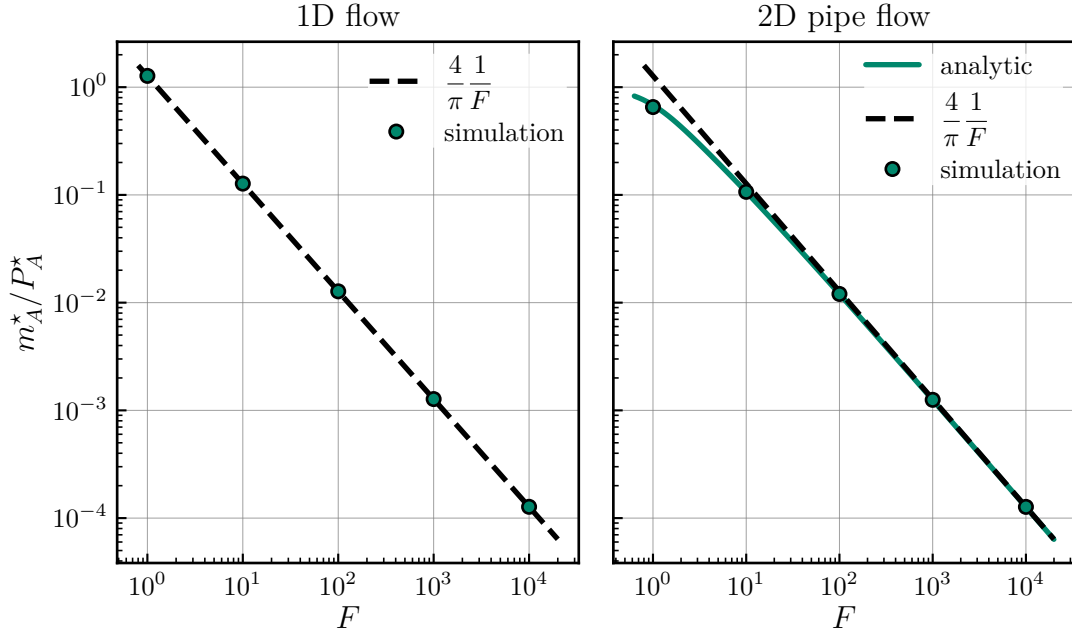


Figure D.13: Normalized ratio of mass flow rate and pressure gradient over normalized frequency (double logarithmic). Simulation results from frictionless 1D (left) and pipe flow (right) simulations are compared with the analytic solution from Eq. (D.12) and the high frequency limit from Eq. (D.11).

should be noted that results from the 1D simulations are normalized with the same parameters as the pipe flow simulations for the sake of comparison in the same plot, that is $P_M = P_{\text{pipe,steady}}$ and $F = R^2 f / \nu$. Otherwise, F cannot be defined for the 1D case because the solution is independent of R and ν and similarly, $P_M = 0$ for 1D steady-state flow as shown in Eq. (D.7). The limiting behavior of $1/P \propto 1/F$ for $F > 1$ can also be clearly seen in Fig. D.13, where both axes are logarithmic. For the 1D simulations on the left, the results are exactly linear in the double-logarithmic plot, while in the pipe flow case, this is only valid for $F \gg 1$. The dashed line shows $m_A^*/P_A^* = 4/(\pi F)$ from Eq. (D.11).

Another effect that occurs for the oscillating pipe flows is a phase shift between the mass flow rate signal and the pressure gradient. At low frequencies ($F \ll 1$), there is no phase shift between the time signal of the pressure gradient signal and mass flow rate, while at high frequencies ($F \gg 1$), the phase shift becomes $\frac{1}{4}$ period or $\frac{1}{2}\pi$.

Again, results from the incompressible and compressible solutions match. However, if the time signals of pressure gradient and mass flow rate are recorded at $x = 1.75$ m on the $L = 2$ m domain, the phase shift evaluated from the simulations exactly matches the experimental data (see the zoomed region in Fig. D.14), which is lower than the analytic solution. On the $L = 10$ m domain, where the signals

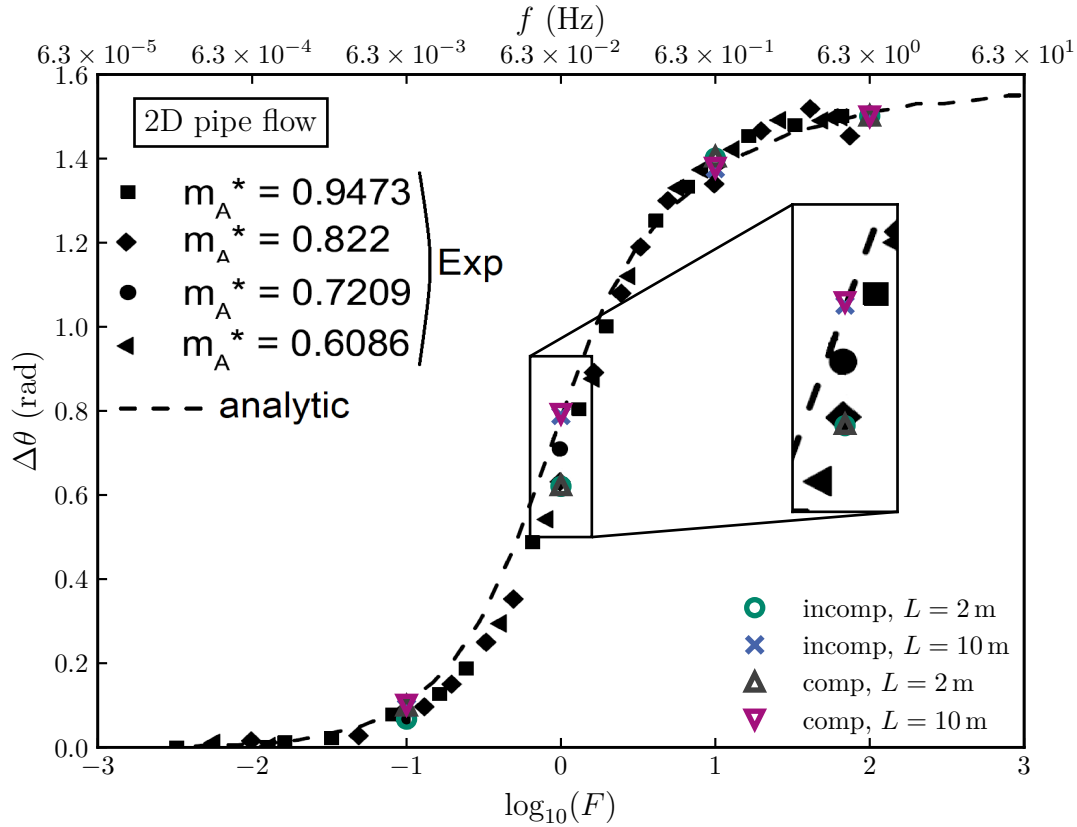


Figure D.14: Phase shift between pressure gradient and mass flow rate from the analytic solution (black dashed line), experimental measurements [217, 222] (black symbols) and pipe flow simulations (colored symbols).

are evaluated at $x = 7.5$ m and the flow is fully developed, the phase shift exactly matches the analytic solution.

The behavior of the phase shift can be explained similarly as before: For $F \rightarrow 0$, $\partial(\rho\vec{u})/\partial t \ll \mu\Delta\vec{u}$ and the setup resembles the steady-state case. There, the pressure gradient fully balances the friction term, which scales with the bulk velocity, as shown in Eq. (D.3). Because of this, an increase in the bulk velocity leads to a linear increase in the friction term, which is balanced by the pressure gradient. Because of this, bulk velocity and mass flow rate signals are in phase with the pressure gradient signal.

For $F \rightarrow \infty$, $\partial(\rho\vec{u})/\partial t \gg \mu\Delta\vec{u}$ and the setup resembles the frictionless 1D setup. In this case, the pressure gradient has to balance $\partial(\rho\vec{u})/\partial t$. But since the unsteady term is the rate of change of the mass flow rate, maxima of the pressure gradient and mass flow rate have to be shifted by a quarter period. The colored symbols in Fig. D.15 are results from the 1D simulations. Again, they approach the pipe flow

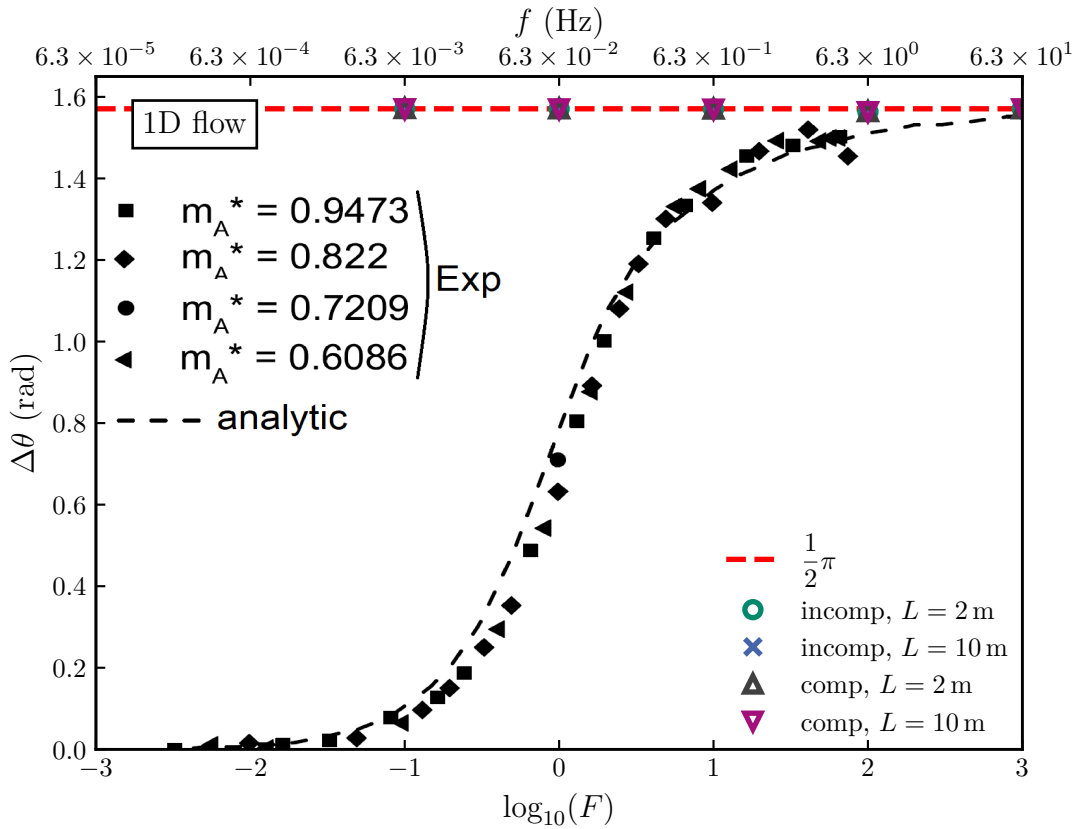


Figure D.15: Phase shift between pressure gradient and mass flow rate from the analytic solution (black dashed line), experimental measurements [217, 222] (black symbols) and 1D simulations (colored symbols).

solution for $F \gg 1$ but due to the absence of friction, the phase shift is always a quarter period, independent of frequency in the 1D simulations.

D.5 Compressibility Effects

If the frequencies are increased further, the results from incompressible and compressible simulations start to differ. The speed of sound in the considered setup can be computed with the fluid properties in Table D.1 to:

$$c = \sqrt{\kappa \frac{p}{\rho}} \approx 348 \text{ m/s} \quad (\text{D.24})$$

This means, the time required to propagate the oscillating pressure signal at the inlet to the end of the pipe is $\tau_p = L/c$, which for the $L = 2 \text{ m}$ pipe yields $\tau_p \approx 0.58 \text{ ms}$. For frequencies with a time scale much larger than this time $1/f \gg \tau_p$, the compressible solution behaves like the incompressible one, as the

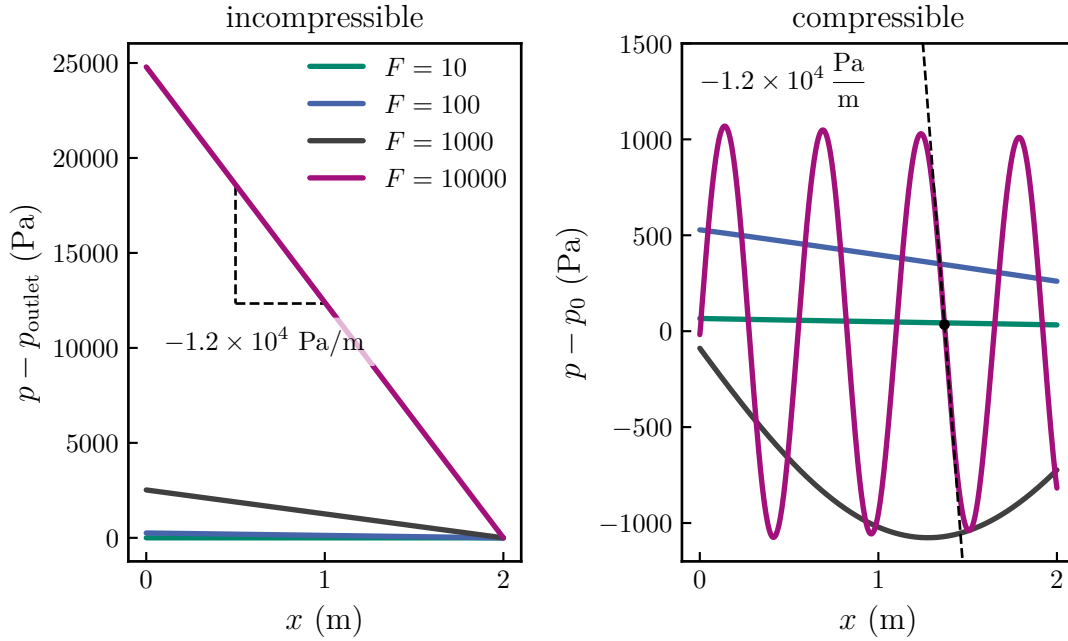


Figure D.16: Spatial profile of pressure at a single time instant during the pipe flow oscillation with different frequencies F . Left: incompressible simulation. Right: compressible simulation.

change in pressure at the inlet reaches the outlet faster than the pressure changes due to the oscillation. This leads to the linear axial pressure distribution. For very high frequencies $1/f \ll \tau_p$, however, the time it takes for the pressure to go from its maximum to its minimum value at the inlet is much faster, than the time required for the pressure signal to travel from the inlet to the outlet. Because of this, there is not enough time for the information to reach the outlet within one oscillation period. In this case, there is not a single column of pressure that oscillates, but a pressure wave that travels along the pipe.

Another way of visualizing this behavior is by considering the wave length λ of the generated pressure wave:

$$\lambda = \frac{c}{f} \quad (\text{D.25})$$

For low frequencies, $\lambda \gg L$ so that the pressure profile appears to be linear. For high frequencies, however, $\lambda \ll L$ and the pressure wave can establish within the length of the pipe.

An example of this behavior is given in Fig. D.16. On the left, the spatial pressure distributions at the time of the maximum pressure gradient during the oscillation period in the pipe are presented. On the left, results from incompressible simulations in the $L = 2 \text{ m}$ pipe are shown. Since the speed of sound for an incompressible fluid is formally infinite, the pressure distribution is always linear.

Table D.2: Dimensionless frequency F , physical frequency f , time scale of the frequency $1/f$ and wave length of the pressure wave λ for the considered high frequency cases.

F	f (Hz)	$\frac{1}{f}$ (s)	$\lambda = c/f$ (m)
1	0.063	16.0	5500
10	0.63	1.6	550
100	6.3	0.16	55
1 000	63	0.016	5.5
10 000	630	0.0016	0.55

The dashed lines on the left mark the rise of the pressure profile for $F = 10\,000$, which is $\partial p/\partial x = -1.2 \times 10^4$ Pa/m. This value is the same as the one derived with Eq. (D.11) in the limit of high frequencies ($P_A = 2\pi f \rho \bar{u} m_A^* \approx 1.2 \times 10^4$ Pa/m).

Figure D.16 on the right shows the axial pressure distribution in the pipe for the same cases as on the left, but from compressible simulations. For the two lowest depicted frequencies, $F = 10$ and $F = 100$, the axial pressure profile is linear. For these two cases, the wave length of the pressure signal is $\lambda_{F=10} = 548$ m and $\lambda_{F=100} = 55$ m and therewith $\lambda \gg L = 2$ m, so that the pressure distribution must be linear (see Table D.2). On the other hand, for $F = 1000$, $\lambda_{F=1000} = 5.5$ m, so half the wave length fits into the pipe, deviating from the linear pressure profile. At $F = 10\,000$, several wave lengths fit into the pipe.

This behavior also has consequences for the maximum pressure difference appearing during the oscillation. As the frequency increases, the unsteady term in the momentum equation must be balanced by the pressure gradient. For the incompressible simulations, the maximum pressure difference Δp is therefore given by $\Delta p = P_A L$ because the pressure profile is always linear. Because of this, Δp increases linearly with L and $P_A \propto f$. For the compressible case, as the frequency rises, the pressure gradient required to balance the unsteady term in the momentum equation is generated by the decreasing wave length of the pressure wave instead of an increasing Δp . Note that Δp for $F = 10\,000$ in the incompressible case is much larger ($\Delta p \approx 50\,000$ Pa) than for $F = 10\,000$ in the compressible case ($\Delta p \approx 2000$ Pa). Note also that Δp is approximately the same for $F = 1000$ and $F = 10\,000$ in the compressible case. As $\partial(\rho u_x)/\partial t$ increases linearly with f , the wave length decreases linearly with f according to $\lambda = c/f$ so that there is no need for a larger Δp to generate the pressure gradient. The dashed line on the right of Fig. D.16 shows that the same pressure gradient is

reached locally for $F = 10\,000$ as in the incompressible case. This also means, that the shorter the pipe, the lower will be Δp .

D.6 Summary

The simulation code has been successfully validated for oscillating flows in frictionless 1D configurations and 2D pipe flows by comparing the results to analytic solutions and experimental measurements. A description has been provided for the dynamics of pressure, pressure gradient and mass flow rate in pipe flows. The results show that in the limit of high frequencies, the frictionless 1D flows (in analogy to the slip boundary condition of the Bunsen flame setup) and the pipe flow cases show the same behavior: the pressure gradients increase linearly with f . The expected total pressure difference can be estimated from the maximum pressure gradient from Eq. (D.11) times the domain length, which for the extreme case of a stoichiometric hydrogen/air flame at atmospheric conditions with $f > s_{L,0}/\delta_{th} > 6000$ Hz can be estimated to

$$\Delta p \approx P_A L = \underbrace{2\pi}_{\mathcal{O}(1)} \underbrace{f}_{\mathcal{O}(10\,000 \text{ Hz})} \underbrace{\rho}_{\mathcal{O}(1 \text{ kg/m}^3)} \underbrace{\bar{u}}_{\mathcal{O}(1 \text{ m/s})} \underbrace{m_A^*}_{\mathcal{O}(1)} \underbrace{L}_{\mathcal{O}(0.01 \text{ m})} \approx \mathcal{O}(100 \text{ Pa})$$

Therefore, due to the generally short domain lengths and the prescribed fully developed velocity profile at the inlet, the pressure difference is not large enough to affect the thermo-physical properties of the flame. In addition, higher absolute pressure differences are avoided due to the compressibility effect, as the pressure wave length at these high frequencies lies on the order of the flame domain length.

Appendix E

Performance Optimizations for Large-scale Parallel Simulations

The simulation method applied in this work utilizes the finite rate chemistry model. This is generally the most accurate way to model chemical reactions but also requires large amounts of computational resources. There are several reasons for this: First, the detailed description of chemical reactions occurring during combustion usually includes hundreds of chemical species and thousands of chemical reactions. For larger hydrocarbon fuels, detailed mechanisms may include tens of thousands of reactions [224–227]. As the computation of chemical reaction rates requires the evaluation of expensive numerical functions like exponential functions, computing the reaction rates alone presents a challenge in terms of efficient implementation. Secondly, the time scales associated with the different chemical reactions can span more than ten orders of magnitudes [14, 18]. Progressing the fluid dynamics simulations with a time step suited for the fastest chemical reactions leads to unacceptable simulation times, as the time scales for the flow are orders of magnitudes larger than the time scales of the fastest chemical reactions. Because of this, different operator splitting techniques are usually applied that decouple the integration of ordinary differential equations (ODEs) related to the chemical reaction rates from the partial differential equations describing the flow. But integrating the ODEs of the chemical system requires special methods too. Due to the vastly different time scales, the resulting system of equations can be very stiff. Additionally, chemical reaction rates depend exponentially on the temperature, which adds to the stiffness. Therefore, special integration techniques have to be applied to efficiently integrate the chemical reaction rates.

Because of the aforementioned reasons, a large portion of the total simulation time is usually spent on computing chemical reaction rates if the finite rate chemistry model is used with detailed reaction mechanisms [228]. Different techniques have been developed to address these challenges, specifically the development of better, faster and more stable algorithms for solving the ODEs related to the chemical reaction rates [229–246]. Similar techniques have also been used in meteorological simulations [247, 248].

Due to the importance of efficient and at the same time accurate computation of chemical reaction rates, this appendix presents two optimization techniques developed during this work which reduce the total simulation time of typical cases by up to 70% without affecting the accuracy. Appendix E.1 gives an overview of the basics how chemical reaction rates are computed. Appendix E.2.1 explains the operator splitting approach used in this work and describes the implementation of the highly efficient ODE solver Sundials CVODE [249] in the OpenFOAM® based DNS solver. Another important optimization leading to large speedups is described in appendix E.2.2, where a converter is developed that automatically generates optimal code for efficient chemistry kernels. Due to the large-scale nature of the reacting flow simulations, load imbalances during parallel execution of the solver is another concern. Because of this, a new load balancing algorithm tailored specifically for large parallel reacting flow cases is presented in appendix E.3.

E.1 Computation of Chemical Reaction Rates

Different types of chemical reactions are supported in the DNS solver. Generally, the forward molar reaction rate \dot{r}'_r of reaction r and its reverse reaction rate \dot{r}''_r are computed by [52, 250]

$$\dot{r}'_r = k'_r \prod_k C_k^{e'_{k,r}}, \quad \dot{r}''_r = k''_r \prod_k C_k^{\nu''_{k,r}} \quad (\text{E.1})$$

k'_r is the rate constant of the forward reaction of reaction r and k''_r the rate constant of the reverse reaction, $C_k = \frac{Y_k}{M_k} \rho$ is the molar concentration of species k and $e'_{k,r}$ the species reaction order, which for elementary reactions is the same as the stoichiometric coefficient $\nu'_{k,r}$ of the reactant species k or product species $\nu''_{k,r}$ and reaction r . For three-body reactions, this procedure is extended by an effective

mixture concentration C_m that physically represents stabilization of intermediate states by absorbing collision energy:

$$\dot{r}'_r = k'_r C_m \prod_k C_k^{\epsilon'_{k,r}}, \quad \dot{r}''_r = k''_r C_m \prod_k C_k^{\epsilon''_{k,r}}, \quad C_m = \sum_k \epsilon_k C_k \quad (\text{E.2})$$

The efficiencies ϵ_k are set to unity by default if no other value is specified. The rate constants k_r for either the forward or reverse reaction are either computed from the standard three-parameter Arrhenius approach

$$k_r = A_r T^{\beta_r} \exp\left(-\frac{E_{a,r}}{\mathcal{R}T}\right) \quad (\text{E.3})$$

or as pressure dependent Lindemann falloff reactions

$$k_r = k_{r,\infty} \frac{p_r}{1 + p_r} F_r, \quad p_r = \frac{k_{r,0} C_m}{k_{r,\infty}}, \quad F_r = 1 \quad (\text{E.4})$$

$$k_{r,0} = A_{r,0} T^{\beta_{r,0}} \exp\left(-\frac{E_{a,r,0}}{\mathcal{R}T}\right), \quad k_{r,\infty} = A_{r,\infty} T^{\beta_{r,\infty}} \exp\left(-\frac{E_{a,r,\infty}}{\mathcal{R}T}\right) \quad (\text{E.5})$$

or as Troe falloff reactions, which are the same as Lindemann reactions except for the blending function F_r which is calculated as

$$\lg F_r = \left(1 + \left(\frac{\lg p_r + c}{n - d(\lg p_r + c)}\right)^2\right)^{-1} \lg F_{r,\text{cent}} \quad (\text{E.6})$$

$$c = -0.4 - 0.67 \lg F_{r,\text{cent}}, \quad n = 0.75 - 1.27 \lg F_{r,\text{cent}}, \quad d = 0.14 \quad (\text{E.7})$$

$$F_{r,\text{cent}} = (1 - \alpha_r) \exp\left(-\frac{T}{T_r^{***}}\right) + \alpha_r \exp\left(-\frac{T}{T_r^*}\right) + \exp\left(-\frac{T_r^{**}}{T}\right) \quad (\text{E.8})$$

A similar reaction type encountered in reaction mechanisms for combustion applications is SRI, which is computed like the Troe reactions but with F_r defined as:

$$F_r = \left(a_r \exp\left(-\frac{b_r}{T}\right) + \exp\left(-\frac{T}{c_r}\right)\right)^{1/(1+\lg^2 p_r)} d_r T^{e_r} \quad (\text{E.9})$$

Strongly pressure dependent rate constants can be expressed as **plog** reactions, where the rate constants are interpolated logarithmically from different pressure levels. The parameters A_r , β_r , $E_{a,r}$ for the rate constant expression k_r from Eq. (E.3) are specified at given pressure levels p_n , where P is the number of pressure levels. Additionally, there may also be more than one set of parameters for the Arrhenius parameters for each pressure level, leading to the summation in Eq. (E.10) over all K rate constants at that pressure level. Given the pressure p ,

the pressure p_n is chosen from all P pressure levels which is closest to p and $p_n \leq p$. This pressure is denoted as p_{low} . The pressure $p_{n+1} > p$ is denoted as p_{high} . The rate constants at the two pressure levels p_{low} and p_{high} are then computed from:

$$k_{r,\text{low}} = \sum_i^K k_{r,i}(p_{\text{low}}) \quad (\text{E.10})$$

$$k_{r,\text{high}} = \sum_i^K k_{r,i}(p_{\text{high}}) \quad (\text{E.11})$$

with the rate constants at the specific pressure levels $k_{r,i}(p_{\text{low}})$ and $k_{r,i}(p_{\text{high}})$ computed from Eq. (E.3). The final rate constant of the `plog` reaction is then logarithmically interpolated from pressure:

$$\hat{k}_r = e^{\log(k_{r,\text{low}}) + (\log(k_{r,\text{high}}) - \log(k_{r,\text{low}})) \frac{\log(p) - \log(p_{\text{low}})}{\log(p_{\text{high}}) - \log(p_{\text{low}})}} \quad (\text{E.12})$$

The parameters A_r , $A_r(p_n)$, β_r , $\beta_r(p_n)$, $E_{a,r}$, $E_{a,r}(p_n)$, $A_{r,0}$, $A_{r,\infty}$, $\beta_{r,0}$, $\beta_{r,\infty}$, $E_{a,r,0}$, $E_{a,r,\infty}$, α_r , T_r^* , T_r^{**} , T_r^{***} , a_r , b_r , c_r , d_r and e_r are read from the reaction mechanism file, which is provided as a text file for the simulation. If reaction r is reversible and the parameters for the reverse rate constant are not explicitly included in the reaction mechanism file, the reaction rate of the reverse reaction is computed via the equilibrium constant K_r assuming ideal gases and perfect mixtures:

$$k_r'' = \frac{k_r'}{K_r}, \quad K_r = \exp\left(-\frac{\Delta G_r^\circ}{\mathcal{R}T}\right) \left(\frac{p^\circ}{\mathcal{R}T}\right)^{\Delta\nu_r} \quad (\text{E.13})$$

p° is a reference pressure (usually 1 atm, specified in the reaction mechanism) and $\Delta\nu_r = \sum_k (\nu_{k,r}'' - \nu_{k,r}')$. The standard Gibbs free energy of formation ΔG_r° is

$$\Delta G_r^\circ = \sum_k (\nu_{k,r}'' - \nu_{k,r}') G_k^\circ, \quad G_k^\circ = \tilde{h}_k - T\tilde{s}_k \quad (\text{E.14})$$

Additionally, reactions can be marked as `duplicate` to allow rate constants of the form $k_r = \sum_i k_{r,i}$. Finally, the reaction rate of species k is obtained with:

$$\dot{\omega}_k = \dot{r}_k M_k = M_k \sum_r (\nu_{k,r}'' - \nu_{k,r}') (\dot{r}_r' - \dot{r}_r'') \quad (\text{E.15})$$

E.2 Optimization of Chemical Reaction Rate Computations

E.2.1 Operator Splitting with Sundials

Including the reaction rates directly from Eq. (E.15) as source term in the balance equation of the species masses in Eq. (3.4) generally requires extremely low time steps due to the large stiffness of the reaction mechanisms and the very small time scales of the fastest reactions. In practice, the balance equations are solved with a time step according to the fluid dynamics Δt_{CFD} . This requires that the chemical reaction rates have to be averaged over an interval Δt_{CFD} . In the DNS solver used in this work, an operator splitting technique is utilized. Before solving the balance equations, the reaction rates are integrated over the CFD time step assuming that no diffusion or convection takes place. In this way, the chemical system can be treated as a closed constant volume batch reactor given by each computational cell. The governing equations for constant volume batch reactors are a system of $N + 1$ ordinary differential equations (ODEs):

$$\int_{T(t_0)}^{T(t_0+\Delta t_{\text{CFD}})} dT = \int_{t_0}^{t_0+\Delta t_{\text{CFD}}} -\frac{\sum_k \dot{\omega}_k e_k}{\rho c_v} dt \quad (\text{E.16})$$

$$\int_{Y_k(t_0)}^{Y_k(t_0+\Delta t_{\text{CFD}})} dY_k = \int_{t_0}^{t_0+\Delta t_{\text{CFD}}} \frac{\dot{\omega}_k}{\rho} dt, \quad k = 1 \dots N \quad (\text{E.17})$$

with $c_v = c_p - \mathcal{R}/\bar{M}$ due to the assumption of ideal gases. The partial specific internal energy e_k is computed from the fundamental equation as the specific internal energy for each species:

$$e_k = \frac{\tilde{e}_k}{M_k} = \frac{1}{M_k} \left(\tilde{h}_k - \mathcal{R}T \right) \quad (\text{E.18})$$

Because the batch reactors have a constant volume, density stays constant during the integration time interval. Pressure is computed from the ideal gas equation. With the mass fractions $Y_k(t_0)$ and $Y_k(t_0 + \Delta t_{\text{CFD}})$ in a specific computational cell at the beginning of the time step, a time step averaged reaction rate is obtained which is then used as the source term in the species mass balance equation of the CFD simulation:

$$\dot{\omega}_k = \rho \frac{\partial Y_k}{\partial t} \approx \rho \frac{Y_k(t_0 + \Delta t_{\text{CFD}}) - Y_k(t_0)}{\Delta t_{\text{CFD}}} \quad (\text{E.19})$$

where $Y_k(t_0 + \Delta t_{\text{CFD}})$ is the species mass fraction in the batch reactor at the end of the integration.

The integration in Eq. (E.16) and Eq. (E.17) is responsible for a large part of the total simulation time. Therefore, it is mandatory to employ computationally efficient algorithms for the integration. In OpenFOAM®, several ODE solvers are available, like the Seulex solver [251], which in theory is well suited for this kind of problem. However, in practice, it has been demonstrated that the CVODE solver by Sundials [249, 252] achieves much better performance than the ODE solvers provided by OpenFOAM® (see appendix E.2.3). Because of this, Sundials has been included as an external library in the DNS solver to achieve efficient integration of chemical reaction rates. Sundials is a highly optimized C code that specializes in the type of stiff ODEs encountered in combustion applications. Based on user-defined tolerances, Sundials chooses the integration time step adaptively for the integration in Eq. (E.16) and Eq. (E.17). However, this leads to load imbalances, which are further discussed in appendix E.3.

E.2.2 Automatic Code Generation for Fast Chemistry Kernels

In most reactive flow simulation tools, the information about the chemical reactions, e.g. which chemical species take place during the reaction, their thermo-physical properties, the type and parameters for each chemical reaction, are provided in text files, which are usually referred to as reaction mechanisms. When the simulation is started, the information from the user specified text file is read and the chemical reaction rates are computed based on the extracted information. This method is very flexible, however it generally prevents the generation of efficient code. For example, modern compilers can emit faster machine code if parameters like the number of species or the number of reactions are known at compile time, not runtime. Another important aspect is the way that information are retrieved from memory. Modern CPUs have different levels of memory caches that can automatically load data from RAM into local caches, so called prefetching [253], and avoids cache misses. This works best if all memory access occurs in a linear way [254]. Additionally, modern CPUs can execute operations like addition and multiplication on more than one number at a time, which is called SIMD (single instruction on multiple data) or vectorization. However, to utilize this feature, the code has to be generated in a specific way. Lastly, additional time savings during computation of chemical reaction rates can be achieved by recognizing redundant operations. For example, if the activation energy $E_{a,r}$ of a reaction is zero, the expensive exponential term in Eq. (E.3) becomes unity and can be ignored in the computation.

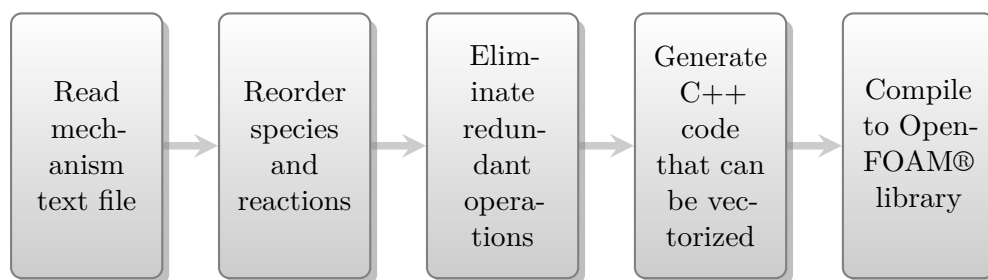


Figure E.1: Working principle and work flow of the converter tool that automatically generates highly optimized C++ code for computing chemical reaction rates.

To enable the computation of chemical reactions in the most efficient way, a converter tool has been developed that automatically generates highly optimized C++ code containing chemistry kernels for computing chemical reaction rates for one specific reaction mechanism. This means, that instead of having a general code like OpenFOAM® that computes reaction rates based on arbitrary reaction mechanisms, different automatically generated codes that are each optimized for one specific reaction mechanism are used.

The working principle of the converter tool is given in Fig. E.1. First, the converter tool reads the text file of the chosen reaction mechanism. Then, reactions of the same type are grouped together as well as species that share the same temperature ranges for their thermo-physical properties. In this way, vectorization can be enabled in a later step described further below and code-branching is minimized. Following this, redundant operations are eliminated. This includes eliminating the evaluation of the exponential function for reactions where the activation energy is zero, or re-using the result of the exponential function evaluation for reactions that have the same activation energy. Then, C++ source code is automatically generated that lays out all information tightly packed and linearly in memory. All loops in the code are written in a way that enables auto-vectorization by the compiler. Additionally, all parameters like the number of reactions and species are now known to the compiler at compile time, which enables optimal decisions regarding loop unrolling. Compiling the automatically generated C++ code results in an OpenFOAM® library, that can be directly used in the reacting flow simulation.

As an example to showcase the converter tool, parts of the automatically generated C++ source code of the popular GRI 3.0 [255] reaction mechanism are presented. The mechanism contains 58 chemical species and 325 chemical reactions. A performance critical step is the computation of rate constants, as it involves the

Reaction	A_r	b_r	E_r
...			
HCCO+NO<=>HCNO+CO	0.900E+13	0.000	0.00
HCNO+H<=>H+HNCO	2.100E+15	-0.690	2850.00
HCNO+H<=>OH+HCN	2.700E+11	0.180	2120.00
HCNO+H<=>NH2+CO	1.700E+14	-0.750	2890.00
HOCN+H<=>H+HNCO	2.000E+07	2.000	2000.00
CH3+N<=>H2CN+H	6.100E+14	-0.310	290.00
CH3+N<=>HCN+H2	3.700E+12	0.150	-90.00
NH3+H<=>NH2+H2	5.400E+05	2.400	9915.00
...			

Figure E.2: Example of the reaction parameters specified in the GRI 3.0 reaction mechanism for a subset of reactions.

evaluation of the exponential function. Compared to Eq. (E.3), the temperature term and pre-exponential factor is evaluated in the argument of the exponential function to avoid additional exponentiation and multiplication:

$$k_r = \exp\left(\log(A_r) + \beta_r \log(T) - \frac{E_{a,r}}{\mathcal{R}T}\right) \quad (\text{E.20})$$

The parameters A_r , β_r and $E_{a,r}$ are given in the reaction mechanism text file, as shown in Fig. E.2.

The automatically generated chemistry kernel that computes the rate constants according to Eq. (E.20) is shown in Fig. E.3. This example serves to showcase many of the previously described optimizations. In lines 1–8, all information about the parameters A_r , b_r (logarithmically) and $E_{a,r}$ are laid out linearly in memory. Although the GRI 3.0 reaction mechanism contains 325 reactions, the rate constants for a total of 354 reactions have to be calculated due to falloff type reactions. However, as lines 14–19 show, only for 228 out of the 354 rate constants, the exponential function in Eq. (E.20) has to be evaluated. Since each memory access inside the loop in line 14 is consecutive, the loop can be auto-vectorized by the compiler. Additionally, the loop counter is a compile-time constant, giving the compiler more information for optimizations.

The reason why only 228 reactions require the full computation of the rate constant is given in the subsequent lines in Fig. E.3. In lines 21–27, the rate constants for reactions are computed where the activation energy $E_{a,r}$ is zero and the temperature exponent β_r is a small integer n . They can be computed efficiently as

$$k_r = A_r T^n \quad (\text{E.21})$$

```

1 alignas(64) static constexpr double A[354] =
2     {3.6558396000357360e+00, 9.1726385047921717e+00, ... };
3
4 alignas(64) static constexpr double b[228] =
5     {2.7000000000000000e+00, 2.0000000000000000e+00, ... };
6
7 alignas(64) static constexpr double E_R[228] =
8     {3.1501544760183583e+03, 2.0128782594366505e+03, ... };
9
10 auto invT = 1./T;
11 auto logT = std::log(T);
12 // compute the 228 rate constants for which an
13 // evaluation of the exponential function is necessary
14 for (unsigned r = 0; r != 228; ++r) {
15     auto blogT = b[r]*logT;           //  $b_r \log(T)$ 
16     auto E_RT = E_R[r]*invT;         //  $E_{a,r}/\mathcal{R}T$ 
17     auto diff = blogT - E_RT;
18     k[r] = std::exp(A[r] + diff);
19 }
20
21 // six rate constants with  $E_{a,r}=0$  and  $b_r$  a small integer
22 auto tmp0 = invT*invT;
23 for (unsigned i = 0; i != 2; ++i)
24     k[i+228] = A[i+228]*tmp0;         //  $k_r = A_r T^{-2}$ 
25 auto tmp1 = invT;
26 for (unsigned i = 0; i != 4; ++i)
27     k[i+230] = A[i+230]*tmp1;       //  $k_r = A_r T^{-1}$ 
28
29 // 100 rate constants with  $E_{a,r}=0$  and  $b_r=0$ 
30 for (unsigned i = 0; i != 100; ++i)
31     k[i+234] = A[i+234];
32
33 // 20 rate constants where  $E_{a,r}$  and  $b_r$  are the same as for
34 // other rate constants that have already been computed
35 for (unsigned i=0; i != 20; ++i)
36     k[i+334] = A[i+334]*k[i+209];

```

Figure E.3: Automatically generated chemistry kernel for the computation of rate constants for the GRI 3.0 reaction mechanism.

Lines 29–31 cover reactions where both the activation energy and the temperature exponent are zero, so that the rate constant computation reduces to

$$k_r = A_r \quad (\text{E.22})$$

In the GRI 3.0 reaction mechanism, this is the case for 100 out of the over 300 reactions. Lastly, lines 33–36 cover reactions where both the activation energy and temperature exponent are the same as for other reactions, so that their values can be re-used. This means that the pre-exponential factor A_r for these reactions is stored divided by the pre-exponential factor of the reaction where the two other parameters are the same.

Compiling the chemistry kernel for the rate constants in Fig. E.3 with full optimizations with the Intel compiler leads to highly efficient machine code. The machine code corresponding to the loop in lines 14–18 is given in Fig. E.4. The instructions for multiplication `vmulpd`, addition `vaddpd` and subtraction `vsubpd` all end in the postfix `pd`, which stands for packed double. This means that each operation inside the CPU acts on four numbers at the same time, proving that the loop has been successfully vectorized. Additionally, the call to the exponential function has been replaced by the compiler with a call to the function `__svml_exp4`, which is the optimized and vectorized version of the exponential function from Intel’s short vector math library.

The second instance where an evaluation of the exponential function is required, is in the computation of the equilibrium constant from Eq. (E.13). The corresponding automatically generated chemistry kernel for the GRI 3.0 reaction mechanism is shown in Fig. E.5. Here, two additional features can be seen. First, the arguments to the function in line 1 and 2 are annotated with `RP`. This is a macro defined depending on the C++ compiler, that corresponds to C’s `restrict` feature. It

```

1 // b[r]*logT
2 vmulpd b(,%r15,8), %ymm8, %ymm1
3 // E_R[r]*invT
4 vmulpd E_R(,%r15,8), %ymm9, %ymm3
5 // A[r]+blogT
6 vaddpd A(,%r15,8), %ymm1, %ymm2
7 // A[r]+diff
8 vsubpd %ymm3, %ymm2, %ymm0
9 // exp(A[r]+diff)
10 call __svml_exp4

```

Figure E.4: Machine code for the loop that computes the rate constants from Eq. (E.20).

```

1 void compute_Kc_gri30(double* RP k_rev,
2   const double* RP G, double T) noexcept
3 {
4   k_rev = (double*)_builtin_assume_aligned(k_rev, 64);
5   G      = (const double*)_builtin_assume_aligned(G, 64);
6
7   // log(p°/(RT))
8   auto logP_RT = std::log(1.0132e+05/(8.3144621e+03*T));
9
10  k_rev[0]   = -2.0 * G[2] + G[3] + logP_RT;
11  k_rev[1]   = -G[1] - G[2] + G[4] + logP_RT;
12  // skip ...
13  k_rev[307] = G[3] - G[6] - G[46] + G[47];
14  k_rev[308] = -G[12] + 2.0 * G[25] - G[46];
15
16  for (unsigned i = 0; i != 309; ++i)
17    k_rev[i] = std::exp(k_rev[i]);
18 }

```

Figure E.5: Automatically generated chemistry kernel for the computation of the equilibrium constant according to Eq. (E.13) for the GRI 3.0 reaction mechanism.

tells the compiler that the memory pointed to by the pointers `k_rev` and `G` will only be accessed through these pointers. This prevents aliasing and makes it possible for the compiler to auto-vectorize certain loops. Another feature is shown in lines 4–5: the input argument pointers are annotated with alignment information. In this case, the vector register size inside the CPU is 64 bytes. Previously, the arrays for `k_rev` and `G` have been allocated with 64 byte alignment. By annotating the two pointers with this information, the compiler is able to create a better vectorized version of this loop than without the annotation. In lines 10–14, the Gibbs enthalpies for the reactions according to Eq. (E.14) are computed and the equilibrium constant is finally evaluated in line 17.

The loop in lines 16–17 can be vectorized again due to the correct memory layout of the data and the annotations concerning aliasing and alignment. Figure E.6 shows the machine code generated by the Intel compiler with full optimizations. Again, all instructions operate on four values at the same time and the optimized version of the exponential function from Intel’s short vector math library is used.

For more information about the converter tool and the presented examples, see [228, 256–258].

```

1  ..B1.2:
2      mov     r12d, esi
3      vmovupd ymm0, YMMWORD PTR [rdi+r12*8]
4      call    __svml_exp4_19
5      add     esi, 4
6      vmovupd YMMWORD PTR [rdi+r12*8], ymm0
7      cmp     esi, 308
8      jb     ..B1.2
9      vbroadcastsd ymm0, QWORD PTR [2464+rdi]
10     call    __svml_exp4_19
11     vmovsd  QWORD PTR [2464+rdi], xmm0

```

Figure E.6: Machine code for the chemistry kernel computing the equilibrium constant from lines 16–17 in Fig. E.5 according to Eq. (E.13) for the GRI 3.0 reaction mechanism.

E.2.3 Evaluation of Performance Improvement

To evaluate the performance gain of using the automatically generated chemistry code together with the Sundials ODE solver, a simple zero-dimensional auto-ignition case is considered and compared to OpenFOAM®’s default reacting flow solver. The test case consists of a single numerical cell, representing a zero-dimensional, constant volume setup. In this way, no convection or diffusion is considered. Initially, the cell is filled with a stoichiometric mixture of methane and air at 1500 K and 1 bar. In the initial state, 0.1 mass-% hydrogen is added to speed up the ignition process. The reaction mechanism is GRI 3.0. The tolerances for the ODE solvers are set to 10^{-11} absolute tolerance and 10^{-5} relative tolerance. The simulation is performed for 0.2 ms until the mixture has auto-ignited. The total time spent on computing the chemical reaction rates t_{chem} is plotted in Fig. E.7.

All timings in Fig. E.7 are obtained on a single CPU core (see [256] for information on the hardware). The first three bars in Fig. E.7 are the timings obtained with standard OpenFOAM®. The first bar on the left is the time required with OpenFOAM®’s standard reactingFoam (RF) solver together with OpenFOAM®’s implementation of the rodas34 ODE integrator. The second bar from the left is OpenFOAM®’s reactingFoam solver with the Rosenbrock34 [259] ODE integrator and the third bar from the left OpenFOAM®’s reactingFoam solver with the seulex ODE integrator. The fourth bar from the left is the optimized DNS solver which includes the automatically generated chemistry kernels and uses Sundials’ CVODE integrator. This shows that there is a 20 times speed up with the optimized simulation tool compared to OpenFOAM®’s default solvers. It

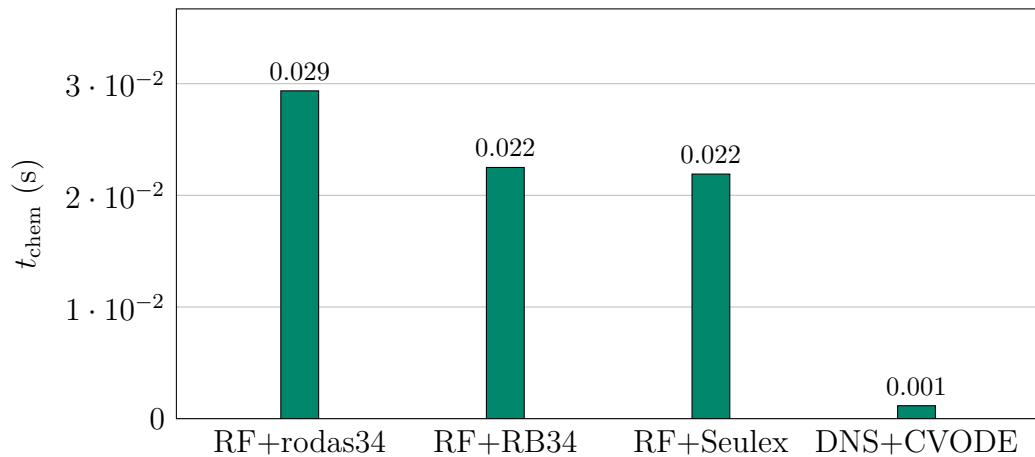


Figure E.7: Time required for computing the chemical reaction rates t_{chem} from OpenFOAM®’s standard reactingFoam solver (RF) (first three columns) together with OpenFOAM®’s implementation of the rodas34 ODE integrator (left), the Rosenbrock34 ODE integrator (second from left) and the Seulex ODE integrator (third from left). The bar on the right is the time for of the calculation of chemical reaction rates required by the optimized DNS solver using Sundials’ CVODE integrator and the automatically generated chemistry kernels.

should be noted that this speedup is achieved by using a more efficient ODE integrator together with the code optimizations in the chemistry kernels. Both optimizations do not simplify the way chemical reaction rates are computed, but use more efficient approaches to calculate the same reaction rates. In this way, the performance gain does not decrease the accuracy of the simulation.

E.3 Load Balancing

Direct numerical simulations of combustion applications have to be run on large supercomputers due to their high computational demand. If thousands or tens of thousands of CPU cores are used for the simulation, it is important that each CPU core receives the same amount of work so that processes do not have to wait for each other. This, however, is not a trivial task. For general fluid dynamic simulations, load balancing is achieved by dividing the computational domain into sub-domains, which have the same number of mesh cells, while minimizing the area between the chunks to reduce parallel communication [260, 261]. In this way, the balance equations are solved for approximately the same amount of cells on each parallel process.

This approach, where the computational load is distributed by subdividing the computational mesh before the simulation is started, has limitations. For example, if adaptive mesh refinement (AMR) is used, the mesh is locally refined or coarsened during the simulation so that the computational load of each process varies. To mitigate this problem, the mesh has to be redistributed among the processes to ensure an even workload for each CPU core.

For combustion applications using the finite rate chemistry model, load imbalances are usually caused by the operator splitting approach described in appendix E.2.1. Because a system of ODEs has to be solved in each computational cell and the time step used for the ODE integration is adaptively chosen depending on the local numerical stiffness, each cell in the mesh requires a different amount of time to compute the chemical reaction rates. In premixed flames, chemical reactions occur mostly in a thin reaction layer. Because of this, the number of cells that require a high number of integration time steps is usually small. Additionally, it is very common for engineering applications that the flame is only present in a small part of the computational domain. For example, the flow upstream of the combustion chamber might be of interest, where fuel and oxidizer are mixed but not yet burned [168, 262]. Parallel processes that get assigned a subdomain in the upstream region do not have to compute chemical reaction rates at all and therefore have to wait for processes that handle subdomains where the flame is present.

Another cause for load imbalances in simulations using the finite rate chemistry model is adaptive mesh refinement. To increase the accuracy of the simulation, the mesh corresponding to the reaction layer of the flame can be locally refined. This not only creates load imbalances because the number of cells on that process is increased, but these cells are the ones that require the most computing time for the chemical reaction rate calculations. In certain circumstances, these load imbalances can be avoided by splitting the computational mesh not according to the number of cells, but the expected workload per cell. However, such an approach only works if the position of the flame is known beforehand [263, 264]. In practical applications, the flame might be turbulent or propagate throughout the domain, so that an a priori mesh decomposition might not be possible.

Because a proper load balancing is an important issue, different approaches have been developed in the past to address this problem [265–269]. In this work, a load balancing method has been developed which utilizes the properties of the chemical system to achieve an adaptive and dynamic load balancing, which is

especially suited for very large-scale simulations and can be combined with other methods such as adaptive mesh refinement [257, 258, 270, 271].

E.3.1 Measurements

Before implementing the load balancing method, first the severity of the imbalances is assessed. A simulation of a laminar methane-air slot-burner flame from [117], using the GRI 3.0 reaction mechanism, has been performed with 100 parallel MPI [272] processes. During the simulation, all parallel communication has been monitored by the tool Extrae [273].

Figure E.8 shows the performance measurements by Extrae. Specifically, the measurements show for every parallel process, when the simulation software performs useful calculations (black) and when it performs parallel communication (blue). In the ideal case, the time spent on parallel communication on every process should be as small as possible. The measurements cover one time step from the simulation. Simulation time is depicted from left to right, where the beginning of the time step is on the left and the end of the time step on the right. Each horizontal line represents one of the parallel MPI processes.

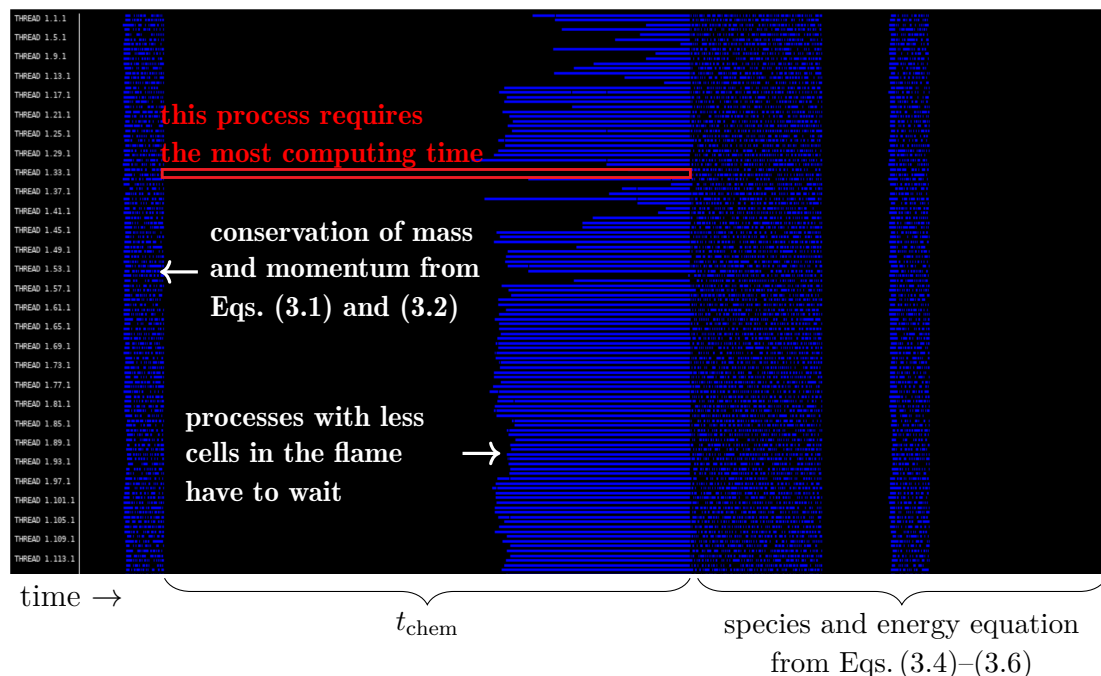


Figure E.8: Measurement of parallel communication with Extrae and visualized with Paraver [274] during one time step of a parallel flame simulation. Each row represents one process. Blue shows the time spent in communication.

The first step in a simulation time step is the solution of the balance equations of total mass and momentum (see Eq. (3.1) and Eq. (3.2) from chapter 2). This is represented in Fig. E.8 by the first column of short messages (blue) on the left. The next step is the calculation of the chemical reaction rates, indicated on the bottom by t_{chem} . In this case, the calculation of chemical reaction rates from the GRI 3.0 reaction mechanism requires about 60 % of the total simulation time. However, the measurement shows that there are only a few processes that actually require the whole t_{chem} time interval because their subdomains happen to have more computational cells within the flame's reaction zone. Most of the processes, however, are done computing the chemical reaction rates much earlier. This can be seen in Eq. (3.1) by the difference between the process marked in red, which performs reaction rate calculations (black) from the beginning of t_{chem} until the end of t_{chem} , while most of the processes only perform their calculations during the first 75 % of t_{chem} and then have to wait (blue) until the slower processes are finished. This means, that during a quarter of the time, most processes spent waiting within parallel communication routines, leading to a very inefficient use of the hardware of high performance clusters. The last 30 % of the time step are spent on solving the species and energy balance equations Eq. (3.4)–Eq. (3.6) as well as computing the mixture properties, like heat capacities, viscosities, diffusion coefficients and temperature from enthalpy.

E.3.2 Load Balancing Implementation

To address the findings from the measurements in appendix E.3.1 and to reduce the overall time spent waiting, a new load balancing approach [270] has been developed and implemented in OpenFOAM®. It has been designed with the following properties:

- *dynamic*: the balancing of the workload is done during the simulation;
- *adaptive*: the amount of work shared between processes adapts automatically to the current simulation state;
- *composable*: can be used together with other techniques like adaptive mesh refinement and even with other load balancing approaches targeting the redistribution of mesh cells;
- *tailored to reaction rate calculations*: because chemical reaction rates are computed from the properties of a single cell only and do not depend on neighboring cells, the workload can be freely shared;

- *suitable for high performance computing*: minimizing the use of expensive all-to-all communication and focusing on pair-communication for reduced memory requirement from internal MPI buffers.

The latter property becomes important if the simulations are performed with more than ten-thousand MPI processes, where all-to-all communication significantly affects parallel scaling behavior (see also appendix E.4).

The load balancing approach is based on forming pairs of processes that share their workload. Figure E.9 shows a simplified example of the load balancing approach with five parallel processes. First, each process measures the time it takes to compute the chemical reaction rates t_{chem} . Then, the list of all processes is sorted by t_{chem} . This step requires an expensive all-to-all communication and is therefore not performed at every time step. Lastly, pairs of processes are formed that share their workload. These pairs contain the slowest and fastest process, the second slowest and second fastest process, and so on.

More specifically, the first part of the load balancing algorithm for determining the process pairs is summarized in Fig. E.10. This step is only performed every N time steps because it entails expensive all-to-all communications. The value of N depends on the type of simulation. For example, if the simulation has reached

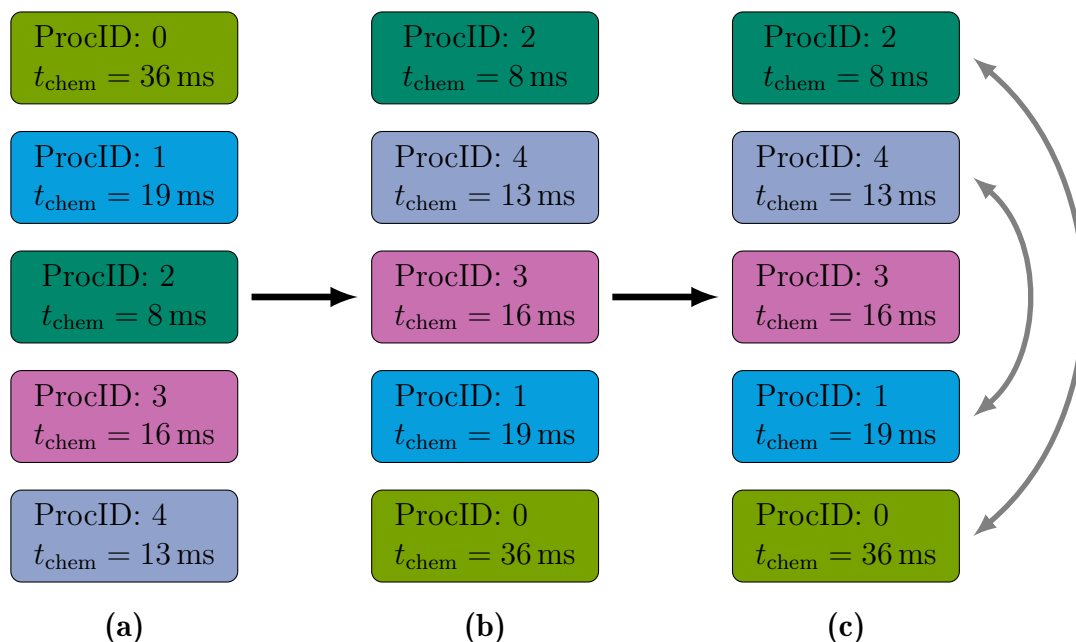


Figure E.9: Principle of the load balancing algorithm: (a) measure the time required to compute the chemical reaction rates t_{chem} on all processes; (b) sort all processes by t_{chem} ; (c) form pairs of processes between the fastest and slowest, the second fastest and second slowest, and so on.

```
1 Every N time steps:  
2 1) Create a list containing the process ID and time required  
3   for the computation of chemical reaction rates  
4 2) gather/scatter the list to all processes  
5 3) Sort the list by reaction rate computing times  
6 4) Assign pairs of processes that will share their workload
```

Figure E.10: First part of the load balancing algorithm. Every N time steps, the process pairs are determined.

steady state, the processor pairs will stay the same and this step can be done only once at the beginning of the simulation. If the flame moves rapidly throughout the domain and changes its position, for example for a turbulent flame, N is commonly set to a value of 1000. In this way, all-to-all communication is only performed when necessary.

Another important aspect of this step is that the processor pairs can be specified freely. In other load balancing approaches which address the number of computational cells on each process, the spatial relation of the cells has to be taken into account. For example, if one process has much more cells than the other processes, and one process has much less cells, the workload can only be shared between these two processes directly if they represent physically neighboring parts of the computational domain. For the reaction rate computations, however, the spatial relations of the mesh are not relevant because chemical reaction rates only depend on local properties so that the workload can be shared between two processes that have no spatial relations to each other in the computational domain. In this way, a process that contains part of the domain representing a combustion chamber can share its workload with a process having a part of the domain from an upstream nozzle without chemical reactions occurring.

The actual sharing of the workload is detailed in Fig. E.11. In each process pair, the process that requires more time for computing the chemical reaction rates is named the **sender** and the other process in the pair is the **receiver**. Based on the time for computing the chemical reaction rates of the two processes from the last time step, the **sender** computes the number of cells N_{shared} , in which the chemical reaction rates should be computed by the **receiver**. In this step, it is crucial to use non-blocking communication to hide as much communication time as possible. Therefore, the **sender** starts to send the temperature, pressure and mass fraction values from the N_{shared} cells to the **receiver** and then computes the chemical reaction rates for the rest of its cells.

```

1 Each time step:
2
3 If (sender)
4   1) Create buffer containing a list of species mass fractions,
5     temperatures and pressures of the last N_shared cells
6   2) Send the buffer to the partner process
7   3) Compute reaction rates for cells 0 to (N_cells-N_shared)
8   4) Receive reaction rates for cells with index N_shared
9     to N_cells
10  5) Send value of N_shared for the next time step to receiver
11
12 If (receiver)
13  1) Compute the reaction rates for all cells on own mesh
14  2) Receive the buffer from sender process
15  3) Compute the reaction rates for all cells in the buffer
16  4) Send additional reaction rates back to the sender process
17  5) Receive the value of N_shared for the next time step

```

Figure E.11: Implementation of workload sharing once the processor pairs have been determined.

The **receiver** first computes the reaction rates for all of its cells and then for the ones from the **sender**. It then sends back the computed reaction rates to the **sender**. For more information about the load balancing implementation, see [257, 258, 270, 271].

E.3.3 Performance Improvement

To evaluate the performance gain achieved with the new load balancing implementation in OpenFOAM®, the simulation from appendix E.3.1 is repeated with and without load balancing. Figure E.12 shows the time required for computing the chemical reaction rates t_{chem} on each of the 100 processes (MPI Rank). On the left, the measurements from one time step without load balancing are shown and on the right, measurements with load balancing.

It can be clearly seen on the left of Fig. E.12, that there are only a few processes that require much more time than the other processes. The total time for the chemistry step is determined by the slowest process (dashed black line in Fig. E.12), so that most of the processes spend a considerable amount of time waiting. By running the simulation with the new load balancing implementation, the gap between the fastest and slowest processes shrinks significantly and the total t_{chem} reduces from 20 s to 13 s, thus decreasing t_{chem} by 35 %. Even though this result is strictly speaking not optimal for a low number of parallel processes, the pair-based

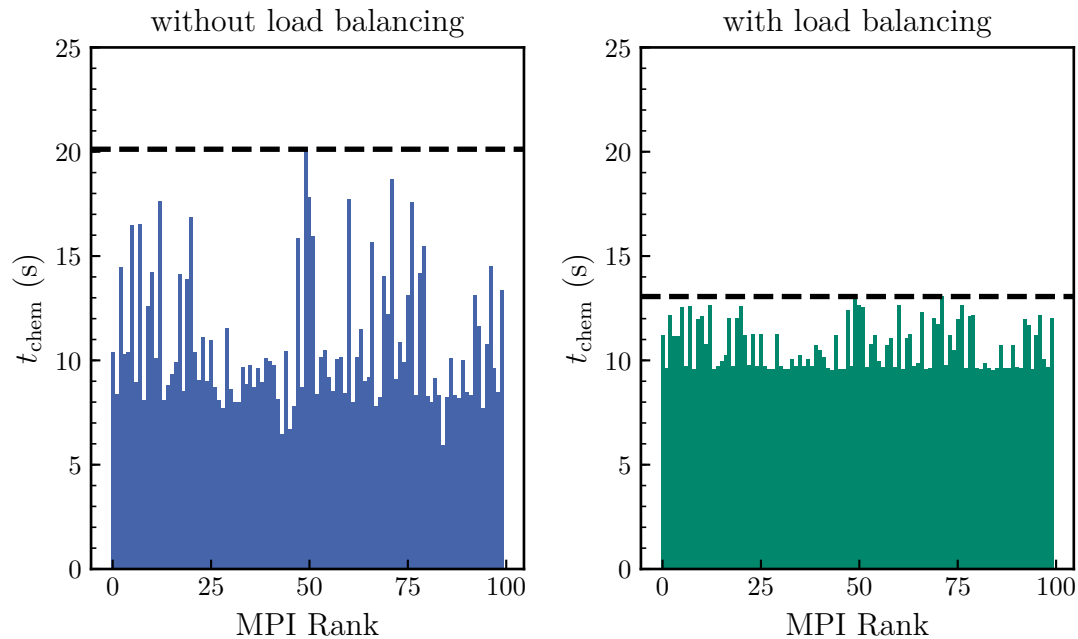


Figure E.12: Time required for computing the chemical reaction rates t_{chem} on each parallel process without (left) and with (right) the new load balancing approach.

communication of this method makes it very well suited for high numbers of parallel processes typically encountered in large-scale direct numerical simulations of combustion applications.

E.4 Parallel Scaling

One important performance metric of a simulation code used on high performance computers is its ability to scale with a large number of parallel processes. Because of this, strong scaling measurements on several high performance clusters are presented in this section.

Figure E.13 shows strong scaling results of a methane-air flame using the GRI 3.0 reaction mechanism for a jet flame [68, 275–277]. The computational mesh consists of 76.5 million finite volumes for the measurements on ForHLR II and 176 million cells for the measurements on Hazel Hen.

The ForHLR II [278] cluster at the Steinbuch Centre of Computing at the Karlsruhe Institute of Technology is composed of compute nodes with two Intel Xeon E5-2660 v3 processors and 64 GB RAM per node. The interconnect is built from InfiniBand 4X EDR. The CRAY XC40 Hazel Hen [279] supercomputer is located at the German national High Performance Computing Center Stuttgart (HLRS).

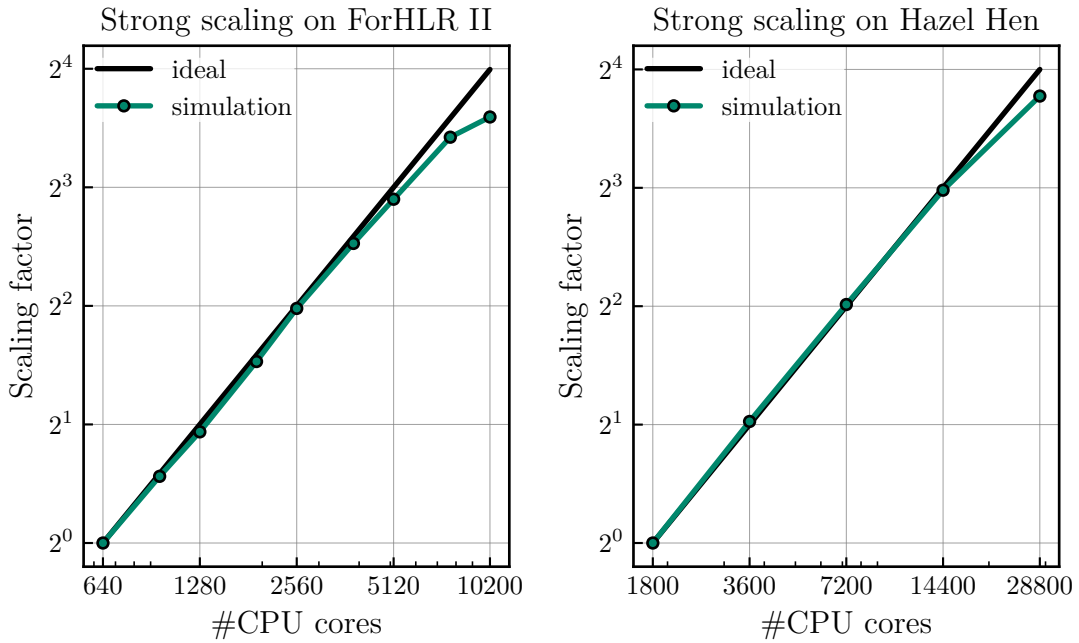


Figure E.13: Strong scaling results on the supercomputers ForHLR II and Hazel Hen on up to 28 800 CPU cores.

Its nodes are composed of two twelve-core Intel Xeon E5-2680 v3 processors and 128 GB DDR4 memory per node.

The scaling factor S_n in Fig. E.13 is computed from

$$S_n = \frac{t_{\text{tot}}(n)}{t_{\text{tot}}(n_0)} \quad (\text{E.23})$$

where $t_{\text{tot}}(n)$ is the average time for the simulation of one time step with n CPU cores and n_0 is the lowest number of CPU cores used in the measurement, i.e. 640 cores for ForHLR II and 1 800 cores for Hazel Hen. The scaling is nearly ideal, meaning a halving of simulation time with a doubling of CPU cores, up to 5 120 CPU cores on ForHLR II and 14 400 CPU cores on Hazel Hen.

Another scaling measurement is presented in Fig. E.14. In this measurement, a reduced reaction mechanism for methane-air with 24 species based on the CRECK model [280] is applied for the simulation of flame-wall interaction [281–284]. The computational mesh consists of about 200 million cells and the simulation has been performed on the supercomputer HoreKa [210] at the Karlsruhe Institute of Technology. The compute nodes are built with two Intel Xeon Platinum 8368 processors and 256 GB RAM. The interconnect uses InfiniBand HDR. Depicted

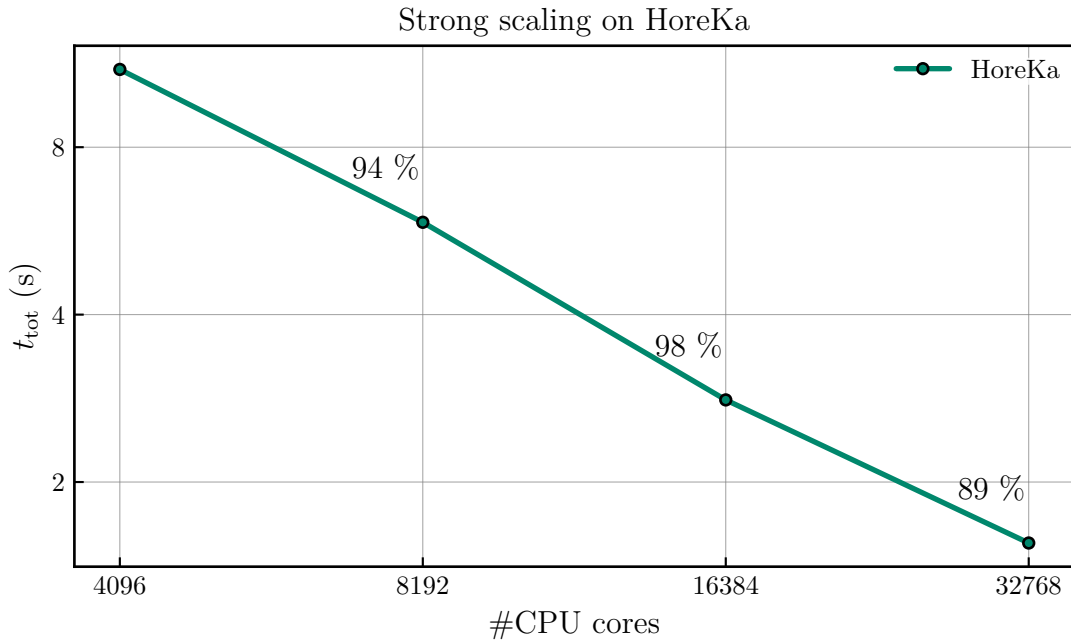


Figure E.14: Strong scaling measurements on the supercomputer HoreKa. Percentages show the scaling efficiency E_n from Eq. (E.24).

is the average time per time step t_{tot} for different numbers of CPU cores up to 32 768 cores. The percentages in the plot show the scaling efficiency from

$$E_n = \frac{t_{\text{tot}}(n_0)}{t_{\text{tot}}(n)} \frac{n_0}{n} \quad (\text{E.24})$$

with $n_0 = 4096$. Again, the scaling results are very good, achieving roughly 90 % efficiency at 32 768 CPU cores.

E.5 Summary

The performance optimizations developed for the DNS code in the context of this work have enabled the simulation of detailed flames on some of today’s largest supercomputers. The key achievements are summarized below.

- i. A converter tool has been developed that automatically generates optimized C++ source code for the computation of chemical reaction rates. The tool analyzes reaction mechanisms to avoid redundant or duplicate computations and reorders reactions and species to enable auto-vectorization. Additional performance is gained by adding information about pointer aliasing and memory alignment to the compiler.

- ii.** Together with the use of Sundials' ODE integrator, the computing time for chemical reaction rates, which can make up 60 % or more of total simulation time, is reduced by 95 % compared to the best setup with standard OpenFOAM® solvers.
- iii.** A new load balancing strategy specifically tailored to chemical reaction rate computations and optimized for large- scale simulations has been implemented into OpenFOAM®, which reduces chemistry related computation times by an additional 30 %.
- iv.** The simulation time reduction by the aforementioned optimization techniques does not lead to a decrease in accuracy, as the same computations are performed but in a computationally more efficient way.
- v.** The parallel scaling of the optimized DNS solver is very good, having a parallel scaling efficiency of 90 % with more than 32 000 CPU cores.

Appendix F

Validation of the DNS Solver

The DNS solver optimized in this work has been used in many previous studies. This includes the simulation of partially premixed flames [168, 262, 285–287], flame-wall interaction [281–283], combustion noise [68, 276], spherically expanding flames [288], Bunsen and slot burner flames [117, 289] as well as ignition phenomena [290–292]. The code parts responsible for molecular diffusion calculations has been used in [293]. In this appendix, different validation cases are presented that test the numerical accuracy of both OpenFOAM® itself and the reacting flow DNS solver.

F.1 Convection-diffusion Equation

The first validation case tests the convergence order by solving a steady-state convection-diffusion equation [143]:

$$\nabla \cdot (\rho \vec{u} \varphi) = \nabla \cdot (\Gamma \nabla \varphi), \quad Pe = \frac{\rho |u| L}{\Gamma} \quad (\text{F.1})$$

φ is an arbitrary scalar quantity and Pe is the Péclet number. The computational domain is one-dimensional, with the boundary conditions $\varphi(x = 0) = 0$ and $\varphi(x = L) = 1$. The analytic solution is

$$\varphi_{\text{exact}}(x) = \frac{\exp(xPe/L) - 1}{\exp(Pe) - 1} \quad (\text{F.2})$$

For the simulation, the mesh is built from equidistantly spaced cells with size Δx . Since all simulations in this work are performed with OpenFOAM®'s cubic interpolation scheme, it is discussed here in more detail. The values of φ at the cell faces f are computed from the cell center values C by fitting the coefficients of the polynomial:

$$\varphi(x) = ax^3 + bx^2 + cx + d \quad (\text{F.3})$$

The coefficients a – d are determined from:

$$\varphi(x = 0) = \varphi_C \quad (\text{F.4})$$

$$\varphi(x = 1) = \varphi_N \quad (\text{F.5})$$

$$\nabla\varphi(x = 0) = \nabla\varphi_C \quad (\text{F.6})$$

$$\nabla\varphi(x = 1) = \nabla\varphi_N \quad (\text{F.7})$$

where the subscript N denotes the cell center of the neighbor cell. The gradients at the cell center of the cell $\nabla\varphi_C$ and the cell center of its neighbor $\nabla\varphi_N$ are discretized explicitly with a second order central difference scheme. Introducing the interpolation factor

$$\lambda \equiv \frac{x_f - x_N}{x_C - x_N} \quad (\text{F.8})$$

where x_C is the position of the cell center, x_f the position of the cell face center and x_N the position of the cell center of the neighbor cell at face f , the final expression for the cubic scheme can be derived:

$$\begin{aligned} \varphi_f = & \underbrace{\lambda\varphi_C + (1 - \lambda)\varphi_N}_{\text{implicit}} \quad (\text{F.9}) \\ & + \underbrace{(2\lambda^3 - 3\lambda^2 + \lambda)(\varphi_N - \varphi_C) + (-\lambda^3 + \lambda^2)\nabla\varphi_C + (-\lambda^3 + 2\lambda^2 - \lambda)\nabla\varphi_N}_{\text{explicit correction}} \end{aligned}$$

Equation (F.9) has been reordered so that the first term is the standard central difference scheme, which is discretized implicitly, and the second term is an explicit correction. Due to the explicit contribution, the scheme is less stable than a fully implicit scheme and therefore low time steps ($CFL \leq 0.2$) are required for the simulation.

Figure F.1 shows the $L_{1,\text{rel}}$ error after the results have converged to a relative residuum of 10^{-7} .

$$L_{1,\text{rel}} \equiv \frac{1}{N} \sum_{i=1}^N |\varphi(x_i) - \varphi_{\text{exact}}(x_i)| \quad (\text{F.10})$$

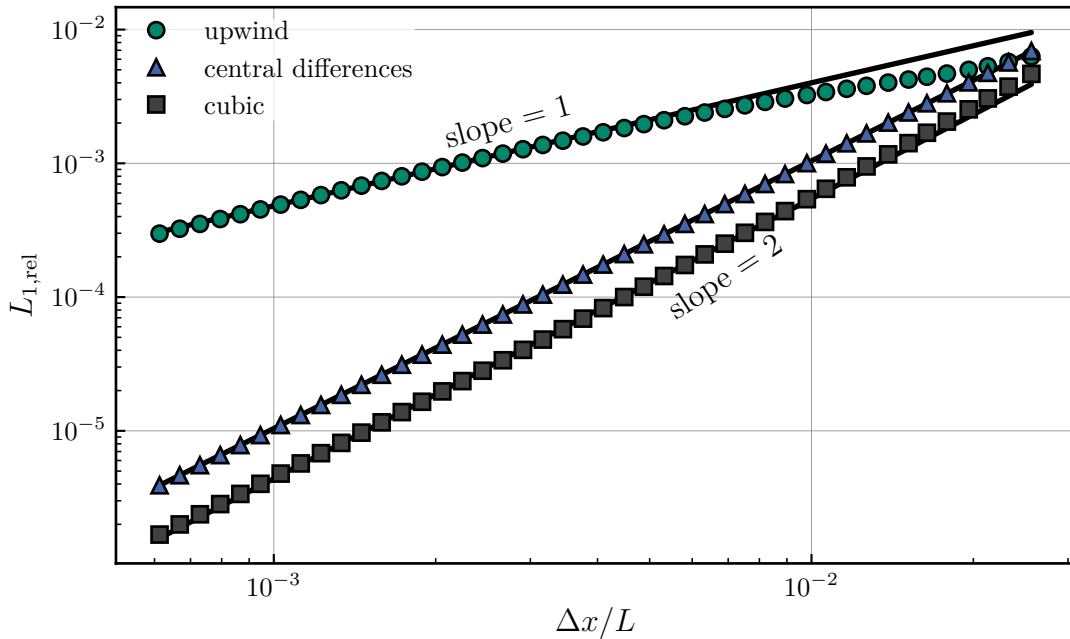


Figure F.1: $L_{1,\text{rel}}$ error for different discretization schemes and mesh resolutions computed with standard OpenFOAM®.

where N is the number of cells. For the discretization of the convective and diffusive term in Eq. (F.1), three different interpolation methods are used to compute the cell face values: the first order upwind scheme, the second order central difference scheme and the fourth order cubic scheme [144, 145].

Although the cubic interpolation scheme is formally of fourth order, the overall convergence order shown in Fig. F.1 is second order, the same as the standard central difference scheme. The reason is, that the cell face integration used in OpenFOAM® is always second order and therefore reduces the overall scheme’s convergence order to two. Nonetheless, the accuracy in terms of the $L_{1,\text{rel}}$ error is lower with the cubic scheme compared to the central difference scheme due to the more accurate face value interpolation. The upwind scheme has an expected convergence order of unity.

F.2 Taylor–Green Vortex

A popular test case for evaluating the numerical accuracy of a simulation code is the Taylor–Green vortex [294–300]. It is a transient, incompressible flow problem, where an analytic solution exists in two dimensions. In this section, the numerical accuracy of OpenFOAM®’s incompressible flow solvers are evaluated using the two-dimensional and three-dimensional Taylor–Green vortex.

F.2.1 2D Taylor–Green Vortex

The two-dimensional Taylor–Green vortex is given by:

$$u_x(x, y, t) = u_0 \sin\left(\frac{2\pi x}{L}\right) \cos\left(\frac{2\pi y}{L}\right) \exp\left(-\frac{8\pi^2 \nu t}{L^2}\right) \quad (\text{F.11})$$

$$u_y(x, y, t) = -u_0 \cos\left(\frac{2\pi x}{L}\right) \sin\left(\frac{2\pi y}{L}\right) \exp\left(-\frac{8\pi^2 \nu t}{L^2}\right) \quad (\text{F.12})$$

$$p(x, y, t) = \frac{\rho u_0^2}{4} \left(\cos\left(\frac{4\pi x}{L}\right) + \cos\left(\frac{4\pi y}{L}\right) \right) \exp^2\left(-\frac{8\pi^2 \nu t}{L^2}\right) \quad (\text{F.13})$$

The initial conditions for pressure and velocity are prescribed at $t = 0$. u_x and u_y are the x and y components of the velocity, p is the relative pressure, $u_0 = 5 \text{ m/s}$, $L = 1 \text{ m}$, $\rho = 1.172 \text{ kg/m}^3$ and $\nu = 1.5896 \cdot 10^{-5} \text{ m}^2/\text{s}$, thereby including viscous dissipation. The dimensionless time is $t_c \equiv L/u_0$.

This case represents four counter-rotating vortices placed at each corner of the computational domain that decay over time. This is illustrated in Fig. F.2 by showing the z -component of vorticity ω at $t = 0$:

$$\vec{\omega} \equiv \nabla \times \vec{u} \quad (\text{F.14})$$

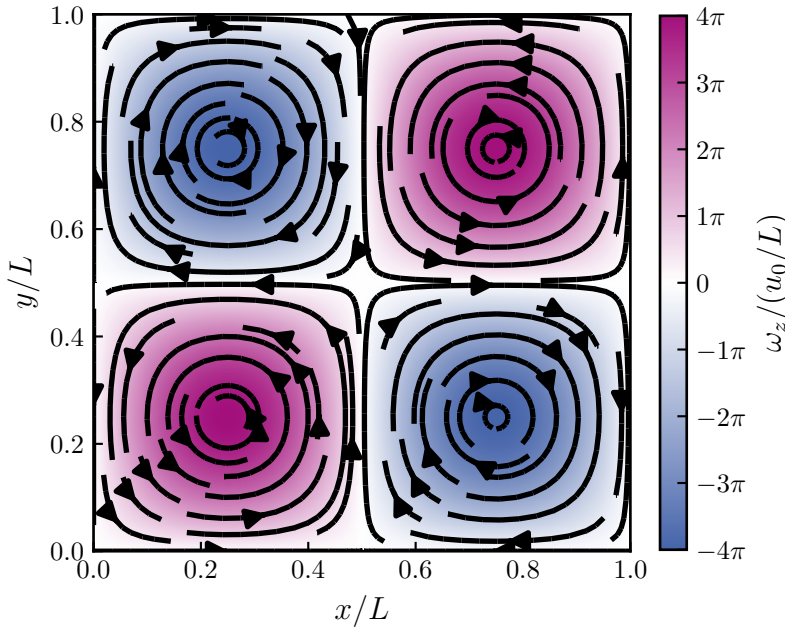


Figure F.2: Initial solution for the two-dimensional Taylor–Green vortex case, showing the z -component of vorticity.

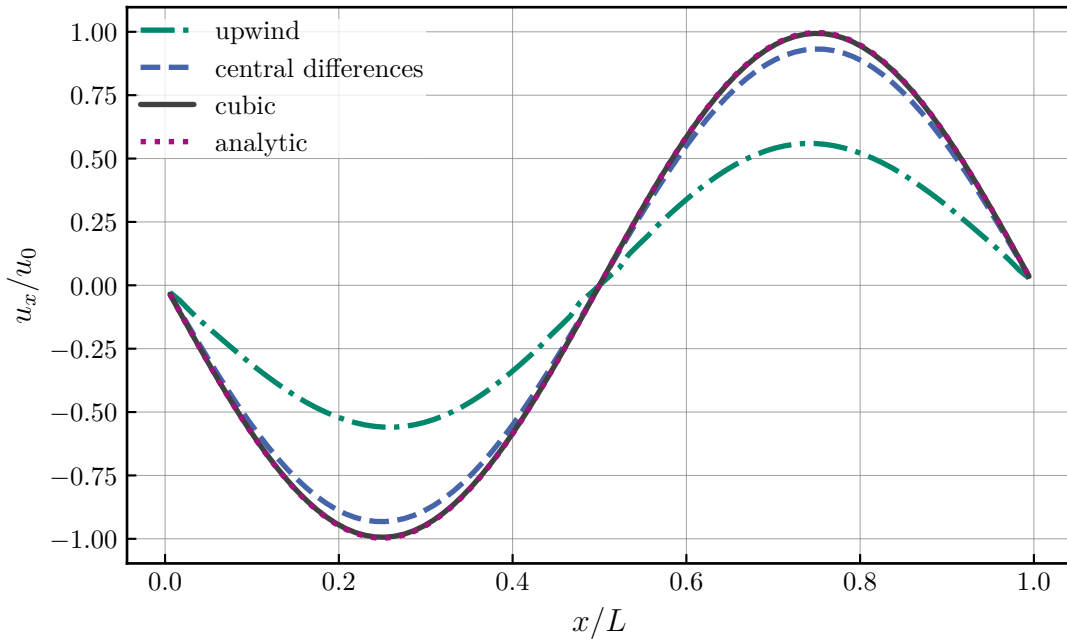


Figure F.3: x -component of the centerline velocity at $t = 10t_c$ with different discretization schemes along with the analytic solution on a mesh with 89×89 cells.

The simulation is performed with OpenFOAM®’s standard incompressible flow solver `pimpleFoam` up to $t = 10t_c$, run at a constant CFL number of 0.03. Again, the simulation is performed with the upwind, central difference and cubic schemes for spatial discretization. For temporal discretization, a first order backward Euler scheme is used in the simulation with the upwind scheme and a second order backward difference scheme for the latter two simulations.

Figure F.3 shows the x -component of velocity along the centerline at $y/L = 0.5$ and $t = 10t_c$ on a mesh with 89×89 cells. The velocity field predicted in the simulation using the first order upwind scheme decays too fast, due to the high numerical diffusion. The central difference scheme is much closer to the analytic solution, but the best results are again achieved by the cubic scheme, which shows less than 1% deviation to the analytic solution.

In the transient flow setup, the convergence order achieved with the cubic scheme can be higher than second order, depending on the mesh resolution and time step. Figure F.4 shows the L_2 error of the velocity from Fig. F.3 for different mesh resolutions.

$$L_2 \equiv \sqrt{\sum_{i=1}^N (u_x(x_i) - u_{x,\text{exact}}(x_i))^2} \quad (\text{F.15})$$

Even though the overall scheme is limited to second order, higher convergence orders can be achieved in practice depending on how sensitive the solution is to the

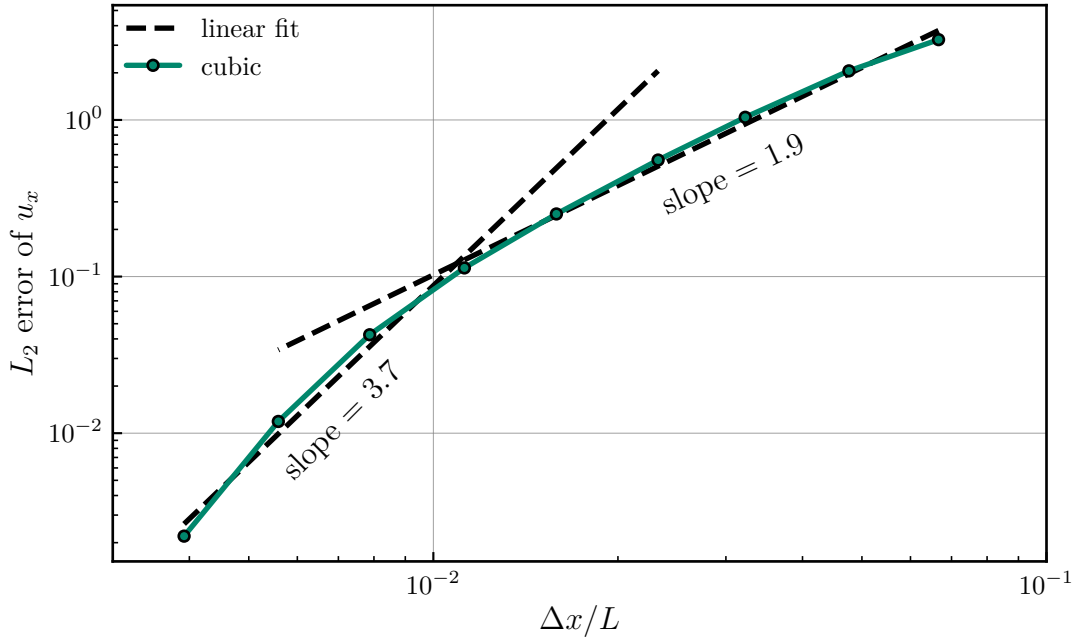


Figure F.4: Convergence order for the simulation using the cubic scheme for the two-dimensional Taylor–Green vortex case.

interpolation accuracy. This, however, is only applicable to perfectly equidistant meshes and does not transfer to the unstructured meshes usually encountered in engineering applications.

F.2.2 3D Taylor–Green Vortex

A more challenging setup is the three-dimensional Taylor–Green vortex. The initial conditions are given by:

$$u_x = u_0 \sin\left(\frac{2\pi x}{L}\right) \cos\left(\frac{2\pi y}{L}\right) \cos\left(\frac{2\pi z}{L}\right) \quad (\text{F.16})$$

$$u_y = -u_0 \cos\left(\frac{2\pi x}{L}\right) \sin\left(\frac{2\pi y}{L}\right) \cos\left(\frac{2\pi z}{L}\right) \quad (\text{F.17})$$

$$u_z = 0 \quad (\text{F.18})$$

$$p = p_0 + \frac{\rho u_0^2}{16} \left(\cos\left(\frac{4\pi x}{L}\right) + \cos\left(\frac{4\pi y}{L}\right) \right) \left(\cos\left(\frac{4\pi z}{L}\right) + 2 \right) \quad (\text{F.19})$$

with $u_0 = 1$ m/s, $L = 1$ m, $p_0 = 0$, $\rho = 1$ kg/m³. Viscosity is set to $1/1600$ m²/s.

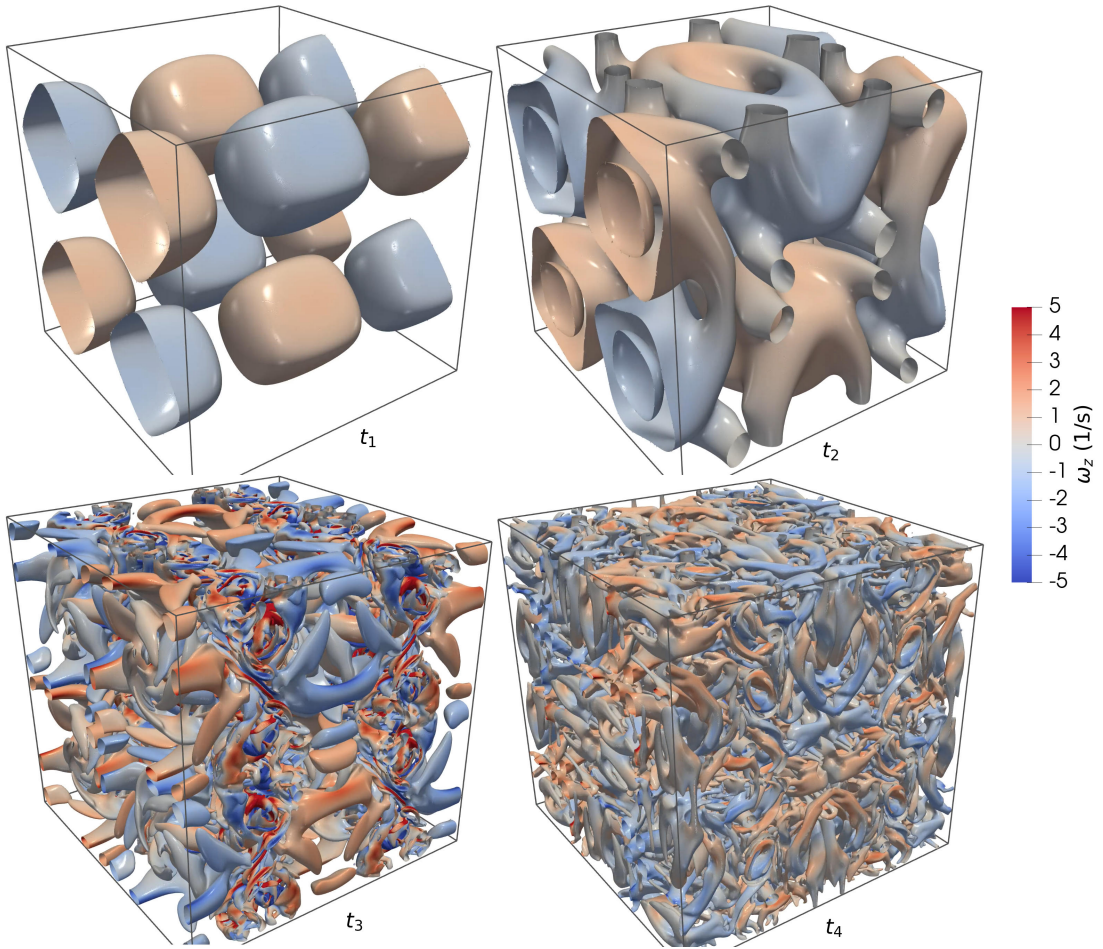


Figure F.5: Flow field of the three-dimensional Taylor–Green vortex visualized by an iso-surface of the Q -criterion, colored by the z -component of vorticity at different times $t_1 = 0.5$ s, $t_2 = 2$ s, $t_3 = 9$ s and $t_4 = 19$ s on a mesh with 512^3 cells.

Figure F.5 shows the resulting flow field. Depicted is an iso-surface of the Q -criterion at 0.1 s^{-2} , colored by ω_z .

$$Q = \frac{1}{2} \left((\text{tr}(\nabla\vec{u}))^2 - \text{tr}(\nabla\vec{u} \cdot \nabla\vec{u}) \right) \quad (\text{F.20})$$

Initially, counter-rotating vortices are placed at the corners of the cubic domain. Over time, the vortices decay into a pseudo-turbulent flow. In contrast to the two-dimensional Taylor–Green vortex, there is no analytic solution. However, there are several results from high-order codes that can be used as reference. Here, comparisons are made with a spectral DNS code [301]. The time step for the simulation is adaptively chosen so that $CFL \leq 0.2$.

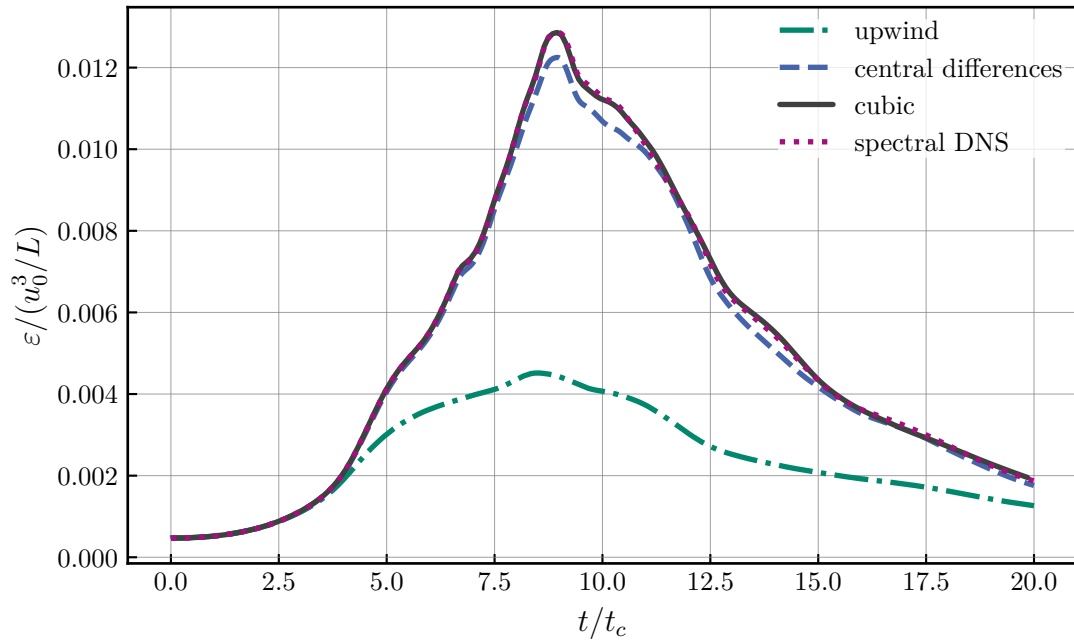


Figure F.6: Normalized volume-averaged dissipation rate over time for different discretization schemes on a mesh with 512^3 cells.

A useful quantity for evaluating the numerical accuracy is the average dissipation rate:

$$\varepsilon = \frac{2\mu}{V} \int \underline{\underline{\mathbf{S}}} : \underline{\underline{\mathbf{S}}} dV, \quad \underline{\underline{\mathbf{S}}} \equiv \frac{1}{2} (\nabla \vec{u} + (\nabla \vec{u})^\top) \quad (\text{F.21})$$

Figure F.6 shows the normalized volume-averaged dissipation rate over time for different discretization schemes on a mesh with 512^3 cells. The results from the spectral DNS have been generated on a mesh with 512^3 cells, too. Again, the first order upwind scheme shows strong deviations to the spectral DNS reference results. The central difference scheme is closer to the reference solution, but shows strong deviation especially at the peak of the dissipation rate, which are by about 5% lower than the reference data. The cubic scheme on the other hand shows good agreement with the spectral DNS on the same mesh and agrees within 1% with the reference data.

F.3 Canonical Flame Setups

To validate the performance optimizations regarding the chemical reaction rate computations described in appendix E.2 and to evaluate the accuracy of the DNS solver for reacting flows, two canonical flame setups are simulated. The evaluation is done by comparing the simulation results from the OpenFOAM®-based DNS solver with Cantera.

F.3.1 Auto-ignition

The first canonical setup is the isochoric auto-ignition. The computational domain consists formally of one cell, as the setup is zero-dimensional. It can be considered as a closed, adiabatic batch reactor (see schematic drawing in Fig. F.7). A mixture of fuel and oxidizer at a temperature above the ignition temperature is introduced into the reactor and the ignition process is simulated over time.

In this simulation, methane and air at 1600 K and 1 bar are considered for the auto-ignition. Initially, hydrogen is added to the reactor to speed up the ignition process. The initial conditions are summarized in the table in Fig. F.7. The GRI 3.0 reaction mechanism is used for the simulation.

Figure F.8 shows the temporal profiles of main (left) and intermediate (right) species during the auto-ignition process. The results from the DNS solver overlap with the results by Cantera. The maximum deviation between the two codes is below 0.01 % [168].

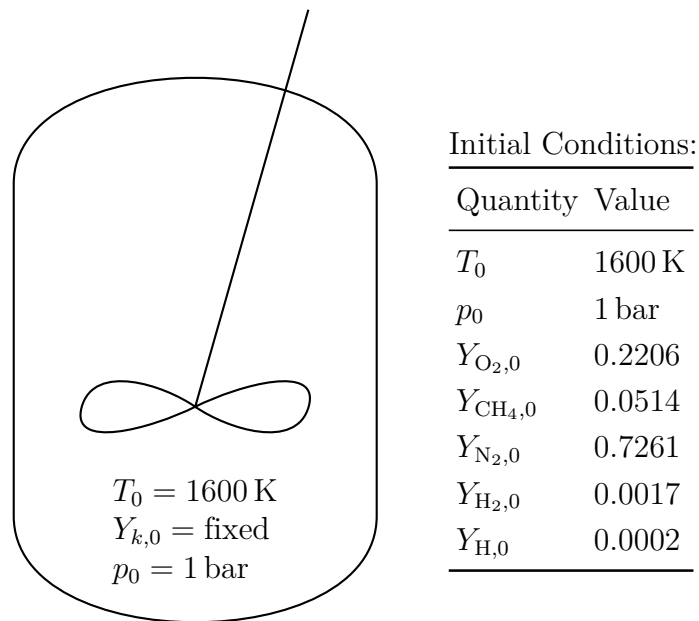


Figure F.7: For the auto-ignition case, a perfectly stirred (zero-dimensional) isochoric reactor is considered. Fuel and air are introduced with an initial temperature of 1600 K and an initial pressure of 1 bar.

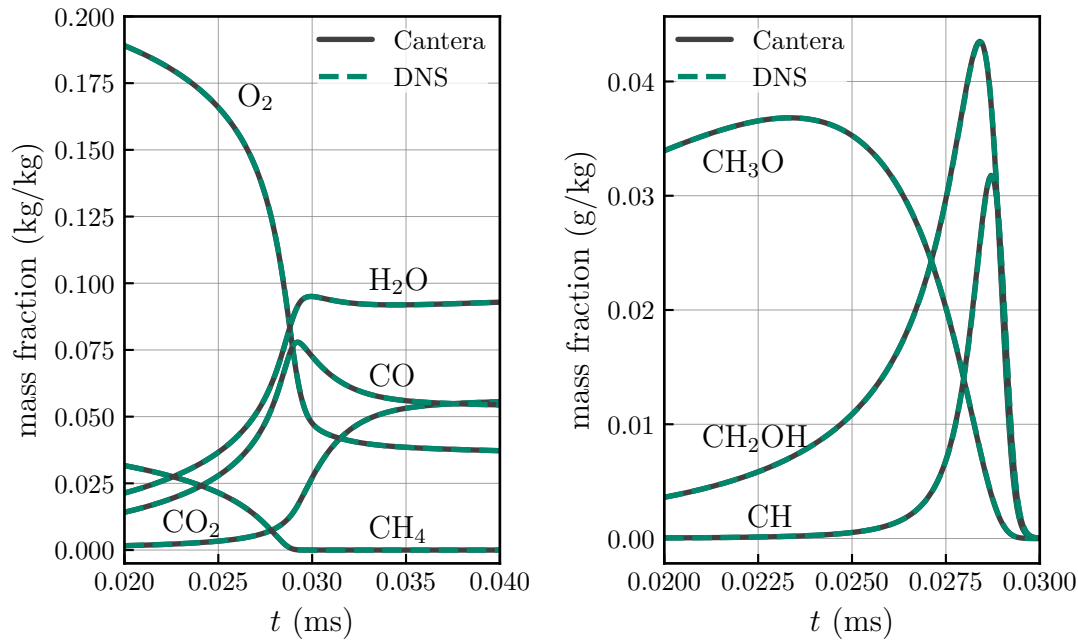


Figure F.8: Temporal profiles of main (left) and intermediate (right) species during the auto-ignition of methane and air computed with the DNS solver and Cantera.

F.3.2 Freely Propagating Flame

The second canonical flame setup is the freely propagating premixed flame. The computational domain is one-dimensional in Cartesian coordinates. Figure F.9 shows the computational domain and the boundary conditions for the DNS solver.

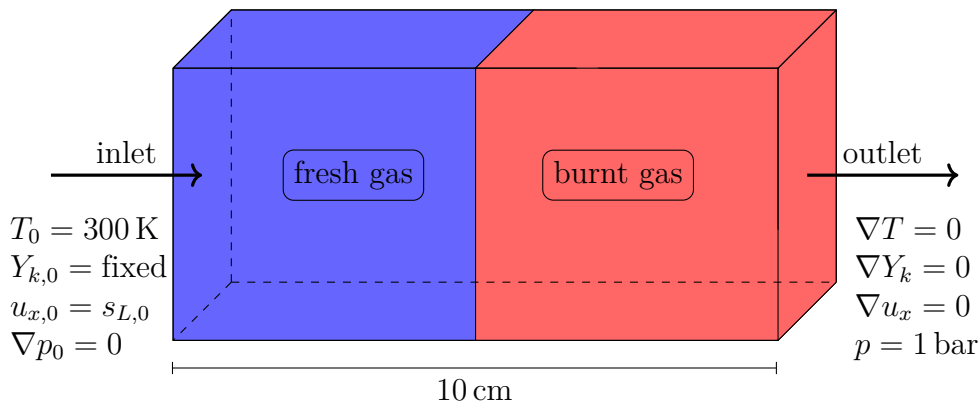


Figure F.9: Computational domain and initial conditions for the simulation of the freely propagating methane-air flame with the DNS solver. The domain is one-dimensional and the left half is initially filled with the fresh gases and the right half with the burnt gases. Mass fractions, temperature and velocity are prescribed at the inlet on the left and a zero gradient for these quantities is enforced at the outlet on the right.

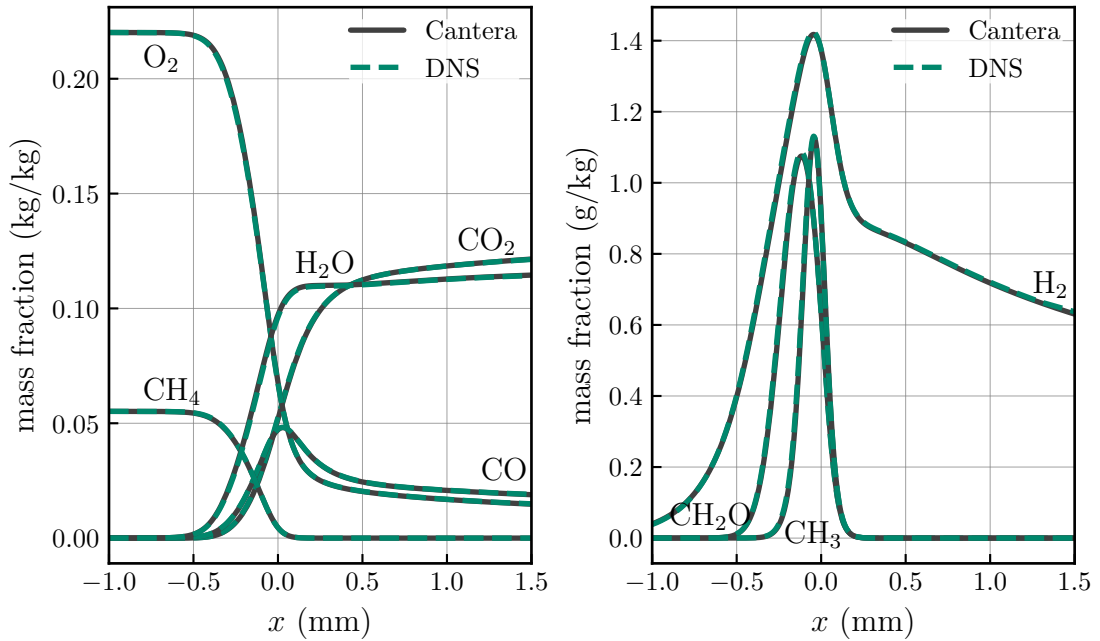


Figure F.10: Spatial profiles of main (left) and intermediate (right) species through the freely propagating methane-air flame computed with the DNS solver and Cantera in the steady state.

Compared to the previous setup, diffusion plays an important role for this flame and therefore the detailed computation of transport coefficients is mandatory. For the simulation, a methane-air mixture at the inlet with an equivalence ratio $\phi = 1$ is prescribed. Again, the GRI 3.0 reaction mechanism is used. The inlet velocity is set to the laminar flame speed determined by Cantera. Initially, the left half of the domain is filled with the unburnt mixture and the right half of the domain with the burnt mixture. At the beginning of the simulation, the unburnt gas near the center ignites and the freely propagating flame develops. After the steady state is reached, the species profiles can be compared to Cantera.

Figure F.10 shows the spatial profiles of main (left) and intermediate (right) species through the freely propagating methane-air flame computed with the DNS solver and Cantera in the steady state. The profiles are aligned so that the location of the maximum heat release rate is located at $x = 0$. Even though different meshes are used (an equidistant mesh in OpenFOAM® with a resolution of $12.5 \cdot 10^{-6}$ m and an adaptively refined mesh in Cantera with a smallest resolution of 10^{-7} m), maximum deviation between the species profiles is below 0.5%.

F.4 Comparison with Experimental Measurements

The last validation case presented in this appendix is the direct comparison with experimental measurements from a laboratory-scale turbulent partially premixed flame, known as the Sydney/Sandia flame [302–305], that has been extensively measured experimentally. Due to the fuel and oxidizer being partially premixed before the flame is ignited, it is a challenging setup for numerical simulations [306–310].

The simulation has been performed in three parts. Here, only the most important aspects are mentioned. For a full description, see [168]. The Sydney burner is simulated in configuration FJ200-5GP-Lr75-57. In this setup, air enters from the annular pipe on the left of Fig. F.11 with $\bar{u}_{\text{air}} = 59.5$ m/s and methane with $\bar{u}_{\text{CH}_4} = 67$ m/s. Along pipe (A), air and methane mix partially. The simulation is performed for domain (B), where a hot pilot consisting of methane-air at chemical equilibrium and $\bar{u}_{\text{pilot}} = 26.6$ m/s ignites and stabilizes the flame. On the outside, a cold air co-flow entering with $\bar{u}_{\text{co-flow}} = 15$ m/s is present.

The simulation domain for (B) consists of 150 million cells with local refinement and a smallest radial resolution of 10^{-5} m. An analytically reduced reaction mechanism by Lu et al. [311] is employed, which includes 19 species and 11 additional quasi-steady state species. The simulation has been performed on Hazel Hen [279], the fastest supercomputer in Germany at that time, on up to 28 800 CPU cores.

The comparison of time mean and root mean squared (rms) radial profiles of the axial velocity component between experiment and simulation is shown in Fig. F.13. The profiles are recorded at different axial positions x/D , where $D = 7.5$ mm is the nozzle diameter of the partially premixed mass flow (see also Fig. F.11).

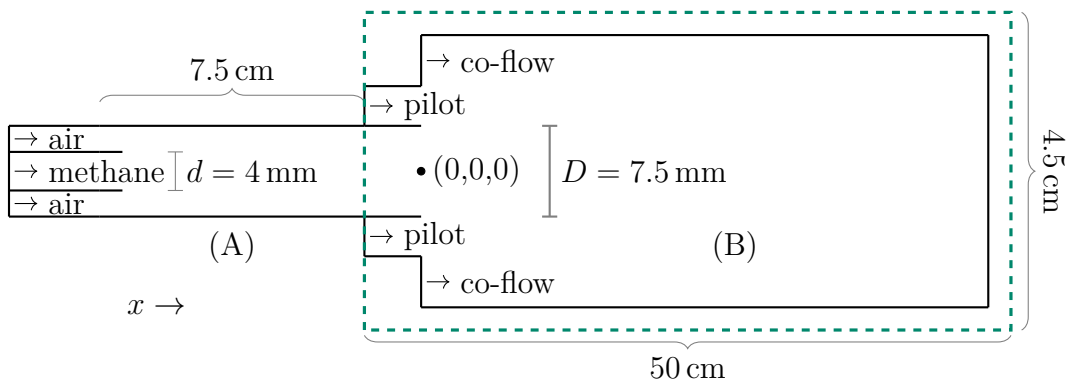


Figure F.11: Schematic view (not to scale) of the simulation setup. Methane and air enter from separate pipes on the left and partially mix in pipe (A). A hot pilot in domain (B) ignites and stabilizes the flame.

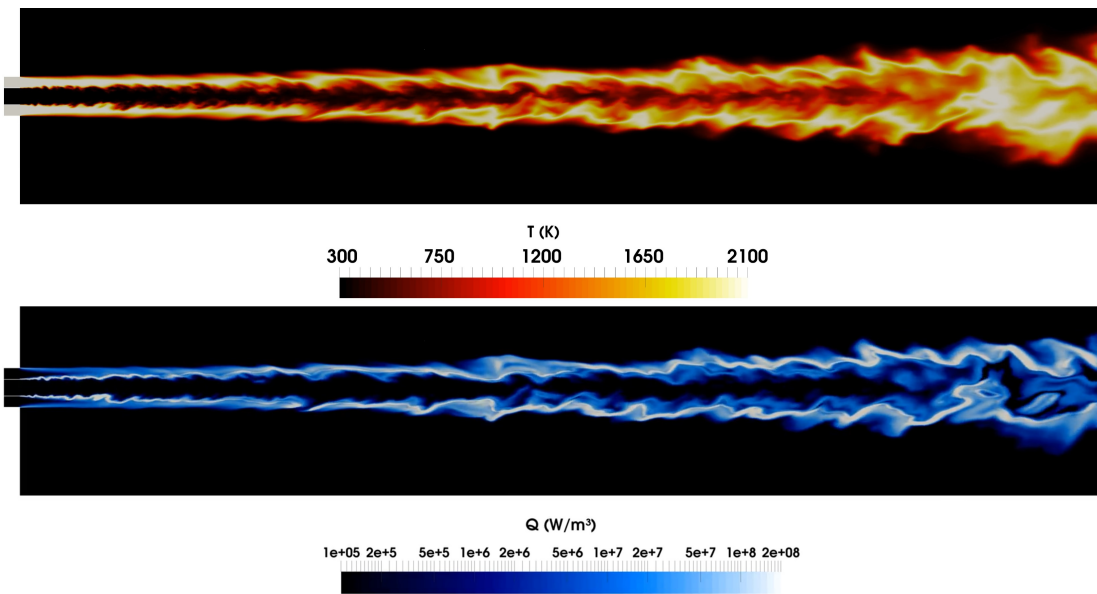


Figure F.12: Instantaneous snapshot of the temperature field (top) and heat release rate (bottom) on a two-dimensional cutting plane in domain (B) from Fig. F.11.

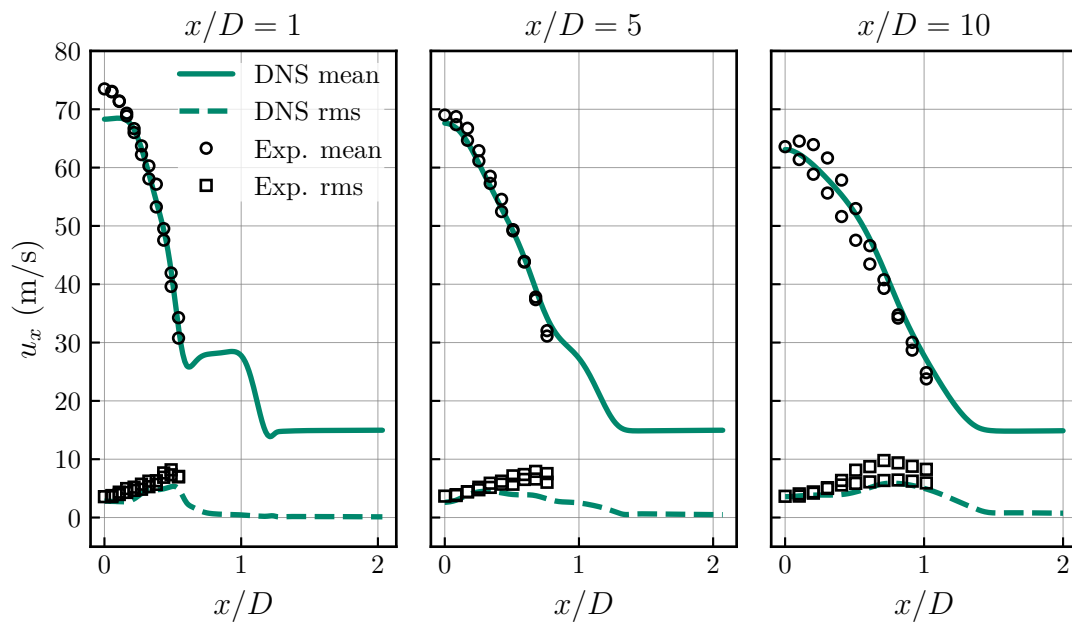


Figure F.13: Mean and rms values of the axial velocity at different axial positions x/D from simulation and experiments [304].

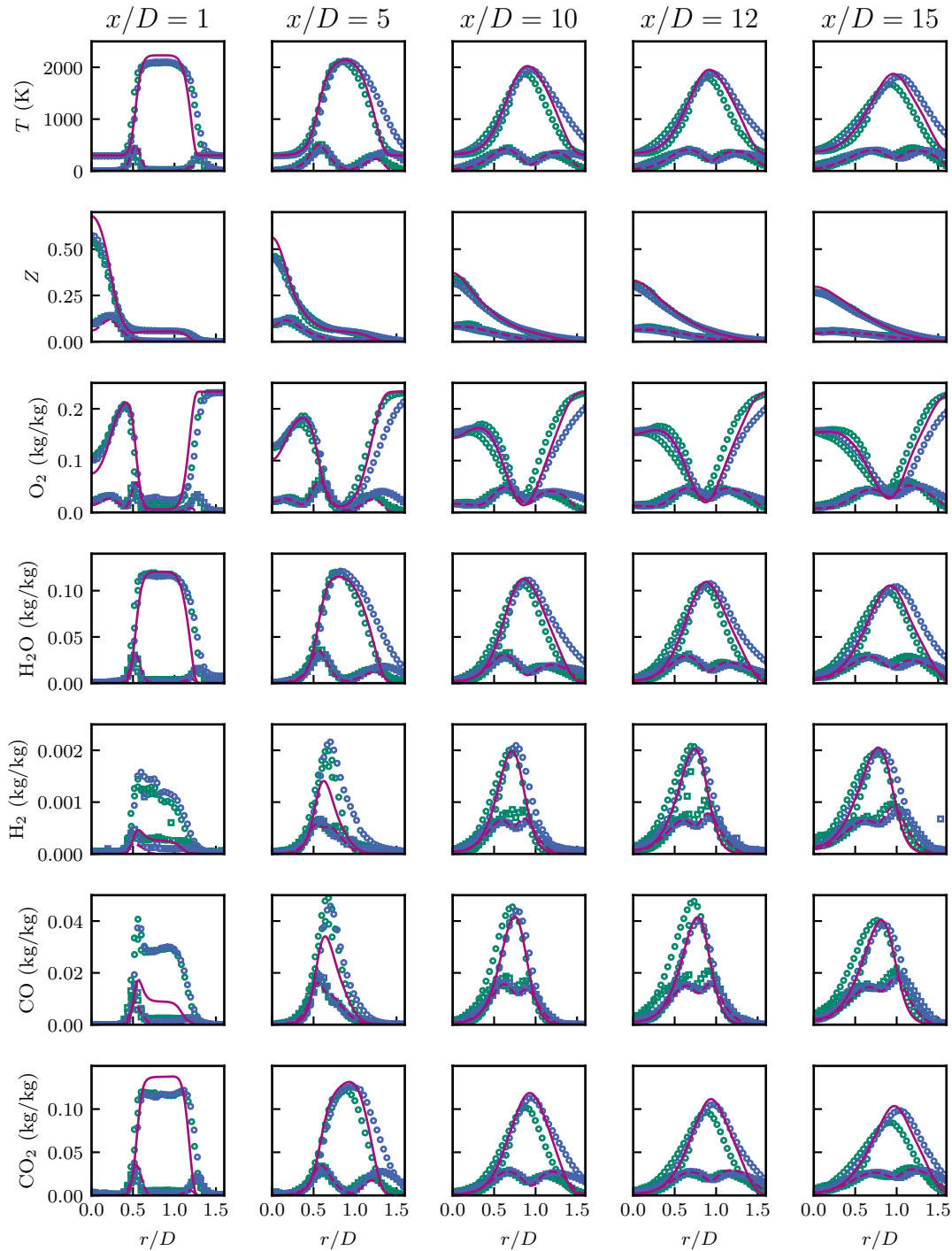


Figure F.14: Reynolds averaged mean and rms values of radial temperature T , mixture fraction Z and mass fraction distributions (top to bottom) at different axial positions (left to right). — Mean from simulation. ○ Mean from Exp. 2013 (I2013-5GP). ○ Mean from Exp. 2015 (I2015-5GP). - - - rms from simulation. □ rms from Exp. 2013. □ rms from Exp. 2015 [304].

The mean and rms values of the radial profiles of temperature T , mixture fraction Z and mass fractions at different axial locations x/D are given in Fig. F.14. The plot contains two measurements, one from 2013 and one from 2015. The overall agreement between simulation results and experimental measurements is very good. There are however some deviations. These are located mainly near the nozzle at $x/D = 1$. There are two main reasons for these deviations: First, the pilot flow in the experiment is a five-component mixture, instead of a purely methane-air mixture before it is burnt. Secondly, the pilot flow is not fully burnt when it enters domain (B) in the experiment, but is assumed to be perfectly at chemical equilibrium in the simulations. This leads to differences in the recorded CO and H₂ profiles, which vanish further downstream. For a more detailed discussion, see [168].

List of Figures

1.1	Correlation between flame speed and flame stretch of a lean premixed laminar steady hydrogen-air Bunsen flame and a turbulent premixed lean hydrogen-air flame.	5
2.1	Different time scales evaluated from freely propagating flames at atmospheric conditions.	16
2.2	Composed Borghi-Peters regime diagram for premixed flame-turbulence interaction.	17
2.3	Stretch resulting from gradients of the absolute velocity \vec{w} along the surface ($\nabla_t \cdot \vec{w} \neq 0$).	22
2.4	Flame stretch $K = \nabla_t \cdot \vec{w}$ expressed by different terms.	24
2.5	Simplified visualization of tangential strain. As a surface is pulled apart in a tangential direction, the area of its surface elements δA changes.	25
2.6	A curved surface moving normal to itself will always increase or decrease its surface area, depending on whether the curvature is convex or concave in relation to the direction of movement.	25
2.7	Diffusive fluxes of energy \vec{q} and species \vec{j}_k at a curved flame front.	26
3.1	Working principle of the in-house DNS solver. OpenFOAM®'s capabilities for solving the balance equations with the finite volume method are combined with Cantera's abilities to compute detailed thermo-physical properties and transport coefficients.	41
3.2	Movement of two flame particles located on an iso-surface of φ at $t = t_0$	45
3.3	Illustration of the first steps from the new flame particle tracking method.	49

List of Figures

3.4	After moving the flame particle (red sphere) to its new position, the shortest distance between the particle and the iso-surface ΔC is computed to correct the particle position.	51
3.5	Two flame consumption speed particles are generated at each flame particle position in each time step of the simulation.	54
3.6	Time for one simulation time step t_{tot} at varying number of parallel processes without particle tracking and with 500 000 flame particles.	56
3.7	One-dimensional domain for spherical symmetry, which is formally represented by a prism shaped block.	58
3.8	Position of the flame particle x_{FP} , temperature at the flame particle position over time and total movement velocity \vec{w} compared against the simplified evaluation valid for a one-dimensional spherical flame.	59
3.9	Validation of the routines computing the curvature (left) as well as total flame stretch K and aerodynamic strain rate K_s (right) for the spherically expanding flame.	60
3.10	Breakup of a liquid jet (yellow region) embedded in a turbulent gas flow.	61
4.1	Laminar flame speed $s_{L,0}$ from unstretched 1D calculations in dependence on the equivalence ratio ϕ for hydrogen-air and methane-air flames at atmospheric conditions.	64
4.2	Initial state of the harmonically oscillating equivalence ratio simulations. The domain has a total length of $60 \delta_{\text{th,max}}$	66
4.3	Snapshot of the spatial profile of equivalence ratio and temperature at the time $t \cdot f = 1.75$ for a hydrogen-air flame oscillating with $f = 1/(20\tau_c)$ and relative amplitude of $\phi_a = 0.1$	68
4.4	Global consumption speed computed at every time point during the oscillation of the upstream equivalence ratio for different frequencies f and constant relative amplitude $\phi_a = 0.05$ around $\phi_0 = 0.7$	70
4.5	Comparison of the flame's response in terms of the global consumption speed for different oscillation amplitudes.	71
4.6	Comparison of the flame's response in terms of the global consumption speed for different ϕ_0 and same ϕ_a	71
4.7	Response of a methane-air flame at $\phi_0 = 0.909$ to upstream equivalence ratio oscillations with $\phi_a = 0.05$ and different frequencies.	73
4.8	Summary of the consumption speed amplitude response of the hydrogen flames to different frequencies and amplitudes of equivalence ratio oscillations.	73

4.9	Summary of the consumption speed amplitude response of methane flames to different frequencies and amplitudes of equivalence ratio oscillations.	74
4.10	Generation of the initial solution.	76
4.11	Temporal evolution of the flame's consumption speed s_c when changing the equivalence ratio instantaneously.	78
4.12	Normalized flame relaxation time \hat{t}_{relax} as a function of ϕ_2 for different ϕ_1 , valid for both lean hydrogen and methane flames at atmospheric conditions.	79
4.13	Computational domain and boundary conditions for the oscillating Bunsen flames.	83
4.14	Correlation of normalized flame consumption speed $s_c/s_{L,0}$ and normalized flame stretch Ka along the steady-state Bunsen flame for the lean (left) and rich (right) case.	85
4.15	Response of the hydrogen-air Bunsen flame at $\phi = 4$ to flow oscillations with different frequencies f	86
4.16	Instantaneous heat release rate field on a two-dimensional cutting plane through the flames at $f = 1/\tau_c$ or $Da = 1$	86
4.17	Example of computing the averaged Markstein number \overline{Ma} from eight time instances based on the conditional mean of flame speed and flame stretch for the lean flame at $Da = 0.5$	87
4.18	Ratio of averaged Markstein number \overline{Ma} to the steady-state Markstein number Ma for the lean and rich flames for different Damköhler numbers Da	88
4.19	Normalized global flame speed s_T for different Da for the lean (left) and rich (right) flames.	89
4.20	Global flame speed plotted against the bulk flow.	90
4.21	Global flame speed fluctuation s'_T divided by the characteristic flow fluctuation u' for different Damköhler numbers from the two-dimensional Bunsen flame simulations and the Schmid model.	91
4.22	Schematic view of flame particles on a steady-state Bunsen flame.	93
4.23	Flame particles, shown as yellow spheres, tracking a fuel mass fraction iso-surface during the oscillation.	94
4.24	Recorded time signals of the balance terms of the fuel species balance equation from a single flame particle, moving from the base of the flame to the tip of the flame with $\phi = 0.5$. Left: steady-state case. Right: oscillation with $f = 1/\tau_c$	95
4.25	Recorded time signals of flame speed, flame stretch and balance terms of the fuel species balance equation for the flame with $\phi = 4$ and $Da = 1$	96
4.26	Computational setup for the simulation of turbulent flames.	99

List of Figures

4.27	Instantaneous snapshot of temperature iso-surfaces colored by the fuel mass fraction.	100
4.28	Turbulent flame speed s_T and surface area of the turbulent flame front A_t over time for the two hydrogen flames.	101
4.29	Efficiency factor I_0 over time for the three turbulent flame cases.	102
4.30	Flame particles (FP) randomly seeded on an iso-surface of $Y_{F,iso}$ for visualization purposes for the flame in case c.	103
4.31	Flame speed to flame stretch correlation from the flame in case b.	104
4.32	Trajectories of the flame particle cluster in space.	105
4.33	Particle trajectories in the flame speed and flame stretch space for the consumption speed, displacement speed and the components of displacement speed.	106
4.34	Particle trajectories in the flame speed and local equivalence ratio space for the consumption speed, displacement speed and the components of displacement speed.	108
4.35	Time signal of $Ka(t)$ and $s_c(t)$ (top) for a single flame particle on the lean hydrogen flame (left) and methane flame (right).	109
4.36	Pearson correlation coefficient $\rho(Ka(t), s_c(t + \Delta t)/s_{L,0})$ for different values of Δt	110
4.37	Correlation of consumption speed and the two components of displacement speed with flame stretch from the particle cluster.	111
4.38	Flame relaxation time Δt as a function of local frequencies or local Damköhler numbers.	112
4.39	Ratio of averaged Markstein number \overline{Ma} to the steady-state Markstein number Ma from oscillating Bunsen flames together with the Markstein number recovered from the turbulent hydrogen flame.	114
4.40	Trajectories of 5000 flame particles on the flame of case b, starting in regions with positive flame stretch and moving to regions with large negative flame stretch.	115
4.41	Joint probability density function of flame speed and flame stretch.	116
4.42	Ensemble average of 50 000 particles for different quantities over the flame particle's lifetime for the three turbulent flame cases.	117
4.43	Time signals of different quantities for a single flame particle on the flame of case b.	119
4.44	Scatterplot of instantaneous consumption speed and instantaneous flame stretch from 10 000 flame particles for the flame in case b. In the moderate flame stretch regime, the scattered data collapse to the blue region when adjusted by the local flame relaxation time Δt	120
C.1	Flame's response in terms of the global consumption speed for different conditions (1).	156

C.2	Flame's response in terms of the global consumption speed for different conditions (2).	157
D.1	Analytic solution and high frequency limit for pulsating pipe flows.	162
D.2	Computational setup of the 2D pipe flow case.	162
D.3	Center-line velocity at $x = 9.9$ m over time.	164
D.4	Pressure distribution at the steady state.	165
D.5	Radial velocity profile at different positions compared to the analytic pipe flow solution.	166
D.6	Radial balance term profiles taken at different positions.	166
D.7	Axial profile of the convective term of the momentum equation from the steady-state solution.	167
D.8	Centerline velocity $ u(r = 0) $ along the pipe length in the steady state for different pressures.	168
D.9	Axial pressure distribution at different phase angles and pressure time signal.	169
D.10	Time signals of the normalized mass flow rate and normalized pressure gradient.	169
D.11	Ratio of normalized mass flow rate amplitude and normalized pressure gradient amplitude from the analytic solution, experimental measurements and simulations.	170
D.12	Ratio of normalized mass flow rate amplitude and normalized pressure gradient amplitude.	171
D.13	Normalized ratio of mass flow rate and pressure gradient over normalized frequency.	173
D.14	Phase shift between pressure gradient and mass flow rate for pulsatile pipe flows.	174
D.15	Phase shift between pressure gradient and mass flow rate for the 1D setups.	175
D.16	Spatial profile of pressure at a single time instant during the pipe flow oscillation with different frequencies.	176
E.1	Working principle and work flow of the converter tool that automatically generates highly optimized C++ code for computing chemical reaction rates.	185
E.2	Example of the reaction parameters specified in the GRI 3.0 reaction mechanism for a subset of reactions.	186
E.3	Automatically generated chemistry kernel for the computation of rate constants for the GRI 3.0 reaction mechanism.	187
E.4	Machine code for the loop that computes the rate constants.	188
E.5	Automatically generated chemistry kernel for the computation of the equilibrium constant.	189

List of Figures

E.6	Machine code for the chemistry kernel computing the equilibrium constant.	190
E.7	Time required for computing the chemical reaction rates.	191
E.8	Measurement of parallel communication with Extrac and visualized with Paraver.	193
E.9	Principle of the load balancing algorithm.	195
E.10	First part of the load balancing algorithm. Every N time steps, the process pairs are determined.	196
E.11	Implementation of workload sharing once the processor pairs have been determined.	197
E.12	Time required for computing the chemical reaction rates t_{chem} on each parallel process without (left) and with (right) the new load balancing approach.	198
E.13	Strong scaling results on the supercomputers ForHLR II and Hazel Hen on up to 28 800 CPU cores.	199
E.14	Strong scaling measurements on the supercomputer HoreKa.	200
F.1	$L_{1,\text{rel}}$ error for different discretization schemes and mesh resolutions computed with standard OpenFOAM®.	205
F.2	Initial solution for the two-dimensional Taylor–Green vortex case, showing the z -component of vorticity.	206
F.3	x -component of the centerline velocity at $t = 10t_c$ with different discretization schemes along with the analytic solution on a mesh with 89×89 cells.	207
F.4	Convergence order for the simulation using the cubic scheme for the two-dimensional Taylor–Green vortex case.	208
F.5	Flow field of the three-dimensional Taylor–Green vortex visualized by an iso-surface of the Q -criterion, colored by the z -component of vorticity at different times.	209
F.6	Normalized volume-averaged dissipation rate over time for different discretization schemes on a mesh with 512^3 cells.	210
F.7	Setup for the zero-dimensional auto-ignition simulation.	211
F.8	Temporal profiles of main (left) and intermediate (right) species during the auto-ignition of methane and air computed with the DNS solver and Cantera.	212
F.9	Computational domain and initial conditions for the simulation of the freely propagating methane-air flame with the DNS solver.	212
F.10	Spatial profiles of main (left) and intermediate (right) species through the freely propagating methane-air flame computed with the DNS solver and Cantera in the steady state.	213

F.11 Schematic view (not to scale) of the simulation setup. Methane and air enter from separate pipes on the left and partially mix in pipe (A). A hot pilot in domain (B) ignites and stabilizes the flame. 214

F.12 Instantaneous snapshot of the temperature field (top) and heat release rate (bottom) on a two-dimensional cutting plane. 215

F.13 Mean and rms values of the axial velocity at different axial positions x/D from simulation and experiments. 215

F.14 Reynolds averaged mean and rms values of radial temperature T , mixture fraction Z and mass fraction distributions (top to bottom) at different axial positions (left to right). 216

List of Tables

3.1	Memory required to store one flame particle (assuming 64 bit floating points and 32 bit integers).	55
3.2	Time for one simulation time step t_{tot} with 1000 CPU cores and different numbers of flame particles.	57
3.3	For validation, the evaluation of different quantities within the flame particle code with their general expressions can be compared with the analytic expression for one-dimensional, spherically expanding flames [129].	58
4.1	Flame transit time and flame thickness for the lean hydrogen flames used in the harmonically oscillating equivalence ratio cases.	69
4.2	t_{relax} in ms for different hydrogen-air flames.	78
4.3	Properties of the freely propagating lean and rich hydrogen flames at atmospheric conditions.	83
4.4	Properties of the corresponding freely propagating flames, turbulence parameters and mesh settings.	100
B.1	Comparison of OpenFOAM®'s tensor notation (denominator notation) and the numerator convention.	151
D.1	Numerical settings for the oscillating flows.	163
D.2	Dimensionless frequency F , physical frequency f , time scale of the frequency $1/f$ and wave length of the pressure wave λ for the considered high frequency cases.	177

Bibliography

- [1] J. D. HUNTER, “Matplotlib: A 2D graphics environment,” *Computing in Science & Engineering*, vol. 9, no. 3, pp. 90–95, 2007. 10.1109/M-CSE.2007.55.
- [2] J. AHRENS, B. GEVECI, AND C. LAW, “Paraview: An end-user tool for large data visualization,” *The visualization handbook*, vol. 717, no. 8, 2005.
- [3] U. AYACHIT, *The paraview guide: a parallel visualization application*. Kitware, Inc., 2015.
- [4] “BP energy outlook,” 2020.
- [5] F. BIROL, “World energy outlook,” *International Energy Agency*, 2020.
- [6] “A hydrogen strategy for a climate neutral europe,” 2020.
- [7] “The national hydrogen strategy.” www.bmwi.de, 2020.
- [8] G. OZTARLIK, L. SELLE, T. POINSOT, AND T. SCHULLER, “Suppression of instabilities of swirled premixed flames with minimal secondary hydrogen injection,” *Combustion and Flame*, vol. 214, pp. 266–276, 2020. 10.1016/j.combustflame.2019.12.032.
- [9] A. LIPATNIKOV, *Fundamentals of premixed turbulent combustion*. CRC Press, 2019.
- [10] T. POINSOT AND D. VEYNANTE, *Theoretical and Numerical Combustion*. R.T. Edwards, 2001. ISBN-10: 1930217056.

Bibliography

- [11] N. PETERS, “Turbulent combustion,” 2001. 10.1017/CBO9780511612701.
- [12] S. B. POPE, “Turbulent flows,” 2001. 10.1017/CBO9780511840531.
- [13] H. TENNEKES AND J. L. LUMLEY, *A first course in turbulence*. MIT press, 2018. ISBN: 9780262200196.
- [14] J. WARNATZ, U. MAAS, R. W. DIBBLE, AND J. WARNATZ, *Combustion*. Springer, 2006.
- [15] R. BORGHI, “On the structure and morphology of turbulent premixed flames,” in *Recent advances in the Aerospace Sciences*, pp. 117–138, Springer, 1985. 10.1007/978-1-4684-4298-4_7.
- [16] N. PETERS, “Laminar flamelet concepts in turbulent combustion,” in *Symposium (International) on Combustion*, vol. 21, pp. 1231–1250, Elsevier, 1988. 10.1016/S0082-0784(88)80355-2.
- [17] C. LAW, *Combustion Physics*. Cambridge University Press, 2010.
- [18] U. MAAS AND S. B. POPE, “Simplifying chemical kinetics: intrinsic low-dimensional manifolds in composition space,” *Combustion and flame*, vol. 88, no. 3-4, pp. 239–264, 1992. 10.1016/0010-2180(92)90034-M.
- [19] C. CHI, A. ABDELSAMIE, AND D. THÉVENIN, “Direct numerical simulations of hotspot-induced ignition in homogeneous hydrogen-air pre-mixtures and ignition spot tracking,” *Flow, turbulence and combustion*, vol. 101, no. 1, pp. 103–121, 2018. 10.1007/s10494-017-9883-1.
- [20] Y. MINAMOTO AND J. H. CHEN, “DNS of a turbulent lifted DME jet flame,” *Combustion and Flame*, vol. 169, pp. 38–50, 2016. 10.1016/j.combustflame.2016.04.007.
- [21] D. K. DALAKOTI, B. SAVARD, E. R. HAWKES, A. WEHRFRITZ, H. WANG, M. S. DAY, AND J. B. BELL, “Direct numerical simulation of a spatially developing n-dodecane jet flame under spray a thermochemical conditions: Flame structure and stabilisation mechanism,” *Combustion and Flame*, vol. 217, pp. 57–76, 2020. 10.1016/j.combustflame.2020.03.027.
- [22] H. WANG, K. LUO, E. R. HAWKES, J. H. CHEN, AND J. FAN, “Turbulence, evaporation and combustion interactions in n-heptane droplets under high pressure conditions using DNS,” *Combustion and Flame*, vol. 225, pp. 417–427, 2021. 10.1016/j.combustflame.2020.11.021.

- [23] M. KLEIN, A. HERBERT, H. KOSAKA, B. BÖHM, A. DREIZLER, N. CHAKRABORTY, V. PAPAPOSTOULOU, H. G. IM, AND J. HASSLBERGER, “Evaluation of flame area based on detailed chemistry DNS of premixed turbulent hydrogen-air flames in different regimes of combustion,” *Flow, Turbulence and Combustion*, vol. 104, no. 2, pp. 403–419, 2020. 10.1007/s10494-019-00068-2.
- [24] M. KLEIN, C. KASTEN, N. CHAKRABORTY, N. MUKHADIYEV, AND H. G. IM, “Turbulent scalar fluxes in H₂-air premixed flames at low and high Karlovitz numbers,” *Combustion Theory and Modelling*, vol. 22, no. 6, pp. 1033–1048, 2018. 10.1080/13647830.2018.1468034.
- [25] N. SWAMINATHAN, “Physical insights on MILD combustion from DNS,” *Frontiers in Mechanical Engineering*, vol. 5, p. 59, 2019. 10.3389/fmech.2019.00059.
- [26] P. TRISJONO AND H. PITSCH, “Systematic analysis strategies for the development of combustion models from DNS: A review,” *Flow, Turbulence and Combustion*, vol. 95, no. 2, pp. 231–259, 2015.
- [27] D. BRADLEY, P. GASKELL, A. SEDAGHAT, AND X. GU, “Generation of PDFs for flame curvature and for flame stretch rate in premixed turbulent combustion,” *Combustion and flame*, vol. 135, no. 4, pp. 503–523, 2003. 10.1016/S0010-2180(03)00181-0.
- [28] C. DOPAZO, L. CIFUENTES, J. HIERRO, AND J. MARTIN, “Micro-scale mixing in turbulent constant density reacting flows and premixed combustion,” *Flow, Turbulence and Combustion*, vol. 96, no. 2, pp. 547–571, 2016. 10.1007/s10494-015-9663-8.
- [29] A. TAKBIRI-BORUJENI AND M. AYOUBI, “Application of physics-based machine learning in combustion modeling,” in *11th US National Combustion Meeting*, p. 10, 2019.
- [30] S. YAO, B. WANG, A. KRONENBURG, AND O. STEIN, “Modeling of sub-grid conditional mixing statistics in turbulent sprays using machine learning methods,” *Physics of Fluids*, vol. 32, no. 11, p. 115124, 2020. 10.1063/5.0027524.
- [31] K. WAN, C. BARNAUD, L. VERVISCH, AND P. DOMINGO, “Machine learning for detailed chemistry reduction in dns of a syngas turbulent oxy-flame with side-wall effects,” *Proceedings of the Combustion Institute*, vol. 38, no. 2, pp. 2825–2833, 2021. 10.1016/j.proci.2020.06.047.

- [32] K. WAN, C. BARNAUD, L. VERVISCH, AND P. DOMINGO, “Chemistry reduction using machine learning trained from non-premixed micro-mixing modeling: Application to DNS of a syngas turbulent oxy-flame with side-wall effects,” *Combustion and Flame*, vol. 220, pp. 119–129, 2020. 10.1016/j.combustflame.2020.06.008.
- [33] M. GAUDING, F. DIETZSCH, J. H. GOEBBERT, D. THÉVENIN, A. ABDELSAMIE, AND C. HASSE, “Dissipation element analysis of a turbulent non-premixed jet flame,” *Physics of Fluids*, vol. 29, no. 8, p. 085103, 2017. 10.1063/1.4991574.
- [34] A. SCHOLTISSEK, F. DIETZSCH, M. GAUDING, AND C. HASSE, “In-situ tracking of mixture fraction gradient trajectories and unsteady flamelet analysis in turbulent non-premixed combustion,” *Combustion and Flame*, vol. 175, pp. 243–258, 2017. 10.1016/j.combustflame.2016.07.011.
- [35] D. DENKER, A. ATTILI, K. KLEINHEINZ, AND H. PITSCH, “Gradient trajectory analysis of the burning rate in turbulent premixed jet flames,” *Combustion Science and Technology*, vol. 192, no. 11, pp. 2189–2207, 2020. 10.1080/00102202.2020.1811242.
- [36] D. DENKER, A. ATTILI, S. LUCA, F. BISETTI, M. GAUDING, AND H. PITSCH, “Dissipation element analysis of turbulent premixed jet flames,” *Combustion Science and Technology*, 2019. 10.1080/00102202.2019.1604517.
- [37] H. PITSCH AND A. ATTILI, *Data Analysis for Direct Numerical Simulations of Turbulent Combustion*. Springer, 2020. 10.1007/978-3-030-44718-2.
- [38] J. C. SUTHERLAND AND A. PARENTE, “Combustion modeling using principal component analysis,” *Proceedings of the Combustion Institute*, vol. 32, no. 1, pp. 1563–1570, 2009. 10.1016/j.proci.2008.06.147.
- [39] O. OWOYELE AND T. ECHEKKI, “Toward computationally efficient combustion DNS with complex fuels via principal component transport,” *Combustion Theory and Modelling*, vol. 21, no. 4, pp. 770–798, 2017. 10.1080/13647830.2017.1296976.
- [40] Z. WANG AND J. ABRAHAM, “Effects of Karlovitz number on flame surface wrinkling in turbulent lean premixed methane-air flames,” *Combustion Science and Technology*, vol. 190, no. 3, pp. 363–392, 2018. 10.1080/00102202.2017.1391232.

- [41] W. SONG, H. DAVE, H. G. IM, S. CHAUDHURI, *ET AL.*, “Local flame displacement speeds of hydrogen-air premixed flames in moderate to intense turbulence,” *arXiv preprint*, 2021. arXiv:2106.08407.
- [42] J. H. CHEN AND H. G. IM, “Correlation of flame speed with stretch in turbulent premixed methane/air flames,” in *Symposium (International) on Combustion*, vol. 27, pp. 819–826, Elsevier, 1998. 10.1016/S0082-0784(98)80477-3.
- [43] N. CHAKRABORTY, M. KLEIN, AND R. CANT, “Stretch rate effects on displacement speed in turbulent premixed flame kernels in the thin reaction zones regime,” *Proceedings of the Combustion Institute*, vol. 31, no. 1, pp. 1385–1392, 2007. 10.1016/j.proci.2006.07.184.
- [44] A. HERBERT, U. AHMED, N. CHAKRABORTY, AND M. KLEIN, “Applicability of extrapolation relations for curvature and stretch rate dependences of displacement speed for statistically planar turbulent premixed flames,” *Combustion Theory and Modelling*, vol. 24, no. 6, pp. 1021–1038, 2020. 10.1080/13647830.2020.1802066.
- [45] S. CHAUDHURI, “Life of flame particles embedded in premixed flames interacting with near isotropic turbulence,” *Proceedings of the Combustion Institute*, vol. 35, no. 2, pp. 1305–1312, 2015. 10.1016/j.proci.2014.08.007.
- [46] D. G. GOODWIN, R. L. SPETH, H. K. MOFFAT, AND B. W. WEBER, “Cantera: An object-oriented software toolkit for chemical kinetics, thermodynamics, and transport processes.” <https://www.cantera.org>, 2021. Version 2.5.1.
- [47] R. YU, T. NILSSON, X.-S. BAI, AND A. N. LIPATNIKOV, “Evolution of averaged local premixed flame thickness in a turbulent flow,” *Combustion and Flame*, vol. 207, pp. 232–249, 2019. 10.1016/j.combustflame.2019.05.045.
- [48] T. NILSSON, H. CARLSSON, R. YU, AND X.-S. BAI, “Structures of turbulent premixed flames in the high karlovitz number regime—DNS analysis,” *Fuel*, vol. 216, pp. 627–638, 2018. 10.1016/j.fuel.2017.12.046.
- [49] K. TSUBOI, R. MATSUGI, AND E. TOMITA, “Evaluation of the local burning velocity using DNS data of turbulent premixed flames,” *Natural Science*, vol. 2014, 2014. 10.4236/ns.2014.612093.
- [50] F. H. VANCE, Y. SHOSHIN, L. DE GOEY, AND J. A. VAN OIJEN, “A physical relationship between consumption and displacement speed for

Bibliography

- premixed flames with finite thickness,” *Proceedings of the Combustion Institute*, vol. 38, no. 2, pp. 2215–2223, 2021. 10.1016/j.proci.2020.06.349.
- [51] J. LI, Z. ZHAO, A. KAZAKOV, AND F. L. DRYER, “An updated comprehensive kinetic model of hydrogen combustion,” *International journal of chemical kinetics*, vol. 36, no. 10, pp. 566–575, 2004. 10.1002/kin.20026.
- [52] R. J. KEE, M. E. COLTRIN, AND P. GLARBORG, *Chemically reacting flow: theory and practice*. John Wiley & Sons, 2005. 10.1002/0471461296.
- [53] N. PETERS, “The turbulent burning velocity for large-scale and small-scale turbulence,” *Journal of Fluid mechanics*, vol. 384, pp. 107–132, 1999. 10.1017/S0022112098004212.
- [54] R. ABDEL-GAYED, D. BRADLEY, AND F.-K. LUNG, “Combustion regimes and the straining of turbulent premixed flames,” *Combustion and Flame*, vol. 76, no. 2, pp. 213–218, 1989. 10.1016/0010-2180(89)90068-0.
- [55] T. POINSOT, D. VEYNANTE, AND S. CANDEL, “Quenching processes and premixed turbulent combustion diagrams,” *Journal of Fluid mechanics*, vol. 228, pp. 561–606, 1991. 10.1017/S0022112091002823.
- [56] J. F. DRISCOLL, J. H. CHEN, A. W. SKIBA, C. D. CARTER, E. R. HAWKES, AND H. WANG, “Premixed flames subjected to extreme turbulence: Some questions and recent answers,” *Progress in Energy and Combustion Science*, vol. 76, p. 100802, 2020. 10.1016/j.pecs.2019.100802.
- [57] G. DAMKÖHLER, “Der Einfluss der Turbulenz auf die Flammengeschwindigkeit in Gasgemischen,” *Zeitschrift für Elektrochemie und angewandte physikalische Chemie*, vol. 46, no. 11, pp. 601–626, 1940. 10.1002/bbpc.19400461102.
- [58] V. ZIMONT, “Theory of turbulent combustion of a homogeneous fuel mixture at high reynolds numbers,” *Combustion, Explosion and Shock Waves*, vol. 15, no. 3, pp. 305–311, 1979. 10.1007/BF00785062.
- [59] H. WANG, E. R. HAWKES, J. H. CHEN, B. ZHOU, Z. LI, AND M. ALDÉN, “Direct numerical simulations of a high Karlovitz number laboratory premixed jet flame—an analysis of flame stretch and flame thickening,” *Journal of Fluid Mechanics*, vol. 815, pp. 511–536, 2017. 10.1017/jfm.2017.53.
- [60] R. PRUD’HOMME, *Flows of reactive fluids*, vol. 94. Springer Science & Business Media, 2010. 10.1007/978-0-8176-4659-2.

- [61] K. K.-Y. KUO AND R. ACHARYA, *Fundamentals of turbulent and multiphase combustion*. John Wiley & Sons, 2012. 10.1002/9781118107683.
- [62] I. GLASSMAN, R. A. YETTER, AND N. G. GLUMAC, *Combustion*. Academic press, 2014. 9780124079137.
- [63] S. TURNS, “An introduction to combustion: concepts and applications,” *Mechanical Engineering Series*. McGraw Hill, 2000. 10.1007/978-3-540-45363-5.
- [64] D. VEYNANTE AND L. VERVISCH, “Turbulent combustion modeling,” *Progress in energy and combustion science*, vol. 28, no. 3, pp. 193–266, 2002. 10.1016/S0360-1285(01)00017-X.
- [65] T. ECHEKKI AND E. MASTORAKOS, *Turbulent combustion modeling: Advances, new trends and perspectives*, vol. 95. Springer Science & Business Media, 2010. 10.1007/978-94-007-0412-1.
- [66] H.-P. SCHMID, *Ein Verbrennungsmodell zur Beschreibung der Wärme-freisetzung von vorgemischten turbulenten Flammen*. Karlsruhe Institute of Technology, 1996.
- [67] H.-P. SCHMID, P. HABISREUTHER, AND W. LEUCKEL, “A model for calculating heat release in premixed turbulent flames,” *Combustion and Flame*, vol. 113, no. 1-2, pp. 79–91, 1998. 10.1016/S0010-2180(97)00193-4.
- [68] F. ZHANG, T. ZIRWES, P. HABISREUTHER, H. BOCKHORN, D. TRIMIS, H. NAWROTH, AND C. O. PASCHEREIT, “Impact of combustion modeling on the spectral response of heat release in LES,” *Combustion Science and Technology*, vol. 191, no. 9, pp. 1520–1540, 2019. 10.1080/00102202.2018.1558218.
- [69] F. ZHANG, T. ZIRWES, P. HABISREUTHER, N. ZARZALIS, H. BOCKHORN, AND D. TRIMIS, “Numerical simulations of turbulent flame propagation in a fan-stirred combustion bomb and bunsen-burner at elevated pressure,” *Flow, Turbulence and Combustion*, vol. 106, no. 3, pp. 925–944, 2021. 10.1007/s10494-020-00209-y.
- [70] B. KARLOVITZ, D. DENNISTON JR, D. KNAPSCHAEFER, AND F. WELLS, “Studies on turbulent flames: A. flame propagation across velocity gradients B. Turbulence measurement in flames,” in *Symposium (international) on combustion*, vol. 4, pp. 613–620, Elsevier, 1953. 10.1016/S0082-0784(53)80082-2.

Bibliography

- [71] F. WILLIAMS, “A review of some theoretical considerations of turbulent flame structure,” in *AGARD Conference Proceeding, 1975*, 1975.
- [72] F. A. WILLIAMS, *Combustion theory*. CRC Press, 2018. 10.1201/9780429494055.
- [73] J. BUCKMASTER, “The quenching of two-dimensional premixed flames,” *Acta astronautica*, vol. 6, no. 5-6, pp. 741–769, 1979. 10.1016/0094-5765(79)90031-6.
- [74] R. A. STREHLOW AND L. D. SAVAGE, “The concept of flame stretch,” *Combustion and Flame*, vol. 31, pp. 209–211, 1978. 10.1016/0010-2180(78)90130-X.
- [75] M. MATALON, “On flame stretch,” *Combustion science and technology*, vol. 31, no. 3-4, pp. 169–181, 1983. 10.1080/00102208308923638.
- [76] S. M. CANDEL AND T. J. POINSOT, “Flame stretch and the balance equation for the flame area,” *Combustion Science and Technology*, vol. 70, no. 1-3, pp. 1–15, 1990. 10.1080/00102209008951608.
- [77] S. H. CHUNG AND C. LAW, “An invariant derivation of flame stretch,” *Combustion and Flame*, vol. 55, pp. 123–125, 1984. 10.1016/0010-2180(84)90156-1.
- [78] K. K. KUO, *Principles of combustion*. Wiley-Interscience, 2005. ISBN: 0471046892.
- [79] J. BEECKMANN, R. HESSE, S. KRUSE, A. BERENS, N. PETERS, H. PITSCH, AND M. MATALON, “Propagation speed and stability of spherically expanding hydrogen/air flames: Experimental study and asymptotics,” *Proceedings of the Combustion Institute*, vol. 36, no. 1, pp. 1531–1538, 2017. 10.1016/j.proci.2016.06.194.
- [80] C. DOPAZO, L. CIFUENTES, J. MARTIN, AND C. JIMENEZ, “Strain rates normal to approaching iso-scalar surfaces in a turbulent premixed flame,” *Combustion and flame*, vol. 162, no. 5, pp. 1729–1736, 2015. 10.1016/j.combustflame.2014.11.034.
- [81] C. DOPAZO AND L. CIFUENTES, “The physics of scalar gradients in turbulent premixed combustion and its relevance to modeling,” *Combustion Science and Technology*, vol. 188, no. 9, pp. 1376–1397, 2016. 10.1080/00102202.2016.1197919.

- [82] C. DOPAZO, J. MARTIN, L. CIFUENTES, AND J. HIERRO, “Strain, rotation and curvature of non-material propagating iso-scalar surfaces in homogeneous turbulence,” *Flow, Turbulence and Combustion*, vol. 101, no. 1, pp. 1–32, 2018. 10.1007/s10494-017-9888-9.
- [83] L. DE GOEY AND J. TEN THIJE BOONKAMP, “A mass-based definition of flame stretch for flames with finite thickness,” *Combustion science and technology*, vol. 122, no. 1-6, pp. 399–405, 1997. 10.1080/00102209708935618.
- [84] R. BASTIAANS, J. VAN OIJEN, AND L. DE GOEY, “Analysis of a strong mass-based flame stretch model for turbulent premixed combustion,” *Physics of Fluids*, vol. 21, no. 1, p. 015105, 2009. 10.1063/1.3059616.
- [85] L. DE GOEY, J. VAN OIJEN, V. KORNILOV, AND J. TEN THIJE BOONKAMP, “Propagation, dynamics and control of laminar premixed flames,” *Proceedings of the Combustion Institute*, vol. 33, no. 1, pp. 863–886, 2011. 10.1016/j.proci.2010.09.006.
- [86] G. MARKSTEIN, “Non-steady flame propagation,” 1964.
- [87] A. P. KELLEY AND C. K. LAW, “Nonlinear effects in the extraction of laminar flame speeds from expanding spherical flames,” *Combustion and Flame*, vol. 156, no. 9, pp. 1844–1851, 2009. 10.1016/j.combustflame.2009.04.004.
- [88] F. HALTER, T. TAHTOUH, AND C. MOUNAÏM-ROUSSELLE, “Nonlinear effects of stretch on the flame front propagation,” *Combustion and Flame*, vol. 157, no. 10, pp. 1825–1832, 2010. 10.1016/j.combustflame.2010.05.013.
- [89] Z. CHEN, “On the extraction of laminar flame speed and markstein length from outwardly propagating spherical flames,” *Combustion and Flame*, vol. 158, no. 2, pp. 291–300, 2011. 10.1016/j.combustflame.2010.09.001.
- [90] F. WU, W. LIANG, Z. CHEN, Y. JU, AND C. K. LAW, “Uncertainty in stretch extrapolation of laminar flame speed from expanding spherical flames,” *Proceedings of the Combustion Institute*, vol. 35, no. 1, pp. 663–670, 2015. 10.1016/j.proci.2014.05.065.
- [91] A. N. LIPATNIKOV, S. S. SHY, AND W.-Y. LI, “Experimental assessment of various methods of determination of laminar flame speed in experiments with expanding spherical flames with positive markstein lengths,” *Combustion and Flame*, vol. 162, no. 7, pp. 2840–2854, 2015. 10.1016/j.combustflame.2015.04.003.

Bibliography

- [92] W. LIANG, F. WU, AND C. K. LAW, “Extrapolation of laminar flame speeds from stretched flames: Role of finite flame thickness,” *Proceedings of the Combustion Institute*, vol. 36, no. 1, pp. 1137–1143, 2017. 10.1016/j.proci.2016.08.074.
- [93] D. BRADLEY, P. H. GASKELL, AND X. GU, “Burning velocities, Markstein lengths, and flame quenching for spherical methane-air flames: a computational study,” *Combustion and flame*, vol. 104, no. 1-2, pp. 176–198, 1996. 10.1016/0010-2180(95)00115-8.
- [94] J. BECHTOLD AND M. MATALON, “The dependence of the Markstein length on stoichiometry,” *Combustion and flame*, vol. 127, no. 1-2, pp. 1906–1913, 2001. 10.1016/S0010-2180(01)00297-8.
- [95] P. CLAVIN AND J. C. GRAÑA-OTERO, “Curved and stretched flames: the two Markstein numbers,” *Journal of fluid mechanics*, vol. 686, pp. 187–217, 2011. 10.1017/jfm.2011.318.
- [96] G. K. GIANNAKOPOULOS, M. MATALON, C. FROUZAKIS, AND A. G. TOMBOULIDES, “The curvature Markstein length and the definition of flame displacement speed for stationary spherical flames,” *Proceedings of the combustion institute*, vol. 35, no. 1, pp. 737–743, 2015. 10.1016/j.proci.2014.07.049.
- [97] M. MATALON, C. CUI, AND J. BECHTOLD, “Hydrodynamic theory of premixed flames: effects of stoichiometry, variable transport coefficients and arbitrary reaction orders,” *Journal of fluid mechanics*, vol. 487, pp. 179–210, 2003. 10.1017/S0022112003004683.
- [98] C. ALTANTZIS, C. FROUZAKIS, A. TOMBOULIDES, M. MATALON, AND K. BOULOUCHOS, “Hydrodynamic and thermodiffusive instability effects on the evolution of laminar planar lean premixed hydrogen flames,” *Journal of fluid mechanics*, vol. 700, pp. 329–361, 2012. 10.1017/jfm.2012.136.
- [99] G. K. GIANNAKOPOULOS, C. E. FROUZAKIS, S. MOHAN, A. G. TOMBOULIDES, AND M. MATALON, “Consumption and displacement speeds of stretched premixed flames-theory and simulations,” *Combustion and Flame*, vol. 208, pp. 164–181, 2019. 10.1016/j.combustflame.2019.06.027.
- [100] K. TSUBOI, E. TOMITA, *ET AL.*, “DNS analysis on the indirect relationship between the local burning velocity and the flame displacement speed of turbulent premixed flames,” *Open Journal of Fluid Dynamics*, vol. 4, no. 03, p. 288, 2014. 10.4236/ojfd.2014.43022.

- [101] T. ECHEKKI AND J. H. CHEN, “Unsteady strain rate and curvature effects in turbulent premixed methane-air flames,” *Combustion and Flame*, vol. 106, no. 1-2, pp. 184–202, 1996. 10.1016/0010-2180(96)00011-9.
- [102] D. DASGUPTA, W. SUN, M. DAY, AND T. LIEUWEN, “Effect of turbulence–chemistry interactions on chemical pathways for turbulent hydrogen–air premixed flames,” *Combustion and Flame*, vol. 176, pp. 191–201, 2017. 10.1016/j.combustflame.2016.09.029.
- [103] T. ZIRWES, F. ZHANG, J. DENEV, P. HABISREUTHER, H. BOCKHORN, AND N. ZARZALIS, “Effect of Elevated Pressure on the Flame Response To Stretch of Premixed Flames,” in *Deutscher Flammentag. Deutsche Sektion des Combustion Institutes und DVV/VDI-Gesellschaft Energie und Umwelt*, vol. 28, pp. 549–561, 2017. VDI-Berichte 2302, ISBN: 978-3-18-092302-4.
- [104] S. BALUSAMY, A. CESSOU, AND B. LECORDIER, “Laminar propagation of lean premixed flames ignited in stratified mixture,” *Combustion and Flame*, vol. 161, no. 2, pp. 427–437, 2014. 10.1016/j.combustflame.2013.08.023.
- [105] S. NAMBULLY, P. DOMINGO, V. MOUREAU, AND L. VERVISCH, “A filtered-laminar-flame PDF sub-grid-scale closure for LES of premixed turbulent flames: II. Application to a stratified bluff-body burner,” *Combustion and flame*, vol. 161, no. 7, pp. 1775–1791, 2014. 10.1016/j.combustflame.2014.01.006.
- [106] X. SHI AND J.-Y. CHEN, “Numerical analysis and model development for laminar flame speed of stratified methane/air mixtures,” *Combustion and Flame*, vol. 184, pp. 233–245, 2017. 10.1016/j.combustflame.2017.06.010.
- [107] F. N. EGOLFOPOULOS, “Dynamics and structure of unsteady, strained, laminar premixed flames,” in *Symposium (International) on Combustion*, vol. 25, pp. 1365–1373, Elsevier, 1994. 10.1016/S0082-0784(06)80779-4.
- [108] F. N. EGOLFOPOULOS AND C. S. CAMPBELL, “Unsteady counterflowing strained diffusion flames: diffusion-limited frequency response,” *Journal of Fluid Mechanics*, vol. 318, pp. 1–29, 1996. 10.1017/S0022112096007008.
- [109] C. SUNG AND C. LAW, “Ignition of oscillatory counterflowing nonpremixed hydrogen against heated air,” *Combustion science and technology*, vol. 129, no. 1-6, pp. 347–370, 1997. 10.1080/00102209708935732.

Bibliography

- [110] T. BROWN, R. PITZ, AND C. SUNG, “Oscillatory stretch effects on the structure and extinction of counterflow diffusion flames,” in *Symposium (International) on Combustion*, vol. 27, pp. 703–710, Elsevier, 1998. 10.1016/S0082-0784(98)80463-3.
- [111] C. SUNG AND C. K. LAW, “Structural sensitivity, response, and extinction of diffusion and premixed flames in oscillating counterflow,” *Combustion and flame*, vol. 123, no. 3, pp. 375–388, 2000.
- [112] C. SUNG, A. MAKINO, AND C. LAW, “On stretch-affected pulsating instability in rich hydrogen/air flames: asymptotic analysis and computation,” *Combustion and flame*, vol. 128, no. 4, pp. 422–434, 2002. 10.1016/S0010-2180(01)00361-3.
- [113] E. J. WELLE, W. L. ROBERTS, C. D. CARTER, AND J. M. DONBAR, “The response of a propane-air counter-flow diffusion flame subjected to a transient flow field,” *Combustion and Flame*, vol. 135, no. 3, pp. 285–297, 2003. 10.1016/S0010-2180(03)00167-6.
- [114] PREETHAM, H. SANTOSH, AND T. LIEUWEN, “Dynamics of laminar premixed flames forced by harmonic velocity disturbances,” *Journal of Propulsion and Power*, vol. 24, no. 6, pp. 1390–1402, 2008. 10.2514/1.35432.
- [115] H. WANG, C. K. LAW, AND T. LIEUWEN, “Linear response of stretch-affected premixed flames to flow oscillations,” *Combustion and flame*, vol. 156, no. 4, pp. 889–895, 2009. 10.1016/J.COMBUST-FLAME.2009.01.012.
- [116] PREETHAM, S. K. THUMULURU, H. SANTOSH, AND T. LIEUWEN, “Linear response of laminar premixed flames to flow oscillations: unsteady stretch effects,” *Journal of propulsion and power*, vol. 26, no. 3, pp. 524–532, 2010. 10.2514/1.41559.
- [117] F. ZHANG, T. ZIRWES, P. HABISREUTHER, AND H. BOCKHORN, “Effect of unsteady stretching on the flame local dynamics,” *Combustion and Flame*, vol. 175, pp. 170–179, 2017. 10.1016/j.combustflame.2016.05.028.
- [118] F. THIESSET, F. HALTER, C. BARIKI, C. LAPEYRE, C. CHAUVEAU, I. GÖKALP, L. SELLE, AND T. POINSOT, “Isolating strain and curvature effects in premixed flame/vortex interactions,” *Journal of Fluid Mechanics*, vol. 831, pp. 618–654, 2017. 10.1017/jfm.2017.641.

- [119] K. YU, C. SUNG, AND C. K. LAW, “Some aspects of the freely propagating premixed flame in a spatially periodic flow field,” *Combustion and flame*, vol. 97, no. 3-4, pp. 375–383, 1994. 10.1016/0010-2180(94)90028-0.
- [120] J. KISTLER, C. SUNG, T. KREUT, C. K. LAW, AND M. NISHIOKA, “Extinction of counterflow diffusion flames under velocity oscillations,” in *Symposium (International) on Combustion*, vol. 26, pp. 113–120, Elsevier, 1996. 10.1016/S0082-0784(96)80207-4.
- [121] R. SANKARAN AND H. G. IM, “Dynamic flammability limits of methane/air premixed flames with mixture composition fluctuations,” *Proceedings of the Combustion Institute*, vol. 29, no. 1, pp. 77–84, 2002. 10.1016/S1540-7489(02)80014-1.
- [122] A. POTNIS, V. R. UNNI, H. G. IM, AND A. SAHA, “Extinction of non-equidiffusive premixed flames with oscillating strain rates,” *Combustion and Flame*, vol. 234, p. 111617, 2021. 10.1016/j.combustflame.2021.111617.
- [123] T. C. LIEUWEN, *Unsteady combustor physics*. Cambridge University Press, 2012. ISBN: 1107015995.
- [124] A. SCHOLTISSEK, P. DOMINGO, L. VERVISCH, AND C. HASSE, “A self-contained progress variable space solution method for thermochemical variables and flame speed in freely-propagating premixed flamelets,” *Proceedings of the Combustion Institute*, vol. 37, no. 2, pp. 1529–1536, 2019. 10.1016/j.proci.2018.06.168.
- [125] A. SCHOLTISSEK, P. DOMINGO, L. VERVISCH, AND C. HASSE, “A self-contained composition space solution method for strained and curved premixed flamelets,” *Combustion and Flame*, vol. 207, pp. 342–355, 2019. 10.1016/j.combustflame.2019.06.010.
- [126] H. BÖTTLER, A. SCHOLTISSEK, X. CHEN, Z. CHEN, AND C. HASSE, “Premixed flames for arbitrary combinations of strain and curvature,” *Proceedings of the Combustion Institute*, vol. 38, no. 2, pp. 2031–2039, 2021. 10.1016/j.proci.2020.06.312.
- [127] D. BRADLEY, “Problems of predicting turbulent burning rates,” *Combustion Theory and Modelling*, vol. 6, no. 2, p. 361, 2002. 10.1088/1364-7830/6/2/312.

Bibliography

- [128] J. F. DRISCOLL, “Turbulent premixed combustion: Flamelet structure and its effect on turbulent burning velocities,” *Progress in Energy and Combustion Science*, vol. 34, no. 1, pp. 91–134, 2008. 10.1016/j.pecs.2007.04.002.
- [129] M. WEISS, *Untersuchung von Flammenfrontstreckungseffekten auf die sphärische Flammenausbreitung laminarer und turbulenter Brennstoff/Luft-Gemische*. Karlsruhe Institute of Technology, 2008.
- [130] M. WEISS, N. ZARZALIS, AND R. SUNTZ, “Experimental study of Markstein number effects on laminar flamelet velocity in turbulent premixed flames,” *Combustion and Flame*, vol. 154, no. 4, pp. 671–691, 2008. 10.1016/j.combustflame.2008.06.011.
- [131] K. N. C. BRAY AND R. CANT, “Some applications of kolmogorov’s turbulence research in the field of combustion,” *Proceedings of the Royal Society of London. Series A: Mathematical and Physical Sciences*, vol. 434, no. 1890, pp. 217–240, 1991.
- [132] S. HEMCHANDRA AND T. LIEUWEN, “Local consumption speed of turbulent premixed flames—an analysis of “memory effects”,” *Combustion and Flame*, vol. 157, no. 5, pp. 955–965, 2010. 10.1016/j.combustflame.2009.10.007.
- [133] H. G. IM, P. G. ARIAS, S. CHAUDHURI, AND H. A. URANAKARA, “Direct numerical simulations of statistically stationary turbulent premixed flames,” *Combustion Science and Technology*, vol. 188, no. 8, pp. 1182–1198, 2016. 10.1080/00102202.2016.1198789.
- [134] H. G. IM AND J. H. CHEN, “Effects of flow transients on the burning velocity of laminar hydrogen/air premixed flames,” *Proceedings of the Combustion Institute*, vol. 28, no. 2, pp. 1833–1840, 2000. 10.1016/S0082-0784(00)80586-X.
- [135] B. MCBRIDE, S. GORDON, AND M. RENO, *Coefficients for Calculating Thermodynamic and Transport Properties of Individual Species*. National Aeronautics and Space Administration, 1993. NASA Technical Memorandum 4513.
- [136] J. O. HIRSCHFELDER, C. F. CURTISS, AND R. B. BIRD, “Molecular theory of gases and liquids,” *Molecular theory of gases and liquids*, 1964.
- [137] B. POLING, J. PRAUSNITZ, AND J. O’CONNELL, *The Properties of Gases and Liquids*. McGraw Hill Professional, 5th ed., 2004. ISBN-10: 0070116822.

-
- [138] G. LEWIS-DIXON, “Flame Structure and Flame Reaction Kinetics. II. Transport Phenomena in Multicomponent Systems,” *Proc. Roy. Soc. A*, vol. 307, no. 1488, pp. 111–135, 1968. 10.1017/CBO9780511754517.
- [139] J. HIRSCHFELDER, C. CURTISS, R. BIRD, AND M. MAYER, *Molecular theory of gases and liquids*, vol. 26. Wiley New York, 1954. ISBN: 978-0-471-40065-3.
- [140] V. GIOVANGIGLI, “Multicomponent flow modeling,” *Science China Mathematics*, vol. 55, no. 2, pp. 285–308, 2012. 10.1007/s11425-011-4346-y.
- [141] R. B. BIRD, E. W. STEWART, AND E. N. LIGHTFOOT, *Transport phenomena*. Wiley, 2007. ISBN: 978-0470115398.
- [142] L. MONCHICK AND E. MASON, “Transport properties of polar gases,” *J. Chem. Phys.*, vol. 35, no. 5, pp. 1676–1697, 1961. 10.1063/1.1732130.
- [143] J. H. FERZIGER, M. PERIĆ, AND R. L. STREET, *Computational methods for fluid dynamics*, vol. 3. Springer, 2002. 10.1007/978-3-319-99693-6.
- [144] F. MOUKALLED, L. MANGANI, M. DARWISH, ET AL., *The finite volume method in computational fluid dynamics*, vol. 113. Springer, 2016. 10.1007/978-3-319-16874-6.
- [145] H. K. VERSTEEG AND W. MALALASEKERA, *An introduction to computational fluid dynamics: the finite volume method*. Pearson education, 2007. ISBN: 9780131274983.
- [146] R. BARRETT, M. BERRY, T. F. CHAN, J. DEMMEL, J. DONATO, J. DONGARRA, V. EIJKHOUT, R. POZO, C. ROMINE, AND H. VAN DER VORST, *Templates for the solution of linear systems: building blocks for iterative methods*. SIAM, 1994.
- [147] H. A. VAN DER VORST, “Bi-cgstab: A fast and smoothly converging variant of bi-cg for the solution of nonsymmetric linear systems,” *SIAM Journal on scientific and Statistical Computing*, vol. 13, no. 2, pp. 631–644, 1992. 10.1137/0913035.
- [148] R. I. ISSA, “Solution of the implicitly discretised fluid flow equations by operator-splitting,” *Journal of computational physics*, vol. 62, no. 1, pp. 40–65, 1986. 10.1016/0021-9991(86)90099-9.

Bibliography

- [149] L. CARETTO, A. GOSMAN, S. PATANKAR, AND D. SPALDING, “Two calculation procedures for steady, three-dimensional flows with recirculation,” in *Proceedings of the third international conference on numerical methods in fluid mechanics*, pp. 60–68, Springer, 1973. 10.1007/BFb0112677.
- [150] E. KOMEN, A. SHAMS, L. CAMILO, AND B. KOREN, “Quasi-DNS capabilities of OpenFOAM for different mesh types,” *Computers & Fluids*, vol. 96, pp. 87–104, 2014. 10.1016/j.compfluid.2014.02.013.
- [151] C. HABCHI AND G. ANTAR, “Direct numerical simulation of electromagnetically forced flows using OpenFOAM,” *Computers & Fluids*, vol. 116, pp. 1–9, 2015. 10.1016/j.compfluid.2015.04.011.
- [152] Y. ADDAD, I. ZAIDI, AND D. LAURENCE, “Quasi-DNS of natural convection flow in a cylindrical annuli with an optimal polyhedral mesh refinement,” *Computers & Fluids*, vol. 118, pp. 44–52, 2015. 10.1016/j.compfluid.2015.06.014.
- [153] G. LECRIVAIN, R. RAYAN, A. HURTADO, AND U. HAMPEL, “Using quasi-DNS to investigate the deposition of elongated aerosol particles in a wavy channel flow,” *Computers & Fluids*, vol. 124, pp. 78–85, 2016. 10.1016/j.compfluid.2015.10.012.
- [154] X. CHU AND E. LAURIEN, “Direct numerical simulation of heated turbulent pipe flow at supercritical pressure,” *Journal of Nuclear Engineering and Radiation Science*, vol. 2, no. 3, p. 031019, 2016. 10.1115/1.4032479.
- [155] X. CHU AND E. LAURIEN, “Flow stratification of supercritical CO₂ in a heated horizontal pipe,” *The Journal of Supercritical Fluids*, vol. 116, pp. 172–189, 2016.
- [156] X. CHU, E. LAURIEN, AND D. M. MCELIGOT, “Direct numerical simulation of strongly heated air flow in a vertical pipe,” *International Journal of Heat and Mass Transfer*, vol. 101, pp. 1163–1176, 2016. 10.1016/j.ijheatmasstransfer.2016.05.038.
- [157] G. TUFANO, O. STEIN, A. KRONENBURG, A. FRASSOLDATI, T. FARAVELLI, L. DENG, A. KEMPF, M. VASCELLARI, AND C. HASSE, “Resolved flow simulation of pulverized coal particle devolatilization and ignition in air-and O₂/CO₂-atmospheres,” *Fuel*, vol. 186, pp. 285–292, 2016. 10.1016/j.fuel.2016.08.073.

- [158] S. VO, A. KRONENBURG, O. T. STEIN, AND E. R. HAWKES, “Direct numerical simulation of non-premixed syngas combustion using OpenFOAM,” in *High Performance Computing in Science and Engineering '16*, pp. 245–257, Springer, 2016. 10.1007/978-3-319-47066-5₁₇.
- [159] S. VO, A. KRONENBURG, O. STEIN, AND M. CLEARY, “Multiple mapping conditioning for silica nanoparticle nucleation in turbulent flows,” *Proceedings of the Combustion Institute*, vol. 36, no. 1, pp. 1089–1097, 2017. 10.1016/j.proci.2016.08.088.
- [160] B. WANG, A. KRONENBURG, D. DIETZEL, AND O. STEIN, “Assessment of scaling laws for mixing fields in inter-droplet space,” *Proceedings of the Combustion Institute*, vol. 36, no. 2, pp. 2451–2458, 2017. 10.1016/j.proci.2016.06.036.
- [161] B. WANG, A. KRONENBURG, G. L. TUFANO, AND O. T. STEIN, “Fully resolved DNS of droplet array combustion in turbulent convective flows and modelling for mixing fields in inter-droplet space,” *Combustion and Flame*, vol. 189, pp. 347–366, 2018. 10.1016/j.combustflame.2017.11.003.
- [162] E. KOMEN, L. CAMILO, A. SHAMS, B. J. GEURTS, AND B. KOREN, “A quantification method for numerical dissipation in quasi-DNS and under-resolved DNS, and effects of numerical dissipation in quasi-DNS and under-resolved DNS of turbulent channel flows,” *Journal of computational physics*, vol. 345, pp. 565–595, 2017.
- [163] L. BRICTEUX, S. ZEOLI, AND N. BOURGEOIS, “Validation and scalability of an open source parallel flow solver,” *Concurrency and Computation: Practice and Experience*, vol. 29, no. 21, p. e4330, 2017. 10.1002/cpe.4330.
- [164] S. ZHONG, Z. PENG, Y. LI, H. LI, AND F. ZHANG, “Direct numerical simulation of methane turbulent premixed oxy-fuel combustion,” tech. rep., SAE Technical Paper, 2017. 10.4271/2017-01-2192.
- [165] E. ZHENG, M. RUDMAN, J. SINGH, AND S. KUANG, “Assessing OpenFOAM for DNS of turbulent non-Newtonian flow in a pipe,” in *21st Australasian Fluid Mechanics Conference*, vol. 21, Australasian Fluid Mechanics Society, 2018.
- [166] G. TUFANO, O. STEIN, A. KRONENBURG, G. GENTILE, A. STAGNI, A. FRASSOLDATI, T. FARAVELLI, A. KEMPF, M. VASCELLARI, AND C. HASSE, “Fully-resolved simulations of coal particle combustion using

Bibliography

- a detailed multi-step approach for heterogeneous kinetics,” *Fuel*, vol. 240, pp. 75–83, 2019. 10.1016/j.fuel.2018.11.139.
- [167] E. ZHENG, M. RUDMAN, J. SINGH, AND S. KUANG, “Direct numerical simulation of turbulent non-Newtonian flow using OpenFOAM,” *Applied Mathematical Modelling*, vol. 72, pp. 50–67, 2019. 10.1016/j.apm.2019.03.003.
- [168] T. ZIRWES, F. ZHANG, P. HABISREUTHER, M. HANSINGER, H. BOCKHORN, M. PFITZNER, AND D. TRIMIS, “Quasi-DNS dataset of a piloted flame with inhomogeneous inlet conditions,” *Flow, Turbulence and Combustion*, vol. 104, pp. 997–1027, 2020. 10.1007/s10494-021-00244-3.
- [169] F. ZHANG, H. BONART, T. ZIRWES, P. HABISREUTHER, H. BOCKHORN, AND N. ZARZALIS, “Direct numerical simulation of chemically reacting flows with the public domain code OpenFOAM,” in *High Performance Computing in Science and Engineering '14* (W. NAGEL, D. KRÖNER, AND M. RESCH, eds.), pp. 221–236, Springer, 2015. 10.1007/978-3-319-10810-0₁6.
- [170] F. ZHANG, T. ZIRWES, P. HABISREUTHER, AND H. BOCKHORN, “A DNS Analysis of the Evaluation of Heat Release Rates from Chemiluminescence Measurements in Turbulent Combustion,” in *High Performance Computing in Science and Engineering '16* (W. NAGEL, D. KRÖNER, AND M. RESCH, eds.), pp. 229–243, Springer, 2016. 10.1007/978-3-319-47066-5₁6.
- [171] “OpenFOAM: The open source CFD toolbox.” www.openfoam.com.
- [172] S. POPE, “The evolution of surfaces in turbulence,” *International journal of engineering science*, vol. 26, no. 5, pp. 445–469, 1988. 10.1098/rspa.1991.0090.
- [173] P. E. HAMLINGTON, R. DARRAGH, C. A. BRINER, C. A. TOWERY, B. D. TAYLOR, AND A. Y. POLUDNENKO, “Lagrangian analysis of high-speed turbulent premixed reacting flows: Thermochemical trajectories in hydrogen–air flames,” *Combustion and Flame*, vol. 186, pp. 193–207, 2017. 10.1016/j.combustflame.2017.08.001.
- [174] C. A. TOWERY, P. E. HAMLINGTON, X. ZHAO, C. XU, T. LU, AND A. POLUDNENKO, “Lagrangian chemical explosive mode analysis of highly turbulent premixed flames,” in *AIAA Scitech 2019 Forum*, p. 1643, 2019. 10.2514/6.2019-1643.

- [175] T. ZHENG, J. YOU, AND Y. YANG, “Principal curvatures and area ratio of propagating surfaces in isotropic turbulence,” *Physical Review Fluids*, vol. 2, no. 10, p. 103201, 2017. 10.1103/PhysRevFluids.2.103201.
- [176] Y. YANG, D. PULLIN, AND I. BERMEJO-MORENO, “Multi-scale geometric analysis of lagrangian structures in isotropic turbulence,” *Journal of Fluid Mechanics*, vol. 654, pp. 233–270, 2010. 10.1017/S0022112010000571.
- [177] T. OSTER, A. ABDELSAMIE, M. MOTEJAT, T. GERRITS, C. RÖSSL, D. THÉVENIN, AND H. THEISEL, “On-the-fly tracking of flame surfaces for the visual analysis of combustion processes,” in *Computer Graphics Forum*, vol. 37, pp. 358–369, Wiley Online Library, 2018. 10.1111/cgf.13331.
- [178] P. SRIPAKAGORN, S. MITARAI, G. KOSÁLY, AND H. PITSCH, “Extinction and reignition in a diffusion flame: a direct numerical simulation study,” *Journal of Fluid Mechanics*, vol. 518, pp. 231–259, 2004. 10.1017/S0022112004001004.
- [179] H. A. URANAKAR, S. CHAUDHURI, AND K. LAKSHMISHA, “Turbulence-transport-chemistry interaction in statistically planar premixed flames and ignition kernels in near isotropic turbulence,” in *Gas Turbine India Conference*, vol. 49644, p. V001T03A016, American Society of Mechanical Engineers, 2014.
- [180] H. A. URANAKARA, S. CHAUDHURI, H. L. DAVE, P. G. ARIAS, AND H. G. IM, “A flame particle tracking analysis of turbulence–chemistry interaction in hydrogen–air premixed flames,” *Combustion and Flame*, vol. 163, pp. 220–240, 2016. 10.1016/j.combustflame.2015.09.033.
- [181] S. CHAUDHURI, “Global and local viewpoints to analyze turbulence-premixed flame interaction,” in *Combustion for Power Generation and Transportation*, pp. 101–123, Springer, 2017. 10.1007/978-981-10-3785-6₆.
- [182] S. CHAUDHURI, “Pair dispersion of turbulent premixed flame elements,” *Physical Review E*, vol. 91, no. 2, p. 021001, 2015. 10.1103/PhysRevE.91.021001.
- [183] H. L. DAVE, A. MOHAN, AND S. CHAUDHURI, “Genesis and evolution of premixed flames in turbulence,” *Combustion and Flame*, vol. 196, pp. 386–399, 2018. 10.1016/j.combustflame.2018.06.030.

Bibliography

- [184] H. L. DAVE AND S. CHAUDHURI, “Evolution of local flame displacement speeds in turbulence,” *Journal of Fluid Mechanics*, vol. 884, 2020. 10.1017/jfm.2019.896.
- [185] M. HATWAR, A. S. NAYAK, H. L. DAVE, U. AGGARWAL, AND S. CHAUDHURI, “Cluster analysis of turbulent premixed combustion using on-the-fly flame particle tracking,” in *Sustainable Development for Energy, Power, and Propulsion*, pp. 389–413, Springer, 2021. 10.1007/978-981-15-5667-8_15.
- [186] D. J. HIGHAM AND N. J. HIGHAM, *MATLAB guide*, vol. 150. Siam, 2016.
- [187] T. ZIRWES, F. ZHANG, P. HABISREUTHER, J. DENEV, H. BOCKHORN, AND D. TRIMIS, “HPC Implementation of Flame Particle Tracking for Studying Laminar and Turbulent Flame Dynamics.” Seventeenth International Conference on Numerical Combustion. MS8-208, Aachen. Germany, 6–8 May 2019. (*Presentation*).
- [188] T. ZIRWES, F. ZHANG, Y. WANG, P. HABISREUTHER, J. DENEV, Z. CHEN, H. BOCKHORN, AND D. TRIMIS, “In-situ Flame Particle Tracking Based on Barycentric Coordinates for Studying Local Flame Dynamics in Pulsating Bunsen Flames,” in *Proceedings of the Combustion Institute*, vol. 38, pp. 2057–2066, Elsevier, 2021. 10.1016/j.proci.2020.07.033.
- [189] T. ZIRWES, F. ZHANG, J. DENEV, P. HABISREUTHER, H. BOCKHORN, AND D. TRIMIS, “Implementation of Lagrangian Surface Tracking for High Performance Computing,” in *High Performance Computing in Science and Engineering '20* (W. NAGEL, D. KRÖNER, AND M. RESCH, eds.), Springer, 2020. 10.1007/978-3-030-80602-6_15.
- [190] T. ZIRWES, F. ZHANG, J. DENEV, P. HABISREUTHER, H. BOCKHORN, AND D. TRIMIS, “Lagrangian Tracking of Material Surfaces in Reacting Flows,” in *OpenFOAM Workshop*, vol. 15, 2020.
- [191] Y. KOZAK, S. S. DAMMATI, L. G. BRAVO, P. E. HAMLINGTON, AND A. POLUDNENKO, “Novel lagrangian-particle tracking method for highly compressible, turbulent, reacting flows,” in *AIAA Scitech 2019 Forum*, p. 1642, 2019. 10.2514/6.2019-1642.
- [192] Y. KOZAK, S. S. DAMMATI, L. G. BRAVO, P. E. HAMLINGTON, AND A. Y. POLUDNENKO, “Weno interpolation for lagrangian particles in highly compressible flow regimes,” *Journal of Computational Physics*, vol. 402, p. 109054, 2020. 10.1016/j.jcp.2019.109054.

- [193] F. ZHANG, T. ZIRWES, T. MÜLLER, S. WACHTER, T. JAKOBS, P. HABISREUTHER, N. ZARZALIS, D. TRIMIS, AND T. KOLB, “Effect of elevated pressure on air-assisted primary atomization of coaxial liquid jets: Basic research for entrained flow gasification,” *Renewable and Sustainable Energy Reviews*, vol. 134, p. 110411, 2020. 10.1016/j.rser.2020.110411.
- [194] F. ZHANG, H. HEIDARIFATASMI, S. HARTH, T. ZIRWES, R. WANG, M. FEDORYK, N. SEBBAR, P. HABISREUTHER, D. TRIMIS, AND H. BOCKHORN, “Numerical evaluation of a novel double-concentric swirl burner for sulfur combustion,” *Renewable and Sustainable Energy Reviews*, vol. 133, p. 110257, 2020. 10.1016/j.rser.2020.110257.
- [195] W. F. NOH AND P. WOODWARD, “Slic (simple line interface calculation),” in *Proceedings of the fifth international conference on numerical methods in fluid dynamics*, pp. 330–340, Springer, 1976.
- [196] B. NICHOLS, C. HIRT, AND R. HOTCHKISS, “Volume of fluid (VOF) method for the dynamics of free boundaries,” *Journal of Computational Physics*, vol. 39, pp. 201–225, 1981. 10.1016/0021-9991(81)90145-5.
- [197] J. G. LEE, K. KIM, AND D. SANTAVICCA, “Measurement of equivalence ratio fluctuation and its effect on heat release during unstable combustion,” *Proceedings of the Combustion Institute*, vol. 28, no. 1, pp. 415–421, 2000. 10.1016/S0082-0784(00)80238-6.
- [198] H. M. ALTAY, R. L. SPETH, D. E. HUDGINS, AND A. F. GHONIEM, “The impact of equivalence ratio oscillations on combustion dynamics in a backward-facing step combustor,” *Combustion and Flame*, vol. 156, no. 11, pp. 2106–2116, 2009. 10.1016/j.combustflame.2009.07.024.
- [199] B. ČOSIĆ, S. TERHAAR, J. P. MOECK, AND C. O. PASCHEREIT, “Response of a swirl-stabilized flame to simultaneous perturbations in equivalence ratio and velocity at high oscillation amplitudes,” *Combustion and Flame*, vol. 162, no. 4, pp. 1046–1062, 2015. 10.1016/j.combustflame.2014.09.025.
- [200] SHREEKRISHNA, S. HEMCHANDRA, AND T. LIEUWEN, “Premixed flame response to equivalence ratio perturbations,” *Combustion Theory and Modelling*, vol. 14, no. 5, pp. 681–714, 2010. 10.1080/13647830.2010.502247.

Bibliography

- [201] S. HEMCHANDRA, “Premixed flame response to equivalence ratio fluctuations: Comparison between reduced order modeling and detailed computations,” *Combustion and flame*, vol. 159, no. 12, pp. 3530–3543, 2012. 10.1016/j.combustflame.2012.08.003.
- [202] C. SCHRÖDINGER, C. O. PASCHEREIT, AND M. OEVERMANN, “Numerical studies on the impact of equivalence ratio oscillations on lean premixed flame characteristics and emissions,” *Combustion Science and Technology*, vol. 186, no. 10-11, pp. 1392–1409, 2014. 10.1080/00102202.2014.934610.
- [203] H. TOMITA, M. R. A. RAHMAN, S. MIYAMAE, T. YOKOMORI, AND T. UEDA, “Flame dynamics of equivalence ratio oscillations in a laminar stagnating lean methane/air premixed flame,” *Proceedings of the Combustion Institute*, vol. 35, no. 1, pp. 989–997, 2015. 10.1016/j.proci.2014.07.061.
- [204] A. ALBAYRAK, R. BLUMENTHAL, A. ULHAQ, AND W. POLIFKE, “An analytical model for the impulse response of laminar premixed flames to equivalence ratio perturbations,” *Proceedings of the Combustion Institute*, vol. 36, no. 3, pp. 3725–3732, 2017. 10.1016/j.proci.2016.06.002.
- [205] J. ZHANG AND J. ABRAHAM, “A numerical study of laminar flames propagating in stratified mixtures,” *Combustion and Flame*, vol. 163, pp. 461–471, 2016. 10.1016/j.combustflame.2015.10.020.
- [206] T. TOMIDOKORO, T. YOKOMORI, H. G. IM, AND T. UEDA, “Characteristics of counterflow premixed flames with low frequency composition fluctuations,” *Combustion and Flame*, vol. 212, pp. 13–24, 2020. 10.1016/j.combustflame.2019.10.004.
- [207] F. GALEAZZO, F. ZHANG, T. ZIRWES, P. HABISREUTHER, H. BOCKHORN, N. ZARZALIS, AND D. TRIMIS, “Implementation of an Efficient Synthetic Inflow Turbulence-Generator in the Open-Source Code OpenFOAM for 3D LES/DNS Applications,” in *High Performance Computing in Science and Engineering '20* (W. NAGEL, D. KRÖNER, AND M. RESCH, eds.), Springer, 2020. 10.1007/978-3-030-80602-6_14.
- [208] M. KLEIN, A. SADIKI, AND J. JANICKA, “A digital filter based generation of inflow data for spatially developing direct numerical or large eddy simulations,” *Journal of computational Physics*, vol. 186, no. 2, pp. 652–665, 2003. 10.1016/S0021-9991(03)00090-1.
- [209] “HPE Apollo Hawk at High Performance Computing Center Stuttgart.” www.hlrs.de/systems/hpe-apollo-hawk, 2020.

- [210] “Horeka at karlsruhe institute of technology.” <https://www.scc.kit.edu/dienste/horeka.php>, 2021.
- [211] U. AHMED, N. CHAKRABORTY, AND M. KLEIN, “Insights into the bending effect in premixed turbulent combustion using the flame surface density transport,” *Combustion Science and Technology*, vol. 191, no. 5-6, pp. 898–920, 2019. 10.1080/00102202.2019.1577241.
- [212] R. YU AND A. N. LIPATNIKOV, “DNS study of the bending effect due to smoothing mechanism,” *Fluids*, vol. 4, no. 1, p. 31, 2019. 10.3390/fluids4010031.
- [213] E. R. HAWKES AND J. H. CHEN, “Evaluation of models for flame stretch due to curvature in the thin reaction zones regime,” *Proceedings of the Combustion Institute*, vol. 30, no. 1, pp. 647–655, 2005. /10.1016/j.proci.2004.08.106.
- [214] S. TRIVEDI, H. KOLLA, J. CHEN, AND R. CANT, “Analysis of flame-flame interactions in premixed hydrocarbon and hydrogen flames,” *Physical Review Fluids*, vol. 5, no. 11, p. 113201, 2020. 10.1103/PhysRevFluids.5.113201.
- [215] P. KELLY, *Solid Mechanics Lecture Notes - An Introduction to Solid Mechanics. Part III: Foundations of Continuum Mechanics*. The University of Auckland, 2013.
- [216] T. PARR AND J. HOWARD, “The matrix calculus you need for deep learning,” *arXiv preprint arXiv:1802.01528*, 2018.
- [217] B. ÜNSAL, *Time-Dependent laminar, transitional and turbulent pipe flows*. PhD thesis, Friedrich-Alexander-Universität Erlangen-Nürnberg (FAU), 2008. ISBN: 978-3-639-08075-9.
- [218] P. LAMBOSSY, “Oscillations forcees d’un liquide incompressible et visqueux dans un tube rigide et horizontal. calcul de la force frottement,” *Helv. Physica Acta*, vol. 25, pp. 371–386, 1952.
- [219] S. GRACE, “XCIV. Oscillatory motion of a viscous liquid in a long straight tube,” *The London, Edinburgh, and Dublin Philosophical Magazine and Journal of Science*, vol. 5, no. 31, pp. 933–939, 1928. 10.1080/14786440508564536.
- [220] K. HADDAD, Ö. ERTUNÇ, M. MISHRA, AND A. DELGADO, “Pulsating laminar fully developed channel and pipe flows,” *Physical Review E*, vol. 81, no. 1, p. 016303, 2010. 10.1103/PhysRevE.81.016303.

Bibliography

- [221] B. ÜNSAL, S. RAY, F. DURST, AND Ö. ERTUNÇ, “Pulsating laminar pipe flows with sinusoidal mass flux variations,” *Fluid dynamics research*, vol. 37, no. 5, p. 317, 2005. 10.1016/j.fluiddyn.2005.06.002.
- [222] S. RAY, B. ÜNSAL, F. DURST, Ö. ERTUNC, AND O. BAYOUMI, “Mass flow rate controlled fully developed laminar pulsating pipe flows,” *J. Fluids Eng*, pp. 405–418, 2005. 10.1115/1.1906265.
- [223] F. DURST, M. ISMAILOV, AND D. TRIMIS, “Measurement of instantaneous flow rates in periodically operating injection systems,” *Experiments in fluids*, vol. 20, no. 3, pp. 178–188, 1996. 10.1007/BF00190273.
- [224] T. LU AND C. K. LAW, “Toward accommodating realistic fuel chemistry in large-scale computations,” *Progress in Energy and Combustion Science*, vol. 35, no. 2, pp. 192–215, 2009. 10.1016/j.pecs.2008.10.002.
- [225] M. MEHL, W. J. PITZ, C. K. WESTBROOK, AND H. J. CURRAN, “Kinetic modeling of gasoline surrogate components and mixtures under engine conditions,” *Proceedings of the Combustion Institute*, vol. 33, no. 1, pp. 193–200, 2011. 10.1016/j.proci.2010.05.027.
- [226] O. HERBINET, W. J. PITZ, AND C. K. WESTBROOK, “Detailed chemical kinetic oxidation mechanism for a biodiesel surrogate,” *Combustion and Flame*, vol. 154, no. 3, pp. 507–528, 2008. 10.1016/j.combustflame.2008.03.003.
- [227] W. J. PITZ AND C. J. MUELLER, “Recent progress in the development of diesel surrogate fuels,” *Progress in Energy and Combustion Science*, vol. 37, no. 3, pp. 330–350, 2011. 10.1016/j.pecs.2010.06.004.
- [228] T. ZIRWES, F. ZHANG, J. DENEV, P. HABISREUTHER, AND H. BOCKHORN, “Automated Code Generation for Maximizing Performance of Detailed Chemistry Calculations in OpenFOAM,” in *High Performance Computing in Science and Engineering '17* (W. NAGEL, D. KRÖNER, AND M. RESCH, eds.), pp. 189–204, Springer, 2017. 10.1007/978-3-319-68394-2_11.
- [229] S. B. POPE, “Computationally efficient implementation of combustion chemistry using in situ adaptive tabulation,” *Combustion Theory and Modelling*, pp. 41–63, 1997. 10.1080/713665229.
- [230] Y. SHI, W. H. GREEN, H.-W. WONG, AND O. O. OLUWOLE, “Accelerating multi-dimensional combustion simulations using GPU and hybrid explicit/implicit ODE integration,” *Combustion and Flame*, vol. 159, no. 7, pp. 2388–2397, 2012. 10.1016/j.combustflame.2012.02.016.

- [231] R. A. WHITESIDES, M. J. MCNENLY, AND D. L. FLOWERS, “Optimizing time integration of chemical-kinetic networks for speed and accuracy,” tech. rep., Lawrence Livermore National Lab.(LLNL), Livermore, CA (United States), 2013.
- [232] M. J. MCNENLY, R. A. WHITESIDES, AND D. L. FLOWERS, “Adaptive preconditioning strategies for integrating large kinetic mechanisms,” tech. rep., Lawrence Livermore National Lab.(LLNL), Livermore, CA (United States), 2013.
- [233] M. FÜRST, P. SABIA, M. LUBRANO LAVADERA, G. AVERSANO, M. DE JOANNON, A. FRASSOLDATI, AND A. PARENTE, “Optimization of chemical kinetics for methane and biomass pyrolysis products in moderate or intense low-oxygen dilution combustion,” *Energy & fuels*, vol. 32, no. 10, pp. 10194–10201, 2018. 10.1021/acs.energyfuels.8b01022.
- [234] C. RACKAUCKAS, Y. MA, V. DIXIT, X. GUO, M. INNES, J. REVELS, J. NYBERG, AND V. IVATURI, “A comparison of automatic differentiation and continuous sensitivity analysis for derivatives of differential equation solutions,” *arXiv preprint*, 2018. arXiv:1812.01892.
- [235] M. J. MCNENLY, R. A. WHITESIDES, AND D. L. FLOWERS, “Faster solvers for large kinetic mechanisms using adaptive preconditioners,” *Proceedings of the Combustion Institute*, vol. 35, no. 1, pp. 581–587, 2015. 10.1016/j.proci.2014.05.113.
- [236] F. PERINI, E. GALLIGANI, AND R. D. REITZ, “An analytical Jacobian approach to sparse reaction kinetics for computationally efficient combustion modeling with large reaction mechanisms,” *Energy & Fuels*, vol. 26, no. 8, pp. 4804–4822, 2012. 10.1021/ef300747n.
- [237] F. PERINI, E. GALLIGANI, AND R. D. REITZ, “A study of direct and Krylov iterative sparse solver techniques to approach linear scaling of the integration of chemical kinetics with detailed combustion mechanisms,” *Combustion and Flame*, vol. 161, no. 5, pp. 1180–1195, 2014. 10.1016/j.combustflame.2013.11.017.
- [238] F. PERINI, B. D. ADHIKARY, J. H. LIM, X. SU, Y. RA, H. WANG, AND R. REITZ, “Improved chemical kinetics numerics for the efficient simulation of advanced combustion strategies,” *SAE International Journal of Engines*, vol. 7, no. 1, pp. 243–255, 2014.

Bibliography

- [239] K. E. NIEMEYER AND C.-J. SUNG, “Accelerating moderately stiff chemical kinetics in reactive-flow simulations using GPUs,” *Journal of Computational Physics*, vol. 256, pp. 854–871, 2014. 10.1016/j.jcp.2013.09.025.
- [240] K. NIEMEYER, N. CURTIS, AND C. SUNG, “pyJac: analytical Jacobian generator for chemical kinetics,” *arXiv preprint*, 2016. arXiv:1605.03262.
- [241] D. A. SCHWER, P. LU, W. H. GREEN JR, AND V. SEMIAO, “A consistent-splitting approach to computing stiff steady-state reacting flows with adaptive chemistry,” *Combustion Theory and Modelling*, vol. 7, no. 2, p. 383, 2003. 10.1088/1364-7830/7/2/310.
- [242] F. PERINI, A. KRISHNASAMY, Y. RA, AND R. D. REITZ, “Computationally efficient simulation of multicomponent fuel combustion using a sparse analytical jacobian chemistry solver and high-dimensional clustering,” *Journal of Engineering for Gas Turbines and Power*, vol. 136, no. 9, 2014. 10.1115/1.4027280.
- [243] C. P. STONE AND F. BISETTI, “Comparison of ODE solver for chemical kinetics and reactive CFD applications,” in *52nd Aerospace Sciences Meeting*, p. 0822, 2014. 10.2514/6.2014-0822.
- [244] S. YANG, X. WANG, H. HUO, W. SUN, AND V. YANG, “An efficient finite-rate chemistry model for a preconditioned compressible flow solver and its comparison with the flamelet/progress-variable model,” *Combustion and Flame*, vol. 210, pp. 172–182, 2019. 10.1016/j.combustflame.2019.08.035.
- [245] J. WU, G. DONG, AND B. LI, “Performance of parallel chemistry acceleration algorithm in simulations of gaseous detonation: Effects of fuel type and numerical scheme resolution,” *Combustion Science and Technology*, vol. 191, pp. 2185–2207, 2018. 10.1080/00102202.2018.1549039.
- [246] H. WU, P. C. MA, AND M. IHME, “Efficient time-stepping techniques for simulating turbulent reactive flows with stiff chemistry,” *Computer Physics Communications*, vol. 243, pp. 81–96, 2019. 10.1016/j.cpc.2019.04.016.
- [247] V. DAMIAN, A. SANDU, M. DAMIAN, F. POTRA, AND G. R. CARMICHAEL, “The kinetic preprocessor KPP—a software environment for solving chemical kinetics,” *Computers & Chemical Engineering*, vol. 26, no. 11, pp. 1567–1579, 2002. 10.1016/S0098-1354(02)00128-X.
- [248] J. C. LINFORD, J. MICHALAKES, M. VACHHARAJANI, AND A. SANDU, “Automatic generation of multicore chemical kernels,” *IEEE Transactions*

- on *Parallel and Distributed Systems*, vol. 22, no. 1, pp. 119–131, 2010. 10.1109/TPDS.2010.106.
- [249] “SUNDIALS: Suite of nonlinear and differential/algebraic equation solvers.” <http://computation.llnl.gov/casc/sundials/main.html>.
- [250] T. ZIRWES, “Effect of stretch on the burning velocity of laminar and turbulent premixed flames,” Master’s thesis, Karlsruhe Institute of Technology, 2016. 10.5445/IR/1000094585.
- [251] G. WANNER AND E. HAIRER, *Solving ordinary differential equations II*, vol. 375. Springer Berlin Heidelberg, 1996.
- [252] A. C. HINDMARSH, P. N. BROWN, K. E. GRANT, S. L. LEE, R. SERBAN, D. E. SHUMAKER, AND C. S. WOODWARD, “SUNDIALS: Suite of nonlinear and differential/algebraic equation solvers,” *ACM Transactions on Mathematical Software (TOMS)*, vol. 31, no. 3, pp. 363–396, 2005. 10.1145/1089014.1089020.
- [253] G. HAGER AND G. WELLEIN, *Introduction to high performance computing for scientists and engineers*. CRC Press, 2010. ISBN: 9781439811931.
- [254] A. FOG, “Optimizing software in c++,” 2020.
- [255] G. SMITH, D. GOLDEN, M. FRENKLACH, N. MORIARTY, B. EITENEER, M. GOLDENBERG, *ET AL.*, “Gri 3.0 reaction mechanism.”
- [256] T. ZIRWES, F. ZHANG, J. DENEV, P. HABISREUTHER, H. BOCKHORN, AND D. TRIMIS, “Improved Vectorization for Efficient Chemistry Computations in OpenFOAM for Large Scale Combustion Simulations,” in *High Performance Computing in Science and Engineering ’18* (W. NAGEL, D. KRÖNER, AND M. RESCH, eds.), pp. 209–224, Springer, 2018. 10.1007/978-3-030-13325-2₁₃.
- [257] T. ZIRWES, F. ZHANG, J. DENEV, P. HABISREUTHER, H. BOCKHORN, AND D. TRIMIS, “Enhancing OpenFOAM’s Performance on HPC Systems,” in *High Performance Computing in Science and Engineering ’19* (W. NAGEL, D. KRÖNER, AND M. RESCH, eds.), pp. 225–239, Springer, 2019. 10.1007/978-3-030-66792-4₁₆.
- [258] T. ZIRWES, F. ZHANG, P. HABISREUTHER, J. DENEV, H. BOCKHORN, AND TRIMIS, “Implementation and Validation of a Computationally Efficient DNS Solver for Reacting Flows in OpenFOAM,” in *Proceedings of the ECCOMAS Congress*, 2021.

Bibliography

- [259] H. ROSENBROCK, “Some general implicit processes for the numerical solution of differential equations,” *The Computer Journal*, vol. 5, no. 4, pp. 329–330, 1963. 10.1093/comjnl/5.4.329.
- [260] F. PELLEGRINI AND J. ROMAN, “Scotch: A software package for static mapping by dual recursive bipartitioning of process and architecture graphs,” in *International Conference on High-Performance Computing and Networking*, pp. 493–498, Springer, 1996. 10.1007/3-540-61142-8_588.
- [261] G. KARYPIS, “Metis: Unstructured graph partitioning and sparse matrix ordering system,” *Technical report*, 1997.
- [262] T. ZIRWES, F. ZHANG, P. HABISREUTHER, M. HANSINGER, H. BOCKHORN, M. PFITZNER, AND D. TRIMIS, “Identification of Flame Regimes in Partially Premixed Combustion from a Quasi-DNS Dataset,” *Flow, Turbulence and Combustion*, 2020. 10.1007/s10494-020-00228-9.
- [263] F. ZHANG, T. ZIRWES, P. HABISREUTHER, AND H. BOCKHORN, “Numerical Simulation of Turbulent Combustion with a Multi-Regional Approach,” in *High Performance Computing in Science and Engineering '15* (W. NAGEL, D. KRÖNER, AND M. RESCH, eds.), pp. 267–280, Springer, 2015. 10.1007/978-3-319-24633-8_18.
- [264] F. ZHANG, T. ZIRWES, P. HABISREUTHER, AND H. BOCKHORN, “Towards reduction of computational cost for large-scale combustion modelling with a multi-regional concept,” *Progress in Computational Fluid Dynamics*, vol. 18, no. 6, pp. 333–346, 2018. 10.1504/PCFD.2018.096616.
- [265] L. ANTONELLI AND P. D’AMBRA, “Dynamic load balancing for high-performance simulations of combustion in engine applications,” in *2011 19th International Euromicro Conference on Parallel, Distributed and Network-Based Processing*, pp. 133–140, IEEE, 2011. 10.1109/PDP.2011.88.
- [266] V. HIREMATH, S. R. LANTZ, H. WANG, AND S. B. POPE, “Computationally-efficient and scalable parallel implementation of chemistry in simulations of turbulent combustion,” *Combustion and flame*, vol. 159, no. 10, pp. 3096–3109, 2012. 10.1016/j.combustflame.2012.04.013.
- [267] J. KODAVASAL, K. HARMS, P. SRIVASTAVA, S. SOM, S. QUAN, K. RICHARDS, AND M. GARCÍA, “Development of a stiffness-based chemistry load balancing scheme, and optimization of input/output and communication, to enable massively parallel high-fidelity internal combustion

- engine simulations,” *Journal of Energy Resources Technology*, vol. 138, no. 5, 2016. 10.1115/ICEF2015-1035.
- [268] J. MUELA, R. BORRELL, J. VENTOSA-MOLINA, L. JOFRE, O. LEHMKUHL, AND C. D. PÉREZ-SEGARRA, “A dynamic load balancing method for the evaluation of chemical reaction rates in parallel combustion simulations,” *Computers & Fluids*, vol. 190, pp. 308–321, 2019. j.compfluid.2019.06.018.
- [269] B. TEKGÜL, P. PELTONEN, H. KAHILA, O. KAARIO, AND V. VUORINEN, “DLBFoam: An open-source dynamic load balancing model for fast reacting flow simulations in OpenFOAM,” *Computer Physics Communications*, p. 108073, 2021. 10.1016/j.cpc.2021.108073.
- [270] T. ZIRWES, F. ZHANG, P. HABISREUTHER, J. DENEV, H. BOCKHORN, AND D. TRIMIS, “Optimizing Load Balancing of Reacting Flow Solvers in OpenFOAM for High Performance Computing,” in *Proceedings of the 6th OpenFOAM User Conference*, 2018.
- [271] T. ZIRWES, F. ZHANG, P. HABISREUTHER, J. DENEV, H. BOCKHORN, AND D. TRIMIS, “Adaptive Load Balancing and Automated Code Generation for Efficient Simulation of Reacting Flows,” in *Proceedings of the 32nd Parallel Computational Fluid Dynamics Conference (ParCFD21)*, vol. 32, 2021.
- [272] D. W. WALKER AND J. J. DONGARRA, “MPI: a standard message passing interface,” *Supercomputer*, vol. 12, pp. 56–68, 1996.
- [273] “Extrae, BSC tools.” <https://tools.bsc.es/extrae>.
- [274] V. PILLET, J. LABARTA, T. CORTES, AND S. GIRONA, “Paraver: A tool to visualize and analyze parallel code,” in *Proceedings of WoTUG-18: transputer and occam developments*, vol. 44, pp. 17–31, Citeseer, 1995.
- [275] H. NAWROTH, C. O. PASCHEREIT, F. ZHANG, P. HABISREUTHER, AND H. BOCKHORN, “Flow investigation and acoustic measurements of an unconfined turbulent premixed jet flame,” in *43rd AIAA Fluid Dynamics Conference*, p. 2459, 2013. 10.2514/6.2013-2459.
- [276] F. ZHANG, T. ZIRWES, H. NAWROTH, P. HABISREUTHER, H. BOCKHORN, AND C. O. PASCHEREIT, “Combustion-generated noise: An environment-related issue for future combustion systems,” *Energy Technology*, vol. 5, no. 7, pp. 1045–1054, 2017. 10.1002/ente.201600526.

Bibliography

- [277] H. NAWROTH AND C. O. PASCHEREIT, “Experimental investigation of the influence of the shear layer on direct combustion noise of a turbulent jet flame,” in *Turbo Expo: Power for Land, Sea, and Air*, vol. 50855, p. V04BT04A019, American Society of Mechanical Engineers, 2017. 10.1115/GT2017-64467.
- [278] “ForHLR II at Karlsruhe Institute of Technology.” www.scc.kit.edu/dienste/forhhr2.php, 2018.
- [279] “CRAY XC40 Hazel Hen at High Performance Computing Center Stuttgart.” www.hlrs.de/systems/cray-xc40-hazel-hen, 2018.
- [280] E. RANZI, A. FRASSOLDATI, R. GRANA, A. CUOCI, T. FARAVELLI, A. KELLEY, AND C. K. LAW, “Hierarchical and comparative kinetic modeling of laminar flame speeds of hydrocarbon and oxygenated fuels,” *Progress in Energy and Combustion Science*, vol. 38, no. 4, pp. 468–501, 2012. 10.1016/j.pecs.2012.03.004.
- [281] F. ZHANG, T. ZIRWES, T. HÄBER, H. BOCKHORN, D. TRIMIS, AND R. SUNTZ, “Near wall dynamics of premixed flames,” *Proceedings of the Combustion Institute*, vol. 38, no. 2, pp. 1955–1964, 2021. 10.1016/j.proci.2020.06.058.
- [282] T. ZIRWES, T. HÄBER, F. ZHANG, H. KOSAKA, A. DREIZLER, M. STEINHAUSEN, C. HASSE, A. STAGNI, D. TRIMIS, R. SUNTZ, *ET AL.*, “Numerical study of quenching distances for side-wall quenching using detailed diffusion and chemistry,” *Flow, Turbulence and Combustion*, vol. 106, no. 2, pp. 649–679, 2021. 10.1016/S0360-1285(98)00026-4.
- [283] M. STEINHAUSEN, Y. LUO, S. POPP, C. STRASSACKER, T. ZIRWES, H. KOSAKA, F. ZENTGRAF, U. MAAS, A. SADIKI, A. DREIZLER, AND C. HASSE, “Numerical investigation of local heat-release rates and thermochemical states in sidewall quenching of laminar methane and dimethyl ether flames,” *Flow, Turbulence and Combustion*, vol. 106, pp. 681–700, 2020. 10.1007/s10494-020-00146-w.
- [284] T. ZIRWES, F. ZHANG, M. STEINHAUSEN, P. HABISREUTHER, H. BOCKHORN, C. HASSE, AND D. TRIMIS, “Numerical database of highly-resolved turbulent flame-wall interaction for model validation,” in *30. Deutscher Flammentag. Deutsche Sektion des Combustion Institutes und DVV/VDI-Gesellschaft Energie und Umwelt*, vol. 30, 2021.

- [285] M. HANSINGER, T. ZIRWES, J. ZIPS, M. PFITZNER, F. ZHANG, P. HABISREUTHER, AND H. BOCKHORN, “The Eulerian stochastic fields method applied to large eddy simulations of a piloted flame with inhomogeneous inlet,” *Flow, Turbulence and Combustion*, vol. 105, pp. 837–867, 2020. 10.1007/s10494-020-00159-5.
- [286] T. ZIRWES, F. ZHANG, P. HABISREUTHER, H. BOCKHORN, AND D. TRIMIS, “Large-Scale Quasi-DNS of Mixed-Mode Turbulent Combustion,” *PAMM*, vol. 19, no. 1, 2019. ISSN: 1617-7061.
- [287] M. SOYSAL, M. BERGHOFF, T. ZIRWES, M.-A. VEF, S. OESTE, A. BRINKMANN, W. E. NAGEL, AND A. STREIT, “Using on-demand file systems in hpc environments,” in *2019 International Conference on High Performance Computing & Simulation (HPCS)*, pp. 390–398, IEEE, 2019. 10.1109/HPCS48598.2019.9188216.
- [288] F. ZHANG, T. BAUST, T. ZIRWES, J. DENEV, P. HABISREUTHER, N. ZARZALIS, AND H. BOCKHORN, “Impact of infinite thin flame approach on the evaluation of flame speed using spherically expanding flames,” *Energy Technology*, vol. 5, no. 7, pp. 1055–1063, 2017. 10.1002/ente.201600573.
- [289] X. CHEN, Y. WANG, T. ZIRWES, F. ZHANG, H. BOCKHORN, AND Z. CHEN, “Heat release rate markers for highly-stretched premixed CH₄/air and CH₄/H₂/air flames,” *Energy & Fuels*, 2021. 10.1021/acs.energyfuels.1c02187.
- [290] T. ZIRWES, F. ZHANG, T. HÄBER, AND H. BOCKHORN, “Ignition of combustible mixtures by hot particles at varying relative speeds,” *Combustion Science and Technology*, vol. 191, no. 1, pp. 178–195, 2019. 10.1080/00102202.2018.1435530.
- [291] T. HÄBER, T. ZIRWES, D. ROTH, F. ZHANG, H. BOCKHORN, AND U. MAAS, “Numerical simulation of the ignition of fuel/air gas mixtures around small hot particles,” *Zeitschrift für Physikalische Chemie*, vol. 231, no. 10, pp. 1625–1654, 2017. 10.1515/zpch-2016-0933.
- [292] Y. WANG, H. ZHANG, T. ZIRWES, F. ZHANG, H. BOCKHORN, AND Z. CHEN, “Ignition of dimethyl ether/air mixtures by hot particles: Impact of low temperature chemical reactions,” in *Proceedings of the Combustion Institute*, vol. 38, pp. 2459–2466, Elsevier, 2021. 10.1016/j.proci.2020.06.254.

Bibliography

- [293] M. HANSINGER, M. PFITZNER, AND V. A. SABELNIKOV, “LES of oxy-fuel jet flames using the Eulerian stochastic fields method with differential diffusion,” *Proceedings of the Combustion Institute*, vol. 38, no. 2, pp. 2665–2672, 2021. 10.1016/j.proci.2020.06.206.
- [294] G. I. TAYLOR AND A. E. GREEN, “Mechanism of the production of small eddies from large ones,” *Proceedings of the Royal Society of London. Series A-Mathematical and Physical Sciences*, vol. 158, no. 895, pp. 499–521, 1937. 10.1098/rspa.1937.0036.
- [295] M. BRACHET, “Direct simulation of three-dimensional turbulence in the Taylor–Green vortex,” *Fluid dynamics research*, vol. 8, no. 1-4, p. 1, 1991. 10.1016/0169-5983(91)90026-F.
- [296] J. DEBONIS, “Solutions of the Taylor–Green vortex problem using high-resolution explicit finite difference methods,” in *51st AIAA Aerospace Sciences Meeting including the New Horizons Forum and Aerospace Exposition*, p. 382, 2013. 10.2514/6.2013-382.
- [297] J. R. BULL AND A. JAMESON, “Simulation of the Taylor–Green vortex using high-order flux reconstruction schemes,” *AIAA Journal*, vol. 53, no. 9, pp. 2750–2761, 2015. 10.2514/1.J053766.
- [298] A. ABDELSAMIE, G. FRU, T. OSTER, F. DIETZSCH, G. JANIGA, AND D. THÉVENIN, “Towards direct numerical simulations of low-Mach number turbulent reacting and two-phase flows using immersed boundaries,” *Computers & Fluids*, vol. 131, pp. 123–141, 2016. 10.1016/j.compfluid.2016.03.017.
- [299] A. ABDELSAMIE, G. LARTIGUE, C. E. FROUZAKIS, AND D. THÉVENIN, “The Taylor–Green vortex as a benchmark for high-fidelity combustion simulations using low-Mach solvers,” *Computers & Fluids*, vol. 223, p. 104935, 2021. 10.1016/j.compfluid.2021.104935.
- [300] P. BOIVIN, M. TAYYAB, AND S. ZHAO, “Benchmarking a lattice-Boltzmann solver for reactive flows: Is the method worth the effort for combustion?,” *Physics of Fluids*, vol. 33, no. 7, p. 071703, 2021. 10.1063/5.0057352.
- [301] W. M. VAN REES, A. LEONARD, D. PULLIN, AND P. KOUMOUTSAKOS, “A comparison of vortex and pseudo-spectral methods for the simulation of periodic vortical flows at high Reynolds numbers,” *Journal of Computational Physics*, vol. 230, no. 8, pp. 2794–2805, 2011. 10.1016/j.jcp.2010.11.031.

- [302] S. MEARES AND A. R. MASRI, “A modified piloted burner for stabilizing turbulent flames of inhomogeneous mixtures,” *Combustion and Flame*, vol. 161, no. 2, pp. 484–495, 2014. 10.1016/j.combustflame.2013.09.016.
- [303] S. MEARES, V. PRASAD, G. MAGNOTTI, R. BARLOW, AND A. MASRI, “Stabilization of piloted turbulent flames with inhomogeneous inlets,” *Proceedings of the Combustion Institute*, vol. 35, no. 2, pp. 1477–1484, 2015. 10.1016/j.proci.2014.05.071.
- [304] R. BARLOW, S. MEARES, G. MAGNOTTI, H. CUTCHER, AND A. MASRI, “Local extinction and near-field structure in piloted turbulent CH₄/air jet flames with inhomogeneous inlets,” *Combustion and Flame*, vol. 162, no. 10, pp. 3516–3540, 2015. 10.1016/j.combustflame.2015.06.009.
- [305] A. MASRI, “Partial premixing and stratification in turbulent flames,” *Proceedings of the Combustion Institute*, vol. 35, no. 2, pp. 1115–1136, 2015. 10.1016/j.proci.2014.08.032.
- [306] K. KLEINHEINZ, T. KUBIS, P. TRISJONO, M. BODE, AND H. PITSCH, “Computational study of flame characteristics of a turbulent piloted jet burner with inhomogeneous inlets,” *Proceedings of the Combustion Institute*, vol. 36, no. 2, pp. 1747–1757, 2017. 10.1016/j.proci.2016.07.067.
- [307] B. A. PERRY AND M. E. MUELLER, “Effect of multiscale subfilter PDF models in LES of turbulent flames with inhomogeneous inlets,” *Proceedings of the Combustion Institute*, vol. 37, no. 2, pp. 2287–2295, 2019. 10.1016/j.proci.2018.07.116.
- [308] B. A. PERRY, M. E. MUELLER, AND A. R. MASRI, “A two mixture fraction flamelet model for large eddy simulation of turbulent flames with inhomogeneous inlets,” *Proceedings of the Combustion Institute*, vol. 36, no. 2, pp. 1767–1775, 2017. 10.1016/j.proci.2016.07.029.
- [309] H. JI, M. KWON, S. KIM, AND Y. KIM, “Numerical modeling for multiple combustion modes in turbulent partially premixed jet flames,” *Journal of Mechanical Science and Technology*, vol. 32, no. 11, pp. 5511–5519, 2018. 10.1007/s12206-018-1049-0.
- [310] L. TIAN AND R. LINDSTEDT, “Evaluation of reaction progress variable-mixture fraction statistics in partially premixed flames,” *Proceedings of the Combustion Institute*, vol. 37, no. 2, pp. 2241–2248, 2019. 10.1016/j.proci.2018.06.129.

Bibliography

- [311] T. LU AND C. LAW, “A criterion based on computational singular perturbation for the identification of quasi steady state species: A reduced mechanism for methane oxidation with no chemistry,” *Combust. Flame*, vol. 154, no. 4, pp. 761–774, 2008. [10.1016/j.combustflame.2008.04.025](https://doi.org/10.1016/j.combustflame.2008.04.025).